Towards a partial discharge free insulation system for the More Electrical Transportation

Presentato da: Luca Lusuardi

Coordinatore Dottorato: **Supervisore:**

Prof. Daniele Vigo   Prof. Andrea Cavallini

Contents

List of Figures

List of Tables

"The science of today is the technology of tomorrow."
- Edward Teller -

"There are no rules here - we're trying to accomplish something."
- Thomas A. Edison -

"Can we survive technology?"
- John von Neumann -

Introduction

One day, not too far away hopefully, the first all-electric aircraft will appear in our skies, just as our roads will be travelled by all-electric vehicles. However, there is still a long way to go before this can be happen. Electric motors and their drives must become less cumbersome and more reliable. Storage systems must improve their power densities and intrinsic safety. End users themselves will probably have to change the paradigms with which they stay on the road, especially in light of the important advances in IoT technologies.

The revolution that has been taking place in recent decades in the field of electricity conversion and the development of power electronic devices is opening up society to technological horizons that were not even vaguely imaginable thirty years ago. For example, still in the early 2000s, AC motors were generally controlled by mechanical speed multipliers, due to the high costs associated with electronic converters [34]. This evidently resulted in significant encumbrances and inefficient control. Today, power electronic devices have seen their costs decrease and their performance increase. Not only is the control significantly higher than it used to be, but the components used are lighter and more efficient.

Another aspect to consider about the reasons that move to an increasing electrification is the pollution, understood not only as the chemical one, but also as the acoustic and thermal one. This argument is particularly felt in the aeronautical sector, where the technologies used are still, for legitimate reasons, those belonging mostly to the last century. In fact, it is necessary to ensure that the installed devices on board the aircraft have a very high level of safety and, therefore, it is physiologically justified to have a longer

scale of time in technological integration. Just think of the fact that there is typically two decades between one generation of aircraft and the next.

However, the technologies are so promising that in summer 2009, ahead of the United Nations Climate Conference in Copenhagen, the aviation industry announced its commitment to a global approach to reduce greenhouse gas emissions from aviation, adopting three high-level targets:

- an average improvement in fuel efficiency of 1.5% per year from 2009 to 2020;

- a cap on net aviation CO_2 emissions from 2020 (carbon-neutral growth);

- a reduction in net CO_2 emissions of 50% by 2050 relative to 2005 levels.

Since the 10's of the new millennium, many national and international agencies involved in transport have produced various documents concerning the environmental impact of vehicles, the most promising technologies to reduce it and the strategies to be undertaken between now and 2050.

Finally, it must be considered that the use of an inverter to drive an electric actuator (or motor) gives the possibility of having a so-called fault-tolerant system. In transport systems, in particular avionics, this is a definite step forward in terms of vehicle safety.

This combination of reasons is leading transport manufacturers and research entities to invest more and more resources and people in the last decade on transport electrification. Of course, the increase of the electrical power on-board makes the efficiency and reliability of the electrical grid, the power generators and the drives a central point in the research for the future technologies. That is why there is such a spread of projects related to the More Electric Aircraft (MEA), More Electric Engine (MEE) and All Electric Aircraft (AEA) applications.

The environmental impact of transport

Whether true or false, the climate emergency is increasingly becoming the most acute social problem. Beyond the experimental evidence that does not yet convince everyone on the true extent of the problem, the various direct effects of pollution on Earth and on man are now established, not to mention the indirect social and cultural effects.
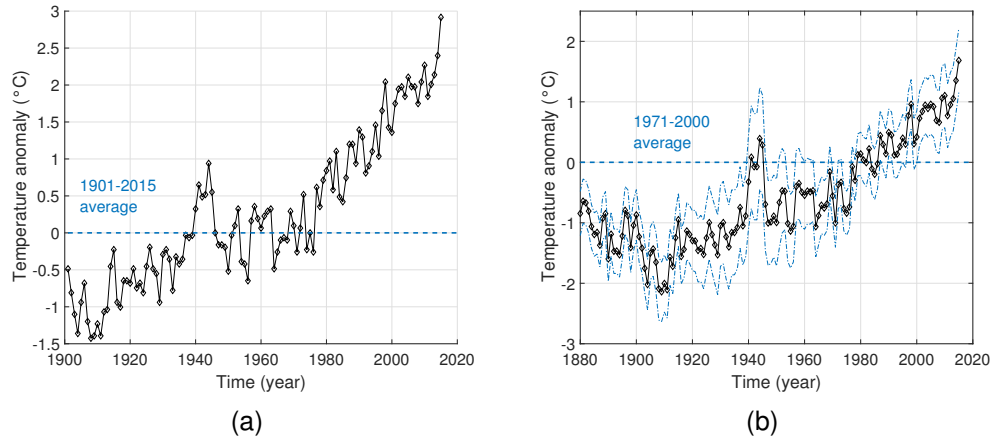
Figure 1: Global average temperature for (a) the atmosphere over years since 1880 and (b) seas over years since 1901. Data from EPA [43].

In order to convince oneself of this, it is sufficient, in any case, to recognize the proven carcinogenic effects of the various incomplete products of combustion, as well as of the fossil fuels themselves. On the other hand, acid rains and the ozone hole are another demonstration of the macroscopic effects of the intensive use of non-renewable resources.

Fig. 1 shows the graphs on the trend of the average global temperature of the air in the atmosphere and the seas: the constant increase in the last 40 years is evident. Recently, someone also said that in order to limit the increase in the average global temperature to $1.5\,°C$ by 2100, it will be necessary to be able to absorb part of the CO_2 in the atmosphere, the limitation of emissions alone will not be sufficient [39].

In this respect, it may also be useful to look at the actual concentrations of some of the most feared pollutants from an environmental point of view. Fig. 2 shows the evolution over the years of the quantity of carbon dioxide and nitrogen oxides dispersed in the atmosphere. The first is a greenhouse gas, rather inert and the largest produced by anthropogenic activity. Several studies have observed the correlation between its concentration and the increase in the absorption of solar radiation by the Earth's atmosphere. The second agent is a pollutant responsible for the phenomenon of acid rain, the production of low altitude ozone (also called photochemical smog) and the onset of lung diseases (such asthma, bronchitis, pneumonia, up to the formation of neoplasms in the most serious cases). As one can see, in recent years the concentration of these two pollutants has increased
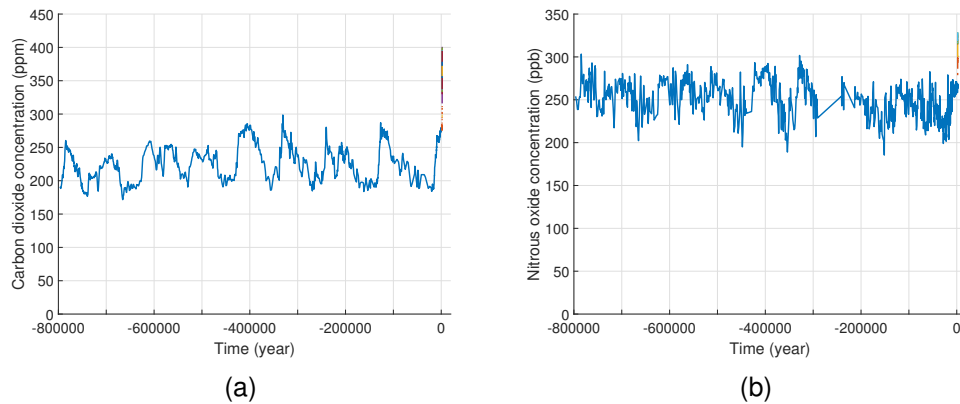
Figure 2: Average global concentration over the years of (a) CO_2 and (b) NO_x. Data from EPA [43].

dramatically and have therefore been identified as two of the main causes that are contributing to worsen the climate emergency [89]. This makes it a priority to invest in all technologies capable of reducing the emissions of this type of molecule into the atmosphere.

At this point, it is interesting to know the impact of the transport sector alone on global pollution. Fig. 3 shows the extent of contributions from different sources of greenhouse gas emissions. It should be noted that the transport sector is responsible for about 17% of total emissions. In this percentage we can then distinguish the contributions of the individual types of transport: as far as Europe is concerned, looking at the data shown in Fig. 4, it is immediately clear that road transport is the undisputed protagonist of this ranking, being responsible for 72.6% of total emissions. Moreover, transport is the only major economic sector in Europe where greenhouse gases have increased since 1990.

However, this does not yet fully justify the growing desire in recent years to fully electrify vehicles. While it is true that the electric vehicle would not pollute residential areas, this does not mean that it would not do so *tout court*. It would just move the problem somewhere else, where the electricity is produced to power them. This is partly true, but it will become much easier to deal with the problem when it cannot be eliminated altogether.

First of all, it must be considered that the replacement of the internal combustion engine with the electric one will double - at least - the efficiency of the traction. In this respect, the infographic extracted from the European report *EEA: Signals 2016* [3] shown in Fig. 5 should be analysed. As
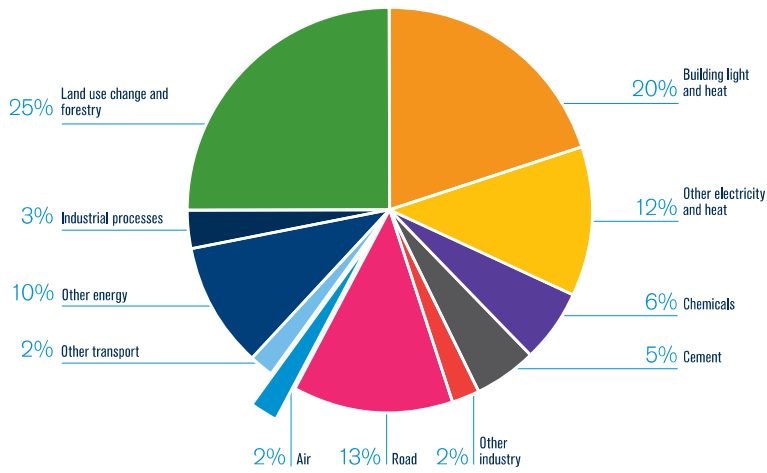
Figure 3: Share of different anthropogenic CO_2 emissions around the world, 2013 (source: [5]).
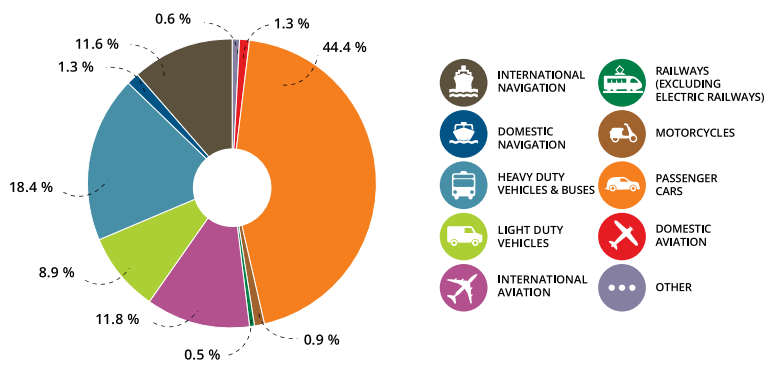
Figure 4: GHG emissions from transport in European Union, 2014, based on provisional data (source: [3]).
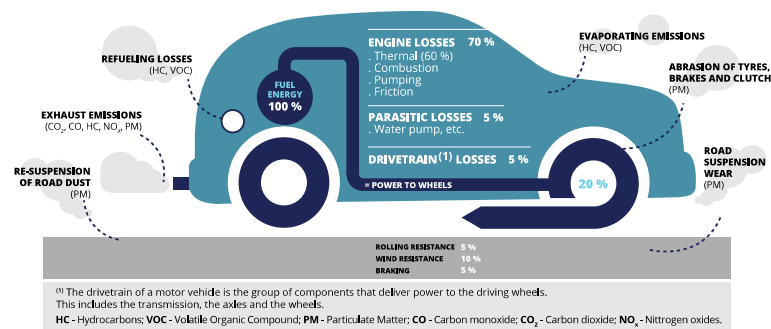
Figure 5: Simplified scheme of the vehicle emissions and efficiency (source: [3]).

much as 60% of the energy obtained from fuel combustion is dissipated in the form of heat during the thermal cycle. Electric motors are known to be characterized by very high efficiencies and especially those used for transport will reach at least 98%.

But the central point remains to understand which system will produce the electricity that will power the electric vehicles. It is clear that the ideal would be a renewable source, for two reasons: on the one hand it would be free energy (net of the energy spent on maintaining and building the device that produces it); on the other hand, assuming that it is part of a distributed national grid, it would mean reduced losses due to the transport of electricity along the distribution lines, from the source that produced it to the power column to which the car is attached.

Finally, we must consider the drastic reduction in noise that would benefit towns and cities if all current vehicles were replaced with full electric models. In fact, the European Union has reported alarming noise levels: according to the European report, an estimated 125 million Europeans (i.e. one in four citizens) are exposed to road traffic noise levels above an average level of $55\,\mathrm{dB}$ per year during the day, evening and night (given the threshold value above which annoyance occurs).

Recent studies suggest that this exposure leads to 20 million European citizens perceiving discomfort and 8 million suffering from sleep disorders. In addition, such high noise levels are responsible for 43000 hospital admissions and at least 10000 premature deaths per year [3].

More Electric Transportation challenges

Electrification of transport is not a trivial objective to be achieved, for many reasons. The spread of e-cars, for example, is fundamentally limited

by

- the maximum attainable power/energy densities of the batteries,

- the uncompetitive prices compared to traditional cars,

- the lack of electrical infrastructure for recharging.

In the aeronautical field, the problem of batteries is dominant and it is unlikely that in the near future it will be possible to build a fully electric aircraft. However, it is possible to think of designing new aircraft with much more installed electrical power. The latter, in fact, are so far operated mainly by hydraulic means.

In addition, all the electrical problems linked to the decrease in atmospheric pressure due to altitude are unknown. This phenomenon is certainly to be taken into account in the aviation sector, but it can also be of interest to the automotive industry, since it must ensure the proper functioning of vehicles even in the mountains. Fig. 6 shows the pressure trend as a function of altitude, highlighting the types of vehicles commonly used in those weather conditions. It should be noted that the air composition also undergoes a significant variation, the impact of which can be important for the in-depth analysis of the electrical systems' reliability.

Furthermore, the primary resources' supply for the construction of the massive number of electric motors that will - hopefully - be sold in the future is also not negligible. Indeed, at the moment, the best electric motor architecture to be implemented in the transport sector seems to be the permanent magnet one, which although it has performances far superior to other types, has the defect of requiring the use of rare-earths (for the magnets). The deposits of these elements, however, are very few, strongly influencing trade policies and prices [14]. This would create an unacceptable commercial dependence on other countries.

Beyond these critical problems, there are also some minor aspects, in order of importance, but not for this reason however negligible. One of these is the design and qualification of the insulation system for electric motors that will be installed in the future in the transport sector, especially on road vehicles. In fact, the requirements of compactness, flexibility and safety impose very stringent constraints on their characteristics, which are completely new for manufacturers of electrical machinery. In addition, a new generation of power devices based on wide-band gap technology (WBG) was introduced to the market, which, according to recent studies and various research institutes [94], increases the electrical stress exerted on insulating systems connected to any static converter based on these new materials (Silicon Carbonide, SiC, or Gallium Nitride, GaN).
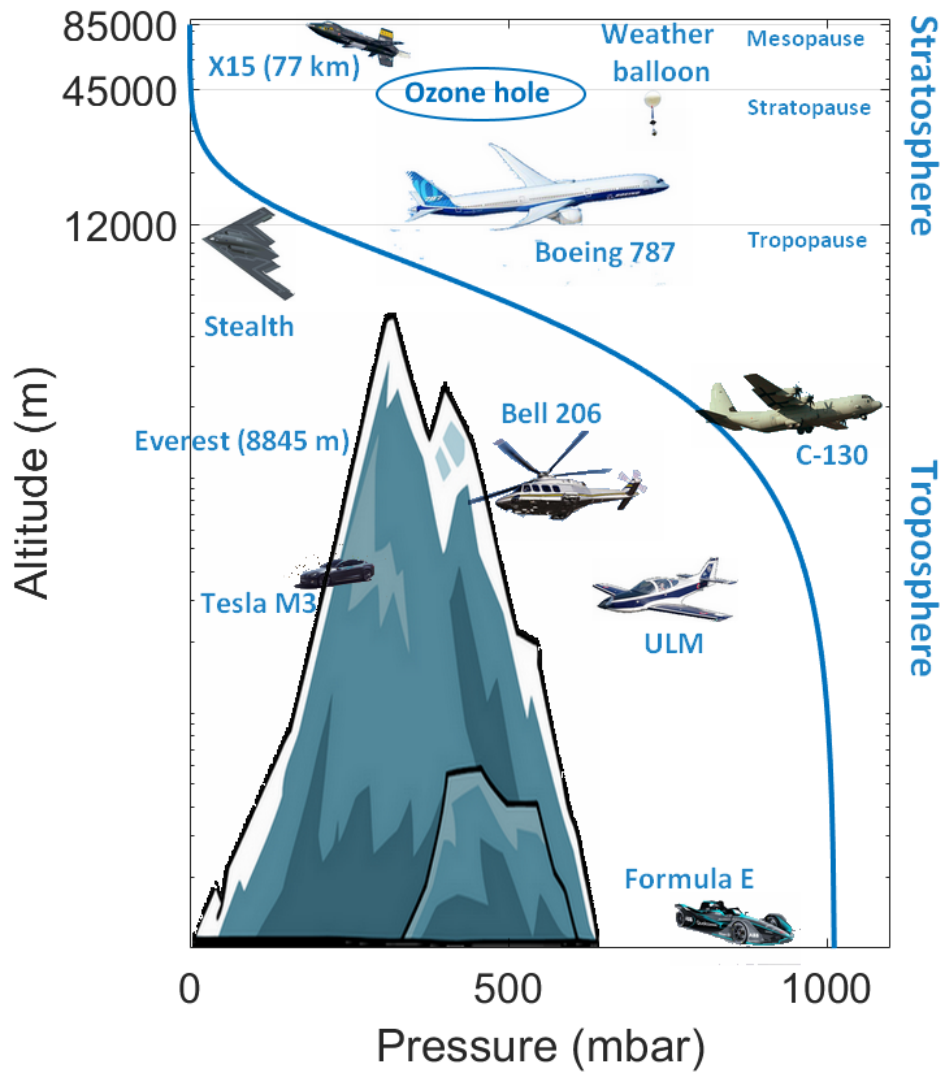
Figure 6: Atmospheric pressure as a function of altitude and main vehicle types.

In particular, it is well known that partial discharges (hereinafter abbreviated as *PD*) are not permitted in low-voltage motors. This is due to the fact that the insulation is of an organic nature, which makes them significantly vulnerable to any type of ion or electronic bombardment. The increase in the nominal voltages used on board aircraft and cars, dictated by the need to reduce overall dimensions and increase efficiencies (for example, the diameter of cables can be reduced by increasing the nominal voltage), clearly forces a more careful study in the insulation thickness sizing.

A matter of reliability

In the light of the above, a broad horizon opens up on the subject of the electric motors' reliability to be used in More Electric Transportation framework. And many of the problems that are emerging recently are due to the different electrical insulation systems installed.

One of the most crucial aspects of the phenomena involved in this research is the fact that they have a largely stochastic behaviour, related on the one hand to the mechanisms of electrical discharge and, on the other hand, to the dynamics of ageing chemical reactions. Historically, this has led to a very experimental approach to this subject, given the lack of analytical models to rely on, and has always favoured dimensioning strategies based more on the sensitivity of the designer than on other factors. Proof of this is the fact that very often in literature one uses - wrongly - the Paschen's curve for the estimation, or comparison, of the electrical machine insulation characteristics [54, 1, 28, 76, 65], when the required hypotheses are totally disregarded for the case in question (uniformity of the electrical field, non-insulated electrodes, quasi-stationary conditions).

Also from the perspective of the studies on ageing there is a lot of uncertainty and it is easy to be misled. The common theme of many surveys is the poor reproducibility of the results, as well as the extreme specificity of the few models designed to estimate the service lives of the components studied. In the case of More Electric Transportation, there is a further problem related to the multiple sources of stress produced by the combination of highly aggressive environments (which can be characterized by high humidity, presence of ice or dust, high pollution, strong vibrations, etc..) and particularly onerous operating conditions (strong acceleration, sudden braking, high speed and efficiency, high altitudes, etc..).

In addition, it should be noted that the reliability problems related with the electric motor are unprecedented for the transport sector. Consequently, it is logical to have little experience in the design and diagnosis of this type

of machine, all the more so if one also considers the innovations introduced in the field of power electronics.

The purpose of this discussion is, first of all, to identify unprecedented problems, highlight the characteristics of the most suitable insulating materials, propose new tools for the design of an effective and efficient insulation and, finally, identify some methods for testing and qualification of new machines.

In detail, this work is divided into four chapters and two appendices, plus a concluding chapter.

In Chapter 1 the characteristics of the main types of electric motor in use, or under consideration, in the field of transport are examined, both to be used as actuators and for the actual traction of the entire vehicle. Particular attention is logically paid to the analysis of insulation systems and their reliability.

Chapter 2 is dedicated to the study of partial discharge phenomena inside low-voltage inverter-fed motors. This chapter, in addition to explaining in detail a deterministic numerical prediction model of the partial discharge inception in the stator windings, illustrates the results of an extensive experimental campaign that had the objective of investigating the impact of each individual design and environmental parameter on this phenomenon. At the end of the chapter, a predictive model of the partial discharge triggering based on a probabilistic approach is introduced, useful to shed light on some measuristic aspects of PD tests.

In Chapter 3, on the other hand, the critical points that are encountered in two different but interlinked situations are addressed: when one wants to test the correct operation of the machine online or offline (at the end of the production chain, during routine maintenance, or even to assess whether it is possible to extend its service life compared to the estimated one) and when one has to carry out the qualification process for a new machine model. This chapter aims to give some practical indications, based on concepts learned from experimental laboratory data and theoretical evaluations, to effectively test the reliability of a real machine or shorten the prototyping time of a new concept machine for the transport sector.

Finally, Chapter 4 introduces the problem of the reliability over time of an electric motor insulation system subjected to some of the various stresses that are present in a vehicle. This is done from an experimental point of view, focusing in particular on the impact of highly irregular operation (typical of vehicles) and the potential damage that partial discharges at different altitudes can have.

1

Rotating machine type-I insulation systems

This chapter aims to introduce the reader to the main types of electrical machines used in More Electric Aircraft framework and the associated insulating systems. Electrification of transport has become one of the great objectives of this century and, for this reason, there are still many technological solutions being considered and tested. A summary on the stator winding manufacturing is given. Of all the parts that make up the electric machine, the stator windings are the most susceptible to failure. This is why the chapter ends with an examination of the main mechanisms of stator failure, a useful framework for the concepts that will be addressed in the following chapters.

1.1 Rotating machines for the electrification of the transport

First of all, in order to better understand the constraints that lead to favouring one architecture rather than another, it is good to identify the characteristics of an electric motor in the context of More Electric Transportation, . Table 1.1 lists the data of a potential electric vehicle in which the electric motors studied could be found. As mentioned earlier, one of the most important challenges for the transport industry is maximizing power density. For current hybrid vehicles, the US Department of Energy has set a target of $6\,\mathrm{kW\,l^{-1}}$ by 2020. Recently, for example, Toyota, with its Prius, and Nissan, with its Leaf, have reached $4.8\,\mathrm{kW\,l^{-1}}$ and $4.2\,\mathrm{kW\,l^{-1}}$

Table 1.1: Example of vehicle data. Adapted from [83].

Quantity	Value
Total mass	$2500\,\mathrm{kg}$
Front area	$3.5\,\mathrm{m}^2$
Vehicle max speed	$180\,\mathrm{km\,h}^{-1}$
Gear box ratio	14:1
Peak wheel torque	$3800\,\mathrm{N\,m}$
Wheel circumference	$2\,\mathrm{m}$
E-machine base speed	$4900\,\mathrm{rpm}$
E-machine max speed	$21\,000\,\mathrm{rpm}$
Power at base speed	$140\,\mathrm{kW}$
Power at max speed	$110\,\mathrm{kW}$
Constant power speed ratio	4.3

respectively [33].

In addition to this, the electric motors will be required a high torque at low rpm to have a good responsiveness at the start, to be able to deal with the steep slopes and allow the *start & stop*. They will also be required to operate at intermediate speeds, for urban travel, and at high speed, when on the highway. Downstream of this, the choice of engine architecture must also take into account vibrations, thermal and structural constraints, costs and safety. This applies as much to vehicles as to aircraft and ships [86].

In recent times, research and industry have focused mainly on three solutions [11]:

- permanent magnet synchronous machines (PMSM);

- induction machines (IM);

- switched reluctance machines (SRM).

The first type of motors, with permanent magnets, is currently the most widespread on the market, and also the most mature in technological terms. As shown in Fig. 1.1(a), IPMSMs have magnets drowned inside the rotor that generate a stable and permanent magnetic field. This peculiarity makes them highly efficient and can exert strong torques, especially at low speeds.

The nature and geometric configuration of the magnets determines the maximum torque that can be achieved by the machine. For example, a V-shaped configuration of these provides saliency and, therefore, an additional reluctance contribute to torque, which facilitates field weakening and thus helps to extend the speed range. This was the construction
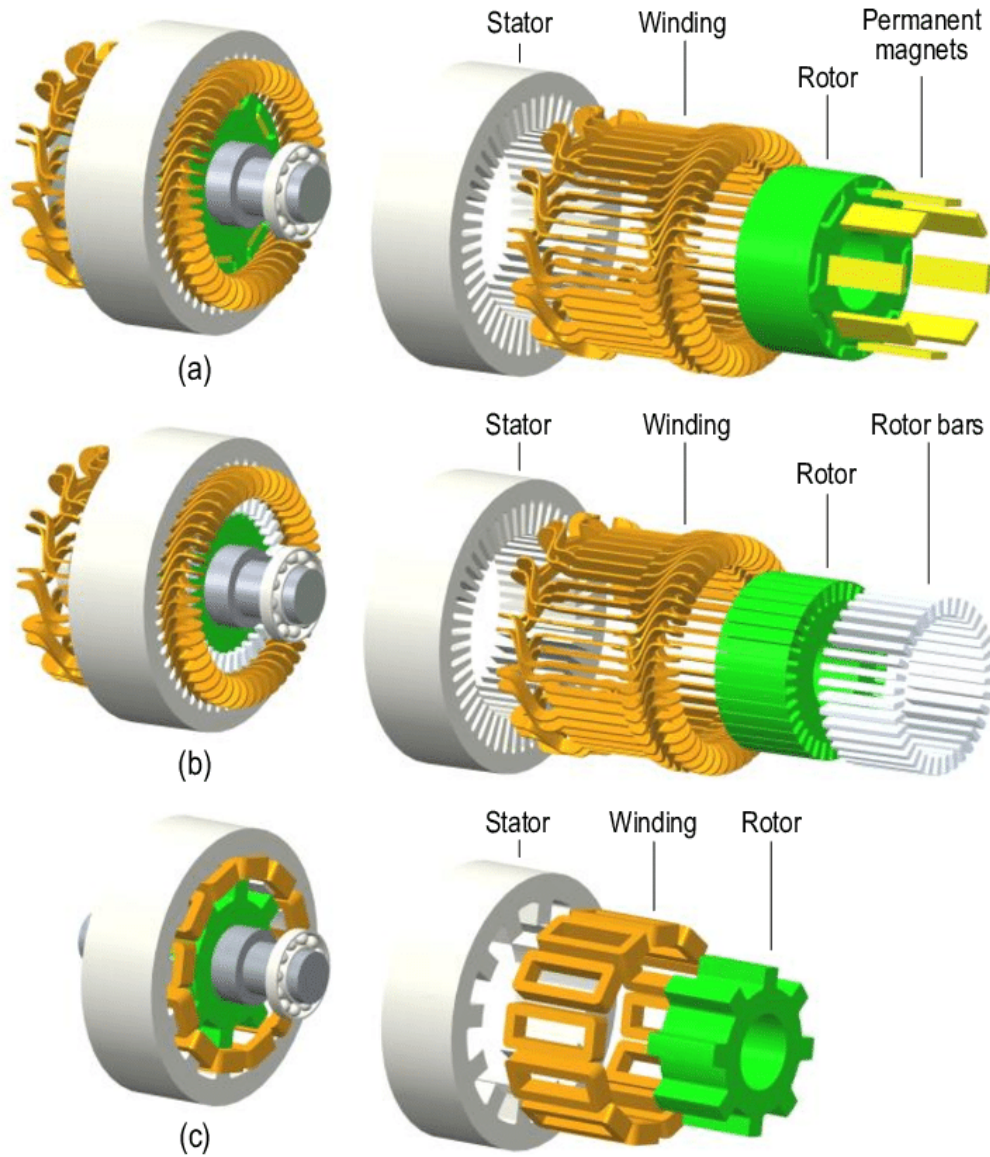
Figure 1.1: Typical electric machine types for traction applications: (a) Interior PMSM, (b) IM, (c) SRM (source: [11]).

solution adopted for the Toyota Prius (peak power of $60\,\mathrm{kW}$, maximum torque of $207\,\mathrm{N\,m}$ and maximum speed of $13\,500\,\mathrm{rpm}$). The 2011 version of the Nissan Leaf, on the other hand, featured a motor with delta-shaped magnets (peak power of $80\,\mathrm{kW}$, maximum torque of $280\,\mathrm{N\,m}$ and maximum speed of $10\,390\,\mathrm{rpm}$). Finally, the Chevrolet Spark has a double-barrier rotor motor (this is a mixed solution) with bar-wound windings that allow higher torques at low speeds (peak power of $105\,\mathrm{kW}$, maximum torque of $540\,\mathrm{N\,m}$ and maximum speed of $4500\,\mathrm{rpm}$).

The great weakness of this architecture lies in its strong point, namely the magnets: they are very expensive and quite sensitive to temperature. When the temperature reaches $160\,\mathrm{°C}$, for example, the torque exerted can be as much as 46% lower than at room temperature. In addition, it should be noted that the number of rare-earth deposits (the elements that make up the magnets) is not large and currently 95% of the market is held by China [14]. This clearly constitutes a strong disincentive to this type of electric motor.

In IMs, the magnetic field is generated by the currents that are passed through the stator winding. It induces the electromagnetic force in the conductors that make up the rotor necessary to produce the electromechanical torque. As shown in Fig. 1.1(b), the rotor is equipped with bars of die-cast conductive material inside longitudinal slots. Since excitation must be provided by the power supply, IMs are characterized by lower efficiencies and lower speeds than PMSMs, for the same power. One of the major disadvantages is the losses in the rotor aluminium, especially during high torque operations, as it can be difficult to extract excess heat.

In order to get around the above mentioned problem as much as possible and to maximize the motor output, Tesla EV (peak power of $310\,\mathrm{kW}$, maximum torque of $600\,\mathrm{N\,m}$ and maximum speed of $14\,000\,\mathrm{rpm}$) installs copper rods in the rotor, which from an electrical point of view make more, being the conductivity greater. However, this solution is more expensive, both in economic terms and in terms of weight: copper has a higher density than aluminium and its die-casting requires higher temperatures and working pressures, also generating greater stresses between the rotor laminations.

Finally, there is always the possibility of installing SRMs. They are by far the most robust, simplest and therefore the most economical machines. As shown in Fig. 1.1(c), the rotor in this case has a salient pole structure made of steel laminates. It is not equipped with magnets or conductors. The SRM stator implemented in the automotive sector also has a salient structure, which means a concentrated winding. This architecture is particularly suitable for high speed and high temperature regimes.

In SRMs, torque generation takes place by means of variations in air-gap reluctance. Since the relative position of the salient poles defines the length of the latter, the torque depends closely on the position of the rotor. This has the considerable disadvantage of causing ripples in the torque, as well as causing unwanted acoustic noise and vibrations in the stator. These factors significantly limit the power density of conventional SRMs. However, the simplicity and robustness of this machine make it an excellent candidate for More Electric Transportation, not to mention its inherent fault tolerance (using multi-phase design, combined with a power segmentation approach).

At present, SRMs have not yet been installed for traction in any model of electric vehicle. On the other hand, there are several cases where it has been used as an actuator in military aircraft (the Lockheed Martin F-22 and the Lockheed Martin F-35 have SR generators [64]) or as a motor for hybrid generation in some John Deere tractors.

Since the integrated generation in particular (motor and converter in a single housing) can have very high operating temperatures of up to $250\,°\text{C}$ in combination with adverse environments, it is also important to mention the possibility of classifying electric motors according to their cooling system. There are three main solutions here, too [53]:

- air cooling;

- water cooling;

- oil cooling.

Air cooling is by far the most widely used approach for low-voltage electric motors. It is economical, simple and guarantees the removal of excess heat in most cases. It is achieved by the use, on the one hand, of an abundant finning all around the external surface of the motor casing, which promotes heat exchange with the surrounding air by natural convection. On the other hand, a fan is usually installed on the motor head to provide forced convection to further increase heat dissipation.

However, the requirements of compactness and weight, as well as sometimes the need to have a hot source for auxiliary systems (for instance, the heating system of cars) may lead to the provision of a liquid cooling system. Depending on the thermal power to be removed, then, one can opt for a water system, cheaper but less efficient, or oil system, more complex, but also more effective.

1.2   Types of stator winding construction

The insulation systems installed inside an electrical machine always and exclusively concern the windings, therefore it is necessary to provide an examination of the main types of the latter.

The architecture and type of windings, together with the characteristics of the voltages and currents fed into them, define the operating modes of the electrical machine. According to their function, the windings can be distinguished in the following categories:

- armature windings;

- other rotating-field windings (e.g. stator or rotor windings);

- field (magnetizing) windings;

- damper windings;

- commutating windings;

- compensating windings.

Evidently, the most stressed insulating systems are those that concern the so-called stator rotating-field windings, since they are those invested with the highest voltage amplitudes, in combination with high temperature conditions. In fact, the component that can most easily suffer a failure is the stator winding [6]. Therefore, in the following, an in-depth analysis will be provided on its construction characteristics, highlighting in particular the properties of the insulation.

In small stators normally the copper conductors have a circular cross section. This is due to the simple processing as compared to non-circular cross sections. Profile wires are only used for special applications. They enable a higher fill factor (the ratio of conductor material to the available winding space), but processing becomes much more difficult due to the manufacturing properties. However, the constraints imposed on electric motors that are beginning to be designed for the automotive and aeronautical fields impose the need to consider also rectangular section conductors.

In general, the following possible solutions for stator winding are currently available:

- random-wound architecture;

- form-wound architecture with litz wires;
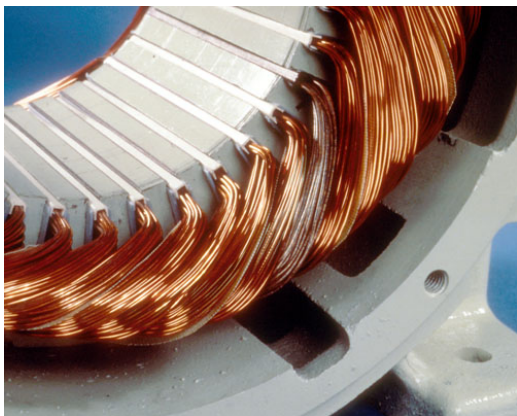
(a)
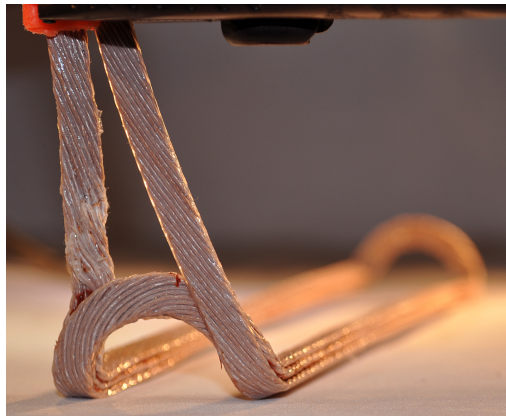
(b)

(c)

Figure 1.2: Possible solutions for the stator winding: (a) random-wound coils, (b) litz wire coils or (c) hairpin form-wound coils.
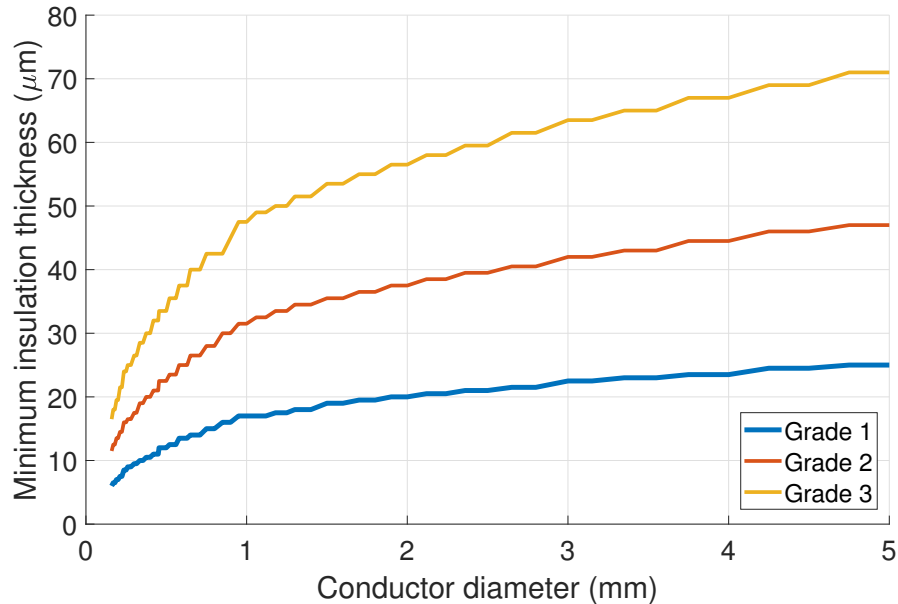
Figure 1.3: Insulation grade specifications for enamelled round copper wire. Adapted from the IEC 60317-0-1 standard guidelines [24].

- form-wound 'hairpin' architecture.

The greatest benefit of using different conductor geometries lies in the fill factor.

As mentioned before, the adoption of a random-wound configuration is the most classic: it is rather cheap (although it does not lend itself to automation), constructively simple to implement and very flexible. The circular section wires are enamelled with one or more polymeric resins, to ensure electrical insulation between the individual conductors. In addition, the slot is usually lined with a sheet of insulating material that ensures to avoid the breakdown between the winding and the stator frame. Finally, insulation tapes or cords around the coil end-windings are applied to ensure the mechanical stability against vibrations. In the most demanding applications, it is also common to use separators between coils of different phases at the output of the head (not shown in Fig. 1.2(a)).

As a rule of thumb, turn insulation is sized to support phase-to-ground voltage. However, the recent introduction of wide band-gap devices, combined with high operating temperatures and the need for compactness, have made this constraint rather stringent. As a result, impregnation actually ensures the completion of the electrical phase-to-phase insulation. Besides the electrical point of view, impregnation can also ensure mechani-

cal stability, improve heat transfer properties and protect the windings from foreign particles and pollutants.

The insulation of round section wires is classified according to the number of insulation layers and is indicated as 'insulation grade'. Currently, the grades are up to 3 [25], as can be verified from Fig. 1.3. Base-coat is typically made up of polyester-imide (PEI), while over-coat is polyamide-imide (PAI). The latter ensures a better adhesion to copper and improves the overall magnet wire properties, especially a better abrasion resistance along with an enhanced temperature endurance.

As mentioned, the random-wound configuration is the most unfavourable in terms of efficiency, as it does not allow to reach high fill factors (according to [45], increasing the fill factor by 10% leads to about a 1% increase in motor efficiency). It is for this reason that the possibility of manufacturing stator windings with a hairpin form-wound configuration has recently been evaluated (see Fig. 1.2(c)).

The main advantage is the maximization of the stator slot filling to obtain a higher power with a more compact motor. Alternatively, for the same size, it is possible to install a liquid cooling system, which improves the reliability of the machine. Furthermore, the process is visible during the assembling, thus granting the total quality-reliability of the implemented product, with finally the possibility of relying on all manufacturing processes fully automatically.

The insulation in the form-wound stators for the transport sector is similar to that of the random-wounds (not so in general), with the difference that at the manufacturing level it is much easier to implement the entire system. Therefore, also in this case, the turn-insulation is guaranteed by the enamel. The degree of insulation of rectangular section wires is up to 2 and the thickness of the insulation does not vary depending on the size. Table 1.2 shows the indications of the standard in this regard [25]. Each slot is also equipped with its own liner, which guarantees mechanical protection and stability, and ensures the ground insulation.

Finally, in the endwinding, the separation of the wires that come out from the slots is ensured by the installation of appropriate separators. These, in addition to having an insulation function, must also ensure mechanical stability, put to the test especially during current transients, which generate thrusts or repulsive attraction between the different conductors.

In the transport sector, the trend is to adopt fundamental frequencies well above $1\,\mathrm{kHz}$. This means that AC losses are not negligible at all, but, on the contrary, are dominant in some cases. From this point of view, the hairpin winding is not a winning choice, as it has important conductor sections and therefore a careful electrical design of the machine must

Table 1.2: Insulation grade specifications for enamelled rectangular copper wire [25].

Grade	Insulation thickness (μm)		
	Minimum	**Nominal**	**Maximum**
1	30	42.75	55
2	60	77.5	85

be carried out to avoid too high losses due to skin and proximity effects. Further, it has the disadvantage of having a low degree of freedom in terms of turns in series per phase, as only few configurations are feasible and can be manufactured [10].

A compromise between the two architectures just described is constituted by the adoption of the Litz wires. Referring to Fig. 1.2(b), they consist of many strands of thin wires, isolated individually and twisted or intertwined together, following one of several carefully prescribed schemes that often involve several levels (the twisted wire groups are in turn twisted together, etc.). The result of these winding schemes is to match the proportion of the overall length along which each strand is outside the conductor, an effect that is not achieved with a simple twisted stranded wire. The term litz wire originates from *Litzendraht*, a German term for twisted or woven wire.

It is commonly used in high frequency transformers or other electronic applications, up to $1\,\mathrm{MHz}$, because it is specially designed to reduce losses caused by the skin effect and the proximity effect in conductors. Recently, its use in high-frequency inverter-fed electric motors (such as those based on SiC or GaN MOSFETs) is also being increasingly evaluated.

The disadvantage of stranded conductors lies in the high efforts required to connect the parallel strands and the reduction of allowed conductor stresses in the winding process due to the reduced cross sections of the strands. Also, they do not guarantee the maximization of the fill factor. On the other hand, for critical applications, one can use profiled (mechanically shaped) litz wires which allow optimal utilization of available winding area due to the superior filling factor of rectangular or square litz wire cross sections. In comparison to a standard round cross section construction, profiled litz wire can increase the filling factor by up to 20%. This clearly increases costs even further.

From the point of view of electrical insulation, the individual wires follow the same standards as described above (EIC 60317), with the necessary variations depending on the characteristics of their section (round or rectangular). However, the turn-insulation is not only due to the enamel, but

also to the taping. The latter is applied all around the entire cable to ensure mechanical stability and to provide an additional barrier from potential external interference (like metallic particles, moisture or pollutants). The material of the tape is chosen according to the operating temperature: it can be polyester (class 105), treated polyethylene (class 180) or polyimide (class 200). This additional insulation layer also contributes, together with the liner, to the ground insulation, and, together with the separators on the end windings, to the phase insulation.

In order to avoid the presence of air cavities between adjacent wires inside a litz cable, a fundamental characteristic in applications with voltages higher than $300\,\mathrm{V}$, a wire-to-wire bond can be accomplished through the use of self-bonding adhesives. An adhesive over-coat is applied to the surface of the base-coat enamel insulation during the production of the individual wires. Different adhesives can be specified depending upon the activation process used by the customer (heat or solvent activation) and/or the ultimate bond strength and re-softening temperature characteristics desired.

1.3 Types of stator winding impregnation

It is standard practice to apply an impregnating resin to the entire stator once the winding has been deposited in the slots. The main purpose of this procedure is to ensure the mechanical stability of the wires, as it stiffens the entire structure, prevents the delamination of the insulating enamel by the mechanical vibrations to which it is subjected during operation and protects the interior from any external compounds (such as moisture, transmission fluids, etc..).

In addition, IEC 60034-18-41 prescribes that partial discharges may not be incepted at any time during the service life of low-voltage electric motors. However, these discharges are only generated in areas with low relative permittivity and composed of a gaseous dielectric. In other words, in machines this can only occur in air-filled cavities inside the insulation, located close to areas subject to a high electrical field. Therefore, a good impregnation makes it much less likely that partial discharges will be triggered, since it drastically reduces the number of sites where this phenomenon can occur. In fact, during the process, the resin infiltrates into the stator and fills any empty space.

A final important advantage of impregnation is that it improves the dissipation of the heat generated inside the winding towards the outside. This is due to the fact that the resins typically used have a heat exchange
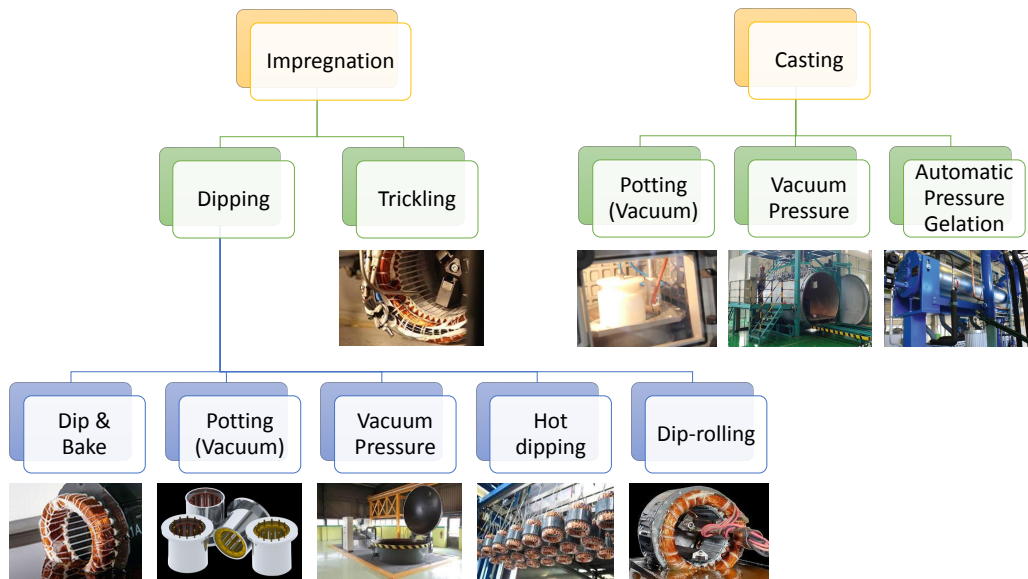
Figure 1.4: Overview of resin based stator secondary insulation processes.

coefficient ten times higher than that of air (the heat transport mechanism, from convective, becomes conductive). Since the winding temperature is one of the main constraints on the power that a machine can reach, an intelligent choice of impregnating material and impregnation, hence, can have a strong impact on its performance [88].

The so-called secondary insulation can be established in different ways. The diagram in Fig. 1.4 summarises the main types of process, all of which have one thing in common: they infiltrate a liquid resin into the stator and between the wires coming out of the machine head and then cure it by heat input. However, a distinction can be made between impregnation and casting processes.

Depending on the process characteristics, impregnation can be by dipping or trickling. In one case, the stator is at one point completely immersed in the liquid resin (dipping), while in the other the parts to be isolated are directly invested with a jet of fluid resin.

The most classic method, and also the cheapest, is certainly the so-called *dip & bake* (D&B). The stator is simply immersed in a reservoir of resin at room pressure for a certain time, after which it is pulled out and placed in the oven at a certain temperature to implement the curing phase.

Alternatively, it is possible to implement the same process under vacuum, drastically increasing the costs and complexity of the procedure, but also the yields. This means that the resin tends to infiltrate much better into the

stator cavities, proceeding by suction instead of pushing. This maximizes the level of impregnating material intrusion into the machine geometry. Subsequently, it is possible to provide for a further phase in which high pressure is applied in order to eliminate the remaining cavities (this typically occurs especially inside the slots). Depending on whether this phase of the process exists or not, the procedure is called Vacuum (VI) or Vacuum Pressure Impregnation (VPI).

The procedures described above have the disadvantage of not allowing the stator to retain all the resin just introduced, when they remove it from the bath. This is due to the fact that the impregnating agent, still fluid, tends to drip out, so that the absorption is rather poor, compared to the amount of material initially inserted. One possible solution to this problem is to heat the windings by the Joule effect, by circulating a certain current during the immersion. This immediately triggers the gelling reactions, preventing the resin from escaping immediately after bathing. The final curing can then be done in oven or by continuing to exploit the Joule effect in combination with ultraviolet light radiation. This process is called hot dipping (HD).

A variant of hot dipping is so-called dip-rolling (DR), which consists of rotating the stator while it is partially immersed in the resin bath. This process can also be combined with Joule heating or, alternatively, curing can be carried out by placing the machine in the oven.

The trickling impregnation (TR), as mentioned, starts from a different assumption, that is to impregnate only the most critical elements of the stator. A thin jet of resin is first directed towards the lower winding head of a stator inclined by about 5-20 degrees, after which the upper part is targeted. The resin infiltrates into the slots by capillarity. This ensures that the stator housing does not come into contact with the impregnating material in any way. In addition, this technique allows precise control of the amount of resin used. Here, too, the final curing can be carried out by Joule effect or in an oven.

In general, the resin used for impregnating electrical machines has a polyester, epoxy or silicone base. The use of one molecule with respect to another changes the viscosity and the process temperature. However, they all have a thermal conductivity of about $0.2\,\mathrm{W/mK}$.

As an alternative to impregnation, the stator casting is used for the secondary insulation. It should be noted that this process can still be used only for the endwinding, once the entire stator has been impregnated.

However, the casting process differs mainly in the use of the mould. The stator is inserted into the mould and the whole process is filled with liquid resin. This allows to design with a certain margin of manoeuvre the external geometry of the secondary insulation, and therefore by extension

the final external shape of the entire stator. Another difference lies in the characteristics of the resins used. In the case of casting, they usually have a much higher viscosity.

In practical terms, one casting process may differ from another in a similar way to impregnation. In the same way as the D&B process, casting can take place at atmospheric pressure. However, this process is not suitable for application on electrical machines.

Instead, it is possible to perform a vacuum casting (VC): before pouring the resin, the vacuum is created inside the mould already containing the piece. This makes it easier for the resin to slip into the windings, reducing the possibility of large cavities remaining. The process is very similar to VI. As a result, it is possible to provide, in the same way as for VPI, a subsequent phase in which strong pressure is exerted, to further improve the characteristics of the resulting insulation. This is vacuum pressure casting (VPC). All the processes described above involve a final phase of permanence in the oven, before the stator is removed from the mould, in order to carry out the curing of the resin.

For mass production, a variant is inserted: the resin starts the gelling inside the mould directly after the casting process. Then, the stator is removed from the mould and placed in the oven to complete the curing. This process is called Automatic Pressure Gelation (APG).

Unlike impregnating resins, the characteristics of casting resins are usually modulated by modifying their composition. In particular, a different amount of filler material is inserted. In this way, the thermal conductivity can vary over a wide range of values, ranging from $0.7\,\mathrm{W/mK}$ up to $3\,\mathrm{W/mK}$. Due to the high viscosity, however, the application of high conductivity resins is only possible for the casting of the head. Finally, it should be noted that it is also possible to modulate the electrical and mechanical properties by acting on the final composition of the resin.

1.4   Main stator failure mechanisms

Some machine failures are the result of an unforeseen event, which does not depend on the original condition of the insulation. There is no way to predict them and they are usually due to human error or environmental accident. Examples of such events may be:

- incorrect connection of the terminals during installation or maintenance, which generates strong currents circulating, resulting in burning of the windings;

- accidental inclusion of metal elements inside the machine during manufacturing or maintenance, which causes instantaneous short-circuiting of the nearest insulation system;

- operating errors, such as unexpected interruption of the cooling system (if any).

On the other hand, most failures occur due to the progressive deterioration over time of some parts of the machine's insulation system, until it is no longer able to withstand the thermal, mechanical and/or electrical stresses to which it is subjected during normal operation.

The reason why only the insulating system is indicated is related to the fact that the polymeric materials that compose it have thermo-mechanical characteristics much lower than those of metals, especially in terms of resilience. Therefore, except for manufacturing defects, it is the insulating system that represents the bottleneck for the extension of the maximum service life.

Below is a detailed description of the main failure mechanisms that the stator of a low-voltage machine typical of the transport sector can encounter. The symptoms for each failure mechanism are also described. These symptoms can be observed with a visual examination of the winding and with some of the diagnostic tests described in Cap. 3.

1.4.1   Thermal deterioration

This mechanism is the most commonly found in motor faults, especially if they are air-cooled, and requires rewinding of the stator. Unless the cooling system is also faulty, the incidence of this type of fault is significantly lower in liquid-cooled electric motors.

Thermal deterioration of winding consists essentially in oxidative chemical reactions. Therefore, when the temperature is high enough to allow this type of reaction, the chemical bonds that hold the polymeric chains together begin to weaken and then break. When this happens, the oxygen then tends to bind to the molecules involved, causing further weakening of the polymer. From a macroscopic point of view, this leads to the material embrittlement and a decrease in its mechanical properties.

For magnet wire in random-wound stators, brittle insulation resulting from thermal ageing is easily cracked as the copper conductors move under vibrations caused by magnetic or inertial forces during start-up or normal operation. The aged insulation can also easily peel off the conductor.

In any case, this can cause a short circuit between two adjacent coils, resulting in an increase in phase current and thus localised overheating where the fault has occurred. In a short time, the temperature can reach values that melt the metallic conductor and the adjacent insulation, causing a ground short-circuit.

In general, modern Class 155 stator windings will not experience thermal ageing during their commercial lifetime if its hotspot temperature remains below $110\,°C$. Clearly, the higher the temperature, the faster the oxidation of the insulating materials will take place and, therefore, the shorter their service life will be. In general, the so-called Montsinger rule [73] is often used to estimate the useful life of the insulation. It states that an increase of 8-10 $°C$ is sufficient to halve the service life of the insulation. Therefore, if the machine is operated at its thermal class, some problem of thermal instability is to be expected after a few years (the thermal class indicates the temperature at which the material is guaranteed to operate for at least 20,000 hours). If, on the other hand, its operating temperature is kept below $30\,°C$, its useful life is estimated to be about eight times longer (about 20 years).

When a machine has deteriorated due to oxidation, it will show evidence of cracked or peeling magnet wire films, as well as discoloured or brittle slot liners and bonding varnish. Furthermore, thermally deteriorated insulation may have a low insulation resistance if any part of the magnet wire surface has cracked or peeled away. Also, there may be a low-surge breakdown voltage. There may also be a small decrease in capacitance and increase in dissipation factor over time [94].

1.4.2   Inadequate resin impregnation or casting

As noted above, stator impregnation/casting is a particularly critical process for electric motors used in combination with a high frequency inverter. Therefore, it is not surprising that a poorly impregnated conventional random-wound stator is much more likely to fail to dirt, pollution, oil and moisture that can be partly conductive.

On the other hand, it is not so remote that, during the winding process, micro-fractures and/or imperfections may have affected the enamel of the wires. If impregnation has not been performed correctly, these defects tend to short-circuit consecutive coils in combination with possible contamination of conductive particles.

In addition, if the windings are not tightly packed, there is the risk that, with electromagnetic forces and vibrations, an abrasive action may take

place which, over time, may lead - again - to the failure of the turn insulation, if not to that of the ground, in the most unfortunate cases.

Another important issue is the heat dissipation, especially in form-wound stators: poor impregnation can lead to the generation of local hotspots characterized by temperatures higher than that of the insulation class. This would indirectly cause a failure due to premature thermal deterioration of the affected part.

Finally, the very presence of micro-cavities means that the absence of partial discharges inside the stator insulation system is not guaranteed. If, by chance, the conditions for triggering the phenomenon were created, this would lead to rapid and inexorable local erosion of the polymeric material until the creation of a carbonized path, with consequent short-circuit.

The reasons that can cause inadequate impregnation of the stator are as follows:

- incorrect resin/varnish viscosity, possibly caused by inadequate mixing or contamination with foreign particles;

- process not carried out correctly, perhaps not in accordance with the supplier's recommendations or caused by excessive pressure losses within the stator;

- use of wire enamel that is not chemically compatible with the resin/-varnish (in random-wound or hairpin windings);

- incompatible resin and insulation tapes (with litz windings).

Poorly performed impregnations are easily observed in random-wound stators, as it is possible to notice micro-cavities on the surface of the impregnated parts, areas where the resin has not been able to penetrate and in general lack of sheen on the surface of the coils and the frame.

On the contrary, in form-wound motors (both with litz wires and with rods) the visual verification is more difficult to do, because the absence of impregnation is more likely to occur near the conductors, far from the surface of the insulation.

The best way to detect poor impregnation is to subject the stator to a PD (Partial Discharge) test. A tan-delta test can also be performed for progressively higher voltage levels and a surge test to detect any weak points in the turn insulation. The main alternative to electrical investigation methods is to dissect a trial stator to determine the goodness of the procedure.

1.4.3   Contamination

Winding contamination results in many problems, including chemical attack, electrical tracking and faster thermal deterioration (due to blocked ventilation). In particular, electrical tracking enables surface currents to flow over the insulation, especially in the end windings, eroding the polymeric material. This can then cause the phase or ground insulation short-circuit.

In general, dust, dirt and particles can easily be deposited on the uncovered surfaces of electric motors. These contaminants, in combination with moisture and the possible presence of oil (usually applied to all rotating parts) produce a conductive layer.

In random-wound machines, which are typically air-cooled, it is easy for this type of deposit to occur on the endwinding. However, there must also be a defect, pinholes or micro-cracks, at some point in the wire to cause accelerated system deterioration. Although rare, this type of defects can also occur on new machines, as the wire standard allows for a very low number of pinholes at the end of manufacturing. In addition, during operation it is always possible that thermal ageing and mechanical stresses create micro-fractures or have an abrasive effect on the enamel of the conductors, such as to leave them exposed at some point.

In any case, if these defects are present, it is easy to establish, with the help of the dirty layer, a surface current that closes on different coils. The time to failure clearly depends on the quantity of defects and the quantity of contaminants present. This type of problem can lead to the random-wound machine breakdown in a few weeks, as in decades of years.

In form-wound motors the mechanism is slightly different, especially in those with higher rated voltages. The contamination failure usually occurs at the end-winding, as the separator acts as a bridge between the two phases concerned.

If the equivalent resistance of the contaminant is greater than the capacitive impedance of the coils, then the contaminated surface is almost at the same voltage as the conductor underneath it, and therefore the nominal voltage is almost applied. If the contaminating layer has a uniform resistivity, this will not cause any major damage to the insulation as the current will be very low (some nA). Unfortunately, there are usually highly resistive zones, so-called dry-bands, in which most of the voltage concentrates, burning the surrounding areas. This makes the region conductive and, consequently, moves the discharge to some other high resistivity point, repeating the process. This mechanism leads to the generation of an electrical track, which progressively erodes the insulation until it breaks completely. The track often has many branches and appears as a carbonized, black network

Inverter

Connection cable

Electrical motor

**Phase/phase voltage at
inverter terminals**

**Phase/phase voltage at
motor terminals**
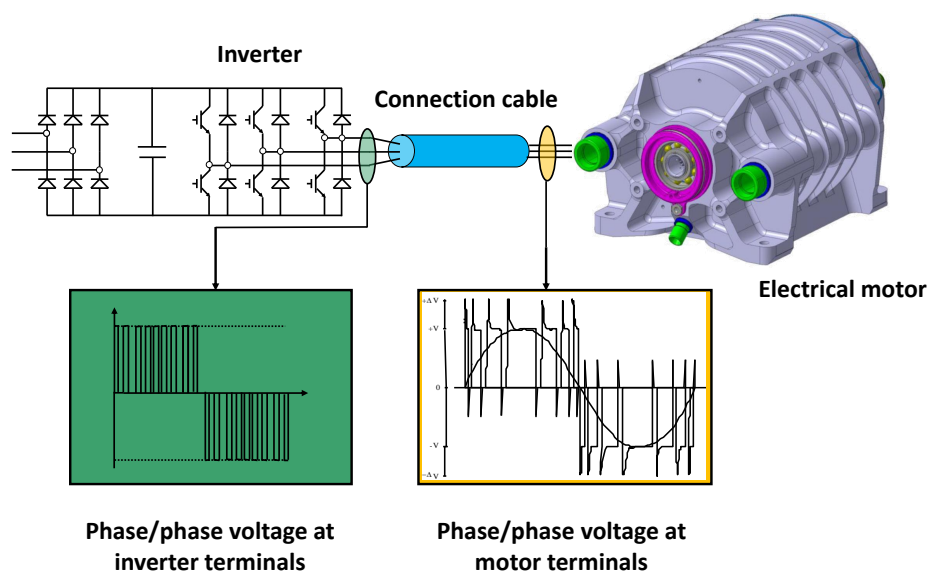
Figure 1.5: Propagation of the voltage wave along the connection line between the inverter and the electrical machine.

of valleys across the separator. Alternatively, tracks can appear between coils in the same phase, if one coil is near the phase end and the other in closed to neutral.

In any case, the mechanism in the form-wound machines is decidedly slow and the failure typically occurs about ten years after the contaminating layer has formed.

1.4.4 Repetitive voltage surges due to drives

Stator failures are not always due to a problem in its insulation system. There are situations where the machine is actually free of defects, but is combined with an inverter in such a way that the wave fronts applied at the terminals are not suitable with the insulation system installed.

Repetitive voltage surges can induce gradual deterioration of the turn insulation and ground/phase insulation. In fact, the voltage waves generated by the converter can be distorted by reflection phenomena. Depending on how the connections are configured at that time, the electrical pulses can spread differently through the windings of the machine, depending on how the impedance mismatch actually is.

In particular, very steep slopes cause the voltage distribution along the windings to be strongly uneven: as the rise time decreases, the voltage

drop on the first loop increases, up to about 90% with a rise time of $10\,\mathrm{ns}$. Therefore, in a random-wound machine there is the possibility that the turn insulation will endure for a very short time, but periodically, a voltage comparable to that of phase-to-ground. This can trigger a partial discharge, if in the immediate vicinity there is a cavity of suitable size.

This can also happen with hairpin machines or machines made with litz wires; however, in these cases it is possible to foresee the voltage distribution, since the winding is distributed neatly, and therefore try to avoid points of excessive overvoltage.

It is virtually impossible to guarantee the absence of cavities within an insulating system. Fortunately, it can be done in such a way that, through adequate impregnation/casting, their characteristic diameter is minimised, so as to avoid the danger posed by partial discharges. However, during verification, it is not certain that two virtually identical random-wound machines are both working. Depending on how the wires are randomly placed inside the slots, in one case there could be a much more stressed turn isolation, to the point of presenting partial discharge activities.

Partial discharges are a phenomenon that has always been known for medium and high voltage form-wound machines, in which the insulation system coexists with it and considers it one of the main ageing factors [19]. In low-voltage ($<760\,\mathrm{V}$) machines, however, this is not so true, nor did one expect to find fault problems due to the triggering of partial discharge activities.

Low-voltage motors, as described above, are characterised by organic insulation materials and, therefore, their insulation system is defined as Type I. The latter is absolutely acceptable when partial discharges are triggered. The fundamental problem is linked to the electronic and ionic bombardment generated by these phenomena to the damage of the insulating surfaces: the chemical bonds that hold together the polymeric chains tend to break easily, leading rapidly to the creation of carbonized paths through which a short circuit can be established. For this reason, the standard states that motors with Type I insulation systems must be designed in such a way that they do not trigger partial discharge activities at any time during their service life.

2

Contributions on PD inception voltage calculation for random-wound stators

As highlighted in the last two sections of the previous chapter, one of the most harmful phenomena from which the low-voltage electrical machine must be protected is partial discharge activity. As this is a relatively new problem in this field of application, the exact impact of the different electrical, environmental and geometric parameters on the phenomenon has not yet been fully clarified, nor are there any tools to produce reliable estimates of Partial Discharge Inception Voltage ($PDIV$). This chapter explains how this dual problem was addressed by applying Schumann's theory to stator windings. Finally, the reader is introduced to the time-volume theory, which could allow, through its statistical approach, a more precise estimate of $PDIV$, overcoming the limits of deterministic theories.

2.1 Partial discharge inception voltage model

The partial discharge, as the name itself suggests, is an temporary transient of a gaseous dielectric breakdown. With reference to insulating systems, they include a wide range of physical phenomena and many of these contribute to the degradation of the insulation, if not sometimes permanent failure.

The first works on partial discharge physics (very often referred to by the term coronas) date back to the 1940s and focused mainly on discharges into the vacuum [63, 69]. Already in the late 1970s, much progress was

made on understanding and observing the mechanisms generating partial discharges [77]. It is precisely in these works that the first qualitative models for their quantitative numerical simulation were developed and the basis for correlating physical processes to measurable signals was obtained.

In general, PD activity caused by defects in the insulation system can be roughly classified into three categories:

- discharges in gases and in the vicinity of solid/gas insulating interfaces;

- discharges in liquids;

- discharges into solids (in the form of charge injection, electrical treeing or water treeing).

In particular, the first category includes partial discharges that can be generated inside low-voltage electric motors and therefore these will be discussed exclusively below.

The choice of the theoretical model to be used is not obvious. First of all, it should be noted that the system considered (the windings in the stator and the housing) has conductors that act as temporary electrodes always covered by a layer of insulating material (depending on the case, either the enamel of the wires, or the impregnating resin, or even the different separators). This means that the Townsend breakdown is to be excluded *a priori* when trying to model the partial discharge inception.

Since the cavities and air gaps between the winding wires, or between them and the housing, are very small (a few tens of μm in the worst case) and have complex shapes, even the Meek's model (Eq. A.29) is not particularly suitable, since it has been proposed for the analysis of long-distance and nearly-homogeneous field corona discharges.

On the other hand, wanting to make a rigorous study of the phenomenon, one could implement the electro-hydrodynamic equations for all the charged species involved (electrons, positive and negative ions), taking into account the several dozen chemical reactions that can occur during the pre-discharge phase. Surely the level of detail and the precision of the forecasts then deduced would be very high, as demonstrated by the works [78, 75, 31]. However, from an engineering point of view, it is not a very inviting solution, mainly because of the numerous numerical instabilities that can be encountered, to be managed case by case every time one changes the geometry of the system considered, and, more generally, because of the large amount of time required to complete the calculations.

In the end, the approach that seemed to be the most appropriate and fastest was the one suggested by Schumann. The criterion he proposed, in

fact, besides being rather simple to implement even in highly non-uniform electric field conditions, allows reasonable calculation times for the parametric analysis of the investigated insulation system. Moreover, although the empirical nature of the formula at the basis of the discharge criterion, the Schumann equation allows to take into account not only the geometry, but also the conditions of temperature, pressure and chemical composition of the air surrounding the winding. This peculiarity, more than any other, has been decisive for the adoption of this criterion in favour of those mentioned above.

Therefore, the following subsections provide a complete description of how Schumann's discharge criterion for predicting the Partial Discharge Inception Voltage ($PDIV$) in the low-voltage motors windings was implemented and the limits of such modelling. In addition, at the end of the section, all the experimental data that have been collected in support of the designed predictive model are provided.

2.1.1 Application of the Schumann criterion in non-uniform electric fields

First, it is necessary to define the geometry of the system. In a similar way to what is suggested by the standards [18], instead of considering the entire complexity of the stator, in a first analysis the single non-impregnated twisted pair is taken into consideration. It corresponds to the worst case, because inside the stator the enamel is the weakest insulation, especially if impregnating resin that fills the air interfaces is absent.

Therefore, to begin with, a simplified FEM analysis of the electrical field in a twisted pair was carried out using COMSOL Multiphysics®. As depicted in Fig. 2.1, the model is in two dimensions and is composed of two circular section conductors, covered by their respective insulating enamels and in contact, immersed in air. One wire is connected to the high voltage, while the other is grounded. Electrostatic simulations for wires having different diameter and insulation thickness (according to IEC 60317-0-1 [24]) were performed initially with a unitary voltage, to obtain a reference. The figure, in fact, also shows the distribution of the electric field around the wires (only the upper half was considered because the system shows an axial symmetry of $x = 0$ axis) and, above all, a reasonable number of electric field lines, fundamental for the Schumann's criterion application.

Assuming a linear behaviour of the materials, the electric field will vary linearly according to the voltage between the two wires. Consequently, at a generic point, the electric field E can be calculated from the electric
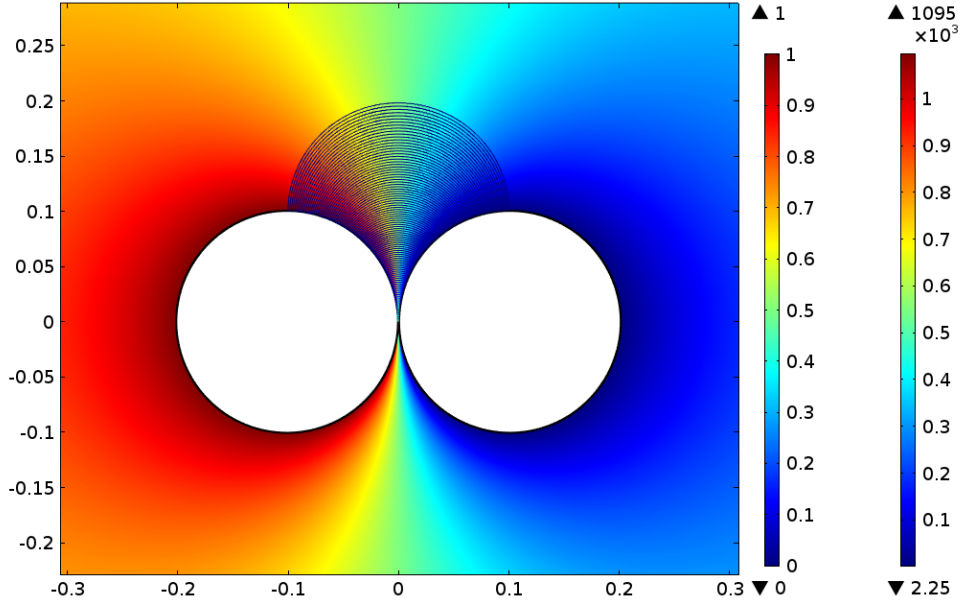
Figure 2.1: Modeling of the electric field of an insulated twisted pair by mean of COMSOL Multiphysics®. The scale of the axes is expressed in cm. The coloured bar on the left indicates the voltage intensity scale (in V), while the one on the right refers to the applied electric field (in $\mathrm{V\,cm^{-1}}$).

reference field E_0 and the voltage actually applied V as follows:

$$E(x, y) = \frac{V}{V_0} E_0(x, y) \qquad (2.1)$$

where V_0 is the reference voltage at which E_0 has been calculated.

Note that before proceeding with the actual application of the Schumann criterion, it is necessary to know the trend of the Townsend effective ionization coefficient as a function of the specific electric field, i.e. the ratio between the electric field and the pressure (see Eq. A.17). In fact, remember that the latter is described by a curve with different characteristics depending on the actual composition of the air. It is also for this reason that, for example, humidity has an impact on the phenomena of partial discharge inception. The strategy adopted to achieve this function will be presented in detail below.

Finally, the impact of temperature must be taken into account. Assuming with good approximation that the air surrounding the wires (regardless of its precise composition) can be considered a perfect gas, it is possible to introduce a so-called equivalent pressure p_H: it is the pressure that would provide, at the reference temperature T_{ref}, the same number of gas

molecules per unit volume observed at the given temperature T_H.

The equivalent pressure is derived considering the perfect gas law:

$$p = nk_BT \tag{2.2}$$

where n is the number of gas moles per unit volume, T is the absolute temperature at which it is located and $k_B = 1.380649 \cdot 10^{-23}\,\mathrm{J\,K^{-1}}$ is the Boltzmann's constant. Therefore, varying the temperature from a reference temperature T_{ref} to an other temperature T_H affects the number of gas moles per unit volume:

$$n_H T_H = n_{ref} T_{ref} \tag{2.3}$$

On the other hand, the increase in temperature in the vicinity of the windings causes the surrounding air density to decrease, while at the same time increasing the average electronic free path. Therefore, introducing the equivalent pressure definition just given to take into account this fact, one can write the following equivalence:

$$\frac{E/p_{ref}}{E/p_H} = \frac{E/n_{ref}}{E/n_H} \tag{2.4}$$

that is

$$p_H = p_{ref}\frac{n_H}{n_{ref}} \tag{2.5}$$

Combining Eq 2.3 with Eq. 2.5 ultimately results in the relationship that allows to take into account the temperature difference:

$$p_H = p_{ref}\frac{T_{ref}}{T_H} \tag{2.6}$$

In principle, this treatment is very similar to the one that leads to Eq. A.20, but with the advantage of being more general, since it is related directly to the ionization coefficient, and can also be applied to pressures other than the environment.

At this point all the ingredients are in place to implement a calculation algorithm for estimating the $PDIV$ of twisted pairs, using Schumann's criterion. Once all parameters are defined, the following iterative approach is used for a given configuration:

1. import the electric field distribution $E_0(x, y)$ at the reference voltage V_0 and evaluate $E(x, y)$ at the new voltage V using Eq. 2.1;

2. determine the Townsend effective ionisation coefficient $\overline{\alpha}$ curve as a function of the specific electric field E/p for the specific air composition (depending on the combination of temperature, pressure, relative humidity and pollution);
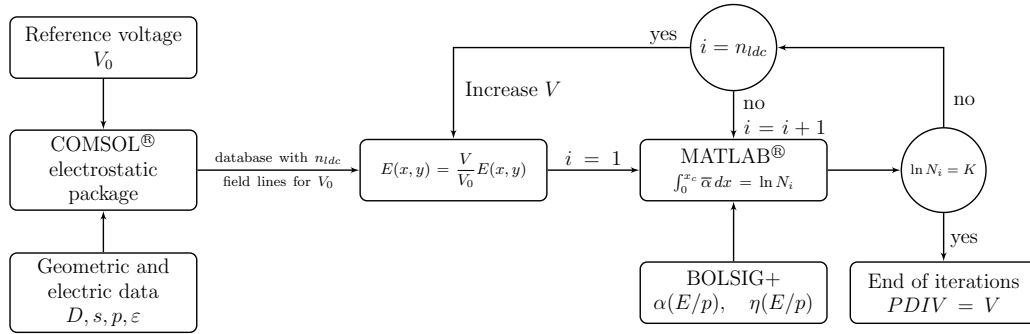
Figure 2.2: Flowchart of the Schumann algorithm in order to predict $PDIV$ in arbitrary non-uniform geometries.

3. verify that the Schumann's criterion, i.e. the Eq. A.34, is met for at least one electric field line. If this does not happen, repeat from step 1 by increasing the voltage by ΔV.

Fig. 2.2 shows in a schematic way the functioning of the iterative approach just described.

The only aspect that remains to be clarified is the choice of the value of Schumann's constant. As has already been pointed out, it has an exquisitely empirical nature and seems to depend on the characteristics of the electrodes (whether they are naked or isolated, whether the geometry is simple or complex, etc.). Consequently, it was necessary to investigate the experimental value of the Schumann constant for twisted pairs or, more generally, for random wound windings. This was done by performing a series of conventional $50\,\mathrm{Hz}$ AC PD tests on twisted pairs (10 samples for each case) with different characteristics.

Once the $PDIV$ experimental values of each case considered were obtained, the following iterative algorithm was adopted to determine the corresponding value of K:

1. import the electric field distribution $E_0(x, y)$ at the reference voltage V_0 and evaluate $E(x, y)$ at the $PDIV$ (in $\mathrm{V_{pk}}$) using Eq. 2.1;

2. determine the Townsend effective ionisation coefficient $\overline{\alpha}$ curve as a function of the specific electric field E/p for the experimental air composition (depending on the combination of temperature, pressure, relative humidity and pollution);

3. set the first attempt value, $K = 18$;

4. evaluate the left term of Eq. A.34 for each field line;
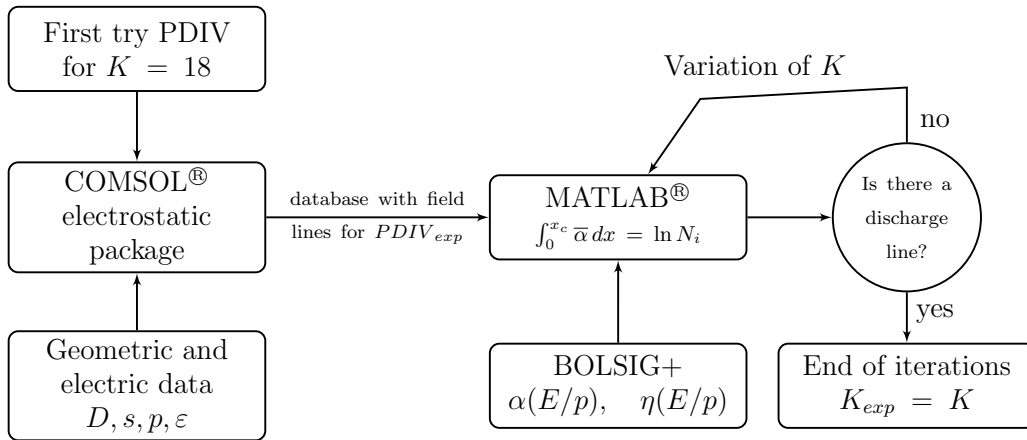
Figure 2.3: Flowchart of the algorithm in order to estimate the experimental value of K_{exp} for each experiment.

5. if Schumann's criterion is met for at least one electric field line, then Schumann's experimental constant K_{exp} has been found, otherwise K is decreased by a quantity ΔK and repeated from step 4.

When step 5 is completed, the shortest electric field line satisfying Eq. A.34 is taken as the discharge (or critical) line. The diagram in Fig. 2.3 visually summarises the procedure described above.

Table 2.1 lists the characteristics of the twisted pairs analysed and the $PDIV$ results obtained. D_{out} is the outer diameter of the wires, s is the thickness of the insulating enamel, ε_r is the relative permittivity of the insulation (determined experimentally separately), $PDIV$ is the inception voltage B10-percentile, while $p \cdot d$ is the product between the pressure and the length of the discharge line deduced by the software. For the sake of completeness, the estimated values of the Weibull parameters associated with each test were also reported through statistical analysis.

To obtain a fairly reliable estimate of K, the values of D_{out}, s and ε_r were not taken from the wire datasheets, but determined experimentally. Initially, the outer diameter D_{out} was measured using a micrometer screw, at 20 different points of the wire at least $5\,\mathrm{cm}$ apart. After that, the insulating enamel was removed by a chemical process that ensured that the conductor was not removed and the same measurement was carried out again to determine, this time, the internal diameter D_{in}. In this way, it was possible to deduce, by difference, the thickness of the insulation s.

To estimate the enamel relative permittivity, a High-Resolution Dielectric Analyzer (Novocontrol Technologies Alpha-N) was used and 10 samples were produced for each type of wire. In particular, the enamel was removed

Table 2.1: $PDIV$ values obtained during the experiments (n=10) and evaluation of the Schumann constant.

Code	$\mathbf{D_{out}}$ mm	$\mathbf{s}$ µm	$\varepsilon_\mathbf{r}$ a.u.	$\mathbf{PDIV_{B10}}$ V_{pk}	η V_{pk}	β a.u.	$\mathbf{p \cdot d}$ bar cm	$\mathbf{K_{exp}}$ a.u.
W1	0.40	16	4.53	567	596	44.66	0.0018	5.79
W2	0.60	18	3.87	578	582	302.2	0.0032	5.36
W3	0.80	24	3.74	623	686	23.23	0.0031	5.3
W4	0.62	29	4.55	712	747	47.04	0.0037	6.08
W5	0.59	30	3.99	734	767	50.89	0.0038	6.26
W6	1.00	30	4.09	756	813	31.22	0.0039	6.58
W7	1.70	40	3.14	854	915	32.63	0.0036	5.94
W8	1.20	42	3.60	848	883	54.35	0.0037	6.12
W9	1.80	43	3.56	877	925	41.84	0.0041	6.42

from one of the two ends of the samples, so that it could be connected to the voltage side of the measurement circuit, while the central part was painted with conductive varnish (with silver particles) to create the earth electrode. The measuring instrument evaluated the apparent capacity of the samples, from which the relative permittivity could be calculated according to

$$\varepsilon_r = \frac{C_p}{2\pi\varepsilon_0 l} \ln\left(\frac{D_{out}}{D_{in}}\right) \tag{2.7}$$

where C_p is the measured capacitance, ε_0 is the vacuum permittivity and l is the wire's painted part length. The value shown in Table 2.1 corresponds to the average value calculated on the 10 samples.

In conclusion, for the $PDIV$ estimation of an arbitrary wire, the average value $K = 5.98$ was considered.

2.1.2 The FEM: modelling considerations

The first reasonable objection that can be made to the modelling strategy is the use of a two-dimensional geometry instead of a three-dimensional one, since the $PDIV$ values measured on twisted pairs were used as a reference.

Indeed, after a first phase of code optimization, a study was launched to understand whether the three-dimensional approach could lead to a better estimate of the $PDIV$ depending on the parameters studied. In particular, it was intended to verify whether the trend of the $PDIV$ as a function of
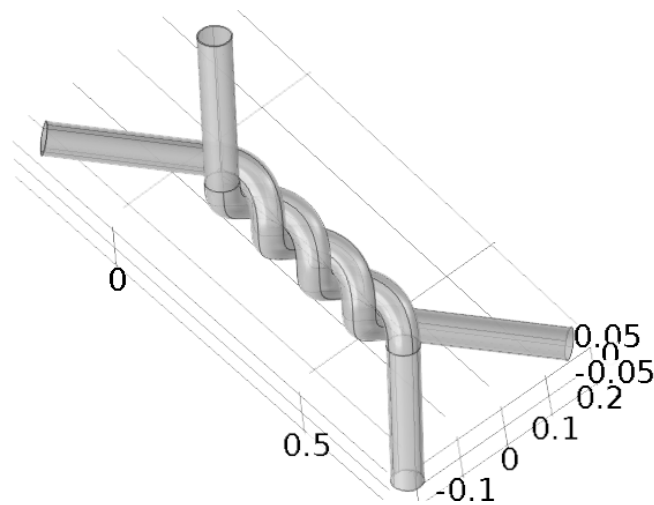
Figure 2.4: Three-dimensional plot of the 5 turns twisted pair model.

the combination of temperature and pressure, and of temperature and relative humidity, was closer to that found experimentally. Fig. 2.4 shows the geometry of the three-dimensional twisted pair model.

Unfortunately, after several attempts to refine the mesh and optimize the calculation code, the project was abandoned. There were two main reasons why the two-dimensional approach was retained: first, it was seen that the behaviour of the $PDIV$, estimated from the real electric field applied (the one in the three dimensions), as a function of the geometric and environmental parameters does not vary significantly in terms of quality. Moreover, the calculation times for the determination of the electric field distribution, as well as for the $PDIV$ estimation, with the three-dimensional approach are excessively long. Table 2.2 lists the details of a simulation carried out with both methods and compares the performance. Fig. 2.5, instead, depicts the trends obtained through the two different calculation approaches and compares them with the data obtained experimentally for the wire studied (AC $50\,\mathrm{Hz}$ PD tests, see Fig. 2.15). Below $100\,\mathrm{mbar}$, both methods no longer follow the experimental trend correctly. As will be explained below, this fact is due to the failure of the initial hypotheses, which result in a growing error in the estimation of the ionization coefficient as a function of the electric field.

However, a positive aspect of this analysis is that it has implemented all the necessary tools, from a numerical and software point of view, to manage the evaluation of the PD inception in three-dimensional geometries. In particular, the software developed for the $PDIV$ prediction is not bound to the geometry of the system under consideration, since it analyses only
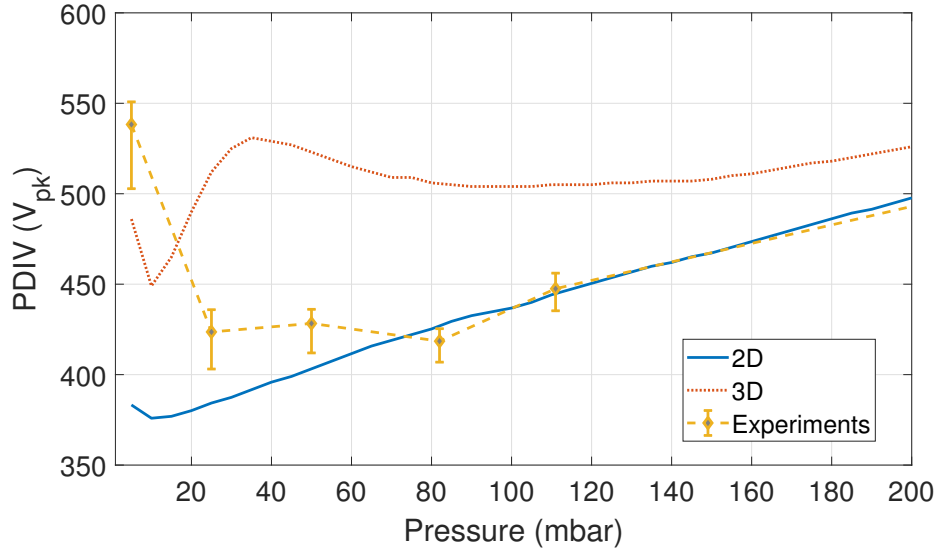
Figure 2.5: $PDIV$ trend as a function of the pressure, estimated with the bi-dimensional approach (blue line), with the three-dimensional approach (red line) and AC experiments (yellow points with associated error bars).

the electric field lines that are given to it. Consequently, in principle, it would be possible to test the software, without any change in the code, by directly loading the calculated electric field distribution for the air zones inside, or near, the stator, and asking it to identify the weak point.

Another important analysis, which was also done later, was to determine the optimal number of field lines to be considered when applying the Schumann criterion. As shown in Fig. 2.1, the electric field lines are drawn using software (COMSOL Multiphysics®) from the point of contact of the two enamelled wires to the centre of the two circumferences. At first, the number of lines drawn was fixed at a constant value, regardless of the actual system geometry considered. Subsequently, it was realized that as the diameter increased, the spacing between one field line and the next would logically increase. As a result, this inevitably had an impact on the accuracy of the $PDIV$ estimates made, and this effect was all the more evident when one goes to reduced values of pressure or high temperatures.

When this problem was noticed, a more precise study of the geometry was made. In other words, a function was identified to determine the number of lines n_{ldc} to be considered depending on the diameter of the conductor D and the thickness of the enamel s, so that a line was no more than $1\,\mu\mathrm{m}$ from the nearest ones. In order to do this, the number of lines required for this condition to be met for different combinations of diameter

Table 2.2: Summary of simulation features and computation times.

Parameter	Value	
Conductor diameter	$0.56\,\mathrm{mm}$	
Insulation thickness	$21.5\,\mu\mathrm{m}$	
Relative permittivity	2.7	
Minimum pressure	$5\,\mathrm{mbar}$	
Maximum pressure	$200\,\mathrm{mbar}$	
Temperature	$20\,^{\circ}\mathrm{C}$	
Number of $PDIV$ estimations	40	
Number of FEM simulations	1	
Number of elements	(2D) $50\,494$	(3D) $2\,019\,481$
Computation time ($PDIV$)	(2D) $194\,\mathrm{s}$	(3D) $6771\,\mathrm{s}$
Computation time (FEM)	(2D) $12\,\mathrm{s}$	(3D) $6632\,\mathrm{s}$
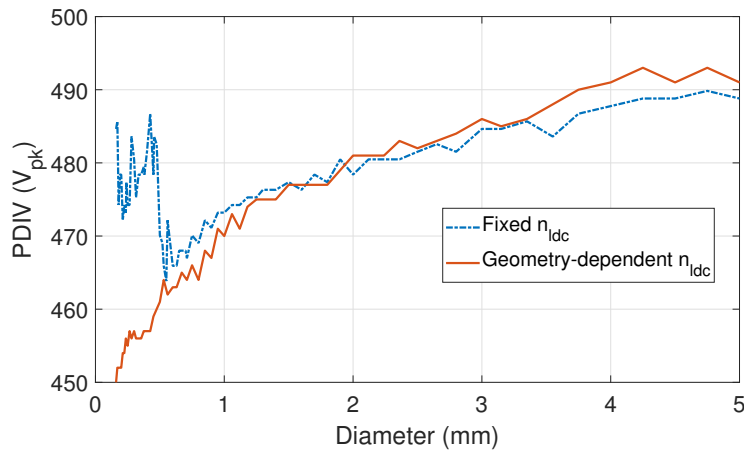
Figure 2.6: $PDIV$ trend for a number of different grade 2 wires at $100\,\mathrm{mbar}$ using a fixed number of electric field lines (blue line) and a geometry-dependent number of electric field lines (red line).

and thickness was first determined. These points were then interpolated to obtain the following function:

$$n_{ldc}(D, s) = 2 \cdot ceil\{200 \cdot [3.922 \cdot (D + s) - 0.02597)]\} \qquad (2.8)$$

where $ceil(x)$ is a function that approximates the real number x by excess to the nearest integer and the parameters D and s must be expressed in mm. When studying the behaviour of the $PDIV$ as a function of pressure, external field lines are also considered, i.e. beyond the centre of the two circumferences. In this situation, the number obtained by applying Eq. 2.8 must be doubled. Fig. 2.6 illustrates the estimated $PDIV$ trend for a number of different wires at $100\,\mathrm{mbar}$ using, in one case, a fixed number of field lines and, in the other, a number of field lines depending on the geometry. It can be seen that the second curve better follows the experimental data trend.

2.1.3 Determination of the effective Townsend ionization coefficient: the Boltzmann equation

The Townsend ionization coefficient and the attachment coefficient are two macroscopic parameters of ionization. In order to obtain their trend as a function of the electric field in relation to pressure (i.e., implicitly, to the average energy possessed by electrons) it is necessary to solve the equation that describes the microscopic behaviour of electrons during ionizing processes, i.e. the equation of electronic transport (or Boltzmann's). It may be written as follows:

$$\frac{\partial f}{\partial t} + \vec{v} \cdot \nabla f - \frac{q_e}{m_e} \cdot \vec{E} \cdot \nabla_{\vec{v}} f = C[f] \qquad (2.9)$$

where q_e is the electronic charge, m_e is the electronic mass, $\vec{E}$ is the electric field, $\vec{v}$ is the electronic velocity vector, $\nabla_{\vec{v}}$ is the Nabla operator in the velocity space and $C[f]$ represents the variation of f due to the collisions, the so-called Boltzmann collisional integral.

It is not considered appropriate here to demonstrate how the electronic growth equation derived from Townsend (Eq. A.1) can be obtained as a particular case from Boltzmann's equation. In this regard please refer to specialized works, such as [46]. On the other hand, there is a free software developed by Gerjan Hagelaar of the LAPLACE laboratory of the University of Toulouse in France that allows to solve numerically the Boltzmann equation for electrons in various types of gas discharges [47].

This software is called BOLSIG+ and there is a version without Graphic User Interface (GUI) that can be easily implemented within MATLAB code: it is BOLSIG-.

Beyond the conditions in which the discharge occurs and the characteristics of the gas, BOLSIG requires the cross sections of all collision reactions that may occur, which are indicated by the user himself.

In the case of modelling partial discharges into the air, it is necessary to consider all possible collision reactions involving oxygen, nitrogen, carbon dioxide, argon and water. It is well known that the average free electronic path in air under standard conditions is about $65\,\mathrm{nm}$ [38]. This means that elastic processes cannot be neglected. The most important ones are those related to nitrogen and oxygen, because of the abundance in concentration. On the other hand, due to air ionisation, logically it is necessary to consider at least the most important ionisation reactions. In particular, direct ionization by electronic impact is responsible for generating cold (or non-thermal) discharges, i.e. in ionized gases where the electronic energies are rather high, while those of neutrals are modest. Finally, attachment phenomena are also to be considered, which play an important role in the balance of air particles when the pressure is below $0.1\,\mathrm{bar}$.

For the estimation of the $PDIV$ of a generic twisted pair, the reactions listed in Table 2.3, 2.4, 2.5, 2.6 and 2.7 were considered, whose associated cross sections were taken from the LXCAT database [60]. Fig.s 2.7, 2.8, 2.9, 2.10 and 2.11 show in detail the cross sections' trend as a function of electronic energy. Note that the reaction 42 is not represented, since it is normalized with respect to the gas density. For this reason, it has been shown separately in Fig. 2.12.

The last missing element is the composition of the air, which for simplicity has been assumed to change only according to the humidity and the temperature. On the other hand, the concentrations of the most important constituents tend not to change according to altitude, except above 80 km above sea level (which is not of interest for the applications studied in this context). Fig. 2.13 shows the concentration trend of the different constituents, apart from that of diatomic nitrogen, as a function of altitude. Beyond the trace constituents, it can be observed that the concentration of diatomic oxygen, Argon and carbon dioxide remains about constant within the first 80 km of altitude.

However, it was not possible to carry out the validation experiments in the laboratory by precisely changing the air composition on the base of the working altitude: the only thing that could be done was to create a vacuum in a chamber previously filled with atmospheric air at sea level. Consequently, it was not considered necessary to take this aspect into

Table 2.3: Nitrogen's reactions to solve Boltzmann's equation. Adapted from [82].

Number	Reaction	Type	$E_{threshold}$(eV)
1	$e^- + N_2 \longrightarrow e^- + N_2$	elastic	-
2	$e^- + N_2 \longrightarrow e^- + N_2(r)$	rotational	0.02
3	$e^- + N_2 \longrightarrow e^- + N_2[v = 1(I)]$	vibrational	0.29
4	$e^- + N_2 \longrightarrow e^- + N_2[v = 1(II)]$	vibrational	1.6
5	$e^- + N_2 \longrightarrow e^- + N_2(v = 2)$	vibrational	1.7
6	$e^- + N_2 \longrightarrow e^- + N_2(v = 3)$	vibrational	1.9
7	$e^- + N_2 \longrightarrow e^- + N_2(v = 4)$	vibrational	2
8	$e^- + N_2 \longrightarrow e^- + N_2(v = 5)$	vibrational	2.1
9	$e^- + N_2 \longrightarrow e^- + N_2(v = 6)$	vibrational	2.2
10	$e^- + N_2 \longrightarrow e^- + N_2(v = 7)$	vibrational	2.3
11	$e^- + N_2 \longrightarrow e^- + N_2(v = 8)$	vibrational	2.5
12	$e^- + N_2 \longrightarrow e^- + N_2(A_3, v = 0 - 4)$	electronic	6.17
13	$e^- + N_2 \longrightarrow e^- + N_2(A_3, v = 5 - 9)$	electronic	7
14	$e^- + N_2 \longrightarrow e^- + N_2(B_3)$	electronic	7.35
15	$e^- + N_2 \longrightarrow e^- + N_2(W_3)$	electronic	7.36
16	$e^- + N_2 \longrightarrow e^- + N_2(A_3, v > 10)$	electronic	7.8
17	$e^- + N_2 \longrightarrow e^- + N_2(B-3)$	electronic	8.16
18	$e^- + N_2 \longrightarrow e^- + N_2(A-1)$	electronic	8.4
19	$e^- + N_2 \longrightarrow e^- + N_2(A_1)$	electronic	8.55
20	$e^- + N_2 \longrightarrow e^- + N_2(W_1)$	electronic	8.89
21	$e^- + N_2 \longrightarrow e^- + N_2(C_3)$	electronic	11
22	$e^- + N_2 \longrightarrow e^- + N_2(E_3)$	electronic	11.9
23	$e^- + N_2 \longrightarrow e^- + N_2(A_1)$	electronic	12.3
24	$e^- + N_2 \longrightarrow e^- + N_2(\text{sum of singlets})$	electronic	13
25	$e^- + N_2 \longrightarrow 2\,e^- + N_2^+$	ionisation	15.6

Table 2.4: Oxygen's reactions to solve Boltzmann's equation. Adapted from [61].

Number	Reaction	Type	$E_{threshold}$(eV)
26	$e^- + O_2 \longrightarrow e^- + O_2$	elastic	-
27	$e^- + O_2 \longrightarrow e^- + O_2(r)$	rotational	0.07
28	$e^- + O_2 \longrightarrow e^- + O_2[v = 1(I)]$	vibrational	0.19
29	$e^- + O_2 \longrightarrow e^- + O_2[v = 1(II)]$	vibrational	5.0
30	$e^- + O_2 \longrightarrow e^- + O_2[v = 2(I)]$	vibrational	0.38
31	$e^- + O_2 \longrightarrow e^- + O_2[v = 2(II)]$	vibrational	5.0
32	$e^- + O_2 \longrightarrow e^- + O_2(v = 3)$	vibrational	0.57
33	$e^- + O_2 \longrightarrow e^- + O_2(v = 4)$	vibrational	0.75
34	$e^- + O_2 \longrightarrow e^- + O_2(\text{singlet } \Delta)$	electronic	0.98
35	$e^- + O_2 \longrightarrow e^- + O_2(\text{singlet } \Sigma)$	electronic	1.63
36	$e^- + O_2 \longrightarrow e^- + O_2$	electronic	4.5
37	$e^- + O_2 \longrightarrow e^- + O_2$	electronic	6
38	$e^- + O_2 \longrightarrow e^- + O_2$	electronic	8.4
39	$e^- + O_2 \longrightarrow e^- + O_2$	electronic	9.97
40	$e^- + O_2 \longrightarrow 2\,e^- + O_2{}^+$	ionisation	12.1
41	$e^- + O_2 \longrightarrow O + O^-$	attachment	4.9
42	$e^- + O_2 + O_2 \longrightarrow O_2 + O_2{}^-$	attachment	5.8

Table 2.5: Water's reactions to solve Boltzmann's equation. Adapted from [102].

Number	Reaction	Type	$E_{threshold}$(eV)
43	$e^- + H_2O \longrightarrow e^- + H_2O$	elastic	-
44	$e^- + H_2O \longrightarrow e^- + H_2O(r)$	rotational	0.04
45	$e^- + H_2O \longrightarrow e^- + H_2O(v = 1)$	vibrational	0.20
46	$e^- + H_2O \longrightarrow e^- + H_2O(v = 2)$	vibrational	0.45
47	$e^- + H_2O \longrightarrow e^- + H + OH$	electronic	7.1
48	$e^- + H_2O \longrightarrow 2\,e^- + H_2O^+$	ionisation	12.6
49	$e^- + H_2O \longrightarrow H_2 + O^-$	attachment	4.9
50	$e^- + H_2O \longrightarrow OH + H^-$	attachment	5.7

Table 2.6: Argon's reactions to solve Boltzmann's equation. Adapted from [100].

Number	Reaction	Type	$E_{threshold}$(eV)
51	$e^- + Ar \longrightarrow e^- + Ar$	elastic	-
52	$e^- + Ar \longrightarrow e^- + Ar^*$	electronic	11.5
53	$e^- + Ar \longrightarrow 2\,e^- + Ar^+$	ionisation	15.8

Table 2.7: Carbon dioxide's reactions to solve Boltzmann's equation. Adapted from [56].

Number	Reaction	Type	$E_{threshold}$(eV)
54	$e^- + CO_2 \longrightarrow e^- + CO_2$	elastic	-
55	$e^- + CO_2 \longrightarrow e^- + CO_2(v=1)$	vibrational	0.08
56	$e^- + CO_2 \longrightarrow e^- + CO_2(v=2)$	vibrational	0.17
57	$e^- + CO_2 \longrightarrow e^- + CO_2(v=3)$	vibrational	0.25
58	$e^- + CO_2 \longrightarrow e^- + CO_2(v=4)$	vibrational	0.29
59	$e^- + CO_2 \longrightarrow e^- + CO_2(v=5)$	vibrational	0.34
60	$e^- + CO_2 \longrightarrow e^- + CO_2(v=6)$	vibrational	0.42
61	$e^- + CO_2 \longrightarrow e^- + CO_2(v=7)$	vibrational	0.51
62	$e^- + CO_2 \longrightarrow e^- + CO_2$	electronic	2.5
63	$e^- + CO_2 \longrightarrow e^- + CO_2$	electronic	7.0
64	$e^- + CO_2 \longrightarrow e^- + CO_2$	electronic	10.5
65	$e^- + CO_2 \longrightarrow CO_2{}^+$	ionisation	13.3
66	$e^- + CO_2 \longrightarrow CO + O^-$	attachment	3.85
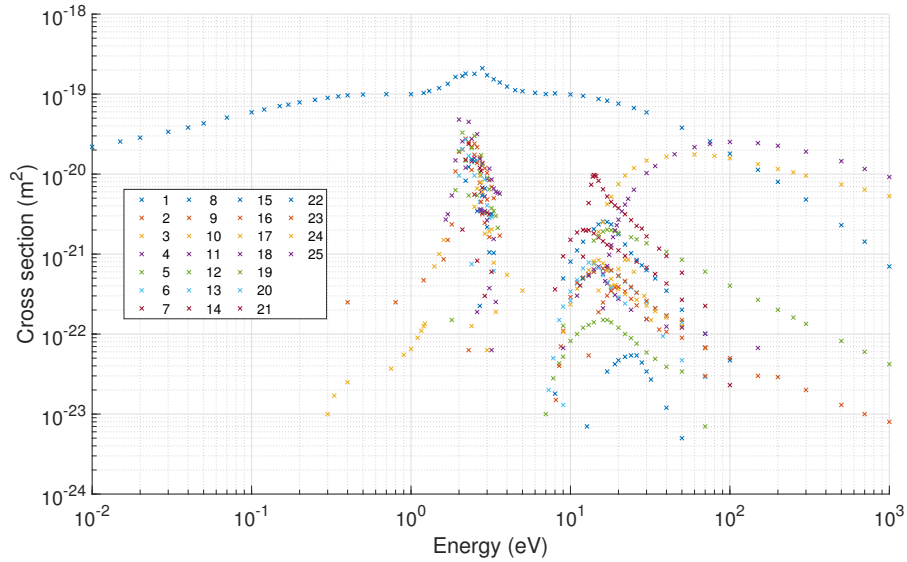
Figure 2.7: The nitrogen cross section as a function of the electronic energy.
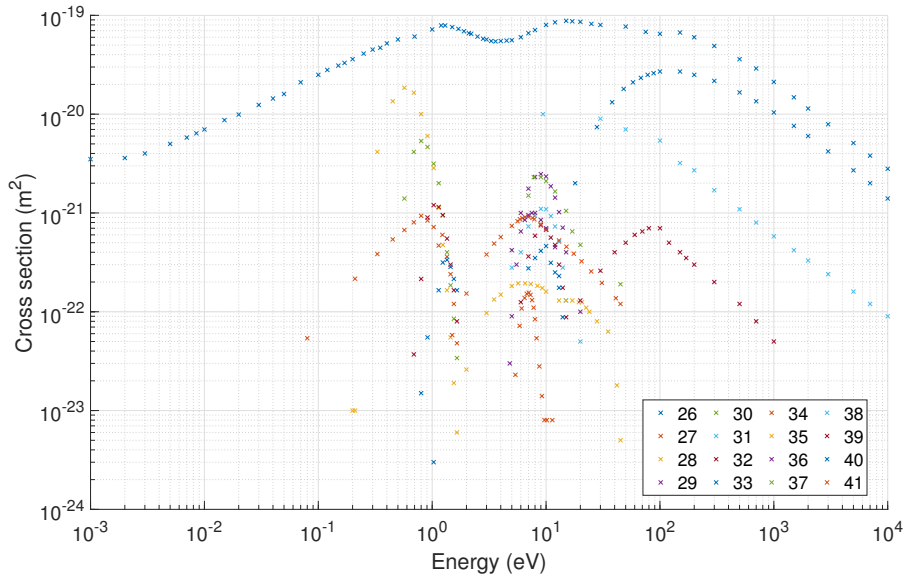
Figure 2.8: The oxygen's cross section as a function of the electronic energy.
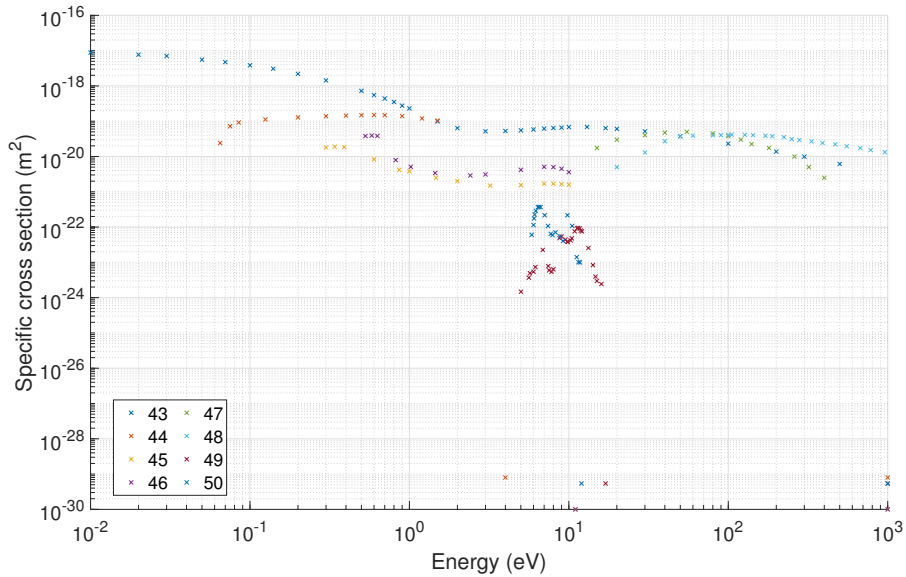
Figure 2.9: The water's cross section as a function of the electronic energy.
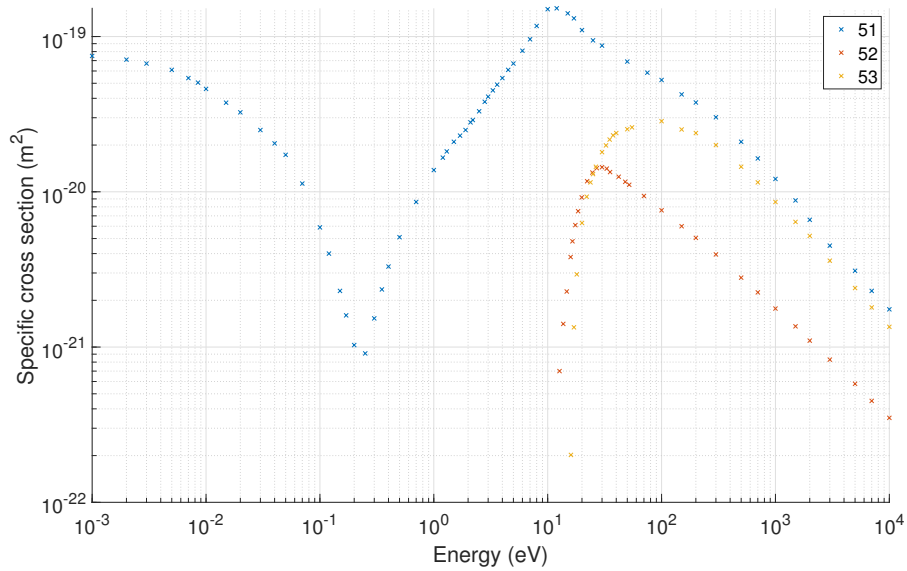
Figure 2.10: The argon's cross section as a function of the electronic energy.
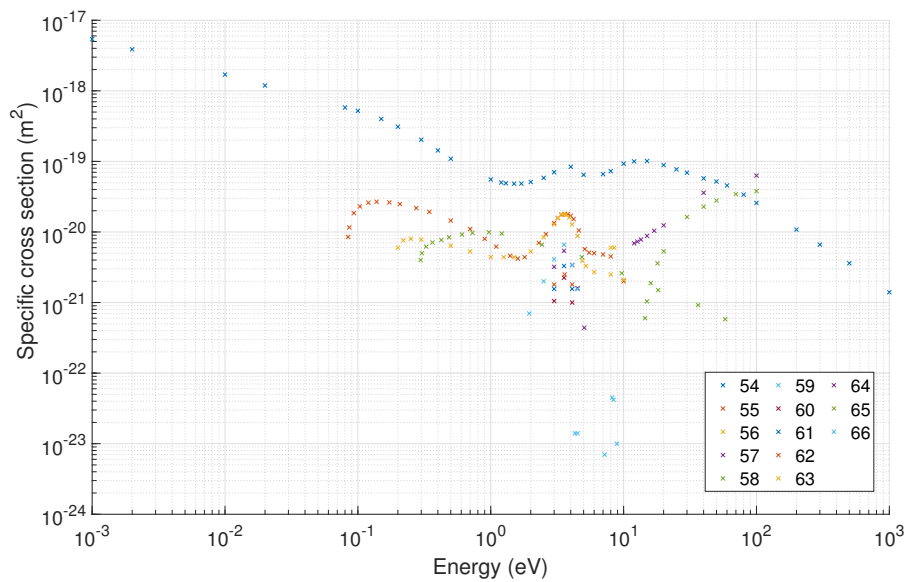
Figure 2.11: The carbon dioxide's cross section as a function of the electronic energy.
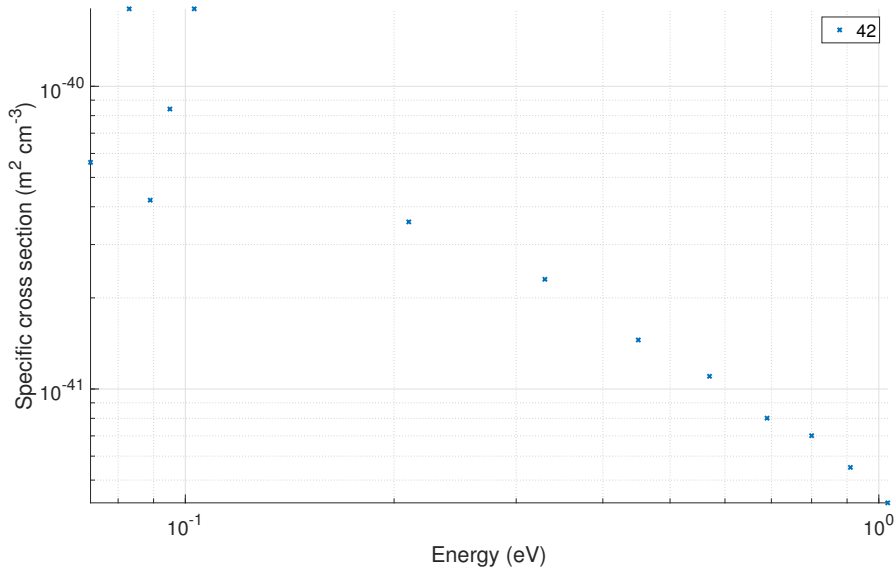
Figure 2.12: The normalized cross section for the oxigen's three-body attachment reaction as a function of the electronic energy.
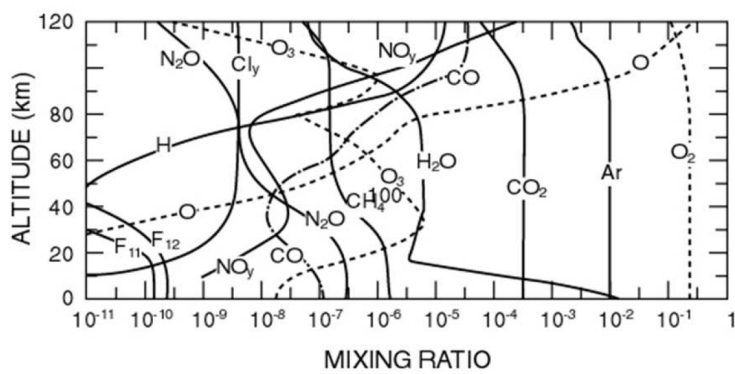
Figure 2.13: Vertical profiles of mixing ratio of selected species at equinox (source: [42]).

consideration in the modelling.

It is initially considered to have a mixture of dry air inside an arbitrarily large container at room temperature ($20\,°C$). Its composition will be as follows [79]:

- 78.08 % Nitrogen;

- 20.95 % Oxygen;

- 0.93 % Argon;

- 0.04 % Carbon dioxide.

Suppose there's $1\,mol$ of oxygen inside the container. Consequently, the molar quantities associated with the other molecules can be determined: $3.73\,mol$ of nitrogen, $0.045\,mol$ of argon and $0.0017\,mol$ of carbon dioxide. At this point, the partial pressure of the water (in Pa), known as the value of relative humidity and temperature (in $°C$), is calculated using the following empirical formula:

$$p_{H_2O} = 611 \cdot RH \cdot 10^{7.5 \frac{t_{amb}}{t_{amb}+237}} \qquad (2.10)$$

This partial pressure, by definition, corresponds to the following molar concentration:

$$x_{H_2O} = 0.622 \frac{p_{H_2O}}{p - p_{H_2O}} \qquad (2.11)$$

where p is the ambient pressure and $M_v/M_a = 0.622$ is the value of the ratio between the molar masses of water and air. Now it is possible to calculate the new amount of total moles if one considers the presence of water:

$$n_{tot} = \frac{n_{N_2} n_{O_2} n_{Ar} n_{CO_2}}{1 - x_{H_2O}} \qquad (2.12)$$

From this, the actual composition of the moist air descends:

$$x_{N_2} = n_{N_2}/n_{tot} \qquad (2.13)$$
$$x_{O_2} = n_{O_2}/n_{tot} \qquad (2.14)$$
$$x_{Ar} = n_{Ar}/n_{tot} \qquad (2.15)$$
$$x_{CO_2} = n_{CO_2}/n_{tot} \qquad (2.16)$$

Fig. 2.14 shows some of the ionization curves calculated in this way for different humidity and temperature conditions.
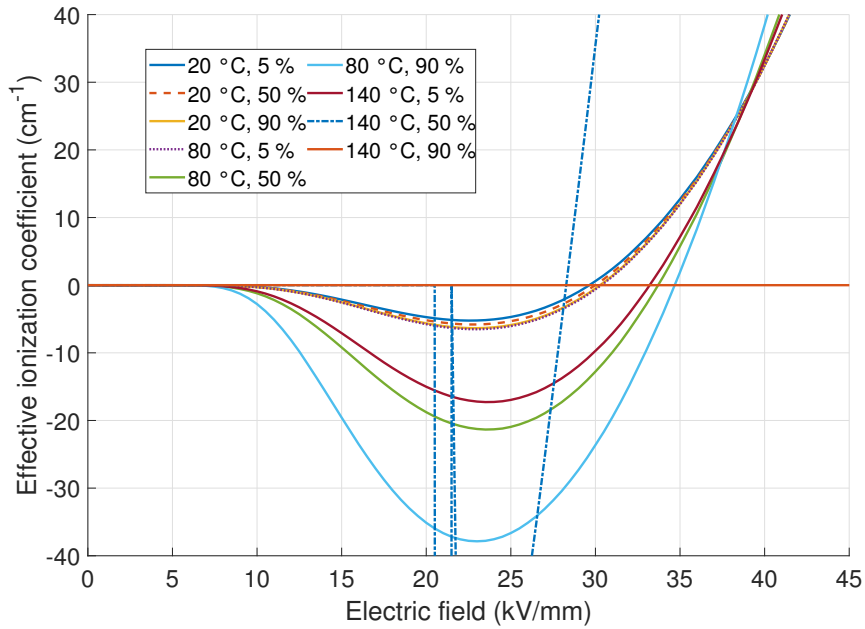
Figure 2.14: Some curves of Townsend's effective ionization coefficient as a function of the specific electric field obtained with BOLSIG.
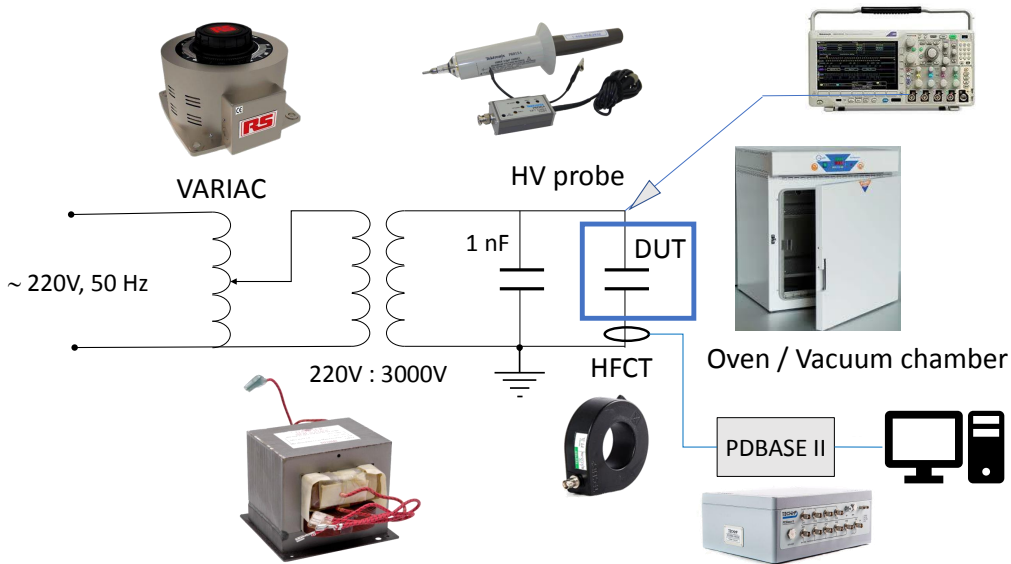
Figure 2.15: Experimental setup for $50\,\mathrm{Hz}$ AC PD test of twisted pair samples at different temperatures and pressures.
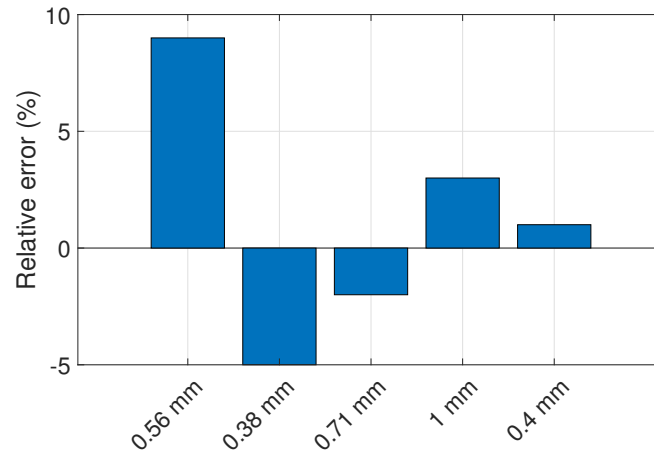
Figure 2.16: Comparison between $PDIV$ estimations and measurements, in terms of relative error committed, at ambient conditions (all wires are grade 2).

2.1.4   Experimental validation

The results of the prediction model described above have been systematically verified over a wide range of situations, with different combinations of geometry, dielectric properties and environmental conditions. For these tests, a $50\,\mathrm{Hz}$ AC generator (a variable autotransformer connected to the grid and, in turn, connected to a medium voltage transformer) and a specific PD acquisition system Techimp®PDBaseII were always used. Each test combination was performed on 10 fresh samples with the same characteristics to have a certain degree of reliability of the measured $PDIV$ value. The sample were not reused to prevent the effects of surface conditioning. In these cases, the value for room temperature has always been taken into account. Fig. 2.15 shows a diagram of the experimental setup.

Table 2.8 lists all the parameters of the PD tests performed and reports both the values recorded for $PDIV$ (10th percentile) and those estimated with the model. For the relative permittivity, the average value measured on 10 different samples using the procedure described previously was considered. Note that it was not possible to take into account the real value of the enamel relative permittivity for temperatures other than the ambient temperature. Fig. 2.16 shows the relative error made in the $PDIV$ estimation, comparing the data obtained with the model with those measured experimentally. It is possible to note that the maximum error committed amounts to 8% in general. Figs. 2.17 and 2.18 show the same comparison, but only high temperature and low pressure cases are shown. Finally, Fig. 2.19 shows the comparison in situations where both the temperature and the

Table 2.8: Experimental results obtained from $50\,\mathrm{Hz}$ AC PD tests at different ambient conditions and wires, and associated predicted $PDIV$ values.

D	t	ε_r	p	T	PDIV$_\mathrm{exp}$			PDIV$_\mathrm{th}$	Error	
mm	μm	a.u.	mbar	°C	$V_\mathrm{pk}^{(B10)}$	max	min	V_pk	Abs.	Rel.
0.56	31.5	2.7	50	20	428.3	412.0	436.1	396	-32	-8%
0.56	31.5	2.7	82	20	418.5	406.9	425.4	423	5	1%
0.56	31.5	2.7	111	20	447.5	435.3	456.1	446	-1	0%
0.56	31.5	2.7	507	20	649.9	631.0	661.6	681	31	5%
0.56	31.5	2.7	1013	20	829.2	793.4	854.4	900	71	9%
0.56	31.5	2.7	82	120	438.0	421.2	448.6	406	-32	-7%
0.56	31.5	2.7	111	120	456.5	444.5	464.4	424	-32	-7%
0.56	31.5	2.7	507	120	597.5	572.5	612.9	612	14	2%
0.56	31.5	2.7	1013	120	764.5	741.4	779.6	800	35	5%
0.38	26	4.1	1013	20	764.1	751.0	771.8	728	-36	-5%
0.71	35	4.4	1013	20	826.9	815.4	834.0	812	-15	-2%
1	57	5.1	1013	20	968.1	943.8	978.8	1001	33	3%
0.4	20	4.0	1013	20	677.3	653.3	691.7	681	4	1%
0.4	16	4.5	1013	150	512.4	507.5	515.4	517	5	1%
0.6	18	3.9	1013	150	576.5	573.4	578.4	563	-14	-2%
0.6	29	4.0	1013	150	701.1	697.2	703.4	649	-52	-7%
0.8	24	3.7	1013	150	587.7	544.5	614.3	621	33	6%
1	30	4.1	1013	150	636.2	601.9	658.1	652	16	2%
1.2	42	3.6	1013	150	787.3	763.4	801.9	771	-16	-2%
1.8	43	3.6	1013	150	780.6	749.5	799.2	776	-5	-1%
0.30	24	7.2	1013	150	513.0	506.6	517.0	526	13	3%
0.62	29	4.5	1013	150	624.8	605.2	636.8	628	3	1%
1.32	51	4.1	1013	150	801.8	788.1	809.8	792	-10	-1%
1.70	40	3.1	1013	150	757.5	734.6	771.7	792	35	5%
0.30	24	7.2	658	25	492.0	478.8	500.1	517	25	5%
0.62	29	4.5	658	25	608.1	656.2	635.4	614	6	1%
1.32	51	4.1	658	25	766.6	730.8	789.3	768	1	0%
1.70	40	3.1	658	25	714.2	668.1	741.5	766	52	7%
0.30	24	7.2	203	25	427.4	380.3	457.4	407	-20	-5%
0.62	29	4.5	203	25	473.8	536	582.2	448	-26	-5%
1.32	51	4.1	203	25	517.6	477.2	541.6	515	-3	-1%
1.70	40	3.1	203	25	558.6	519.6	583.7	531	-28	-5%
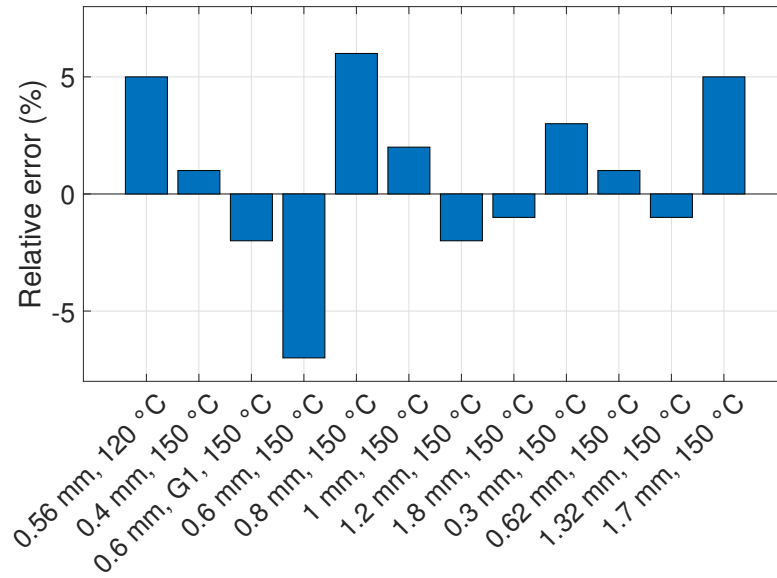
Figure 2.17: Relative error on $PDIV$ estimations in cases where the temperature was different from the ambient temperature (all wires are grade 2, except one).
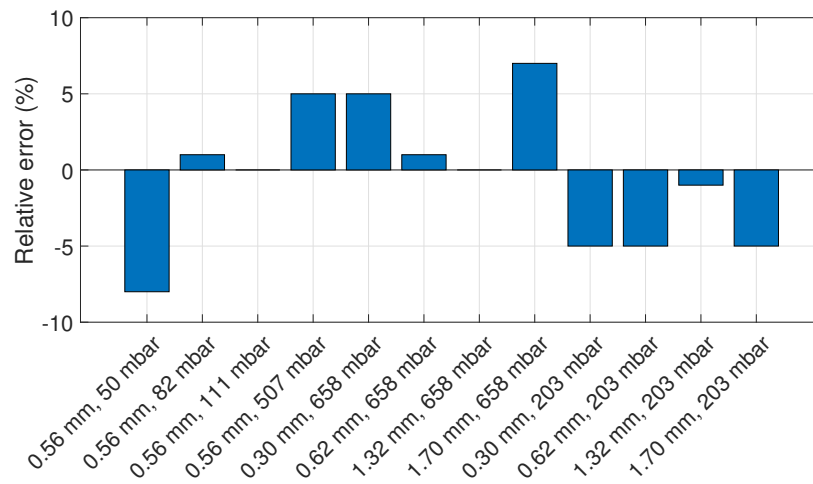
Figure 2.18: Relative error on $PDIV$ estimations in cases where the pressure was different from the ambient pressure (all wires are grade 2).
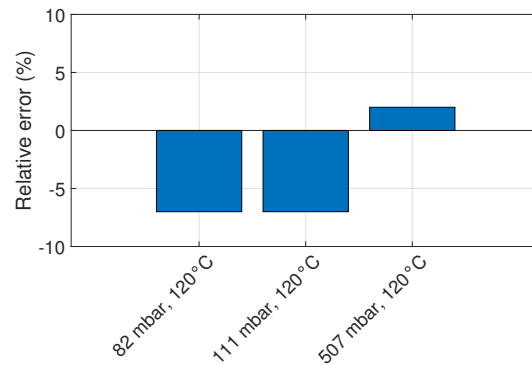
Figure 2.19: Relative error on $PDIV$ estimations in cases where the temperature and pressure were different from the ambient values at the same time (only one wire is used, $D = 0.56$ mm, grade 2).

pressure were different from the ambient values. As can be seen, in general the modelling tends to be imprecise at low pressure values, below 100 mbar, clearly touching the boundaries of validity of the Schumann criterion. In this region, in fact, the $PDIV$ value tends to be overestimated, up to 25%.

2.2   A PDIV **automatic test bench**

The $PDIV$ measurement is a long and tedious task because of the need to have at the same time the combination of three factors: initial electron, adequate electric field conditions and sufficient space. In addition to this, there is the further complication of electromagnetic interference from the generator, especially when equipped with power switches. This makes it difficult to recognize discharge signals when using antenna detectors.

Every PD detection and measuring is based on the exchange of energy which takes place during the discharge event, which are:

- electrical pulse currents;

- electromagnetic radiation;

- dielectric losses;

- radiation of light;

- sound generation;

- chemical reactions.

The most frequently used and successful detection methods are the electrical ones, which indeed are explained in the IEC standards [27].

However, given the particular test conditions (low pressure, high switching frequencies, impulsive waveforms), and especially the intention to use converters made with Silicon Carbide (SiC) MOSFETs, which provide ramps of $7\,\mathrm{ns}$, an optical detection system was adopted, inspired by what done in the past by Okubo and colleagues [49].

The purpose of this system is to measure, with good precision, the $PDIV$ for a wide range of samples in impulsive mode. This is why an optical detection technique is preferred to an electrical one. In order to have a pulsed regime, it is inevitably necessary to use converters, which generate an electromagnetic noise so intense that it is impossible to identify, by means of electromagnetic sensors, the first partial discharge. On the other hand, the switching frequencies that characterize electronic power devices are of the order, at least, a few kHz, so even magnetic detectors (such as current transformers), which would be more robust systems from the point of view of sensitivity to radiated noise, are not usable for the discharge detection.

Another important aspect of the $PDIV$ tests is the repeatability, because in each case at least 5 samples have to be tested. Consequently, it was decided to design, develop and implement a fully automatic system that, depending on the test parameters, would perform the measurement in complete autonomy, without the intervention of the operator.

2.2.1   Overview of the system

The whole system is shown in Fig. 2.20. Suppose that a complete $PDIV$ test is to be carried out, with a bipolar square wave at the f_{user} frequency, at the T_{user} temperature and p_{user} pressure, starting from voltage V_0 and carrying out voltage steps ΔV, each to be maintained for a time Δt.

First of all, the desired test specimen (a motorette or a twisted pair) is inserted inside the vacuum tank, in the appropriate fixture, so as to connect it to the high voltage and at the same time place it in the heating area. Then the tank is hermetically sealed and the vacuum inside is created by means of the rotary vacuum pump.

At this point, the desired test parameters are entered into the software (made in MATLAB®) and the measurement is started. Initially, the system will heat, through the DC power supply, a double highly resistive winding in parallel (Khantal A1 $10\,\Omega/\mathrm{m}$), which by convection and radiation will raise the temperature in the test area. The latter is monitored by a PT100, installed
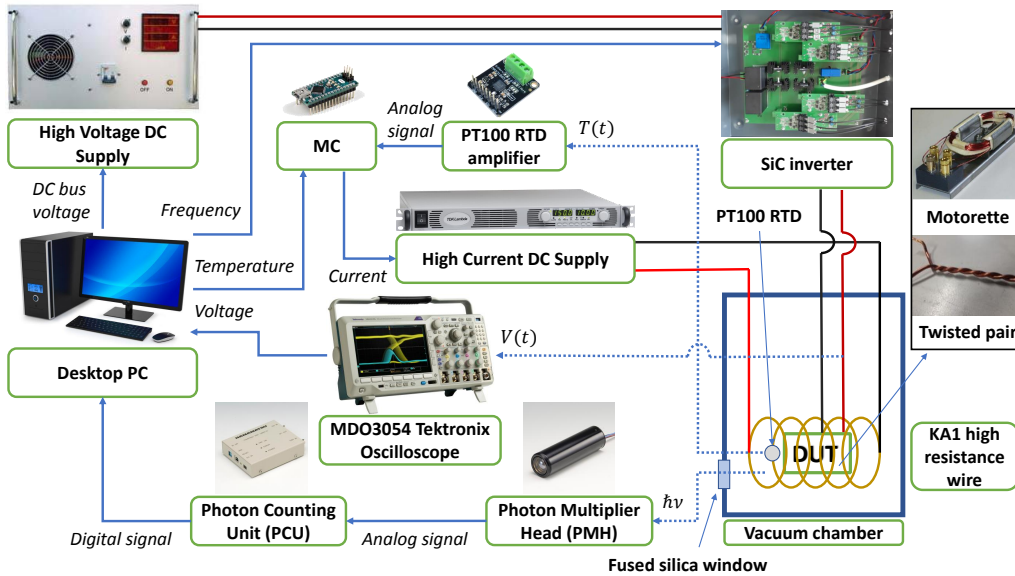
Figure 2.20: Schematic representation of the $PDIV$ automatic test bench system.

near the test specimen, so that the current can be adjusted by means of a PID feedback system (implemented with Arduino®). This guarantees a high stability of the test temperature.

Once the appropriate ambient conditions have been reached, the actual test begins with the application of the initial voltage V_0 via a digital signal to the high-voltage DC generator. The HV DC bus voltage will be sent to the inverter (equipped with SiC-based switches), which will convert it into a bipolar square wave at the chosen frequency and, in turn, will send the wave train to the test specimen terminals. In particular, the connection is made via a vacuum high voltage pass-through. It is here that the voltage is monitored by means of a Tektronix®THDP0100 high voltage differential probe, connected in parallel to the terminals of the above mentioned loop.

The measurement ends when the Photon Counting Unit displays more photons per second than 150% of the background noise (which is typically 3-4 photons per second). In fact, the Photon Counting Unit is connected to a Photon Multiplier Head capable of detecting the photons' generation due to the partial discharge activity. This PMH is located outside the tank to avoid potential damage due to low pressures, but it overlooks a fused silica window, which has a transmission spectrum that allows the passage of light radiations of interest (characterized by a wavelength of around 180-400 nm).

Just before turn off the high voltage supply, the last applied value of the
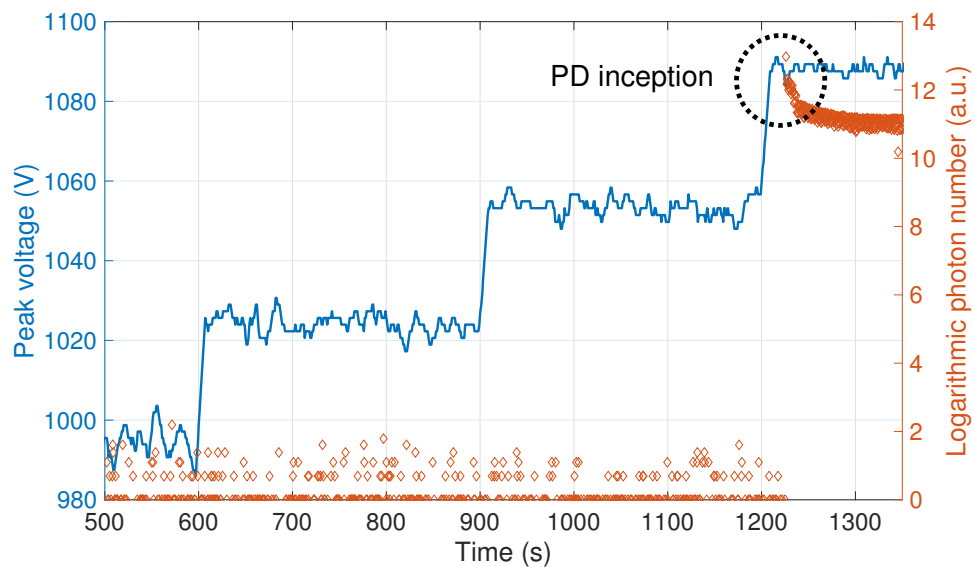
Figure 2.21: Measurement of PD activity through the automatic $PDIV$ test bench during a test on a twisted pair. The highlighted area indicates the PD inception.

DC voltage is recorded and two complete voltage wave periods measured at the test specimen terminals are recorded using the Tektronix®MDO3054B oscilloscope. In this way it is possible to determine the $PDIV$ both in peak-to-peak and DC-bus terms. Fig. 2.21 shows an example of what is displayed on the screen at the end of a test, in which the trigger point is highlighted.

Optionally, the tank is designed to connect additional sensors, other than optical ones (such as antennas, chemical detectors or current transformers), or add other PMHs (through the installation of other windows). This characteristic has made it very easy to verify the correct functioning of the whole system.

2.2.2 Specifications and limits

Table 2.9 lists the main specifications of the automated system. As one can be see, it is flexible enough to cover a wide range of situations.

Moreover, although it has never been tested, the system should also be able to carry out tests in a controlled atmosphere (inert or oxidising), thanks to the seal, ensured by the O-rings placed in the various gaskets, and to the internal chrome-plating of the tank walls.

The system is equipped with a two-pole high-voltage feed-through (up

Table 2.9: Specifications of the automatic $PDIV$ test bench.

Parameter	Description/Value
Maximum counter rate	$50\,\mathrm{MHz}$
Average background noise	2 photons per second
Minimum vacuum pressure	$0.1\,\mathrm{mbar}$
Maximum temperature	$200\,°\mathrm{C}$
Maximum DC-bus voltage	$1500\,\mathrm{V}$
Maximum output current	$5\,\mathrm{A}$
Maximum converter frequency	$200\,\mathrm{kHz}$
Nominal slew rates	$100\text{ - }200\,\mathrm{kV\,\mu s^{-1}}$
Converter output	differential
Converter polarity	unipolar, bipolar
Available voltage waveforms	PWM, square wave, impulse
Test volume	
without temperature control	$11\,000\,\mathrm{cm^3}$
with temperature control	$250\,\mathrm{cm^3}$

to $20\,\mathrm{kV}$). This allows to connect also high voltage generators with differential output, ensuring the safety of the operator thanks to the grounding of the tank.

Note that there are five through holes distributed on the mantle (three placed in a radial at half height, offset by 120° from each other, one on the cap and one on the bottom), with a diameter of $40\,\mathrm{mm}$. They allow the insertion of one or more low-voltage pass-through (for connection inside low-pressure tolerant sensors) or the placement of windows for direct observation during the vacuum test. The latter are in fused silica and their transmission curve is shown in Fig. 2.22(a), of particular importance if one takes into account that the radiation emitted by partial discharges is typically characterized by a wavelength between 180 and $400\,\mathrm{nm}$. Figure 2.22(b), on the other hand, shows for the sake of completeness the sensitivity curve of the sensor inserted inside the PMH. As an example, in Fig. 2.23 one can clearly see, through the window, the violet radiation emitted by the intense partial discharge activity in vacuum.

The limits imposed on the vacuum level and temperature are estimated. The system has been tested up to $1\,\mathrm{mbar}$ pressure and at most up to $120\,°\mathrm{C}$ temperature. However, it is believed that this estimate of the pressure and temperature limits is quite reliable for the following reasons. On the one hand, it has been shown that, already at $1\,\mathrm{mbar}$, air infiltration through the gaskets increases the pressure inside by about $0.1\,\mathrm{mbar\,h^{-1}}$. On the other

(a)

(b)
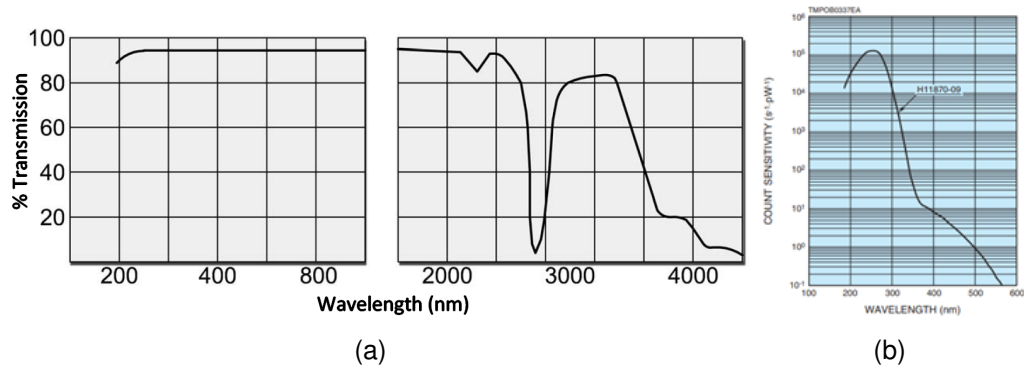
Figure 2.22: (a) Transmission curve of the silica fused windows and (b) sensitivity curve of the PMH's sensor.

hand, the heating system is rather limited in power, because if the resistive wires crossed by current reach a temperature higher than about $400\,°C$, they begin to emit light in the visible spectrum, blinding the optical sensor essential for the partial discharge detection.

Another limitation of the system is the test volume. Since this is a first prototype, the project was carried out by carefully choosing the dimensions. Consequently, especially with regard to temperature tests, the space allowed for the test specimens is very small. This necessarily means that it is possible to test, at least in temperature, only twisted pairs, at most small motorettes. However, for the latter it is probably necessary to prepare a fixture for the connection to the test zone. If the temperature test is not necessary, the heating system can be removed, thus allowing the study of much larger specimens. In this configuration, for example, even small motors could be tested.

In this regard, i.e. on the test of complex samples (such as small transformers, motorettes or even actual motors), the system suffers a drop in sensitivity, since the line of sight of the optical sensor with any discharge areas is no longer guaranteed. In this respect, measurements were carried out on some impregnated dry-type flat transformers and on small motors for industrial use, by means of a single PMH, comparing the results with those obtained by a traditional detection system (connected in parallel so that the measurement can be made simultaneously).

Fig. 2.24 shows how the system, all in all, is somehow able to detect discharge activity, however the detection of $PDIV$ is not guaranteed. In fact, from the experimental evidence, it seems that a fraction of photons can escape from the stator frame and/or the impregnating resin. Probably the installation in different points of several optical sensors, and their coor-
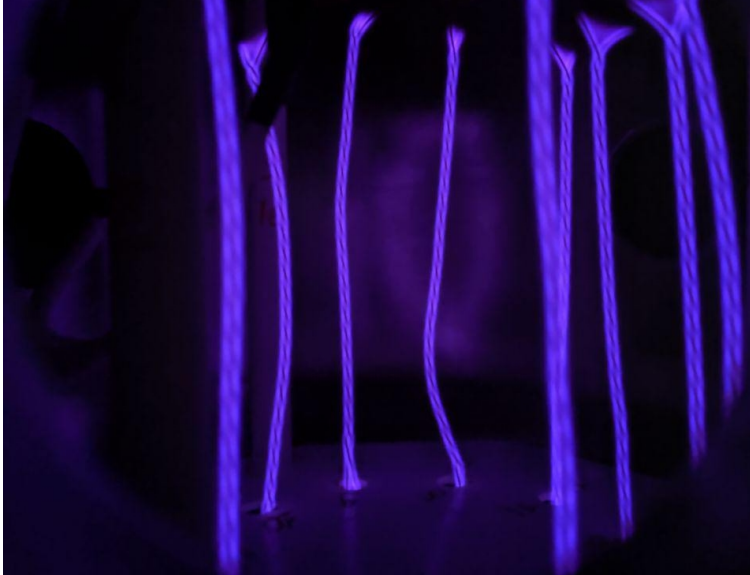
Figure 2.23: PD activity on twisted pairs, seen through the fused silica window, under $10\,\mathrm{mbar}$ and voltage 50% higher than the experimental $PDIV$.
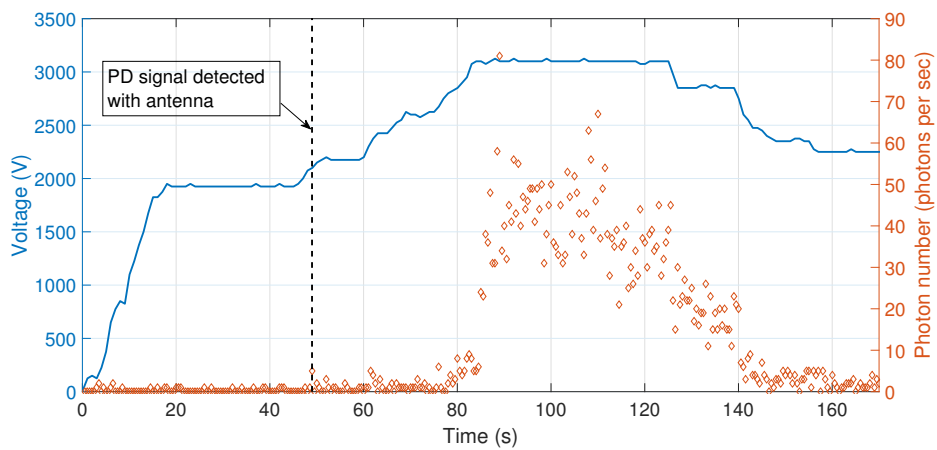
Figure 2.24: Measurement of PD activity using the optical sensor and a traditional (antenna) detection system during a test on a small motor in AC $50\,\mathrm{Hz}$.

dination, would allow a greater sensitivity and, therefore, the possibility of having a system capable of measuring the $PDIV$ even of whole motors. For the time being, this conjecture has not yet been verified. In Chapter 3 the subject will be explored further.

2.2.3 Validation tests

Optical detection of partial discharges is virtually immune to electromagnetic interference. This guarantees an enormous sensitivity of the system, provided that the discharge zone is visible from the optic sensor (PMH). This has been demonstrated repeatedly by making measurements in which conventional PD detection systems have also been installed. In particular, it has been used:

- capacitive coupling ($1000\,\mathrm{pF}$) combined with a high frequency current transformer (HFCT); the signal was then processed by a specialized acquisition system (TechImp®PDBaseII).

- capacitive coupling ($1000\,\mathrm{pF}$) combined with a high frequency current transformer (HFCT) and a Tektronix®Hall effect probe; the sensors were connected directly to a Tektronix®DPO 5034B oscilloscope.

- UHF horn antenna connected to a specialized acquisition system (TechImp®PDBaseII) via a frequency shifter for band adaptation.

A $50\,\mathrm{Hz}$ variable voltage sinusoidal source (variac powered by the grid, connected to a high voltage transformer with a 1:11 transformation ratio), was used for the validation. Fig. 2.25 shows an example of a circuit for measuring partial discharges, as indicated by the IEC 60270 standard [23].

All the measurements carried out on twisted pair samples confirmed the reliability of the system, detecting the phenomenon inception at the same time as what was done by conventional systems. In some cases it even proved to be more robust to electromagnetic noise, making it much easier to detect partial discharges.

2.3 Study of parameters influencing the partial discharge inception

The previous sections have illustrated both the modelling part of the partial discharges and the experimental part. In particular, the previous
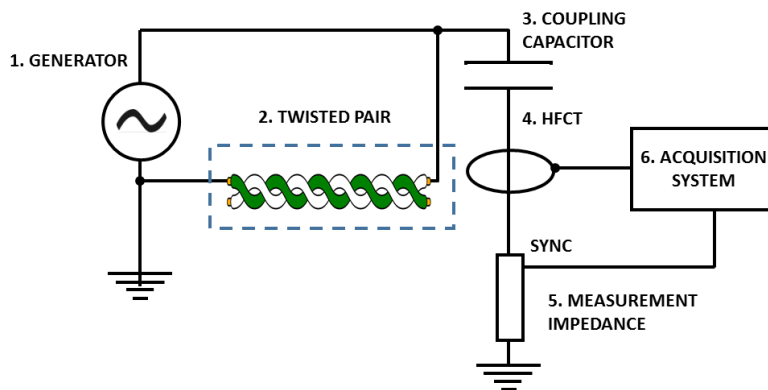
Figure 2.25: Conventional PD test circuit using AC $50\,\mathrm{Hz}$ high voltage supply.

section provided the technical details that characterize the bench test that was used mainly to carry out empirical investigations. However, it was not the only setup used. To investigate the role played by air humidity on the phenomenon, a matrix of tests was also performed in the climatic chamber. Overall, it is assumed that the ideal PD test was carried out by applying a $50\,\mathrm{Hz}$ sinusoidal voltage progressively increasing, until the moment when the first discharge was detected. The waiting time between one voltage step and the next is to be long enough to consider certain the probability of triggering at least a partial discharge. In some cases, due to the extensive use of electronic power converters, it was also necessary to use square wave generators. In which case, it will be specified.

In the following it will be illustrated the impact that every single parameter has on the partial discharge inception. The extensive work carried out, both on a theoretical and practical level, allows to provide a deep understanding of the phenomenon and manages to highlight the synergies between the different parameters. All this has the final objective of putting in the best possible conditions the low-voltage motor electrical insulation designer, in order to minimize the size and maximize the effectiveness, depending on the specific parameters of the project.

Table 2.10: Suggested waiting times, between one voltage step and the next, depending on the pressure.

Pressure mbar	Waiting time
1013	$30\,\text{s}$
507	$60\,\text{s}$
111	$5\,\text{min}$
82	$8\,\text{min}$
50	$10\,\text{min}$
25	$20\,\text{min}$

2.3.1 The effect of pressure and temperature

The first study carried out was with the aim of better understanding the influence of pressure and temperature (and a combination thereof) on $PDIV$. From a theoretical point of view, the Eq. 2.4, combined with the perfect gas law (Eq. 2.2), should allow a rather accurate estimate of the $PDIV$. On the other hand, a too strong gas rarefaction makes us move away from the initial hypotheses, in particular the one that establishes that the energy distribution of electrons is similar to that of Boltzmann-Maxwell (or, more simply, that the gas can be treated as ideal). This means, therefore, that the specific ionization coefficient α/p estimated by BOLSIG is not entirely reliable.

From an experimental point of view, it was clear from the outset that measurements at low pressure levels would take longer. Using sinusoidal voltage waveforms, it was observed that $PDIV$ confidence intervals increase as pressure decreases [70], keeping the waiting times between one voltage step and the next unchanged. This phenomenon is justifiable if one considers that the photo-ionization of gas molecules provides the initial electrons necessary to trigger the PD. At low pressure, since the gas is more rarefied, the average time between two consecutive ionizations $\overline{\Delta t_e}$ is greater than at ambient pressure. According to [77], $MTBE$ should scale as:

$$MTBE(p) = \frac{p_0}{p}\, MTBE(p_0) \qquad (2.17)$$

To address this problem, the voltage was increased in steps, waiting for each one a time depending on the level of vacuum applied. Table 2.10 lists some waiting times, with the associated pressure level highlighted. The values listed are the result of extensive experimental work and are a compromise to achieve good accuracy over a reasonable waiting time [70].
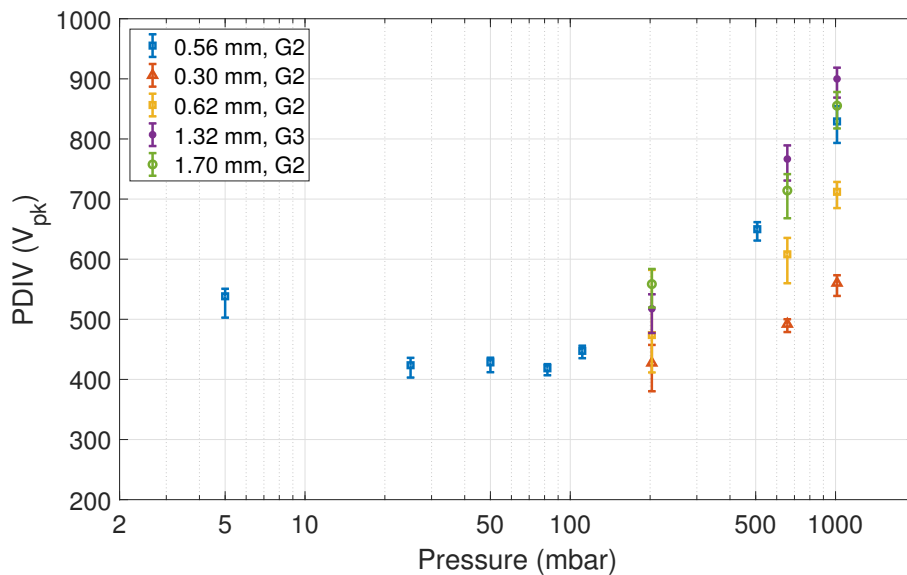
Figure 2.26: Result of the PD tests carried out on different twisted pairs, highlighting the impact of the pressure (each point represents the 10th percentile of the $PDIV$ distribution measured on 10 samples).

Fig. 2.26 shows the result of PD measurements carried out on five different types of twisted pairs as a function of pressure (refer to the values in Table 2.8). Interestingly, twisted pairs with grade 3 of insulation behave differently from those with grade 2. Moreover, down to $100\,\mathrm{mbar}$, it can be claimed that $PDIV$ decreases linearly with pressure.

The increase in temperature also tends to make the air more rarefied, but unlike pressure reduction, the energy of the heavy molecules is increased at the same time. This means that there is no need to increase waiting times when one goes up to temperature. Moreover, since the average energy possessed by electrons also increases, the energy gap separating them from the ionization threshold decreases, making the latter phenomenon more likely.

Fig. 2.27 shows the result of measurements made on twisted pairs made with different wires that had the purpose of highlighting the $PDIV$ trend as a function of temperature. Note that $PDIV$ values may also be affected by changes in the relative permittivity of enamels with temperature, but unfortunately it was not possible to monitor them. In general, a decreasing trend as the temperature increases is confirmed for all, as was also expected theoretically.

It should be noted that pressure and temperature are related to density,
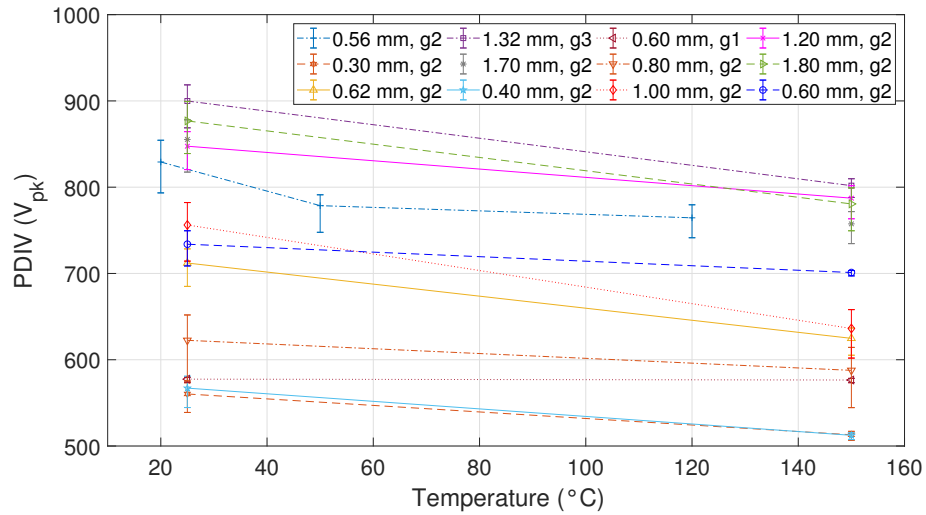
Figure 2.27: Result of the PD tests carried out on different types of twisted pairs, highlighting the impact of the temperature (each point represents the 10th percentile of the $PDIV$ distribution measured on 10 samples).
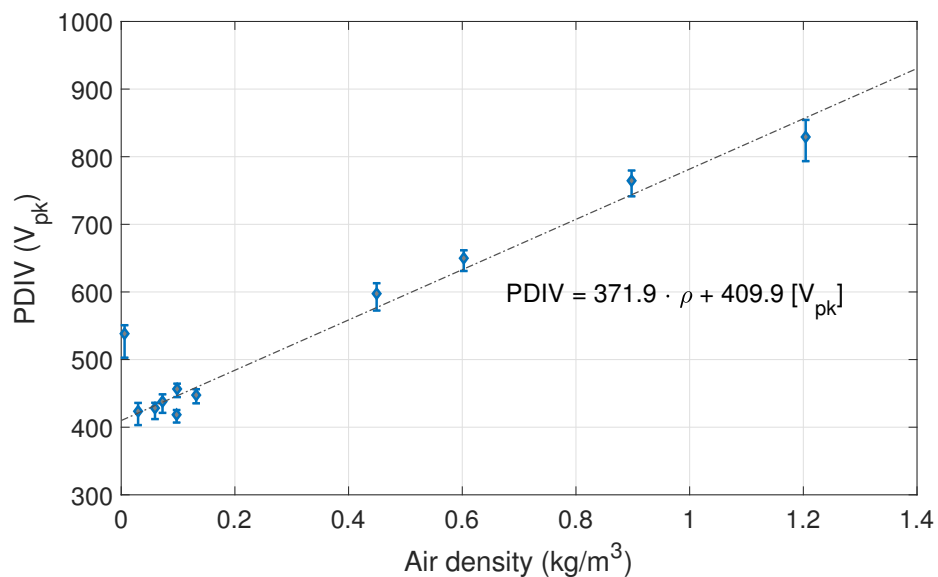
Figure 2.28: Result of the PD tests carried out on twisted pairs, made of a grade $2/0.56\,\mathrm{mm}$ wire, highlighting the impact of the density (each point represents the 10th percentile of the $PDIV$ distribution measured on 10 samples).
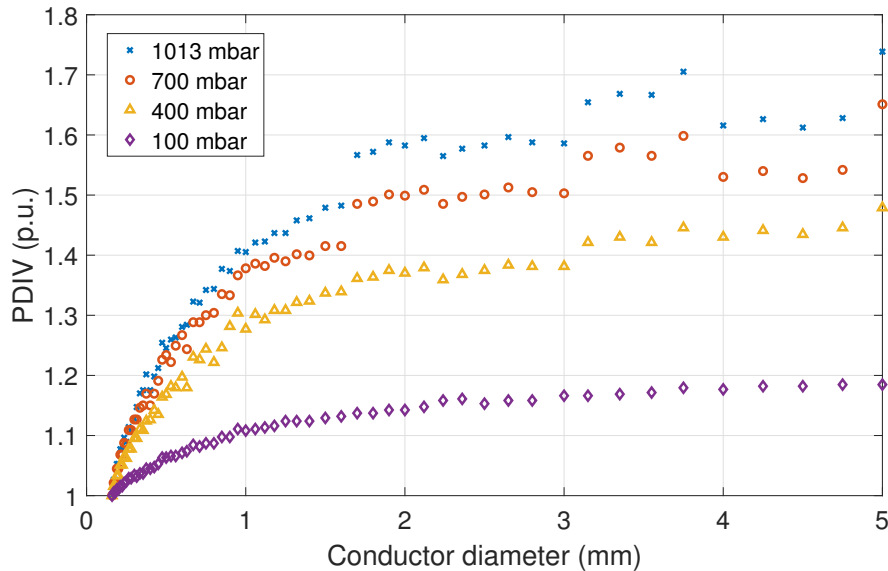
Figure 2.29: Estimated $PDIV$ trend by model depending on the grade 2-wire chosen for four levels of pressure. The reference values are the $PDIV$ obtained with the thinnest wire, for each pressure level.

assuming that the air behaves as an ideal gas (hypothesis founded until it becomes too rarefied). Consequently, it might be interesting to highlight the $PDIV$'s dependence on this last quantity, to see if it is not possible to replace two parameters with just one. Fig. 2.28 shows the result of PD measurements carried out on a single type of twisted pair (made of wire with a conductor diameter equal to $0.56\,\mathrm{mm}$ and insulation grade 2) as a function of density, by combining values obtained at pressures other than atmospheric at sea level and at temperatures other than the standard temperature (refer to the values in Table 2.8). This shows that, until the air density becomes really rarefied ($\rho < 0.01\,\mathrm{kg\,m^{-3}}$), it is actually possible to correlate linearly the $PDIV$ measured under standard environmental conditions ($1\,\mathrm{bar}$ and $20\,^{\circ}\mathrm{C}$) with the one that would have at nominal service conditions, calculating the relative air density value.

On the modelling side, it is possible to add an additional final remark. Looking at the graph in Fig. 2.29, which shows the $PDIV$ trend as a function of the conductor diameter of the wires defined by the IEC 60317-0-1 standard [24] (whose enamel thickness changes at the same time as the conductor diameter) for different pressure values, it can be seen that the effectiveness of the increase in insulation with the diameter loses its effectiveness, falling with the pressure. In other words, assuming a grade 2
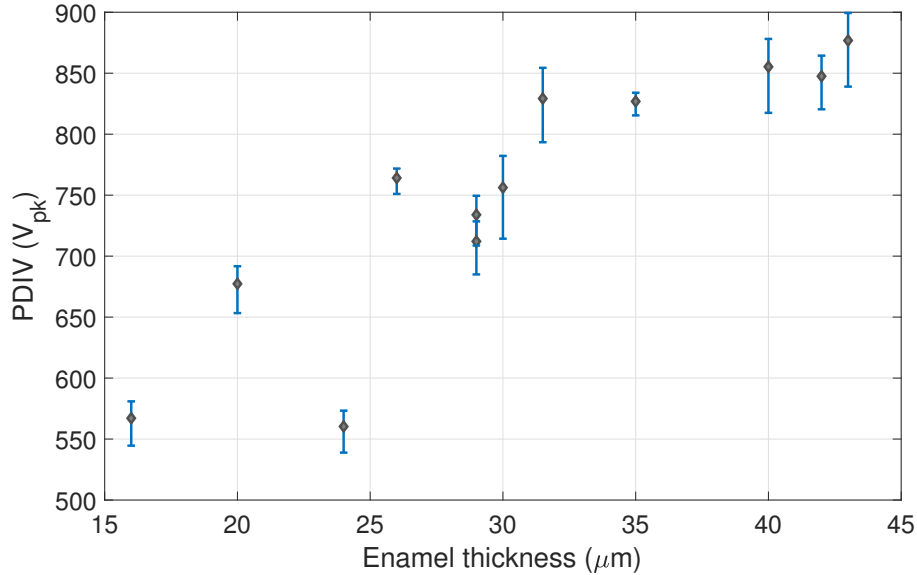
Figure 2.30: Result of the PD tests carried out for different grade 2 wires highlighting the impact of the insulation thickness (each point represents the 10th percentile of the $PDIV$ distribution measured on 10 samples).

insulation is chosen, moving from a wire with a diameter of $0.4\,\mathrm{mm}$ to a wire with a diameter of $5\,\mathrm{mm}$, the $PDIV$ increases by 70 % at ambient pressure, while it increases by only 10 % at a pressure of $100\,\mathrm{mbar}$.

2.3.2   The effect of wire geometry

Of all the parameters that can be influenced, the thickness of the insulation is certainly the most important. Fig. 2.30 shows the result of laboratory experiments on twisted pairs, with the uncertainty highlighted. As can be seen, taking into account that each wire has a diameter and a enamel relative permittivity a little different from those of the others, one is led to think that the $PDIV$ increases with the insulation thickness.

A theoretical analysis of the impact of this parameter on the $PDIV$ revealed that this suspicion is well-founded. As can be seen in Fig. 2.31, there is a correlation between the insulation thickness and the $PDIV$, and it is all the more pronounced the higher the conductor diameter. In fact, in Fig. 2.30 the experimental point that results to deviate more from the general trend, corresponds to the wire with the smallest diameter.

Although this analysis leads to a conclusion, all in all, quite easy to understand, it should be noted that the insulation thickness may decrease
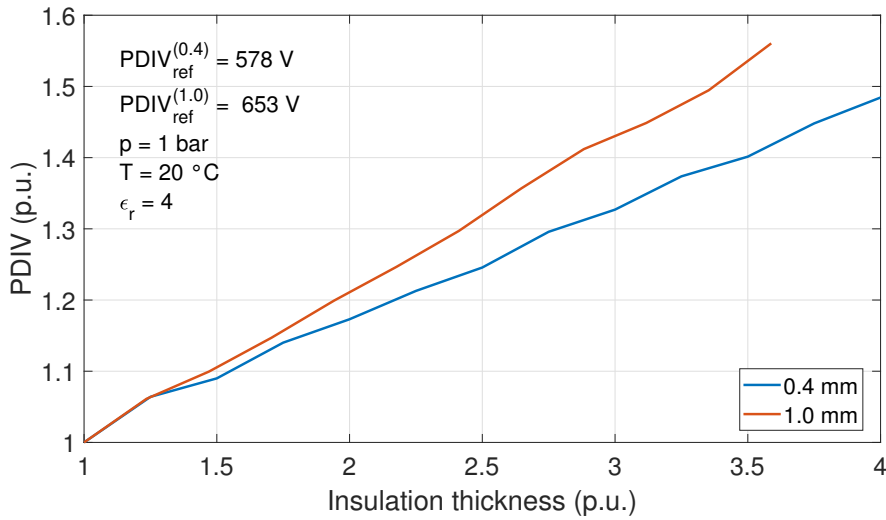
Figure 2.31: Estimated $PDIV$ trend by model depending on the insulation thickness for two wires with different conductor diameter. The simulations were carried out considering a range of values between 15 and $60\,\mu\mathrm{m}$ for the enamel's thickness.
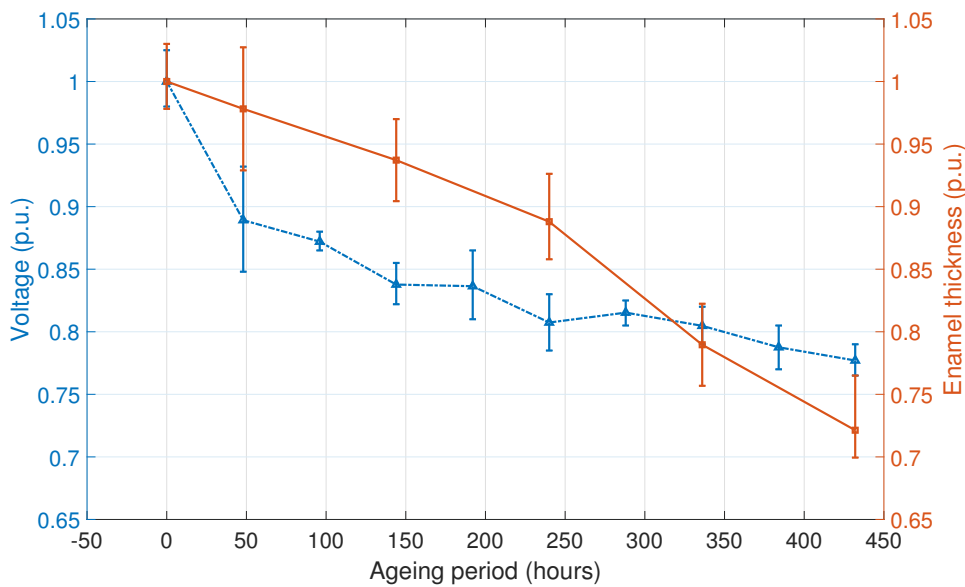
Figure 2.32: $PDIV$ and enamel thickness of twisted pairs during ageing. The plot shows average values along with 95 % confidence intervals. Reference levels: $PDIV(0\,\mathrm{hours}) = 758\ \mathrm{V_{pk}}$ and $t(0\,\mathrm{hours}) = 36.6\ \mu\mathrm{m}$.
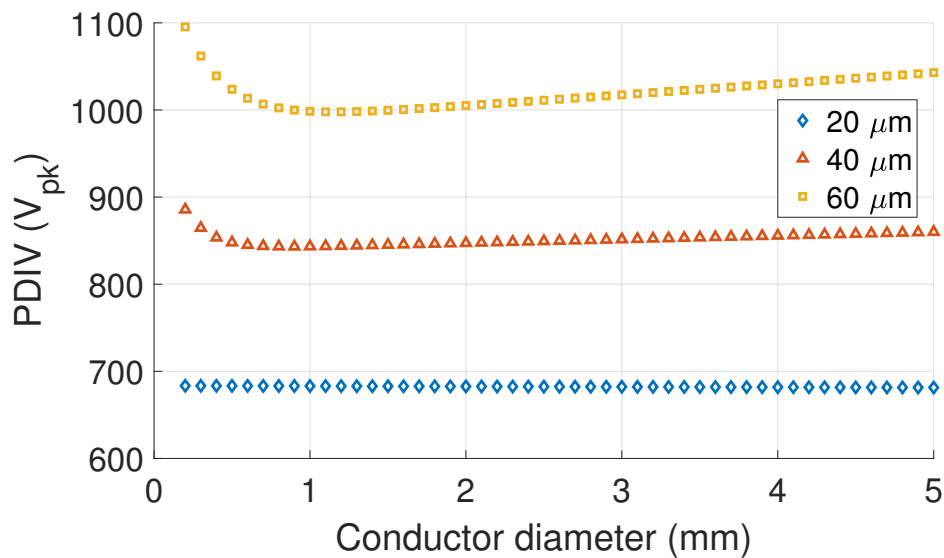
Figure 2.33: Estimated $PDIV$ trend by model depending on the conductor diameters for three different enamel thickness.

over time as a result of thermal ageing. At this point, it is important to be able to estimate, with a certain degree of precision, the decrease in $PDIV$ as a function of this parameter. Experiments conducted in the laboratory, in which the temporal evolution of the magnet wire enamel state, subjected to accelerated thermal ageing, was monitored, showed how out-gassing phenomena can take place on the surface of the insulating material, drastically reducing its size and decreasing $PDIV$ (see Fig. 2.32).

The conductor diameter, on the other hand, has very little impact on the $PDIV$, if taken individually, as can be seen from the graph in Fig. 2.33, which shows the $PDIV$ behaviour as a function of the latter parameter for three different insulation thicknesses.

2.3.3   The effect of the enamel's electrical properties

Beyond the insulating enamel conductivity, which will be discussed below, in the section on the impact of moisture, there is another important electrical parameter that can significantly influence the $PDIV$ of a twisted pair, namely the enamel's relative permittivity. Consider the separation interface between the insulating material covering the wire and the air
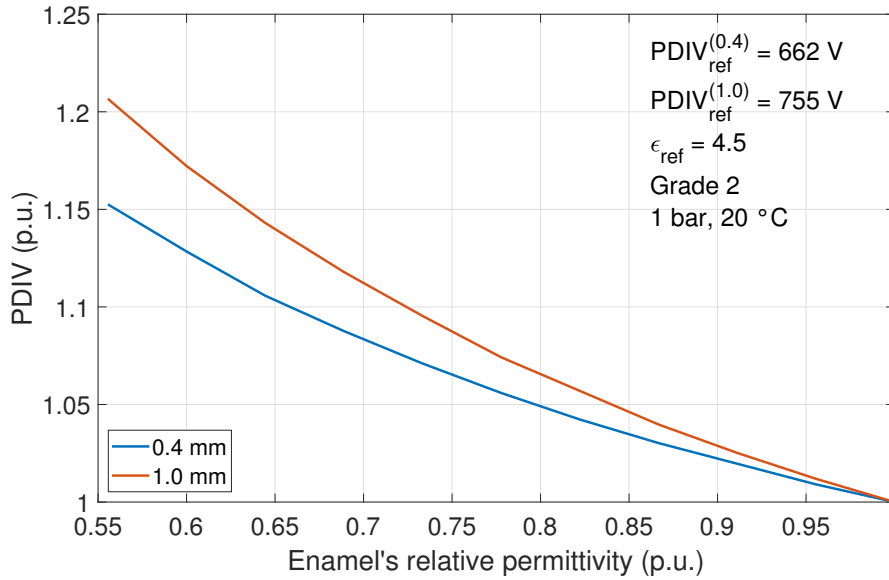
Figure 2.34: Estimated $PDIV$ trend by model depending on the relative permittivity for two different grade 2 wires. The simulations were carried out considering a range of values between 2.5 and 4.5 for the relative permittivity of the insulation.

surrounding it. At this point, the energy and charge balance must be valid:

$$\begin{cases} \hat{n} \times (\vec{E}_{insul} - \vec{E}_{air}) = 0 \\ (\vec{D}_{insul} - \vec{D}_{air}) \cdot \hat{n} = \sigma_{surf} \end{cases} \tag{2.18}$$

where $\times$ is the vector product operator, $\cdot$ is the scalar product operator, $\hat{n}$ is the normal unit vector to the interface surface, $\vec{E}$ is the electric field vector, $\vec{D}$ is the electric displacement field vector and σ_{surf} is the surface conductivity. Assuming that the surface conductivity is zero, being an insulating material, and remembering that in general $\vec{D} = \varepsilon \vec{E}$, then one obtains:

$$E_{air} = E_{insul} \frac{\varepsilon_{insul}}{\varepsilon_{air}} \approx E_{insul} \cdot \varepsilon_{insul} \tag{2.19}$$

From this last equation, it follows that as the relative permittivity of the enamel increases, so does the intensity of the electric field in air, with the same applied voltage. Consequently, the $PDIV$ will necessarily have to increase as the relative permittivity decreases.

Fig. 2.34 is an illustration of the expected trend using the $PDIV$ model as a function of the enamel's relative permittivity for two wires of different diameters. For example, a 20 % reduction in relative permittivity (i.e. from 4.5 to 3.6) for a grade 2/1 mm wire increases the inception voltage by 5 %.

2.3.4 The effect of moisture

The impact of moisture on the phenomenon of partial discharge is the most complex to study and model, especially when combined with temperature variations, because of the amount of hidden parameters that are indirectly changed when acting on the moisture concentration in the air. The main problem lies in the fact that the presence of humidity alters the chemical kinetics of the air, modifying the interactions between the latter and the applied electric field. Moreover, high humidity concentrations can drastically modify the distribution of the electric field in the air, especially if there are solid-gas interfaces. To date, the mechanisms by which the concentration of water vapour in the air influences the partial discharge inception are still not entirely clear, especially when the combined effect of temperature is taken into account.

The first experiment is conducted in the climatic chamber. The aim was to measure the $PDIV$ of twisted pairs under $50\,\mathrm{Hz}$ AC voltage at different relative humidity values in standard ambient conditions ($1\,\mathrm{bar}$ and $20\,°\mathrm{C}$). The results are showed in Fig. 2.35. The reference values vary from wire to wire and are the $PDIV$s measured at the lowest relative humidity level. It can be observed that in general $PDIV$, at room temperature, tends to decrease with increasing relative humidity.

However, the extent of the variation varies greatly from wire to wire. As a rule, the surface of all wires is pre-treated with a solvent at the time of manufacture, after which the fresh twisted pairs (yet to be tested) are stored in a container with no more than 30 % relative humidity inside (thanks to the presence of silica grains that absorb excess moisture). Consequently, effects due to external contamination are excluded. The only possible explanation is that the different composition of the enamels interacts differently with the humidity and therefore gives rise to slightly different mechanisms for triggering the discharges. On the other hand, this effect has also been observed by several other authors [57, 67, 36].

As soon as the impact of humidity at standard ambient temperature was confirmed, new measurements were made on the basis of relative humidity at progressively increasing temperature values, repeating the same experimental procedure. It should be noted, however, that these tests were conducted on a single type of twisted pair, the one made with grade 2 wire and a conductor diameter of $0.56\,\mathrm{mm}$. The result of the measures, shown in Fig. 2.36, shows a much more complex scenario than was initially assumed. In particular, the $PDIV$ at 90 °C tends to increase, instead of decrease, with the relative humidity rise. As shown by the figure itself, even the use of absolute humidity, as suggested by Fenger
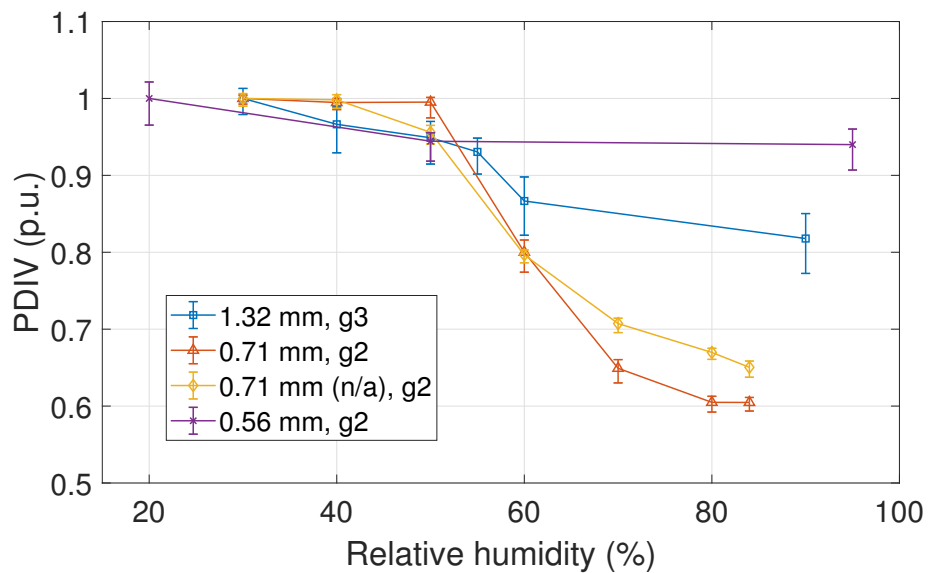
Figure 2.35: Result of the PD tests carried out at $20\,°\mathrm{C}$ on three different types of twisted pair, highlighting the impact of the relative humidity (each point represents the 10th percentile of the $PDIV$ distribution measured on 10 samples). The term 'n/a' indicates a twisted pair made from a wire whose enamel has been nano addittivated.
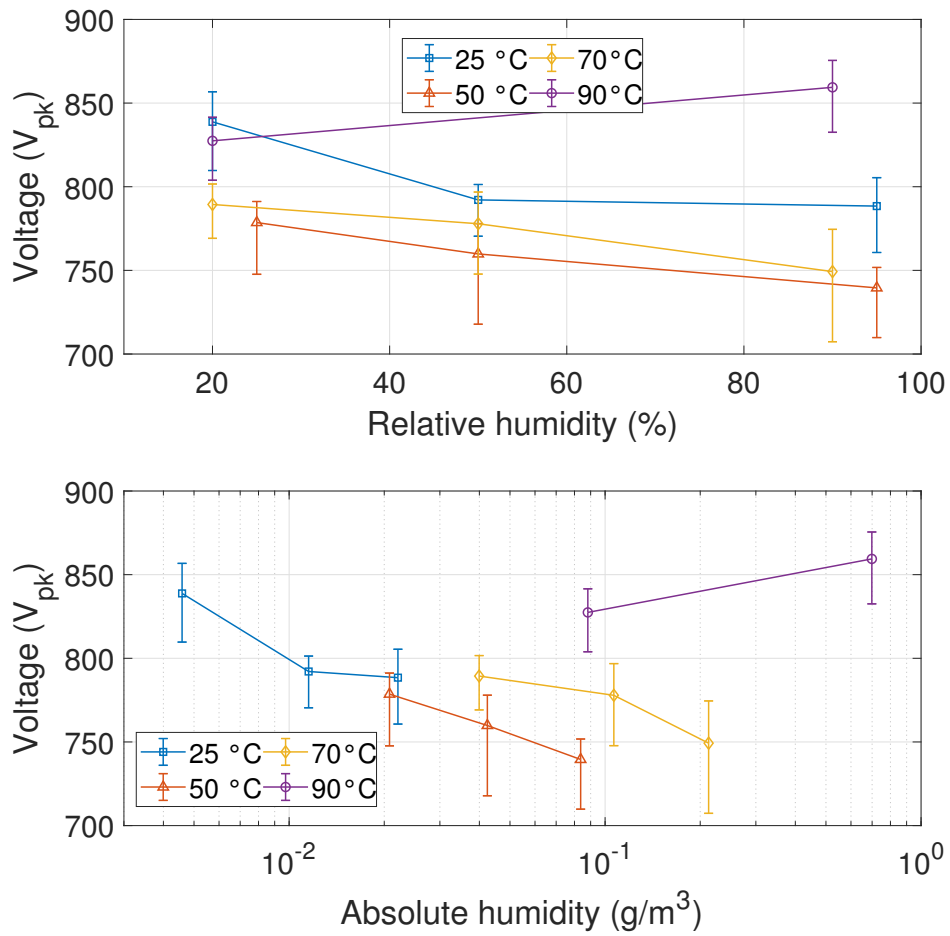
Figure 2.36: Result of the PD tests carried out on twisted pairs, made of a grade $2/0.56\,\mathrm{mm}$ wire, highlighting the impact of the air's water content (each point represents the 10th percentile of the $PDIV$ distribution measured on 10 samples) at different temperatures.
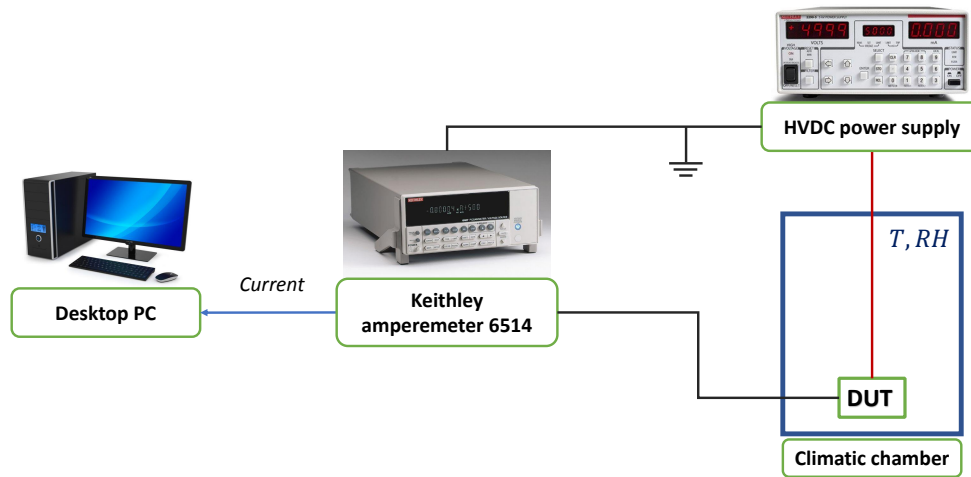
Figure 2.37: Scheme of the surface conductivity test.

and Stone [36], in place of the relative humidity, does not improve the understanding of the phenomenon, which at first glance seems strongly non-linear. However, it should be noted that the same result was obtained by Kikuchi and colleagues [57].

In an effort to improve the understanding of the data obtained, a conductivity test has been executed on a $5\,\mathrm{cm}$ long straight piece of wire, applying a DC voltage of $500\,\mathrm{V}$. The specimen was placed inside the climatic chamber and connected in series, by means of two clamps in direct contact with the wire enamel, to a Keithley 6514 ammeter, so as to measure the small surface conduction currents induced by a Keithley 2290 HVDC power supply. A circuit diagram is shown in Fig. 2.37. The aim was to find out if there was a strong interaction between water vapour and the interface of the enamelled wires.

The results of the tests are depicted in Fig. 2.38, and makes clear that the surface conductivity increases with increasing temperature (which increases the kinetics of the molecules, including any ions in the vicinity of the insulating surface) and relative humidity (which increases the availability of water molecules). This could justify the increase in PDIV, when there is a high concentration of water vapour, caused by a strong attenuation of the electric field near the contact points of the two wires.

Another effect that can induce to vary the $PDIV$, identified by Kaufhold and colleagues [55], is the increase in the enamel permittivity as a result of
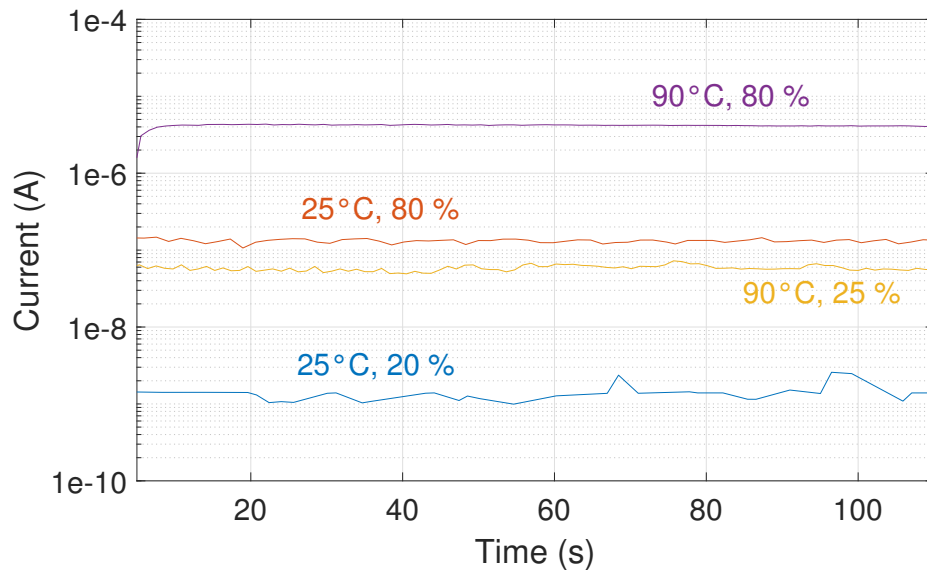
Figure 2.38: Surface conductivity tests on $5\,\mathrm{cm}$ long wire specimens applying a DC voltage of $500\,\mathrm{V}$ with different temperature and humidity conditions.

Table 2.11: Dielectric constant and loss tangent at $1\,\mathrm{MHz}$ as a function of temperature for water. Adapted from [103].

Temperature °C	Dielectric constant	Loss tangent
1.5	87	0.0190
5	85.5	0.0220
15	81.7	0.0310
25	78.2	0.0400
35	74.8	0.0485
45	71.5	0.0590
55	68.2	0.0720
65	64.8	0.0865
75	61.5	0.1030
85	58	0.1240
95	55	0.1430
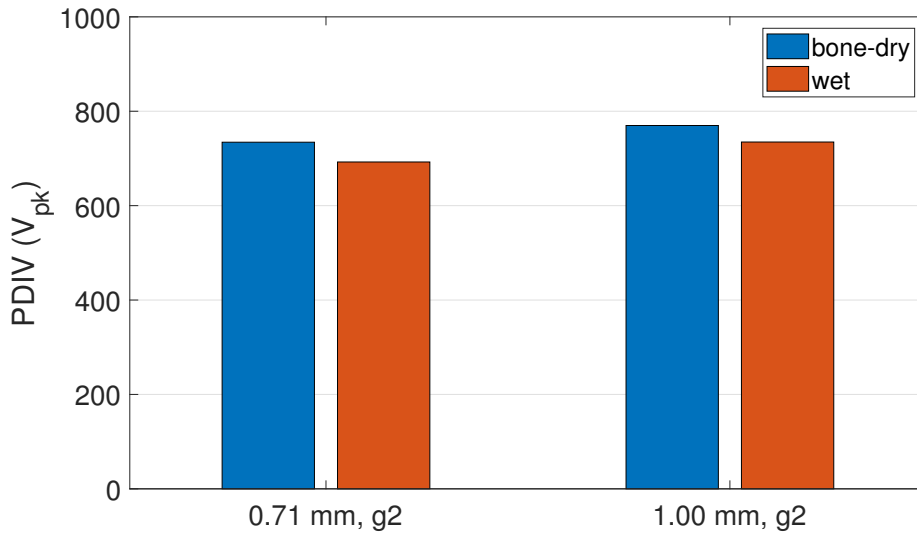
Figure 2.39: Effect of water absorption of coating on $PDIV$ values (each point represents the 10th percentile of the $PDIV$ distribution measured on 10 samples) for two different wires.

the diffusion of water molecules within the insulating material surface. In this regard, by virtue of Eq. 2.19, as the relative permittivity of the enamel increases the applied electric field necessarily increases. In particular, the resulting relative permittivity of the enamel ε_{insul} can be estimated by means of Lichtenecker's formula [92]:

$$\log[\varepsilon_{insul}(T)] = w \cdot \log[\varepsilon_{H_{20}}(T)] + (1 - w) \log[\varepsilon_{insul}^{(0)}] \qquad (2.20)$$

where w is the mass fraction of water absorbed and $\varepsilon_{insul}^{(0)}$ is the insulation permittivity when $w = 0$. However, observing the values reported in Table 2.11, it should also be noted that the relative permittivity of water decreases with temperature, so that the impact of this mechanism is less pronounced at high temperature.

To examine the correlation between water absorption and the magnet wire's operating electrical performance, PD tests were performed on pretreated twisted pairs at two different humidity levels for a certain period of time. The term 'bone-dry' refers to the state after exposure to $120\,°C$ for one hour in the oven, while 'wet' to the state of immersion in water for 48 hours (corresponding to 4 % water absorption by mass from datasheet). Fig. 2.39 shows the effects of the water absorption of the coating on $PDIV$s. The experimental and analysis values revealed that the $PDIV$ slightly decreases with higher absorption of the coating.

As suggested by Kikuchi and colleagues, a further explanation for increasing the $PDIV$ as relative humidity increases at high temperatures may be the fact that the attachment coefficient η increases considerably near the enamel surface (where condensation is more likely, among other things). This would reduce the electronic population able to trigger discharges where the electric field is most intense and, as a result, would increase the $PDIV$. From a modelling point of view, a similar effect has been predicted, but the activation temperature is higher: looking at the graph in figure 2.14, it can be seen that at $140\,°\mathrm{C}$ the ionization curves begin to show signs of instability with a relative humidity greater than 50 %, until they tend to almost zero when they are at 90 %. The difference between experimental measurements and modelling estimates could therefore be due to the practical difficulty of implementing the possible effects of water condensation on the surface of the insulator when the temperature is below $100\,°\mathrm{C}$.

2.3.5   The effect of the drive switching frequency

Another debated extensively in literature question is the impact of frequency on the phenomena of discharge inception. In the literature, there are several authors who have highlighted, in general, a variation of the $PDIV$ as a function of frequency [81], although at a theoretical level this result is unexpected. Similarly, there are other authors who report the opposite [67, 35], i.e. that the $PDIV$ does not change as a function of frequency.

To clarify the issue, PD tests were performed to evaluate the influence of frequency on the discharge mechanisms. Both a high frequency sinusoidal generator and a square wave generator were used, and the frequency was increased up to $100\,\mathrm{kHz}$. The choice to use two different types of generators is due to the fact that, in this way, it is possible to identify, if any, a possible impact of the different harmonic content of the voltage waves on the PD inception phenomenon.

The results are shown in Fig. 2.40. It can be observed that there is no appreciable change in the $PDIV$ as a function of frequency in any case. This leads to the conclusion that the frequency has no direct influence on the partial discharge inception mechanisms.
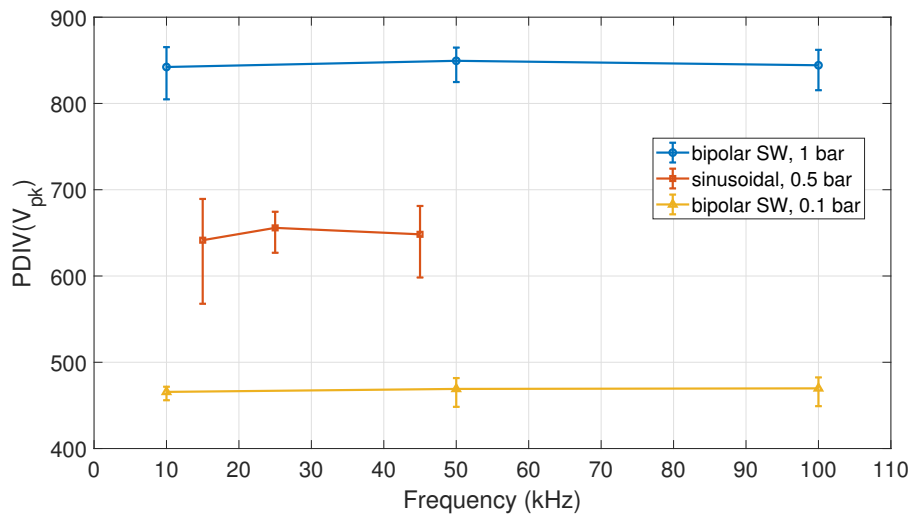
Figure 2.40: Result of the PD tests carried out on twisted pairs, made of a grade 2/0.56 mm wire, highlighting the impact of the frequency (each point represents the 10th percentile of the $PDIV$ distribution measured on 10 samples).

2.3.6   The effect of the voltage polarity

Several authors have found that PD tests performed with a unipolar voltage generator (or, better, characterized by a DC component) are influenced by the accumulation of charge in the bulk of the insulation [55, 35]. This is due to the fact that, in general, the charge accumulated near the interface tends to reduce the electric field in correspondence of the air between the two wires, thus increasing the $PDIV$.

Based on this premise, PD tests were carried out on a single type of twisted pairs using a square wave generator that can operate in both unipolar and bipolar modes. Fig. 2.41 shows the results of these experiments. As it can be seen, the peak-to-peak values are almost identical for the two modes, as also noted by various other authors [34, 54].

However, a further phenomenon of which the PD test in unipolar regime is affected is to be highlighted, compared to the bipolar case. As discussed later in Chapter 3, it was noted that in unipolar mode, very often, after a short time from the first partial discharge onset, there is a sudden extinction of the discharge activity, which may not resume, even with a further slight increase in voltage. An example of this behaviour is shown in Fig. 2.42, where it is compared with the detection carried out under the same conditions using the same generator in bipolar mode. This is always due to the accumulated charge influence on the electric field. This mechanism, although positive for
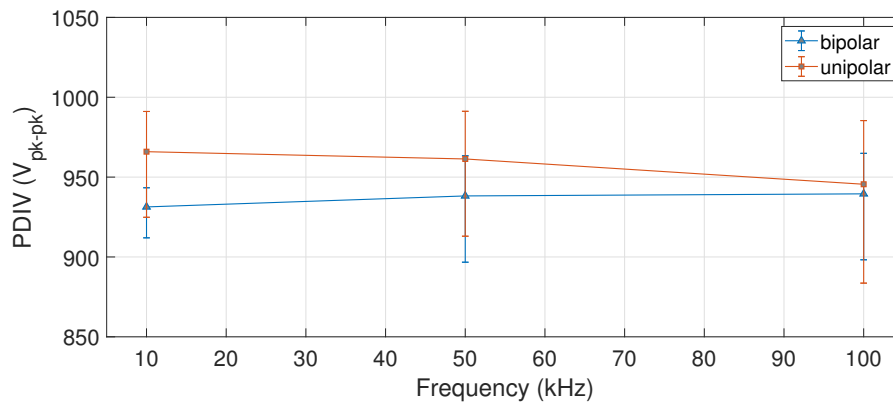
Figure 2.41: Result of the PD tests carried out on twisted pairs, made of a grade $2/0.56\,\mathrm{mm}$ wire, highlighting the impact of the polarity (each point represents the 10th percentile of the $PDIV$ distribution measured on 10 samples). The tests were caried out at $100\,\mathrm{mbar}$ due to the voltage limitations of the generator when used in unipolar mode.

insulation, makes it difficult to measure $PDIV$, especially if electromagnetic sensors are used, for which the signal-to-noise ratio is low.

2.3.7 The effect of the slew rate (rise time)

Like the frequency, the slew rate is also a parameter that is not yet known exactly what impact it has on the phenomenon of partial discharge inception. In particular, several authors detect a decrease in $PDIV$ as the rise time (which is related) increases [50, 98]. Consequently, it was considered necessary to carry out further experiments in this direction.

Fig. 2.43 shows the result of PD tests carried out on a single type of twisted pair using a voltage converter that generates square waves at very low rise time and selectable. By acting on the gate resistance of the MOSFETs in SiC it is possible to increase or reduce the switching time. The frequency used for the generator was $10\,\mathrm{kHz}$ and measurements were made at two different pressure levels (waiting for the times indicated in Table 2.10 between one test step and the next).

An unclear behaviour of the $PDIV$ as a function of the rise time can in fact be observed. There is also a certain breadth of confidence intervals to be highlighted: theoretically, within these limits, it is still possible to assume an invariance of the $PDIV$ as the rise time varies. On the other hand, this would only confirm the thesis of some authors according to which, as the rise (or fall) time decreases, the probability of having the availability

(a)

(b)
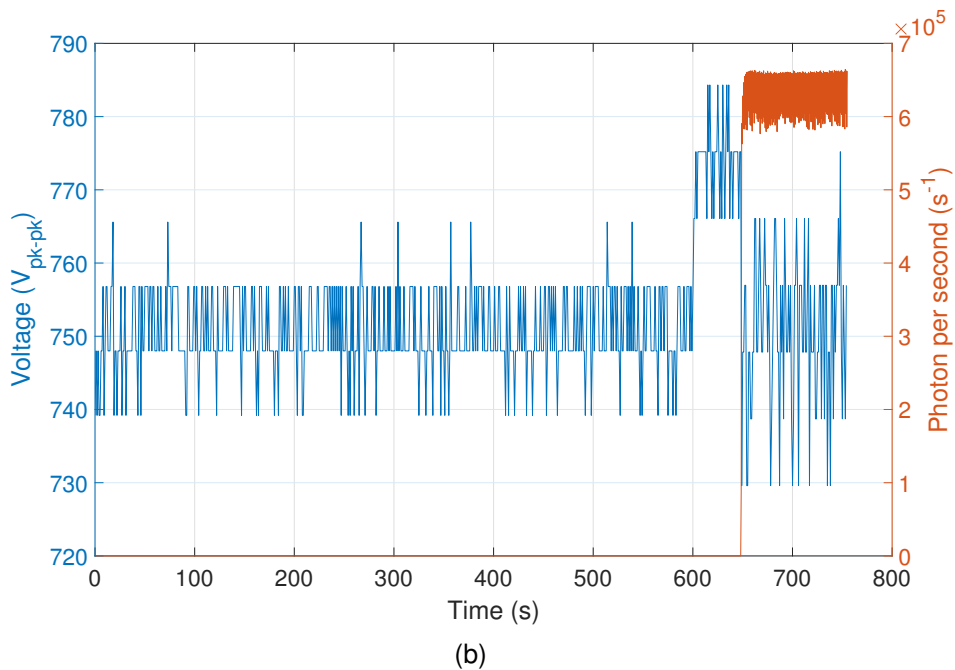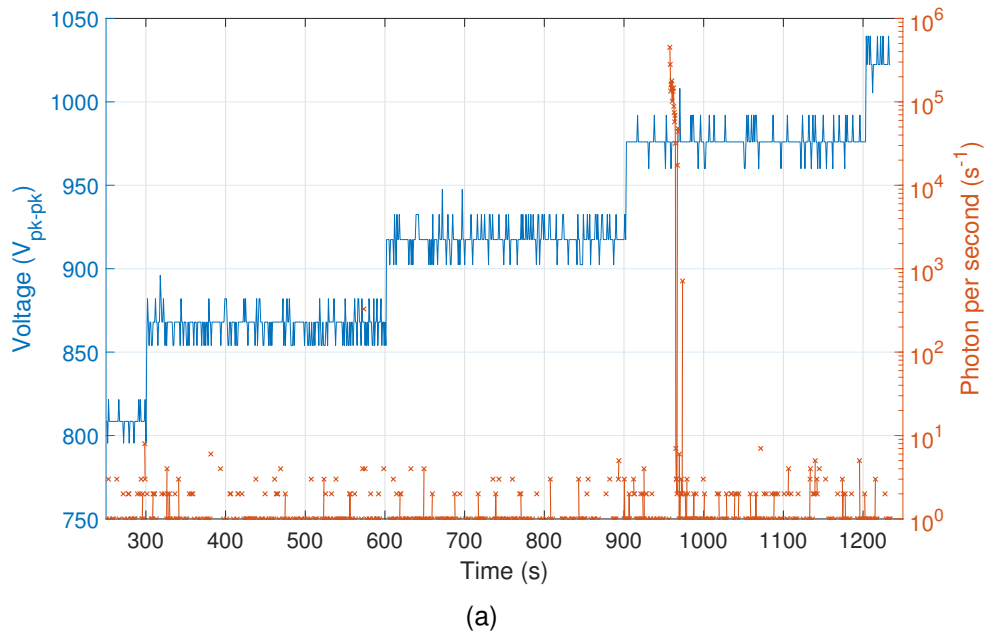
Figure 2.42: PDIV measurement performed with PMH at $10\,\mathrm{kHz}$ and $100\,\mathrm{mbar}$ using (a) unipolar square wave generator and (b) bipolar square wave generator. Blue line is the peak-to-peak value of the supplied voltage, while red line represents the photon emission rate. Note the sporadic PD activity a little before $1000\,\mathrm{s}$.
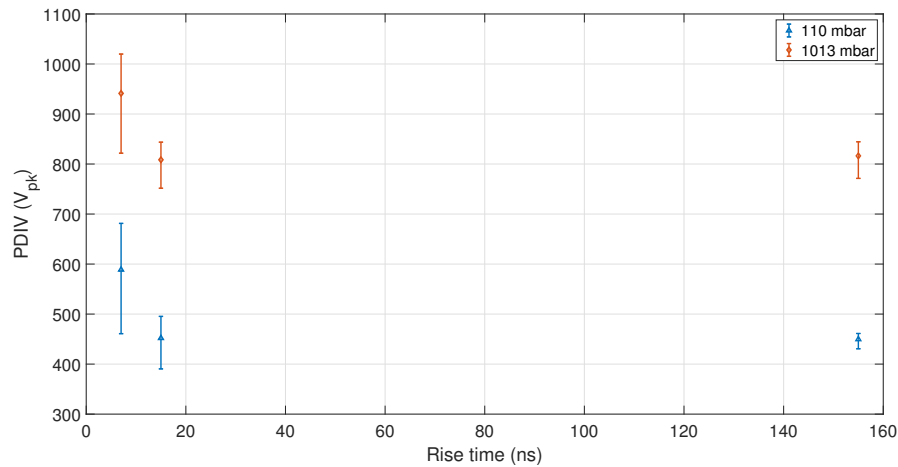
Figure 2.43: Result of the PD tests carried out on twisted pairs, made of a grade $2/0.56\,\mathrm{mm}$ wire, highlighting the impact of the rise time (each point represents the 10th percentile of the $PDIV$ distribution measured on 10 samples). It was used a square-wave generator with a switching frequency of $10\,\mathrm{kHz}$.

of an initial electron that triggers the discharge near the area of the most intense field decreases. This would necessarily lead to an increase in the dispersion of data as the rise time decreases.

2.3.8 The effect of the impregnation quality

The impregnation process is a fundamental aspect to guarantee the insulation of the electric motor. Without it, it will not be possible to adopt the nominal voltages desired for the world of transport. However, as is well known, the application of impregnation alone is not enough, but it must also be ensured that the microcavities created inside have a characteristic size below a certain threshold. In other words, it must be ensured that the final impregnation porosity is below a certain value.

Through the numerical model it has been asked which is the cavity equivalent diameter value above which the impregnation is useless. In other words, the threshold has been determined below which the average characteristic size of air intrusions must certainly be, otherwise it makes the presence of the impregnating agent ineffective.

Fig. 2.44 shows a graph in which, for all three degrees of insulation, it shows the critical discharge line length at the discharge inception voltage as a function of the standardised wire that is considered. In other words, this is the length below which one must certainly stay, because if the design
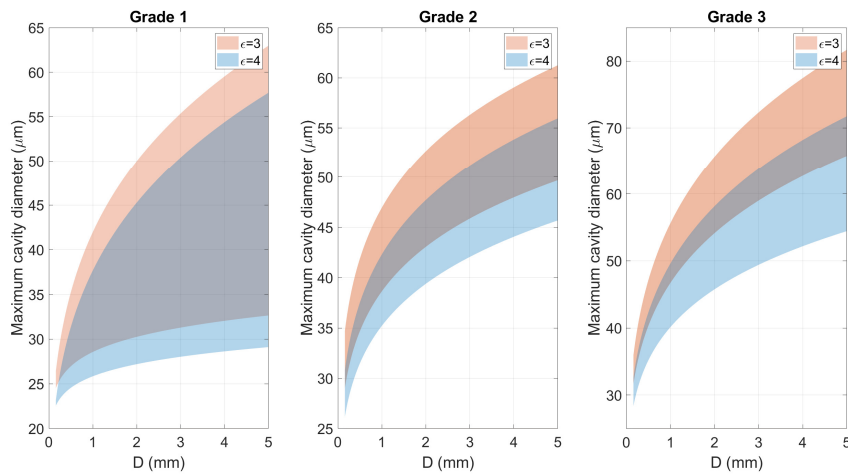
Figure 2.44: Length of the discharge lines when the voltage is equal to the $PDIV$ for the wires defined by the IEC 60317-13 standard (identifiable by the conductor diameter shown on the x-axis), considering a temperature of $200\,°C$ and an ambient pressure of $1\,\mathrm{bar}$.

voltage were to be exceeded, even by a small amount, a discharge would be triggered, regardless of whether or not impregnation was present.

2.4 The PDIV **probabilistic model**

What has been seen so far always refers to a deterministic approach. This presupposes that when the appropriate conditions are met, a partial discharge is actually triggered. However, this assumption is not always fully respected.

Think, for example, of the case at high altitude: the environmental pressure is very low, consequently the air is rather rarefied. This means that the production of electrons due to background decay or natural ionization of the air due to cosmic radiation is low and, therefore, one has to wait long enough for an available electron to trigger the electronic avalanche. This increases the phenomenon variability, so much so that in laboratory measurements it is necessary to increase the permanence time at each voltage step as a function of the depression level. However, in the situation of the real motor, it is not certain that a partial discharge will actually occur, even if the theoretical conditions would be respected, all the more so if the times in which the voltage is high are very short (as in the case of the voltage spikes applied to the turn-to-turn insulation when a converter is

applied).

Another obvious example is when feeding a phase through a very low rise-time converter. If there is a large cavity near the windings (maybe because of a poor impregnation) and the peak voltage is sufficiently high to theoretically incept a partial discharge in the turn-to-turn isolation, it is not certain that it does, because the overshoot time is so short that it is unlikely that an initial electron will be available.

These cases could therefore give the design engineer more room to manoeuvre in dimensioning the electrical machine insulation for the transport sector. However, this requires a probabilistic approach to $PDIV$ estimation, combining the probability associated with the initial electron availability with the electrical inception conditions.

The following discussion starts with Gallimberti's pioneering work on discharge theory [40] in the 1970s, which was then independently refined by Niemeyer [77], and Okubo and colleagues [50]. Starting from a probabilistic approach involving the application of Schumann's criterion, the goal is to take into account the temporal evolution of the voltage applied to the insulating system so as to be able to estimate the actual impact of partial discharges on the latter.

2.4.1 The volume-time theory

The volume-time theory provides a model for estimating the probability density of generating the initial electron, which is essential for triggering the electronic avalanche that causes the partial discharge. First of all, therefore, one must clarify the mechanisms that determine the generation of an electron in air. These can be divided into two classes: volume processes and surface processes.

The volume generation involves two possible phenomena:

- electronic detachment from negative ions caused by high electric fields;

- ionisation of the air caused by ambient ultraviolet radiation or high energy photons emitted by background radioactive decay.

In any case, the number of initial electrons emitted in the potential discharge zone, i.e. where condition $\alpha > \eta$ is met, is:

$$\dot{N}_e^{(vol)} = \eta_i(\text{gas}, E, ...) \cdot p \cdot V_{eff} \cdot \left(1 - \frac{\eta}{\alpha}\right) \tag{2.21}$$

where the function η_i indicates the particular ionization process and generally depends on the kind of gas, the electric field E, the relative humidity, and further parameters. The other quantities are the pressure p, the effective gas volume V_{eff} in which the discharge can occur and $(1 - \eta/\alpha)$ is the so-called Legler function which gives the probability that a single electron develops into an avalanche.

In the case of radiative ionization it was shown by Niemeyer that η_i can be written as:

$$\eta_i^{(rad)} = C_{rad}\Phi_{rad}\left(\frac{\rho}{p}\right)_0 \tag{2.22}$$

where C_{rad} features the interaction between radiation and gas, Φ_{rad} is the quantum radiation flux density and $(\rho/p)_0$ is the ratio between gas density and pressure. Note that the radiative contribution plays a greater role, in particular, in the cavities enclosed in the insulating materials.

In the case of electronic detachment, η_i is proportional to the negative ions concentration and is highly dependent on the electric field. However, this contribution is negligible until geometries with at least one bare electrode are taken into account.

The initial electron surface generation includes electronic detrapping from insulation surface, electron release by ion impact and by the surface photo effect. Niemeyer states that this type of emission in general obeys approximately Richardson-Schottky's law:

$$\dot{N}_e^{(sur)} = \frac{A}{e}S\exp\left[\frac{\Phi - \sqrt{eE/(4\pi\varepsilon_0)}}{k_BT}\right]\left(1 - \frac{\eta}{\alpha}\right) \tag{2.23}$$

where A is the emitted surface, e is the electronic charge, Φ is an effective work function, E is the electric field in surface correspondence, k_B is the Boltzmann constant and T is the absolute temperature. The Schottky term, $\sqrt{eE/(4\pi\varepsilon_0)}$, takes into account the effect of the electric field on the electronic extraction work, while the function S characterizes the nature of the emitting surface material.

Leaving aside the influence of a possible conductive surface (case of bare electrodes), of greater interest for this treatment is to explore the impact that an insulating surface can have in the initial electron generation. It is known in the literature the presence of electronic traps of different electronics on the surface of a generic insulating material. The fact is that it can emit charges only if discharges have occurred previously, so that some electrons or ions are trapped inside. The function S so can be expressed

by the following formula:

$$S = \nu_0 e \frac{N_{dt}}{A}$$ (2.24)

where $\nu_0 \approx 10^{13}$ to $10^{14}\,\text{s}^{-1}$ is the fundamental phonon frequency and N_{dt}/A is the surface density of detrappable charge carriers.

2.4.2 The probabilistic Schumann model

The proposed model is based on two hypotheses:

1. the conditions for the discharge inception can be determined using Schumann's criterion;

2. the time left between two consecutive $PDIV$ tests is large enough to allow the charge deposited on the insulation surface to resorb or recombine. In other words, it is assumed that a discharge event can only be incept by ionisation in air.

In virtue of the hypothesis (2), it can be assumed that the initial electron production's hazard rate is constant; therefore, the probability density function is of exponential type with parameter λ_{eff}:

$$f_e(t) = \lambda_{eff} \cdot e^{-\lambda_{eff} t}$$ (2.25)

where $\lambda_{eff} = \eta_i p \cdot V_{eff}$, being V_{eff} the volume of the region where a free electron can incept a PD, also called critical (or effective) volume.

To determine the space region (and therefore a measurement of it) in which an electron can initiate the electronic avalanche that will generate the discharge, on the basis of the hypothesis (1), the Schumann model described in the previous sections can be used. However, in this case not only the critical discharge line, i.e. the only electric field line along which the electronic avalanche develops under $PDIV$ conditions, but also all the other discharge lines that occur when the voltage exceeds the threshold value, will be identified.

With reference to Fig. 2.45, it can be observed that as the voltage increases, and thus the distance from the threshold value increases, the effective volume increases.

Suppose an arbitrary but periodic waveform voltage is applied. Since the exponential probability distribution has no memory, it is possible to write that:

$$P(\tau > t + \Delta t | \tau > t) = P(\tau > \Delta t)$$ (2.26)
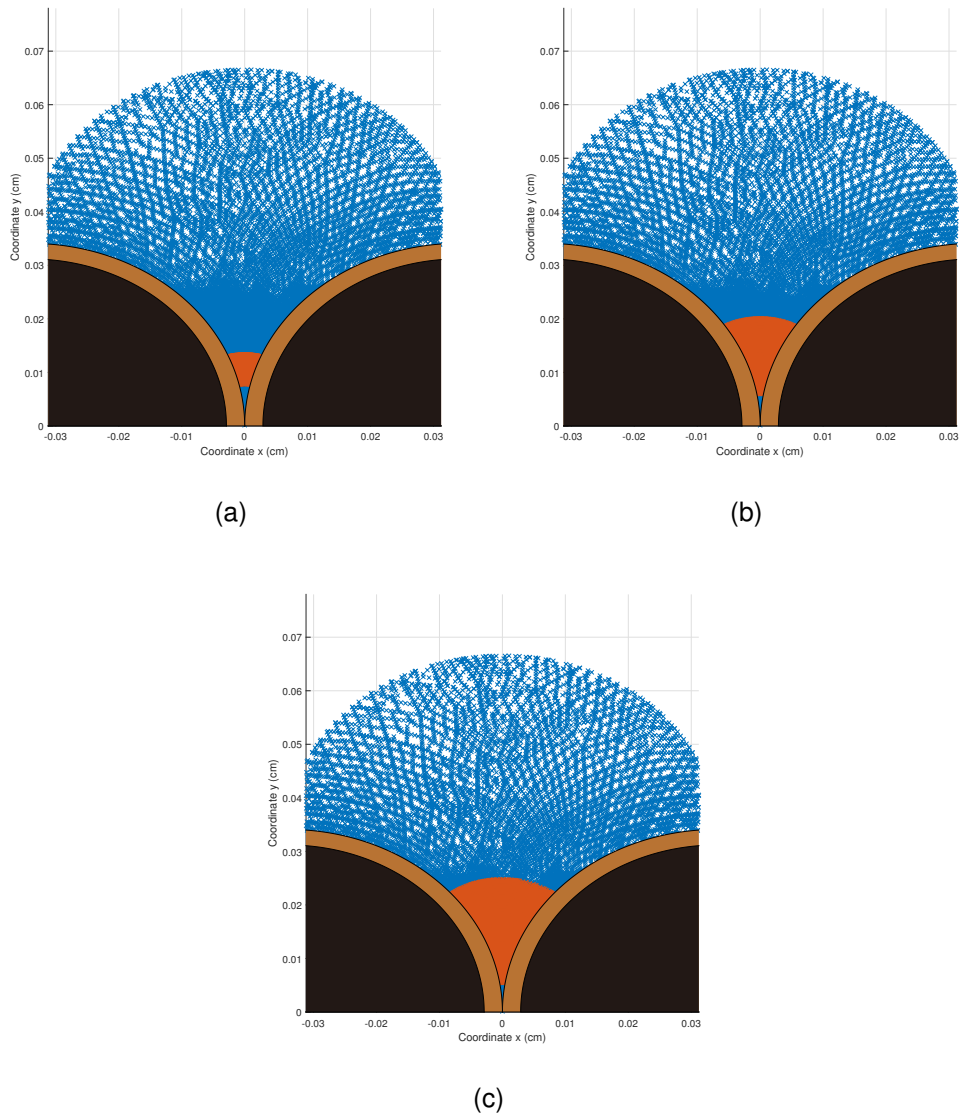
Figure 2.45: Schematic illustration of critical volume V_{eff} (red area) for (a) $750\,\mathrm{V_{pk}}$, (b) $1\,\mathrm{kV_{pk}}$ and (c) $1.25\,\mathrm{kV_{pk}}$.

so that, the probability of observing an initial electron in non-overlapping intervals of length Δt_i is equal to

$$P(n_e \geq 1) = \sum_i e^{-\eta_i p \Delta t_i} \tag{2.27}$$

At this point it is possible to determine the overall probability of obtaining a discharge event over an entire period of the applied voltage:

$$\pi = P(n_{PD} \geq 1) = \int_0^T \eta_i p V_{eff}[v(\tau)] \cdot e^{-\eta_i p V_{eff}[v(\tau)]} \, d\tau \tag{2.28}$$

where $v(\tau)$ is the instantaneous applied voltage. Note that $\eta_i p V_{eff}[v(t)] \ll 1$, therefore it is possible to introduce an approximation in Eq. 2.28 so as to obtain:

$$\pi \approx \eta_i p \int_0^T V_{eff}[v(\tau)] \, d\tau = \eta_i p T \langle V_{eff} \rangle \tag{2.29}$$

where $\langle V_{eff} \rangle$ is the expected value of the effective volume in a period. It should be noted that when the applied voltage is below the $PDIV$, the effective volume is zero:

$$V_{eff}[v(t) < PDIV] = 0 \tag{2.30}$$

It is still unclear how to calculate the probability associated with the partial discharge inception after a certain period of time when the waveform has repeated itself cyclically, possibly with a progressive increase in the supply voltage.

Consider the situation in which the operator periodically increases the voltage, adopting ideal steps so that at the i-th step there is a peak voltage equal to $v_i^{pk} = \max_t(v_i(t))$. Note that v_0^{pk} indicates the peak voltage of the first step. π_i should then be used to indicate the probability that an initial electron will be generated when applying an entire waveform characterised by a peak voltage v_i^{pk}:

$$\pi_i = \eta_i p \int_0^T V_{eff}[v_i(\tau)] \, d\tau \tag{2.31}$$

Suppose also that the operator always waits the same amount of time between one step and the next, so that during a holding period N_c waveforms, all of which are the same, follow one another.

Now it is time to distinguish between the two possible events:

$$A = \text{ PD occurs at } v_i^{pk} \tag{2.32}$$

$$B = \text{ PD does not occur at } v_j^{pk} \, \forall \, j < i \tag{2.33}$$

Defined the probability of not triggering a partial discharge, considering only the i-th voltage step, with

$$Q_i = (1 - \pi_i)^{N_c} \tag{2.34}$$

the total probability Π_i of observing a discharge, having reached the i-th step, is expressed as follows:

$$\Pi_i = Pr(A|B)Pr(B) + Pr(A|\bar{B})Pr(\bar{B}) = Pr(A|B)Pr(B) \tag{2.35}$$

where $Pr(A|\bar{B})Pr(\bar{B}) = 0$, since the test ends when the first discharge is observed.

The probability expressions appearing in Eq. 2.35 can be written as follows:

$$Pr(A|B) = 1 - (1 - \pi_i)^{N_c} \tag{2.36}$$

$$Pr(B) = \prod_{j=0}^{i-1} Q_j = \prod_{j=0}^{i-1} (1 - \pi_j)^{N_c} \tag{2.37}$$

Therefore, including Eqs. 2.36 and 2.37 in Eq. 2.35 gives the final formula for determining the PD inception probability during a complete $PDIV$ test, taking into account the entire history of the applied voltage and its waveform, whether it is a sine wave or a square wave:

$$\Pi_i = [1 - (1 - \pi_i)^{N_c}] \cdot \prod_{j=0}^{i-1} (1 - \pi_j)^{N_c} \tag{2.38}$$

It should be noted that Eq. 2.38 can take into account all the environmental variables, as does the corresponding deterministic model, since it depends, through Eq. 2.31, on the effective volume, which is calculated making use of the latter.

Several case studies will be shown in the next paragraphs. Keep in mind that these examples are intended to be exclusively qualitative, since the precise estimation of the probability density functions is only possible by knowing exactly the contact surface length, the radiation factor and the theoretical $PDIV$.

2.4.3   Application with a two-levels square waveform

Consider a square wave affected by initial overshoots. In a first analysis, to better understand the underlying phenomena, one could approximate
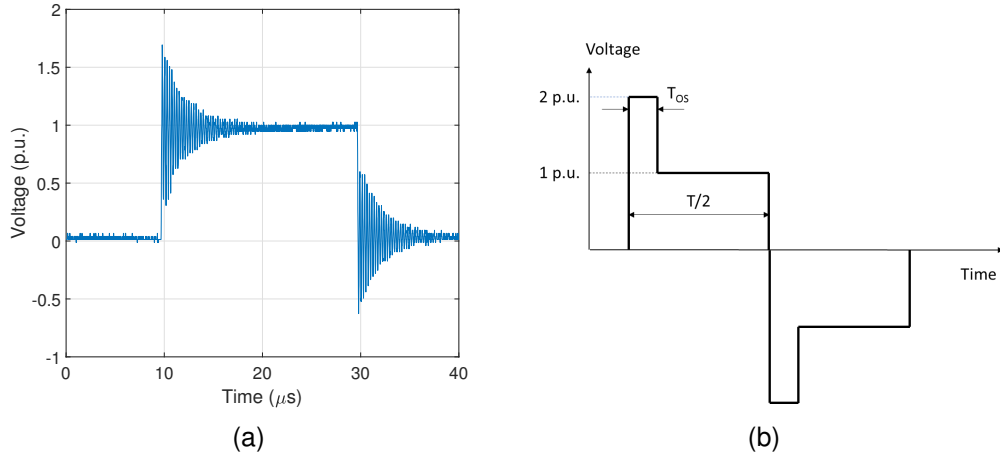
Figure 2.46: Approximation of a real voltage square waveform: from (a) the voltage waveform at $50\,\mathrm{kHz}$ generated by a SiC-based inverter to (b) the simplified voltage waveform used to highlight the dependence of $PDIV$ probability density function.

this waveform in a simpler one composed of two different square waves, one high and narrow, the other low and wide, as shown in Fig. 2.46. At the same time, again referring to Fig. 2.46, the overshoot fraction δ is introduced:

$$\delta = \frac{T_{OS}}{T} \tag{2.39}$$

where T_{OS} is the overshoot time in a semi-period and T is the main period of the square wave. In the following graphs, 'cumulative probability' means the value of Π_i at the associated voltage V_i.

The first interesting thing to observe is that the waiting time between one voltage step and the next has a huge impact on the probability distribution of triggering the first PD. Observing the results obtained with the probabilistic prediction model shown in Fig. 2.47, increasing the waiting time, the average value of the measured $PDIV$ should tend to drop, until it coincides with the deterministic theoretical inception point. At the same time, the curve tends to lengthen and tighten, in other words decreasing the variance associated with the distribution.

Another important observation is the impact of the total length of the twisted pairs tested. In fact, the modelling shows that this parameter also plays an important role in the probability distribution of triggering PDs. On the other hand, it is reasonable to think that it is easier to have the availability of the initial electron near an extended surface, rather than in a reduced one, and that consequently it is easier to incept, at the theoretical
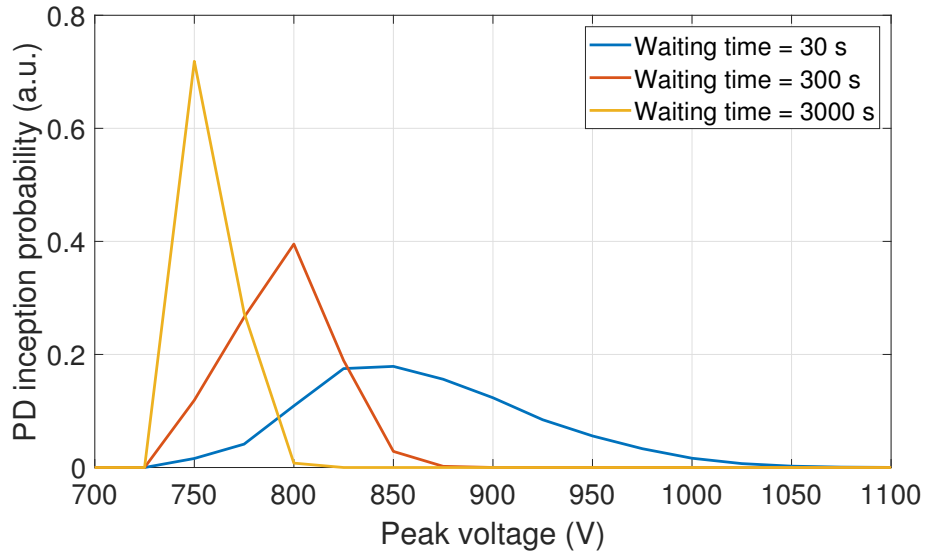
Figure 2.47: Estimated $PDIV$ probability density function using a square wave with $\delta = 0$ (ideal case), varying the waiting time between a voltage step and the next one.
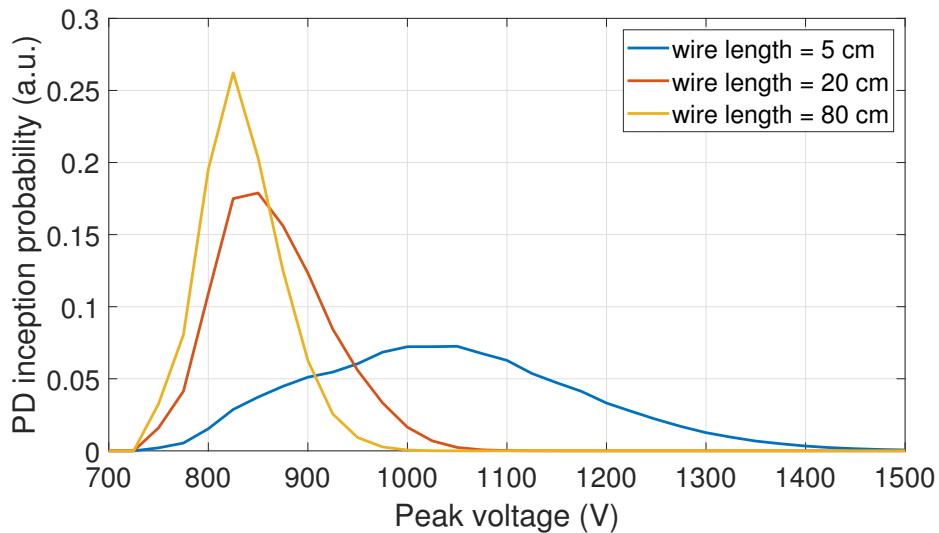
Figure 2.48: Estimated $PDIV$ probability density function using a square wave with $\delta = 0$ (ideal case), varying the wire length.
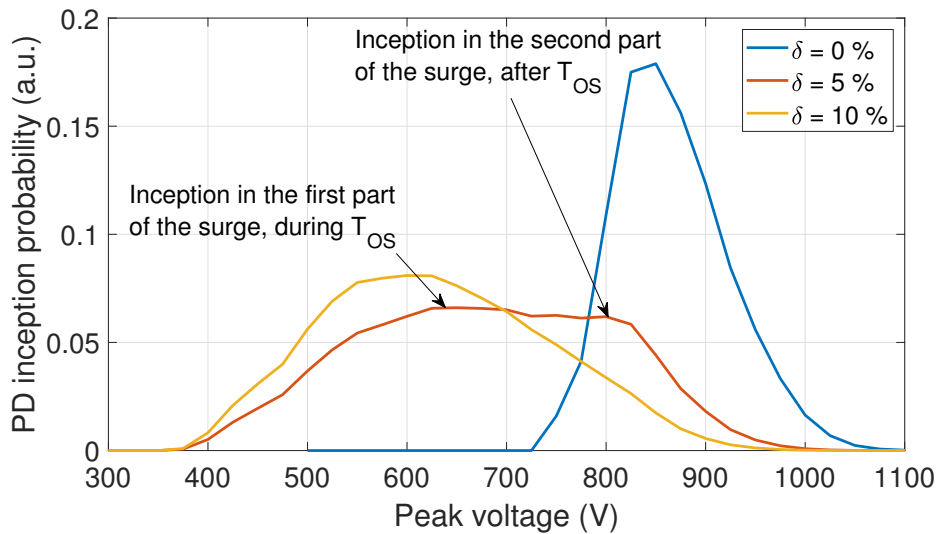
Figure 2.49: Estimated $PDIV$ probability density function using a square wave affected by ringings, varying its overshoot fraction.

minimum $PDIV$, the discharge on a long twisted pair, rather than on a short one. This mechanism is well represented in Fig. 2.48, where several simulations have been made in which the wires' length has changed from time to time.

Finally, it is also useful to study the behaviour of $PDIV$ distribution density as a function of overshoot fraction, to better understand the role that plays, during a PD test, the presence of any ringings in the waveform. As can be seen in Fig. 2.49, the longer a voltage spike's dwell time is compared to the main period, the more likely it is that the discharge will trigger at low voltage. It is also worth noting to highlight the shape of the distribution curve, which can be guessed to be substantially composed by the union of two distinct curves, thus showing a bi-modal nature. The mode corresponding to the lower $PDIV$ values is associated with the ringings of the waveform, while the mode corresponding to the highest values is related to the flat part at 1 p.u. (i.e., the DC bus voltage). As δ increases, the bimodal behaviour of the probability density function becomes less and less evident.

At the beginning, the purpose of the model was to better understand how to determine the true $PDIV$ (that is, the voltage at which, with infinitely small probability, the first discharge is triggered) of an insulating system starting from the 10th percentile of the values' distribution obtained experimentally. This is what is called in statistics a typical problem of ex-
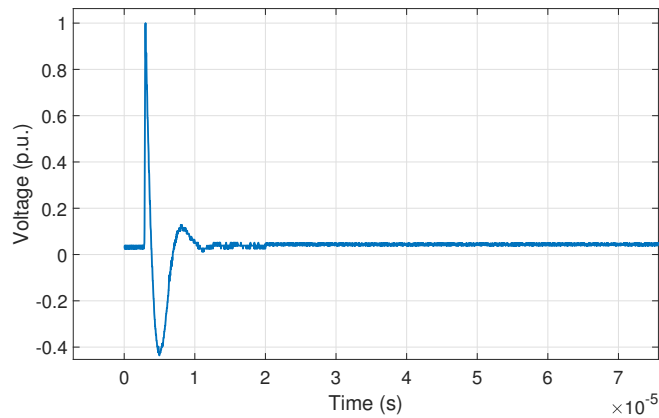
Figure 2.50: First moments of the surge wave. Pulse repetition frequency is $1\,\mathrm{Hz}$.

treme values, which has no immediate solution at all, especially because it is not possible to define an analytical function for the probability density distribution when using real waveforms.

2.4.4 Application with surge waveform

The use of the probability model for $PDIV$ estimation has also been useful to better understand the dynamics of using a surge generator for PD testing. As will be noted later in Chapter 3, measurements made using this type of generator are affected by a greater inaccuracy.

The surge waveform is shown in Fig. 2.50. Please note that these generators are usually designed to send one pulse per second and can only act on the number of pulses to be applied during the same peak voltage step. Based on this premise, Fig. 2.51 shows the result of the simulations considering to apply the above voltage wave on a $20\,\mathrm{cm}$ long twisted pair. At the same time, for the purpose of comparison, the $PDIV$ probability density distribution behaviour was simulated by applying an ideal square wave (without ringings) at the frequency of $1\,\mathrm{Hz}$ and waiting for $10\,\mathrm{s}$ between one voltage step and the next (therefore, in fact sending 10 pulses also in this case at each voltage step). As can be seen, the curve associated with the surge is characterized by a much higher variance and by an average value shifted much further ahead, demonstrating also from the theoretical point of view a certain intrinsic inaccuracy of the approach.
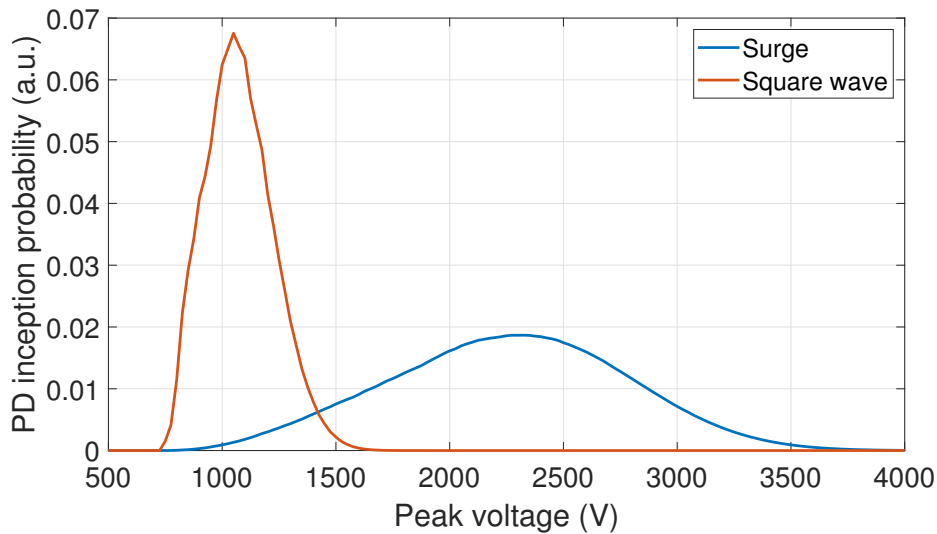
Figure 2.51: Estimated $PDIV$ probability density function using a square wave with $\delta = 0$ (ideal case) at $1\,\mathrm{Hz}$ and waiting $10\,\mathrm{s}$ between a voltage step and the next (blue line), and using a surge generator feeding 10 impulses at each voltage step (red line).

2.4.5 Application at low-pressure environments

The probabilistic model allows to quantify, in some way, the impact that the pressure has on the waiting time between one voltage step and the next during the PD tests. Here it will therefore be possible to fully justify the decision to increase this parameter as the vacuum level, at which measurements were made on twisted pairs, decreases.

In the first instance, consider the effect of a decrease in pressure on a PD test performed on a $20\,\mathrm{cm}$ long twisted pairs, using an ideal square wave generator and letting a $30\,\mathrm{s}$ interval pass between one voltage step and the next. Fig. 2.52 shows the results of the simulations with these parameters. It can be observed that as the pressure decreases, the distribution curve of the $PDIV$ tends to widen and flatten, meaning that the variance increases, and therefore that the measurement will be increasingly inaccurate. The increase in the waiting time logically counterbalances this effect, since, as observed previously in Fig. 2.47, it tends to tighten the bell of the curve, i.e. to decrease the variance of the distribution.

Fig. 2.53 shows the new $PDIV$ probability density distributions taking into account the waiting times commensurate with the value of the pressure applied (see Table 2.10). It can be seen that the values of the variance are very close to that of reference (i.e., the pressure at sea level).
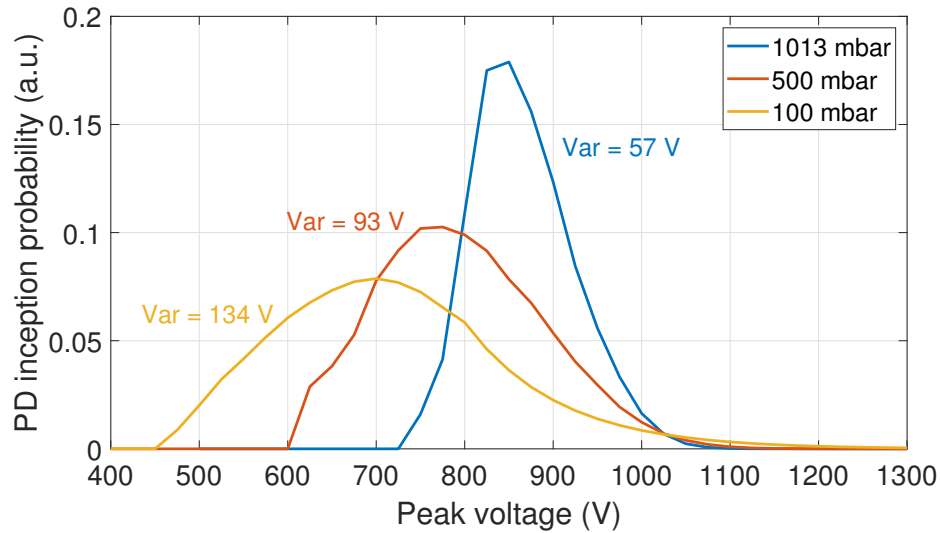
Figure 2.52: Estimated $PDIV$ probability density function using a square wave with $\delta = 0$ (ideal case), varying the pressure and waiting $30\,\mathrm{s}$ between a voltage step and the next.
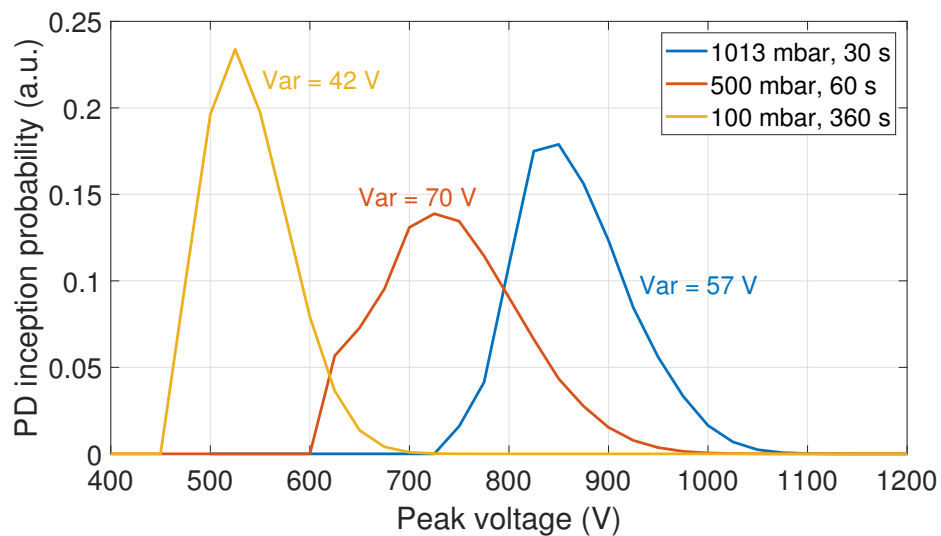
Figure 2.53: Estimated $PDIV$ probability density function using a square wave with $\delta = 0$ (ideal case), waiting the times listed in Table 2.10 between a voltage step and the next, on the basis of the pressure value.

3

Evaluating insulation systems of low-voltage electric motors and actuators

In the previous chapters we have deliberately tried to maintain a certain generality in discussing the problems affecting the insulation system of the electrical machine. This chapter deals with the testing and qualification strategies of electric motors specifically used in the aeronautical sector, which must operate under more severe conditions than other sectors and for which, therefore, additional stress factors must be taken into account.First of all, an overview of the current regulations will be given, valid for all low-voltage electrical machines. Afterwards, the reader is provided with a series of suggestions and strategies useful for carrying out type and qualification tests of electric machines called to operate at high altitude, with DC bus supply voltages higher than $500\,\mathrm{V}$ and/or driven by inverters equipped with MOSFET in Sic or GaN.

3.1 Definitions

From the point of view of electrical insulation, IEC 60034-18-41 and 60034-18-42 distinguish between two types of machines: those with an insulation that is not expected to be subject to partial discharge activity and those with an insulation is instead designed to withstand their presence. This means that, in one case, partial discharges are considered a failure phenomenon, while in the other a stress factor.

This difference is substantial to understand how to test and qualify a low

voltage electric motor. IEC 60034-18-41 states that good operation will be verified when, at maximum operating voltage, there is no partial discharge activity at any point of the machine. The qualification process will be a bit more complicated, since it will have to take into account the ageing as the hours of operation and the age increase. In this case, the norm suggests to use representative test objects of the insulating system (motorettes or twisted pairs), in order to perform on them a series of accelerated ageing tests with different stress levels. If the samples are PD-free at the end of this process, it will be possible to proceed to the realization of the actual machine.

In any case, the fundamental parameter is the Partial Discharge Inception Voltage ($PDIV$), already seen before, whose formal definition is finally given below:

> *Lowest voltage at which partial discharges are initiated in the test arrangement when the voltage applied to the test object is gradually increased from a lower value at which no such discharges are observed.*

However, there are also two other parameters often mentioned in the standard: the Partial Discharge Extinction Voltage ($PDEV$) and the Repetitive Partial Discharge Inception Voltage ($RPDIV$). The first has the following definition:

> *Voltage at which partial discharges are extinguished in the test arrangement when the voltage applied to the test object is gradually decreased from a higher value at which such discharges are observed.*

When the first discharge is triggered, a space charge is generated and it influences any subsequent events, acting directly on the electric field distribution. Consequently, the $PDIV$ rarely corresponds to the $PDEV$, and the latter is usually lower. In the event that a discharge occurs inside a machine, it must be ensured that the operating voltage remains below the $PDEV$, and not the $PDIV$, to prevent complete failure.

The $RPDIV$ is a parameter of a different nature, defined exclusively for impulse voltages and indicated in V_{pk-pk} (the others are specified in V_{rms}). Its definition is justified by the technical difficulties of detecting the $PDIV$ when the voltage is not sinusoidal, caused by electromagnetic noise induced by the voltage generator. Its formal definition is:

> *Minimum peak-to-peak impulse voltage at which more than five PD pulses occur on ten voltage impulses of the same polarity.*
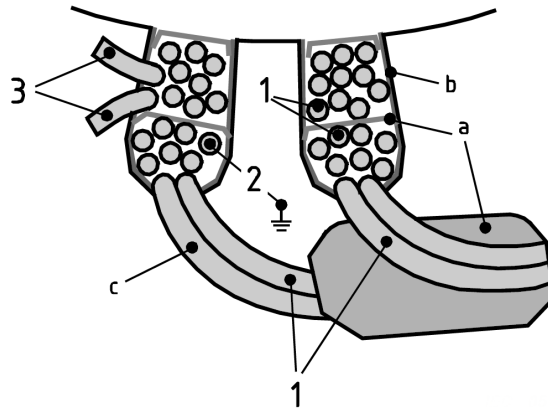
Figure 3.1: Example of electric machine insulation systems (source: [18]). 1: phase to phase, 2: phase to ground, 3: turn to turn, a: overhang insulation, b: mainwall insulation, c: turn insulation.

Hence, this replaces the $PDIV$ in case of impulsive tests.

However, it should be noted that it is always better to consider $PDIV$, rather than $RPDIV$, when the sensitivity of the measuring instruments allows it. This is because PD triggering, even if sporadic and at low intensity, must be absolutely avoided in electric motors characterized by a type-I insulation system, for the reasons already discussed in the previous chapters.

Another important parameter to mention is the thermal (or temperature) index of the insulation. It indicates the temperature at which, in stationary mode, an operation of 20000 hours is guaranteed for the insulation. More generally, the standard defines it as [22]

> *[..] the numerical value of the temperature in* $^\circ C$ *at which the time taken for deterioration of a selected property to reach an accepted end-point is that specified (usually 20 000 h).*

This parameter is essential to define the thermal class of an insulation system. The latter is a categorization that allows to define the maximum exposure times allowed at different temperature levels.

Typically a machine is required to operate even more than 20000 hours (about 2 years), therefore it is essential to choose the material in such a way that the nominal operating temperature is always a few dozen degrees lower than its thermal index. Since the service life follows an exponential law with the temperature, it is customary, for a preliminary assessment, to double the estimated service life each time the operating temperature decreases by $10\,^\circ C$ (Montsinger's rule [73, 94, 91]).
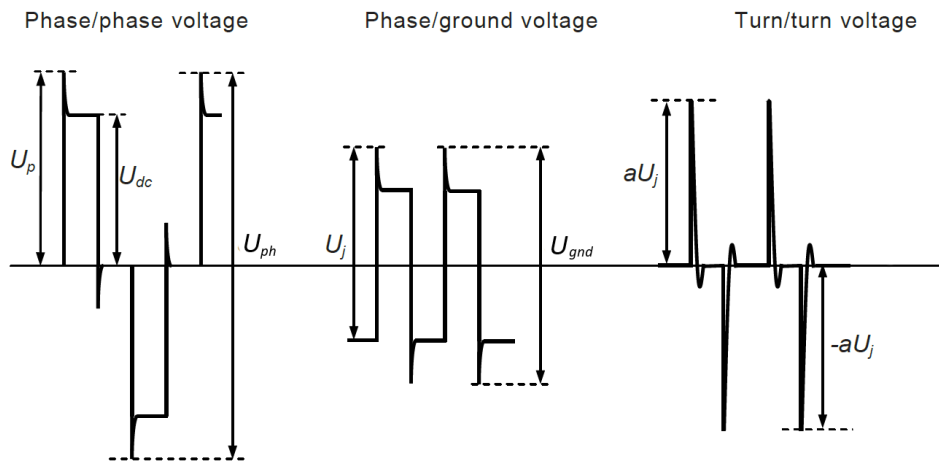
Figure 3.2: Time evolution of the voltage applied to the three electrical stator isolation systems when the machine is fed by a bipolar square wave with overshoot due to impedance mismatch (source: [18]).

Finally, for the sake of completeness, it is important to remember the insulating systems present inside a low-voltage electrical machine. They are (see Fig. 3.1):

- turn insulation;

- phase-to-phase (or phase) insulation;

- mainwall (or ground) insulation.

3.2 Type tests

To check that the insulation system works properly during routine diagnostics, or simply to check that the machine has no defects at the end of production, it is necessary to do a PD test. IEC 60034-18-41 gives some indications, depending on the specific insulating system to be tested, about the characteristics of the voltage to be applied to the machine terminals.

At the moment, the standard is lacking in the configuration to be used for the connections when it is necessary to verify the correct functioning of the turn insulation. The only directive present is the one that obviously cannot be used a sinusoidal generator if only the phase terminals are accessible.

Moreover, it is not even exactly clear in advance how the voltage is distributed along the windings, when the voltage is not sinusoidal, because

it depends on the arrangement of the wires inside the slots (impossible to know for random-wound stators), the connection characteristics between the inverter and the motor, and finally the specifications of the inverter itself. As an example, Fig. 3.2 shows the waveform of the impulse voltages applied to the three different isolation systems when a bipolar square wave is supplied with overshoots due to the impedance mismatch between the converter and the machine. The parameters reported have the following definition:

- U_p is the phase-to-phase voltage, expressed in V_{pk};

- U_{dc} is the DC bus voltage;

- U_{ph} is the phase-to-phase voltage, expressed in V_{pk-pk};

- U_j is the jump voltage at the impulse frequency, expressed in V_{pk};

- U_{gnd} is the maximum phase-to-ground voltage, expressed in V_{pk-pk};

- a is the impulse factor defined as the ratio between the maximum turn-to-turn voltage and the jump voltage.

The above parameters are interlinked and can all be expressed as a function of the DC bus voltage and the maximum overvoltage reached due to overshoots. In particular, for a n-level converter, one can write that

$$U_p = U_{dc} + U_b \tag{3.1}$$

where U_b represents the maximum overvoltage with respect to the DC bus voltage due to the overshoots. At this point, the phase-to-phase and phase-to-ground voltages can be expressed in a compact manner:

$$U_{gnd} = \sqrt{2} \cdot U_p = \frac{\sqrt{2}}{2} \cdot U_{ph} \tag{3.2}$$

while the jump voltage at the impulse frequency U_j is given by

$$U_j = \frac{\sqrt{2}}{2} \left(\frac{U_{dc}}{n-1} + U_b \right) \tag{3.3}$$

Finally, it is also possible to express the turn-to-turn voltage U_{turn} as a function of the DC bus voltage, taking into account the overshoot factor a:

$$U_{turn} = a \cdot U_j = \frac{a\sqrt{2}}{2} \left(\frac{U_{dc}}{n-1} + U_b \right) \tag{3.4}$$

Once the nomenclature has been clarified, it is quite simple to provide a definition for the voltage to be applied to the machine terminals during type tests, depending on the insulation whose correct operation is to be verified.

Assuming that a two-level converter is used for PD testing, the final formula will be as follows:

$$U_{test} = WF \cdot OF \cdot SF \cdot TF \cdot AF \cdot U_{dc}^{(max)} \tag{3.5}$$

The factors appearing in Eq. 3.5 must take account of a number of circumstances, which are listed below:

- WF is the winding factor, which takes into account the type of insulation being tested,

$$WF = \begin{cases} a\sqrt{2}/2, & \text{turn insulation} \\ \sqrt{2}, & \text{mainwall insulation} \\ 2, & \text{phase insulation} \end{cases} \tag{3.6}$$

- OF is the overshoot factor, which takes into account the overvoltage due to impedance mismatch between the inverter and the electric motor,

$$OF = 1 + \frac{U_b}{U_{dc}} \tag{3.7}$$

- $SF = 1.25$ is the safety factor, which takes into account the fact that in case of PD ignition, in order to extinguish the PD activity, it is necessary to reach a voltage level lower than 25%;

- TF is the temperature factor, which takes into account the fact that measurements are made at room temperature rather than at stator operating temperature; it depends on the investigated insulation:

$$TF = \begin{cases} 1.3, & \text{turn insulation} \\ 1.1, & \text{mainwall insulation} \\ 1.3, & \text{phase insulation} \end{cases} \tag{3.8}$$

- AF is the ageing factor, which takes into account the progressive deterioration of the insulation with the hours of service, due to thermal exposure,

$$AF = \max\left[1; 1.2\left(1 - \frac{T_{class} - T_o}{T_{class}}\right)\right] \tag{3.9}$$

where T_{class} is the thermal class and T_o is the operating temperature;

- $U_{dc}^{(max)}$ is the maximum applied DC bus voltage in operating conditions.

The introduction of broadband devices, made of Silicon Carbide or Gallium Nitride, has meant that the electromagnetic noise produced by the generators used for testing is exactly overlapping with the PD spectrum to be detected with antenna systems (only possible way in high frequency). This has led to the natural consequence of a real difficulty in performing PD tests when the voltage slew rates are very high, and consequently when the rise times are very small.

In the following it is intended to analyse all the aspects mentioned so far, providing and discussing different results obtained in the laboratory. They can help to devise a strategy to circumvent any problems that may be encountered during the type test of a real machine.

3.2.1 Measure partial discharges with wide band-gap converters

The first really difficult problem to face is how to reduce, if not eliminate, the electromagnetic noise generated by the converters during PD tests. Very often this problem led to a misunderstanding of the measurements made, leading to the conclusion, for example, that the switching frequency of the converter could affect the $PDIV$ value of an insulating system, although it was not possible to give a satisfactory explanation to this phenomenon [70].

As explained in detail in Chapter 2, one way around this problem is to change the detection technique, using an optical detector instead of an antenna. This approach certainly has the advantage of eliminating almost all electromagnetic noise. However, there are serious limitations on the test conditions, which are:

- completely dark test environment or sensor blind to visible light;

- clear line of sight between the specimen and the detector;

- concentrated discharge activity in a single area.

These characteristics have made this method always unattractive for the industrial world, since it was necessary to know *a priori* the site of discharge (and consequently the nature of the defect that triggered them) and it was necessary to have large areas dedicated for testing. However, as far as low-voltage motors and, more generally, all the systems that one might
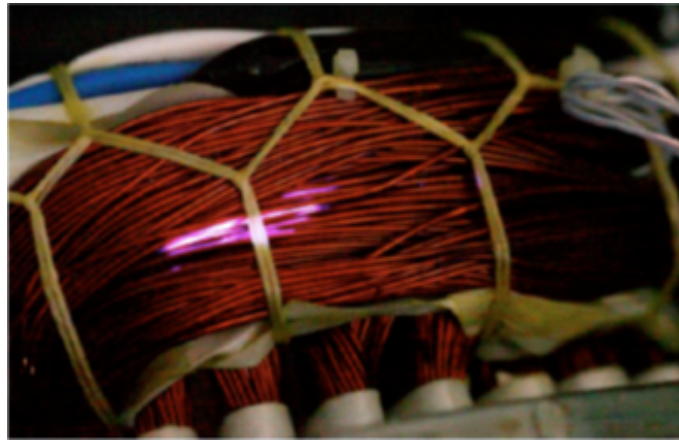
Figure 3.3: Typical phase-to-phase insulation failure in correspondence of random-wound electric motor's endwinding (source: [12]).

encounter in a hybrid or full electric vehicle distribution line are concerned, this is no longer entirely true.

The main reason why a paradigm shift can occur is because of the average size of these devices, which is quite small. Consequently, through a careful positioning of the optical fibres, it could be possible to detect partial discharge activity, even online. In addition, low-voltage motors have a simpler insulation system (for example, they do not have field control systems) than medium-voltage machines, thus reducing the number of possible failures and even weak points.

The problem that has recently emerged, linked to the partial discharge inception, is due to the introduction of converters, which however stress the stator insulation systems at very specific points: at the endwinding (see Fig. 3.3) and in any cavities between coils between which the voltage drop is high. Consequently, it is possible to imagine a monitoring system, such as the one that is installed for thermal detection, that allows to identify online the possible PD inception, at least in the first two mentioned points of the machine. In this respect, a low-voltage wire-wound motor has already been used to detect surface discharge activity by means of an optical sensor, despite the presence of the entire housing and rotor, as shown in Fig. 2.24.

As far as the other systems with which a vehicle is equipped are concerned, the problem is a bit simpler, since the object dimensions are usually smaller and their insulating system is much less complex. Think for example of the high voltage MOSFETs: their insulating system is certainly complex, because it is all miniaturized and must withstand, at certain points, extremely high electric fields (up to $100\,\mathrm{kV\,mm^{-1}}$), but their size is so small

(a)   (b)
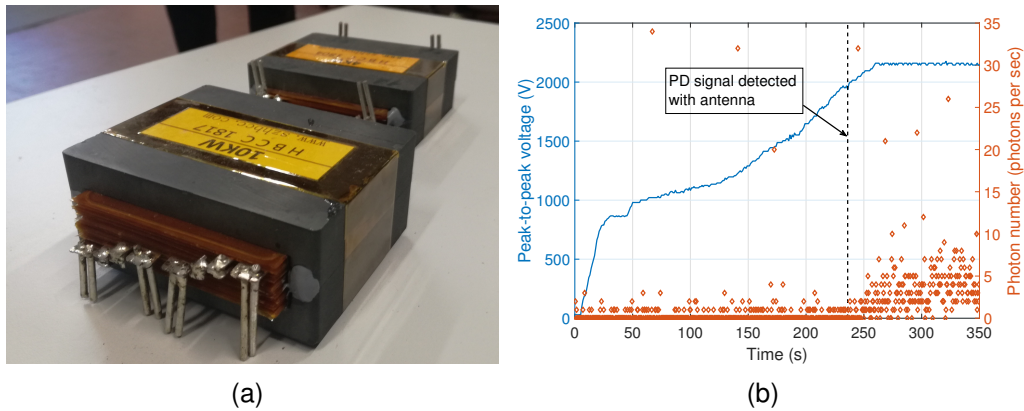
Figure 3.4: PD test results at $50\,\text{Hz}$ for a planar high-frequency ferrite power transformer for DC-DC converters using both an antenna and an optical sensor. (a) The transformer sample and (b) the optical PD pattern.

that the photons possibly generated by PD activity can be detected without difficulty by a single optical sensor placed in the immediate vicinity.

The same observations apply to the high-frequency transformers used in DC-DC converters, with the difference that in this case the insulation system is simpler, although the size is a bit larger. As an example, Fig. 3.4 shows the result of a PD test carried out at $50\,\text{Hz}$, using simultaneously an antenna and an optical sensor for detection. It can be observed that the measured number of photons increases drastically with the ignition of the discharges (detected by the antenna), although not with the same marked trend as with a twisted pair. This testifies to the possibility of using this type of detection both online and offline, even on real devices.

Alternatively, to try to get around the problem related to electromagnetic noise, it is possible to think of moving the PD signal analysis, acquired with the antenna, from the time domain to the frequency domain. In the laboratory, a PD test was performed on a twisted pair, feeding it through a converter with SiC-based MOSFETs and using at the same time two different acquisition systems: one is based on the optical sensor, described in Chapter 2, while the other consists in the acquisition of the electromagnetic spectrum in the frequency range between $1\,\text{kHz}$ and $2\,\text{GHz}$ through a homemade $5\,\text{cm}$ diameter disk antenna (see Fig. 3.5), connected to a Tektronix RSA306B USB spectrum analyser. The objective was to determine whether it was possible to detect the partial discharge inception through the latter technique, using the support of the optical sensor for the confirmation.

The PD test was performed at a pressure of $100\,\text{mbar}$, starting from

Figure 3.5: An image of the home-made $5\,\mathrm{cm}$ diameter diskette antenna used for the electromagnetic spectrum acquisitions.

an initial voltage of $300\,\mathrm{V_{pk}}$. Every $5\,\mathrm{min}$ the voltage increased by $10\,\mathrm{V_{pk}}$ until the ignition point detected by the optical sensor was reached. At each multiple of $100\,\mathrm{V_{pk}}$, the electromagnetic spectrum captured by the antenna was acquired. The partial discharge triggering was detected at $600\,\mathrm{V_{pk}}$.

Fig. 3.6 shows the different electromagnetic spectra captured by the antenna at 300, 400, 500 and $600\,\mathrm{V_{pk}}$. In the last one it can be seen that, at $0.9\,\mathrm{GHz}$ and $1.3\,\mathrm{GHz}$, there are slight peaks, which could represent the electromagnetic footprint emitted by the partial discharge activity. For a better understanding, Fig. 3.7 depicts the percentage differential ratio between the measured electromagnetic spectra and the reference one captured at $300\,\mathrm{V_{pk}}$, showing that at $600\,\mathrm{V_{pk}}$ there are isolated ridges at $0.9\,\mathrm{GHz}$ and $1.3\,\mathrm{GHz}$.

These peaks are in correspondence of the first resonance harmonics of the cylindrical tank in which the tests were carried out. It is possible to consider the box as formed by a section of circular waveguide, having its back and front faces enclosed with conducting plates. The system can be described in cylindrical coordinates of variables ρ, ϕ and z, as shown in Fig. 3.8, with $a = 113$ mm and $h = 312$ mm. Various field configurations (modes) can exist inside a circular waveguide except the TEM (Transverse Electro Magnetic) mode, which does not satisfy the boundary conditions on the waveguide wall. On the contrary, Transverse Electric (TE) or Transverse Magnetic (TM) modes can satisfy the boundary conditions of a circular cavity and, consequently, of a resonant cavity derived from a section of waveguide. In addition, when the ratio $h/a > 2.03$, the TE mode is dominant over the TM mode. Since this is the case ($h/a = 2.76$), it is possible to overlook the contribution of the TM mode [7].

The resonant frequency $(f_c)_{mnp}^{(TE)}$, where the subscripts m, n and p are designated to describe the modes along the ρ, ϕ and z axis respectively,
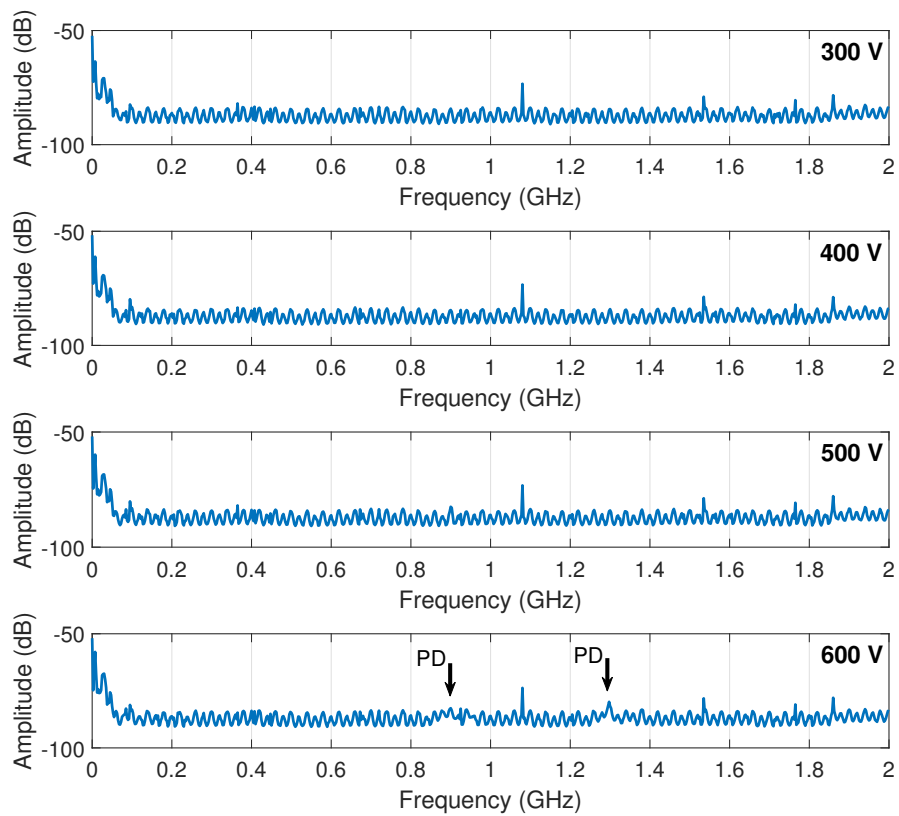
Figure 3.6: Electromagnetic spectra acquired by the antenna, at different levels of the applied voltage. PD activity is confirmed by optical detection system.
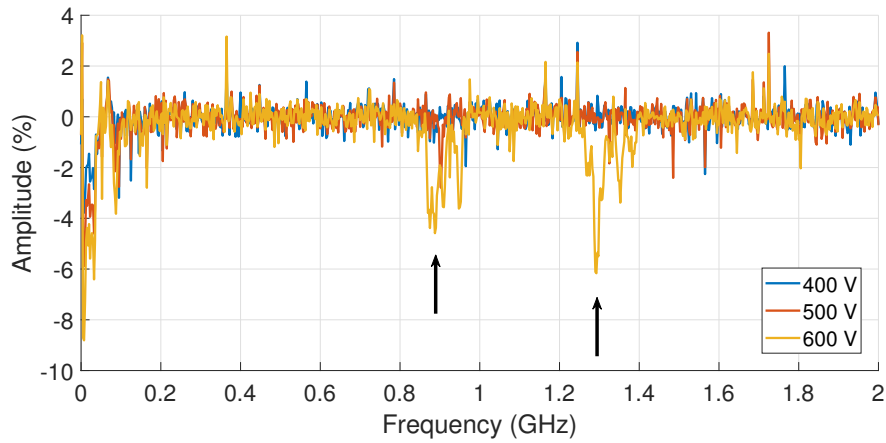
Figure 3.7: Difference between the electromagnetic spectra acquired at different applied voltage levels and the background spectrum measured at $300\,\mathrm{V_{pk}}$. The arrows highlight the electromagnetic PD footprints. PD activity is confirmed by optical detection system.
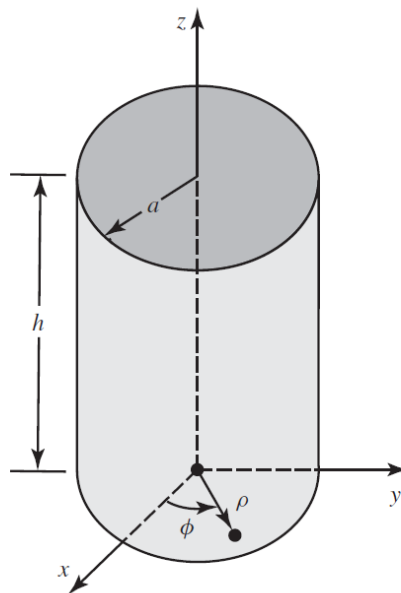
Figure 3.8: Geometry for circular cavity.

Table 3.1: Some TE propagation modes inside the tank.

m	n	p	$(f_c)^{(TE)}$ MHz
1	1	1	914
2	1	1	1376
3	1	1	1838
1	2	1	2302
1	3	1	3636
1	1	2	1236
1	1	3	1638
2	1	2	1608
3	1	2	2017

can be evaluated as follows [7]:

$$(f_c)^{(TE)}_{mnp} = \frac{1}{2\pi\sqrt{\mu\varepsilon}}\sqrt{\left(\frac{\chi'_{mn}}{a}\right)^2 + \left(\frac{p\pi}{h}\right)^2} \tag{3.10}$$

where χ'_{mn} represents the nth zero ($n = 1, 2, 3, ...$) of the derivative of the Bessel function J_m of the first kind and of order m ($m = 0, 1, 2, 3, ...$), $\mu = \mu_0 \cdot \mu_r$ is the magnetic permeability of the material inside the cavity and $\varepsilon = \varepsilon_0 \cdot \varepsilon_r$ is its dielectric permittivity.

Table 3.1 lists some of the resonance frequencies obtained by applying Eq. 3.10. For $n = 1$ and $p = 1$, the first three resonance frequencies are $914\,\mathrm{MHz}$, $1376\,\mathrm{MHz}$ and $1838\,\mathrm{MHz}$. In particular, the first two correspond almost exactly to the peaks shown in Fig. 3.7. This means, in theory, that if the system whose $PDIV$ is to be measured were to be characterized in advance, one or two narrow bands of frequency could be identified on which to focus during monitoring with the spectrum analyzer. This would drastically improve the signal-to-noise ratio and ensure an accurate measurement of the $PDIV$.

It should be pointed out, however, that with a real machine it is not possible to carry out a theoretical analysis, such as the one just carried out, to identify *a priori* the resonance frequencies of the system. This is due to a combination of factors: first of all, the geometry of the system is very complex and it is difficult to reduce it to a combination of circular or rectangular waveguides. In addition, different materials coexist within a machine, which therefore modify the dielectric permittivity and the magnetic permeability. Finally, the site where the partial discharges are triggered is

not known in advance, and consequently it is not known where the source is positioned within the geometry. However, it is always possible to think of a preliminary calibration phase, to identify these resonance frequencies on a real machine, using a noise generator.

This analysis therefore shows that it is perhaps still possible to use a traditional acquisition method for PD testing when using high frequency switching converters. However, it seems necessary to move the analysis to the frequency domain, with all that this entails (for example, especially when testing in unipolar mode, the detection of the actual $PDIV$ could be lost). Additional measurements are required to verify that one is able to recognize the initiation of partial discharges with the aid of the antenna alone, on different sample types. Optimising the size and type of antenna could probably improve the signal-to-noise ratio.

3.2.2   Some notes on the enhancement factors

The in-depth parametric analysis presented in Chapter 2 provides some insight on the environmental and system factors which must actually be taken into account during a qualification procedure.

First, it can be noted that the indication given by the standard for the temperature factor TF (Eq. 3.8) is empirical. The proposal may be twofold in this respect. On the one hand, an expression for TF can be introduced for turn and phase insulation that takes into account the actual service temperature T in °C:

$$TF = \frac{T + 273.15}{T_0 + 273.15} \tag{3.11}$$

where $T_0 = 20$ °C is the reference ambient temperature.

Alternatively, a Climate Factor CF can be defined, to replace the current TF, which takes into account both service temperature T and altitude h at the same time. Its final expression is derived from the experimental results already discussed in Chapter 2, which showed a practically linear dependence of $PDIV$ with air density ρ, for pressures above $100\,\mathrm{mbar}$ (equivalent to about $16\,\mathrm{km}$ altitude). As a result, the interpolation of the above data led to:

$$CF = \max \left[1.7, \quad \frac{1}{0.5016 \cdot \dfrac{\rho(T,h)}{\rho_0} + 0.5177} \right] \tag{3.12}$$

where the maximum value of 1.7 corresponds to the minimum point of the $PDIV$ in the graph shown in Fig. 2.28.

The air density, assuming it behaves like a perfect gas, can be expressed in general as follows:

$$\rho(p, T) = \frac{m}{V} = \frac{M_a}{V}n = \frac{pM_a}{R_0 T} \tag{3.13}$$

where $M_a = 28.9647 \, \text{kg} \, \text{kmol}^{-1}$ is the dry air molar mass and $R_0 = 8314.4598$ $\text{J} \, \text{kmol}^{-1} \, \text{K}^{-1}$ is the universal gas constant.

Replacing Eq. 3.13 in 3.12 gives the following result:

$$\frac{\rho}{\rho_0} = \frac{p_0}{T_0}\frac{T}{p} \tag{3.14}$$

Assuming that the air in the atmosphere is in hydrostatic conditions, Stevin's law applies:

$$d\,p = -\rho g_0 \, dz \tag{3.15}$$

where $g_0 = 9.80665 \, \text{m} \, \text{s}^{-2}$ is the gravitational acceleration, $d\,p$ is the differential pressure and $d\,z$ is the differential height. Dividing both members of Eq. 3.15 by pressure, introducing Eq. 3.13 and finally integrating the resulting expression from the surface to the altitude h, one has:

$$p = p_0 \exp\left(-\int_0^h \frac{Mg_0}{R_0 T}d\,z\right) \tag{3.16}$$

Assuming a linear temperature fall with the quota $T = T0 - L \cdot z$, where L is the so-called temperature lapse rate, and that the gravitational acceleration and the air molar mass remain constant, one obtains the so-called first barometric formula from Eq. 3.16:

$$\frac{p}{p_0} = \left(\frac{T_0}{T_0 - L \cdot h}\right)^{\frac{Mg_0}{R_0 L}} \tag{3.17}$$

If, instead, the temperature is supposed to be constant, Eq. 3.16 would be re-written as follows:

$$\frac{p}{p_0} = \exp\left(-\frac{Mg_0 h}{R_0 L}\right) \tag{3.18}$$

This is called the second barometric formula.

A value remains to be attributed to the lapse rate temperature L just introduced. The air temperature in the atmosphere is not monotonous as a function of height. Therefore, it is necessary to define it at times. Moreover,

Table 3.2: U.S. Standard Atmosphere reference levels.

Subscript b	Height above sea level m	Static pressure Pa	Standard temperature K	Temperature lapse rate $\mathrm{K\,m^{-1}}$
0	0	101325	288.15	-0.0065
1	11000	22632.10	216.65	0
2	20000	5474.89	216.65	0.001
3	32000	868.02	228.65	0.0028
4	47000	110.91	270.65	0
5	51000	66.94	270.65	-0.0028
6	71000	3.96	214.65	-0.002

in some sections it remains constant, therefore in some situations Eq. 3.17 will be used to determine the atmospheric pressure, while in others Eq. 3.18 will have to be applied.

A very popular model in the aeronautical field is the one presented by the U.S. Committee on Extension to the Standard Atmosphere, which was updated in 1976 [79]. It is very similar to the International Standard Atmosphere: it differs mainly in the proposed temperature distribution as a function of height, for high altitudes. In this model, the atmosphere is divided into 7 layers, according to the indications given in Table 3.2. On the basis of this division, the following formula is applied to determine the pressure p that one has at altitude h:

$$p(h) = \begin{cases} p_b \left(\dfrac{T_b}{T_b + L_b(h - h_b)} \right)^{\frac{M_a g_0}{R_0 L_b}}, & L_b \neq 0 \\[2em] p_b \exp\left[-\dfrac{M_a g_0 (h - h_b)}{R_0 T_b} \right], & L_b = 0 \end{cases} \tag{3.19}$$

where b is such that $h_b < h < h_{b+1}$.

Fig. 3.9 shows the trend of the air temperature and density as a function of altitude, obtained by applying the model just described.

At this point, it is possible to replace Eq. 3.19, combined with Eq. 3.13, in the CF definition in order to obtain:

$$CF = \max\left[1.7, \quad \frac{1}{0.5016 \cdot \dfrac{p(h)}{\rho_0} \dfrac{M_a}{R_0 T} + 0.5177} \right] \tag{3.20}$$
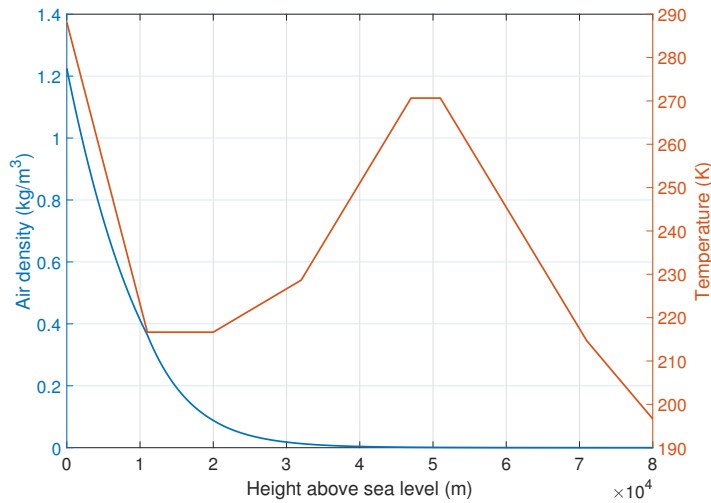
Figure 3.9: U.S. Standard Atmosphere graph of geometric altitude against air density and temperature obtained from Eq. 3.19. The pressure trend can be derived from these two curves by applying Eq. 3.13.

where $\rho_0 = 1.2041 \; \mathrm{kg \, m^{-3}}$ is the reference air density, h is the altitude and T is the service temperature (in K).

Once the exact role played by temperature and pressure has been established, the effect of humidity still remains outside. As discussed in Chapter 2, air humidity is linked to several hidden parameters that each contribute differently to influencing the final $PDIV$ value of an insulation system. The result is a strongly non-linear behaviour of the insulation system as a function of relative air humidity and temperature.

Consequently, on the basis of the observations made, an additional enhancement coefficient taking into account the effect of moisture could be prudently introduced. Since in the worst case (at $25 \, °\mathrm{C}$) a drop of about 40 % in the $PDIV$ has been measured experimentally, when the behaviour of the wires in relation to humidity is not known in advance, the following new enhancement factor can be established:

$$HF = 1.65 \qquad (3.21)$$

This line of thought, which in practice provides for a further weighting of the insulation system, is justified by the fact that an electric motor, especially when installed on board a vehicle, will almost certainly experience a wide range of humidity values in combination with a wide range of operating temperatures. This means that it is almost certain that it will also work in the worst possible combination of conditions in this respect. In addition, it

should be noted that in terms of absolute humidity, it is very unlikely, if not in specific applications, to reach the equivalent values that would be in an environment at $90\,°C$ and 20 % relative humidity.

It should be noted that this approach could be all too conservative, especially if an electrical actuator or motor intended for the aeronautical sector is to be tested. It is not yet clear whether the effect of humidity, in combination with low pressure levels, is really relevant. If this is not the case, a single enhancement factor of 1.7 could be used, taking into account both the situation where there is high humidity under standard ambient conditions and the case of low surrounding air density.

The good news, on the other hand, is that the slew-rate and frequency do not seem to have a direct impact on the partial discharge inception phenomenon. They are to be taken into consideration only to determine the maximum voltages to which the different insulating systems of an electric machine are subjected (i.e. in the determination of WF). If necessary, it must be ensured that the frequency does not play a significant role in the intrinsic electrical ageing, which would affect the AF value. However, since these are low-voltage electric motors, which correspond to maximum electric field strengths all in all modest (about $20\,kV\,mm^{-1}$ in the worst case), this possibility is considered remote.

3.2.3   Generators for the impulsive PD test

As already mentioned, neither the frequency nor the slew-rate characterizing the voltage waves sent to the terminals of an electric motor directly influence the phenomena of partial discharge inception. However, a certain impact of the polarity and waveform (which depends indirectly on the slew-rate and frequency) on the discharge mechanisms, and consequently on the measured $PDIV$ value of the insulating system, has been highlighted. If the mainwall and phase insulation are to be tested using the same pulsed voltage generator used to test the turn insulation, it is necessary to investigate the impact of this choice on the actual $PDIV$ estimate (if any).

In laboratory, three different types of PD tests were performed (each with a voltage generator characterized by a different waveform) on twisted pairs made with three different enamelled wires. Table 3.3 lists the specific properties of the latter, while Table 3.4 specifies the features of the three generators used. Finally, Fig. 3.10 shows the two different pulsed waveforms of the voltage applied to the twisted pairs, while Fig. 3.11 illustrates the generalized circuit for testing. Note that to use the surge generator it

Table 3.3: Features of the magnet wires used in the tests.

Code	Material	Grade	Conductor diameter	Insulation thickness
			mm	μm
A	Polyamid-imide loaded with ceramic nanoparticles	2	0.38	20
B	Polyamid-imide	2	0.71	26.5
C	Polyamid-imide loaded with unspecified nanoparticles	3	1.00	42.5

Table 3.4: Features of the voltage generators used in the tests.

Type	Rise time	Maximum voltage	Frequency	Polarity
	ns	kV	Hz	
Repetitive square wave	300	10	500	Negative
Sinusoidal	-	3	50	Bipolar
Surge	300	6	1	Bipolar

is necessary to have always connected an inductive load and that is why a medium voltage coil has been inserted in parallel to the test specimens (which has been made sure that the PD ignition point is much higher than that of the twisted pairs). Under these conditions, it was possible to use a traditional antenna detection technique, following the dictates of IEC-TS 61934 [27]. The acquisition system consists of a Techimp PDBaseII®device. As specified by the IEC 60034-18-41 standard [18], the $RPDIV$ has been detected.

The AC tests at $50\,\mathrm{Hz}$ have been carried out to obtain a reference. The results for the three wires are reported in Figs using Weibull probability charts. The graphs show also the $PDEV$ recorded during tests with AC sinusoidal waveforms.

Already from a visual inspection of these graphs, it can be concluded that the surge tests are characterized by a greater degree of uncertainty than the other two. On the other hand, this is not surprising, since several authors have observed that repetitive surges promote the formation of space charge, which in turn tends to trigger PD more easily [97, 51, 58].

However, this poses a problem in estimating the machine insulation features. In particular, the use of a surge generator seems to create serious difficulties in correctly estimating the maximum tolerable voltage, with relative errors of up to 40 % on the single sample. Moreover, they are always overestimates, which would lead to a guarantee for a maximum
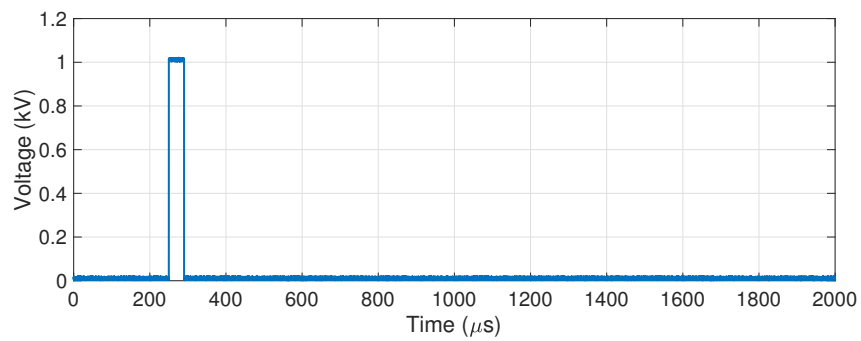
(a)
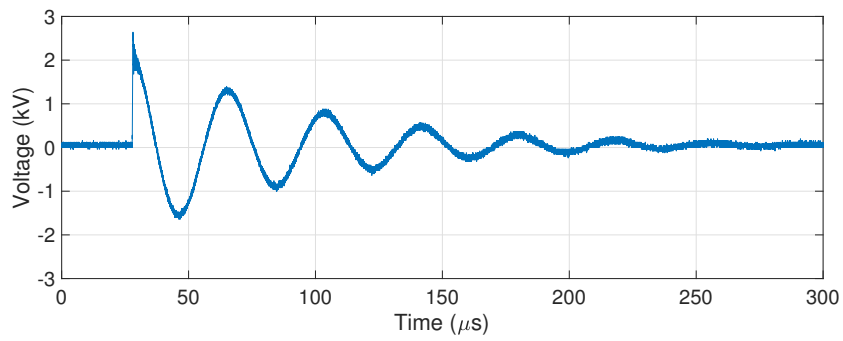
(b)

Figure 3.10: Voltage waveform provided by (a) repetitive square wave generator and (b) surge generator connected to a twisted pair (in the latter case, the twisted pair was connected in parallel to a medium-voltage coil).
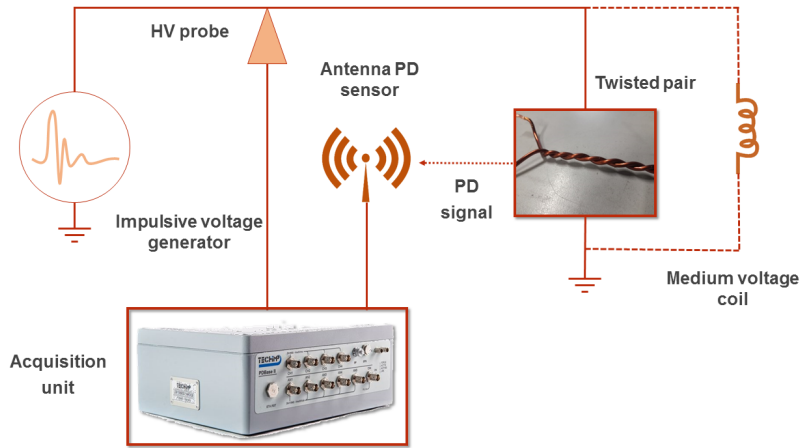
Figure 3.11: Generalized test circuit to analyse the impact of the impulse generators on the $PDIV$ measurement.
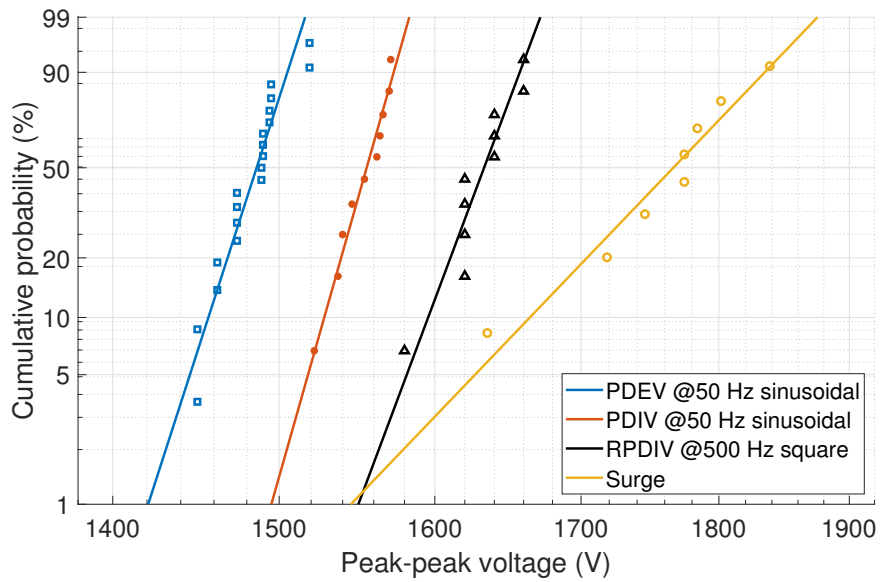
Figure 3.12: $RPDIV$ results obtained using wire A.
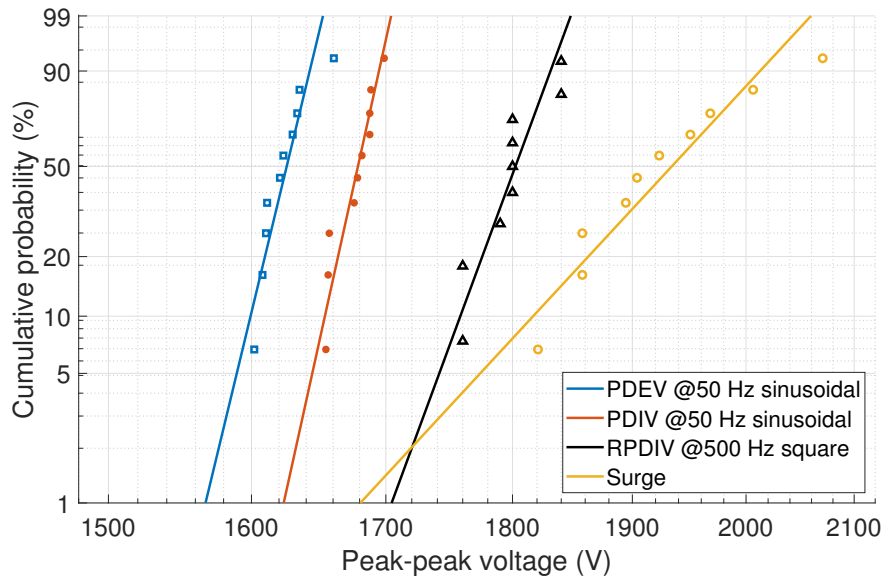
Figure 3.13: $RPDIV$ results obtained using wire B.
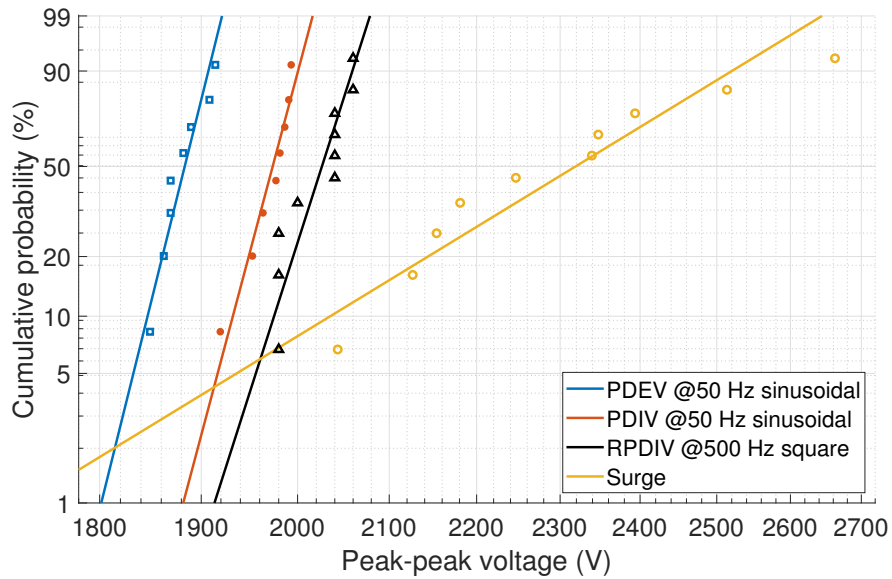
Figure 3.14: $RPDIV$ results obtained using wire C.
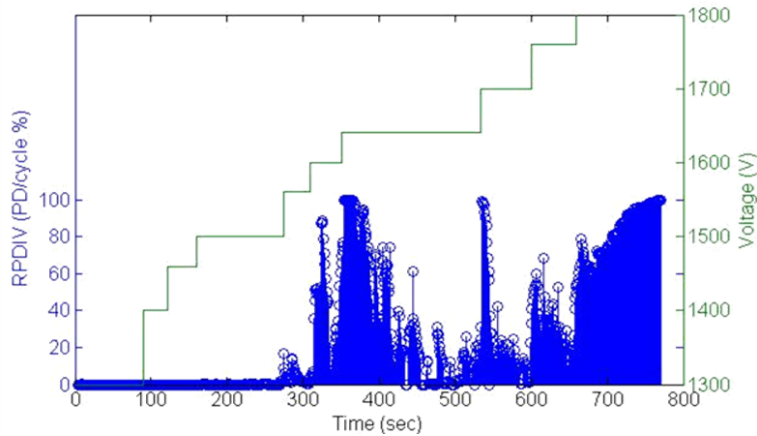
Figure 3.15: Temporal evolution of the PD ratio and applied voltage, recorded during a PD test on wire B using the square wave generator.

nominal voltage that in reality the machine would be better not to reach. The use of a square wave generator, on the other hand, seems to lead to a fairly precise measurement of the $RPDIV$, bearing in mind that the latter is necessarily greater than the $PDIV$. This could make it a good candidate as an impulsive generator with which to perform the complete PD test of a machine. Nevertheless, it should be noted that the surge generator is much more compact in size than the square pulse generator: the first is portable, while the second is not.

Another critical issue that emerged during the measurements, using the square wave generator, was the time evolution of partial discharges. To introduce the problem, first define the so-called PD ratio r_{PD}:

$$r_{PD} = \frac{\text{number of cycles where PD are detected}}{\text{total number of cycles}} \quad (3.22)$$

Since the $RPDIV$ is defined as the minimum peak-to-peak impulse voltage at which more than five PD pulses occur on ten voltage impulses of the same polarity [18], r_{PD} was used as an indicator to decide whether or not the $RPDIV$ has been reached ($RPDIV$ occurs when $r_{PD} \geq 0.5$). Fig. 3.15 shows the time evolution of r_{PD} during a PD test, together with the trend of the peak voltage applied. After the first discharge is triggered, several moments of intense discharge (with r_{PD} equal to 1) can be clearly seen, separated by periods when there is no or almost no activity, despite the fact that the voltage has increased in the meantime.

This phenomenon makes it more difficult to correctly determine the $RPDIV$, since it is not clear what criterion is to be used to identify it.
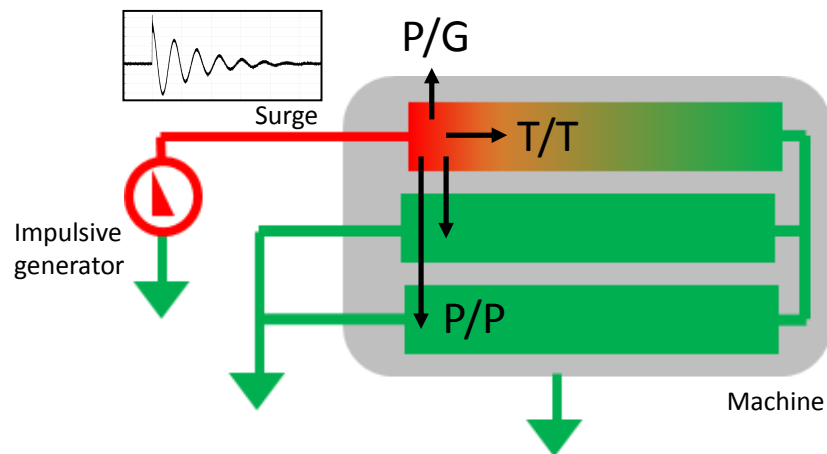
Figure 3.16: Schematic representation of the stresses applied on the low-voltage stator insulation systems when injecting voltage through an impulse generator.

With reference to Fig. 3.15, according to the standard, the $RPDIV$ should be fixed at about $1600\,\mathrm{V}$. However, the discharge activity is not stable and after a while it is extinguished: this means that the insulation could be subjected to this voltage, since there would be no continuous activity of partial discharges. The real $RPDIV$, which guarantees a stabilized discharge activity over time, is the one that occurs at $1800\,\mathrm{V}$. In other words, it is not clear the minimum waiting time to consider to be sure not to have a sudden extinction of the PD activity.

However, this behaviour may be caused by the DC component of the applied voltage: the voltage waveform is unipolar with a duty cycle equal to 5 %. This means that a certain amount of charge tends to accumulate inside the enamel, helping to intensify the electric field. When the first partial discharges occur, the accumulated charge is extinguished, bringing the electric field back to lower values and consequently causing the discharge activity to be extinguished. If this were the case, one possible solution would be to use a bipolar generator instead of a unipolar one.

3.2.4   Discussion on the best connection configuration

So far, it has been assumed that all three insulation systems constituting a low-voltage electric motor can withstand the nominal voltage applied to the terminals, ensuring a pd-free operation. However, recently nominal voltages have risen to such an extent that a method has become necessary to verify that a machine is actually PD free. Unfortunately, there is no
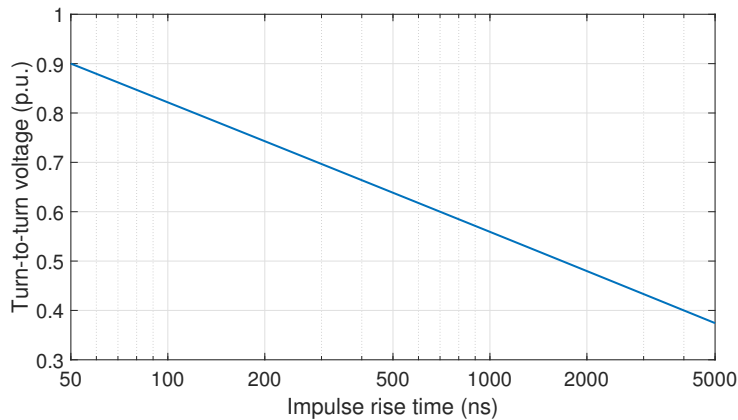
Figure 3.17: Worst case voltage stressing the turn insulation in a variety of random wound stators as a function of the impulse rise time. The reference is the peak phase-to-ground voltage at the machine terminals. Adapted from [18].

standard that explains exactly how to perform such a PD test, on a real machine. In particular, the main problem lies in the fact that, by applying voltage to any of the terminals, all the insulation systems are stressed at the same time (see Fig. 3.16). Moreover, the electrical stress applied will not be uniform. This is due to the fact, already mentioned in Chapter 1, that the voltage distribution along the phase winding is inhomogeneous, since the voltage supplied to the machine terminals is no longer sinusoidal.

The fact that the three electrical insulation systems operate at very different temperatures must be taken into account. In particular, for phase and turn insulation, the maximum temperature that can be reached by the conductors is considered, while for ground insulation, a lower temperature is assumed due to the heat removal by the stator.

This has a strong repercussion on the voltages to be applied to the different insulations during the tests. For example, take the case of a machine with a nominal voltage of $500 \, V_{rms}$ (corresponding to a DC bus voltage of $675 \, V$) and a *severe* stress category ($OF = 2$). The peak phase-to-ground (P/G) voltage at the machine terminals will therefore be $1350 \, V_{pk}$. Assuming, for simplicity, to be in the worst case, without losing generality, there is an overall enhancement factor of 1.95 for phase and turn insulations, and 1.65 for ground insulation. This means that the peak voltages to be applied on the different insulation systems are as follows (P/P is the phase-

Table 3.5: Summary of chosen possible test configurations

Type	Terminal connection			
	U	V	W	Frame
A	HV	GND	GND	GND
B	HV	GND	GND	FLOAT
C	HV	GND	FLOAT	FLOAT
D	HV	GND	FLOAT	GND
E	HV	HV	HV	GND
F	HV	HV	FLOAT	GND
G	HV	HV	GND	GND

to-phase voltage and T/T is the turn-to-turn voltage):

$$V_{P/P} = 2633\,\mathrm{V_{pk}} = 1.7\,\text{p.u.} \tag{3.23}$$

$$V_{P/G} = 1559\,\mathrm{V_{pk}} = 1.0\,\text{p.u.} \tag{3.24}$$

$$V_{T/T} = 790\,\mathrm{V_{pk}} = 0.6\,\text{p.u.} \tag{3.25}$$

where it was assumed, in the worst case, to have a voltage drop of 60 % on the first turn (corresponding to a rise time of about $700\,\mathrm{ns}$, observing the graph in Fig. 3.17). The phase-to-ground voltage has been selected as the reference value. It is then observed that, wanting to test the turn isolation, a voltage of about $1316\,\mathrm{V}$ must be applied with the DC bus, obtaining a phase-to-ground pulsed voltage with a peak value equal to $1843\,\mathrm{V_{pk}}$, higher than the threshold established for the mainwall insulation.

This example has shown the need to identify a set of optimal configurations for the connection converter-machine, so as not to unintentionally stress an insulating system while trying to test another one. To do this, it is first necessary to understand how the voltage is distributed along the windings when using a pulsed waveform generator, for different connection configurations.

In the beginning, therefore, a set of configurations was chosen for testing. This choice was based on the desired requirements for the test procedure and on the proposal of [20], namely:

- use of only the square wave generator for testing all insulation systems (so that no more than one generator has to be used);

- identification pf the faulted system in the event of a *no-go* test result;

- star-point access not required;

- maximum detection sensitivity.

Table 3.5 and Fig. 3.18 show the possible configurations chosen.

From a practical point of view, there are two parameters that are of practical relevance (since they can be varied by acting directly on the generator): the rise time and the slew rate that characterize the square wave fed to the machine terminals. The first, in combination with the total length of the wire of a phase (which, however, is not known in advance), determines exactly how the reflection and transmission phenomena of the voltage waves along the stator winding occur. The second establishes the harmonic content of these waves and the inhomogeneity of voltage distribution along the winding. Since the slew rate is not very dependent on the characteristics of the machine and much more on those of the converter, this parameter is the only one that will be referred to in the following.

The machine used to evaluate the propagation of surge waveforms within a stator is a random-wound three-phase unit with star-connected phases having $20\,\mathrm{kV\,A}$ of rating. Windings are double layer with two slot-pitches. Each phase consists of 16 coils with 14 turns each. Each coil is accessible so that the voltage drop across the coil can be measured. The mainwall insulation is based on Mylar sheets and the same material is interposed between coils in the over-hang. The turn insulation is based on polyester enamels. The machine is provided with a wound-rotor with two salient poles. The circuital scheme is shown in Fig. 3.19. By virtue of these features, a square wave has been injected along the windings, in all the configurations envisaged, and its evolution has been followed by sampling the voltage (with respect to the ground) at five different points, namely, with reference to the diagram in Fig. 3.19:

- G1 (input);

- G2 (first input coil);

- G6 (in the middle of the phase);

- G19 (star-point);

- G20 (first coil after star-point).

This procedure has been repeated for all configurations, with three types of square waves, each characterized by a different slew rate (no-load). It should be noted, however, that the square wave slew rate varied according to the tested configuration (since the equivalent impedance seen by the generator is modified). However, the idea was to feed it with a

(a)   (b)

(c)   (d)

(e)   (f)

(g)
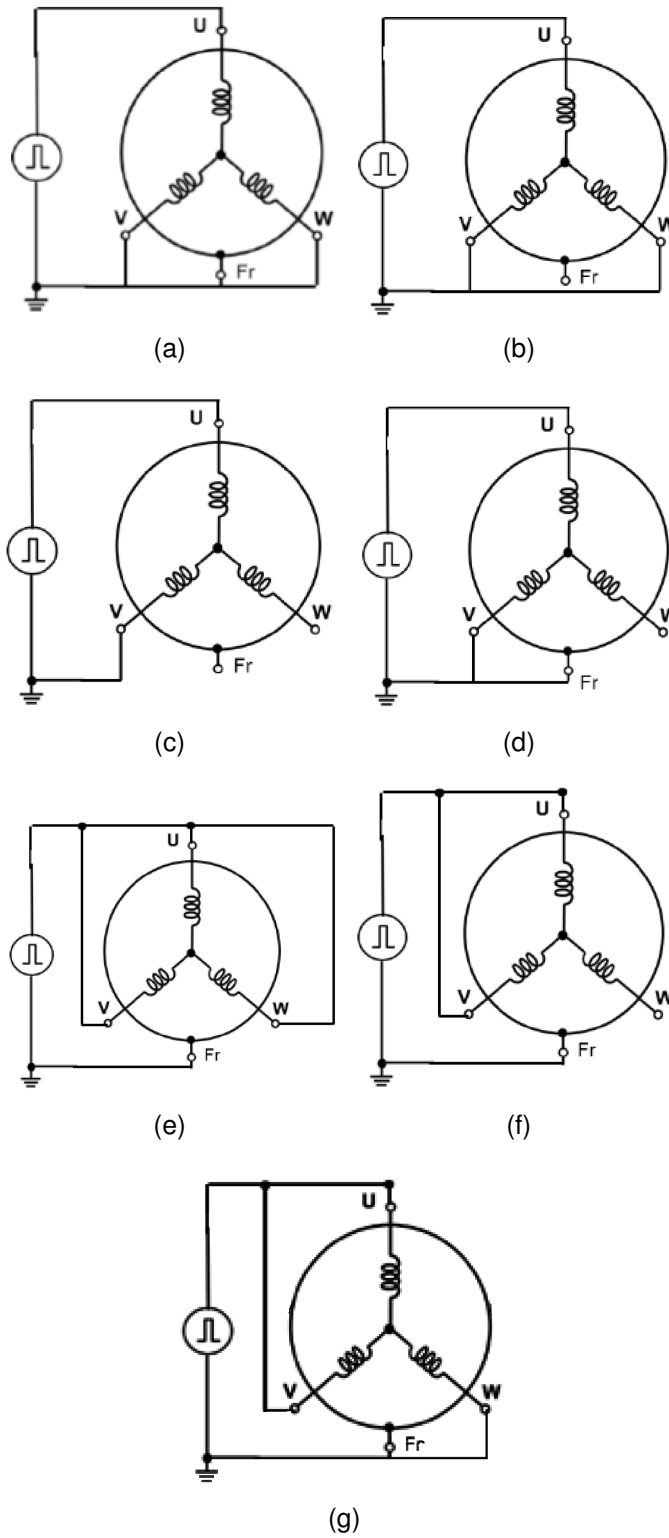
Figure 3.18: Connection diagrams for the configurations listed in Table 3.5.
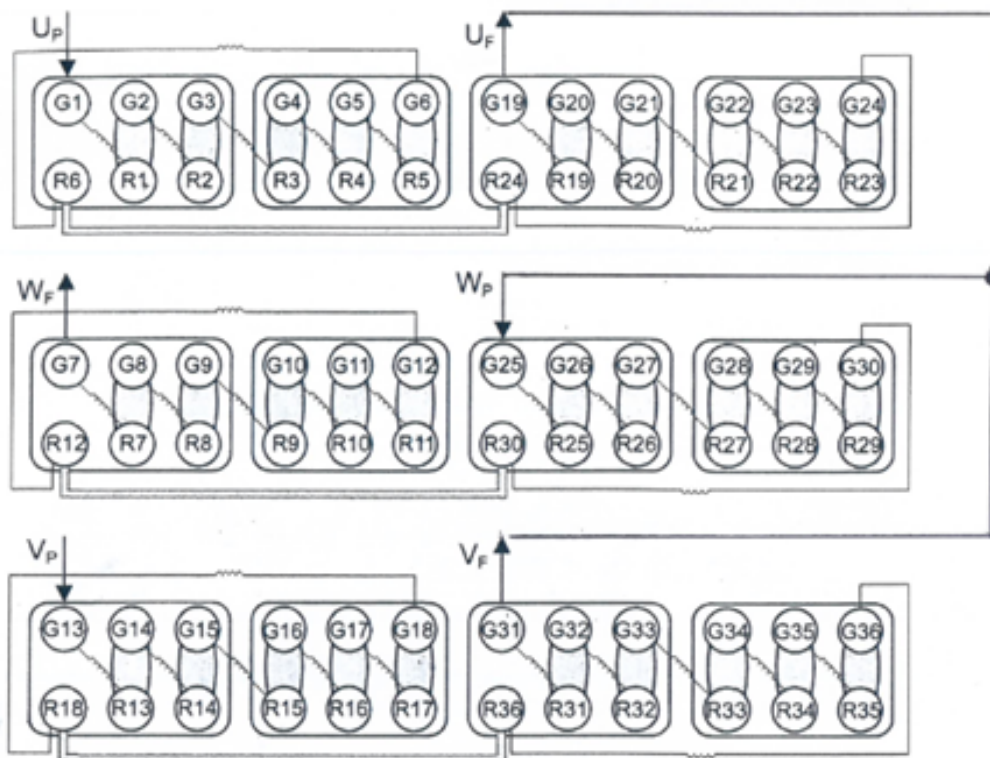
Figure 3.19: Final diagram of the connections of the machine on which the propagation of the voltage pulses along the windings has been studied.

wave characterized by a very high slew rate (greater than $1\,\mathrm{kV}\,\mu\mathrm{s}^{-1}$) and another with a very low slew rate (less than $0.1\,\mathrm{kV}\,\mu\mathrm{s}^{-1}$), so as to highlight any differences during propagation. Consequently, the actual value will be indicated in the following, if necessary, depending on the case under consideration.

Measurements were made using different generators (to obtain different slew rates). The connection cable between the power supply and the machine terminals has always been kept as short as possible to avoid reflection phenomena already at the motor input. In cases of low and moderate slew rate, a PicoScope oscilloscope with a $20\,\mathrm{MHz}$ bandwidth and a differential voltage probe with a $15\,\mathrm{MHz}$ bandwidth were used. When the generator with a high slew rate voltage wave was used, a Tektronix differential probe with a $100\,\mathrm{MHz}$ bandwidth connected to a Tektronix oscilloscope with a $2.5\,\mathrm{GHz}$ GHz bandwidth was implemented.

As an example, Fig. 3.20 shows the voltage waves measured along the different winding points for configurations A and F applying a wavefrom with high slew rate. In the first case, a strong voltage reduction can be observed as one proceeds towards the star-point. In the second case, the voltage does not decrease, but on the contrary, there is a huge over-voltage at the star-point.

This phenomenon can be explained looking at Fig. 3.21. Let Z_0 the characteristic impedance of a phase. Using configuration F, the surge travels on two phases in parallel and is reflected by a single phase. The reflection coefficient at the star point is:

$$\Gamma_F^{(Y)} = \frac{Z_0 - Z_0/2}{Z_0 + Z_0/2} = \frac{1}{3} \tag{3.26}$$

This means that the transmission coefficient will necessarily be equal to $1 - 1/3 = 2/3$: in other words, only 67 % of the voltage is propagated in the W phase. Arriving at the phase W terminal (open circuit) this voltage is doubled, reaching, theoretically, a value of 1.34. This analysis predicts in a rather accurate way the peak voltage of the phase W terminal, as shown in Fig. 3.20(b). In the same way, the overvoltage shown in Fig. 3.20(a) in configuration A, although attenuated, can be justified. The reflection coefficient at the star point is:

$$\Gamma_A^{(Y)} = \frac{Z_0/2 - Z_0}{Z_0 + Z_0/2} = -\frac{1}{3} \tag{3.27}$$

However, in this case there is constructive interference between the voltage wave that has propagated to the star centre and the waves that have undergone more than one reflection.

(a)

(b)
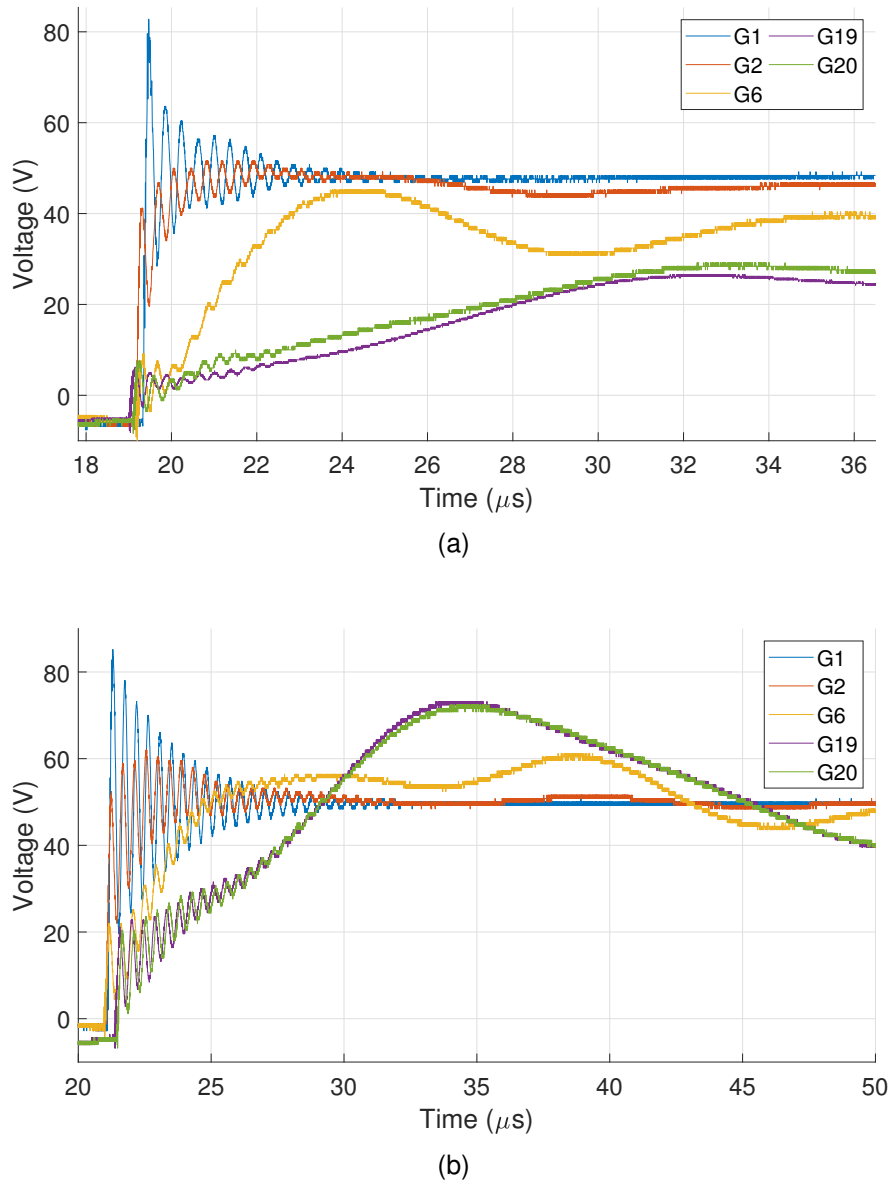
Figure 3.20: Potential of the different points, applying a waveform with high slew rate, in (a) configuration A and (b) configuration F.
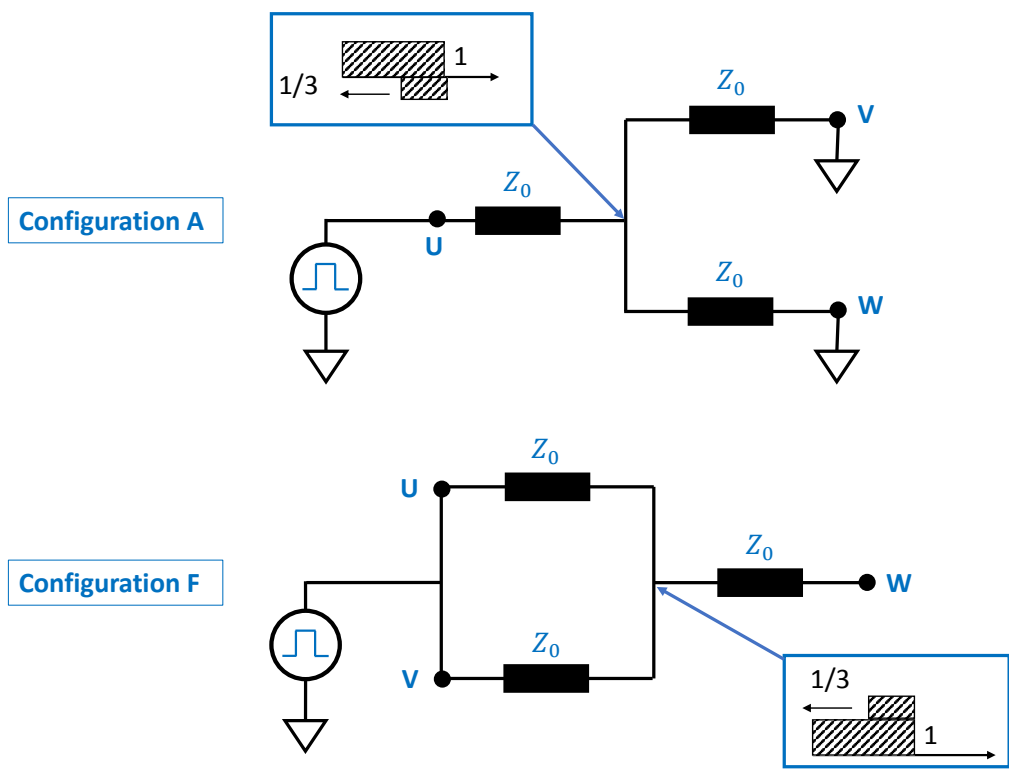
Figure 3.21: Schematic representation and comparison of the surge propagation in configuration A and F.
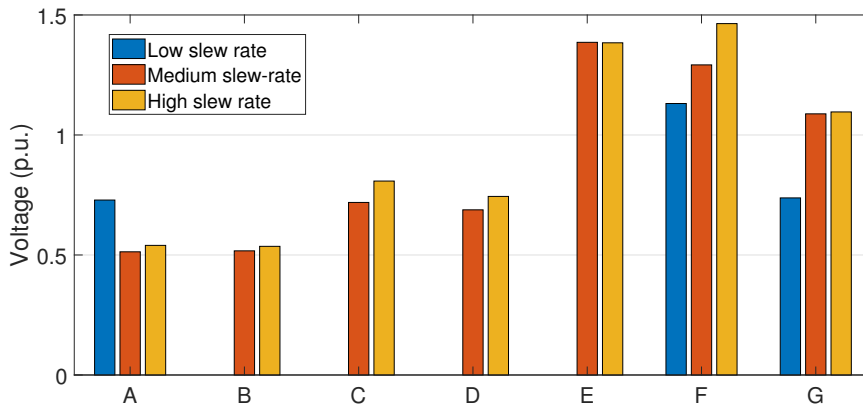
Figure 3.22: Peak voltages between star point and frame in the three cases considered and in all configurations. With the lowest slew rate, measurements were only made in A, F and G configurations.

Another interesting thing to note is the immediate attenuation of the initial ringings in all the configurations considered. This phenomenon is due to the fact that the machine winding, in any configuration considered, behaves like a low-pass filter, by virtue of the presence of parasitic capabilities, with a cut-off frequency below ten MHz. In this way, the high frequency harmonics that characterize the ringings and the voltage spikes of the fed wave undergo a strong attenuation propagating along the stator winding.

All data are reported in per unit of the peak voltage at the signal generator output and are summarized in Figs 3.22, 3.23 and 3.24. Fig. 3.22 shows the peak voltage measured in correspondence of the star centre in the three cases of slew rate and in all the configurations taken into consideration.

Fig. 3.23 instead illustrates the peak value of the voltage drop measured across the closest coil to the line terminal, in the different configurations and with the different slew rates considered. According to these results, it can be guessed that as the slew rate drops, the voltage drop on the first turns decreases at the same time.

Finally, Fig. 3.24 shows the peak voltage of the phase-to-phase voltage measured at moderate slew rates for all seven configurations. Since the three-phase system is virtually balanced, only the configuration of the connections influences the phase voltage applied between the different terminals. Consequently, for simplicity's sake, the result of the measurements made with the other slew rates has been omitted. As can be seen, to test phase insulation, A-D configurations offer the maximum applicable voltage. However, their value does not differ significantly from the phase-to-ground
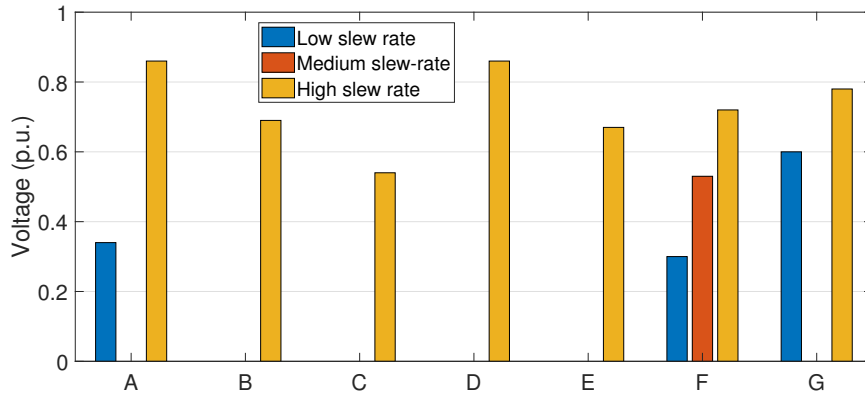
Figure 3.23: Peak voltages across the closest coil to the line terminal, in the three cases considered and in all configurations. With the lowest slew rate, measurements were only made in A, F and G configurations. In the case of an average slew rate, the resulting voltage drop was measured only in configuration F.
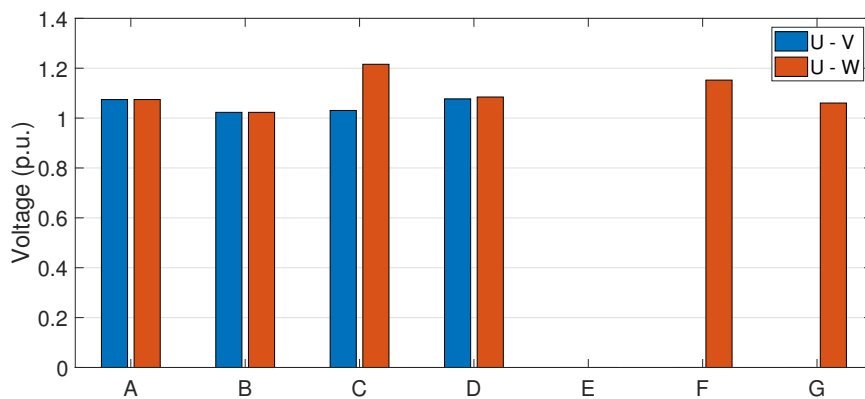
Figure 3.24: Phase-to-phase peak voltages in all configurations measured with the medium slew rate waveform.
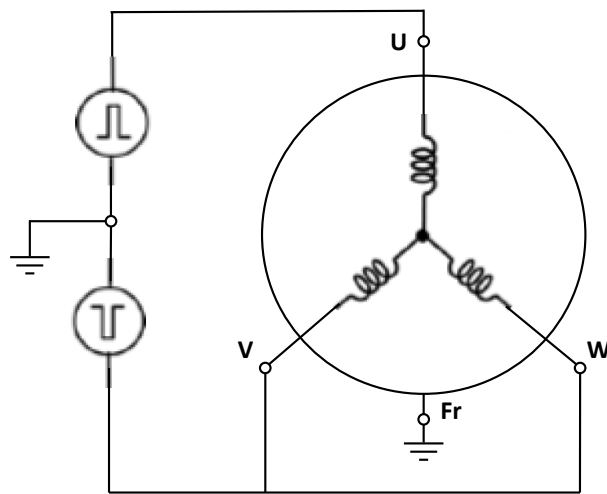
Figure 3.25: Phase-to-phase insulation check scheme using a center-tapped transformer or a bipolar surge generator.

voltages and consequently the mainwall insulation would also be stressed.

In the light of these measurements, having at disposal a pulse generator in which it was possible to vary the slew-rate, the following procedure could be proposed for the test of a complete machine whose star point is not accessible:

1. test the mainwall insulation in phase W using configuration E with the lowest slew rate possible (or alternatively an AC generator). This would ensure that the phase-to-ground limit stress is applied when keeping the turn-to-turn stress in all phases below its limit value. In addition, this ensures that the phase insulation is not stressed at all.

2. test the turn insulation using configuration A with the highest slew rate possible. In particular, to stay below the threshold stresses for the phase and mainwall insulation, it is necessary that the slew-rate of the test generator is higher than the nominal one of the converter that will be combined with the machine.

3. Phase insulation is the most complicated to test, precisely because it is difficult not to stress other insulation systems while doing so. There are three possible modes, each with its own advantages and disadvantages:

(a) the G configuration can be used using an AC or square-wave (lowest-rise time possible) voltage generator. In this way, a current that heats the conductors can be supplied for a few tens of minutes in advance. Once a temperature of at least 100 ℃ has been reached (within the limits of the thermal class of the machine, the higher the temperature, the lower the stress applied to the ground insulation), the voltage calculated using Eq. 3.5 can be applied without taking into account the thermal coefficient.

(b) Using a center-tapped transformer, the machine can be connected as shown in Fig. 3.25. In this way, without heating the windings, it is possible to test the phase insulation by applying the nominal stress and at the same time exerting a little more than half of the nominal voltage on the ground insulation. The use of an AC generator ensures that the turn insulation is not (or almost is) stressed at all.

(c) Finally, it is possible to think of using a bipolar surge generator. In this way, using the same configuration as in Fig. 3.25, it is possible to stress the phase insulation with a pulse wave, without applying the full nominal voltage to the other two insulation systems. Compared to the previous approach, there is the advantage of applying a stress with characteristics closer to the actual operating characteristics.

4. If needed, and if the star point is accessible, the insulation between the star point and the frame can be tested using configuration F and the nominal working slew-rate to ensure that the overvoltage does not incept PD activity.

The approach 3(a) is certainly effective, but may take quite a long time to test, as the winding must be expected to reach stationary temperature conditions. Method 3(b) also has the advantage that it is easy to apply and allows precise $PDIV$ measurement (because the AC test is done without the problem of switch interference), but on the other hand it does not realistically stress phase insulation. The procedure 3(c) seems the most natural one to adopt, however it is complex to implement (dedicated generator), it is the one that requires the largest generator size and it would be difficult to measure the $PDIV$ (for the already known problems of electromagnetic interference).

Now let's consider again the case study discussed above. Suppose to have a square wave test generator with a slew rate that can be controlled between $50\,\mathrm{kV\,\mu s^{-1}}$ and $0.5\,\mathrm{kV\,\mu s^{-1}}$.

Initially the mainwall insulation is tested using the E configuration for connections and applying to the phase U a voltage of $1575\,\mathrm{V_{pk}}$ characterized by a slew rate of $0.5\,\mathrm{kV\,\mu s^{-1}}$. The resulting rise time is $4456\,\mathrm{ns}$, equivalent to a factor of about 0.4 for the turn-to-turn voltage (Fig. 3.23). As a result, turn insulation is being stressed, in the worst case, with a voltage drop of $450\,\mathrm{V_{pk}}$, i.e. well below its threshold. At the same time, it is certain that the phase voltage is zero, as all three phases are being supplied at the same time. If discharge activity is detected under these conditions, it is very likely that it is caused by a fault in the main-wall insulation.

Continue, assuming no partial discharge activity has been detected. At this point it is necessary to check the turn insulation. Select the highest possible slew rate and then connect the machine to the test generator in configuration A, starting by evaluating phase U (which will then be the high voltage terminal). Since the rise time will be about $50\,\mathrm{ns}$, it is estimated a factor of about 0.9 for the turn-to-turn voltage. It will therefore be sufficient to apply a voltage of $1241\,\mathrm{V_{pk}}$ to terminal U, which will correspond at the same time to the maximum stress applied to the mainwall insulation, thus remaining below the threshold. On the other hand, the phase-to-phase voltage, for all three phases, will be $1755\,\mathrm{V_{pk}}$: also in this case the maximum stress threshold for phase insulation is far above. Consequently, it is reasonable to conclude that, if discharge activity is detected, this will be due to a fault in the turn insulation along phase U. This procedure should be repeated logically for the other two phases.

Finally, assuming that no faults have been detected so far, it will be necessary to verify the proper functioning of the last remaining insulation system: the phase one. Therefore, the machine must be connected in configuration G to the test generator (assumes to connect phase W to ground), select the lowest possible slew rate and apply a line voltage equal, for example, to the nominal one ($945\,\mathrm{V_{pk}}$), so as to supply a certain current. In this way the phase insulation will heat up on contact with the winding that dissipates heat due to the Joule effect. When a temperature of $100\,^{\circ}\mathrm{C}$ is reached, the voltage is raised to the nominal test value, without taking into account the temperature factor TF in the calculation, i.e. to about $1212\,\mathrm{V_{pk}}$. At the lowest possible slew rate there is a rise time of about $2.4\,\mathrm{\mu s}$ ($WF = 0.45$), equivalent to a voltage drop of $386\,\mathrm{V_{pk}}$ in the worst case. However, it must be taken into account that also the turn insulation is in temperature, so the equivalent stress at room temperature would be $386 \times 1.3 = 501\,\mathrm{V_{pk}}$, however well below the threshold of operation. At the same time, a voltage of about $1713\,\mathrm{V_{pk}}$ is applied to the mainwall insulation. Also in this case, being the machine in temperature, it is reasonable to think in terms of equivalent stress at room temperature: taking into account

<table>
<tr><td>(a)</td><td>(b)</td></tr>
</table>
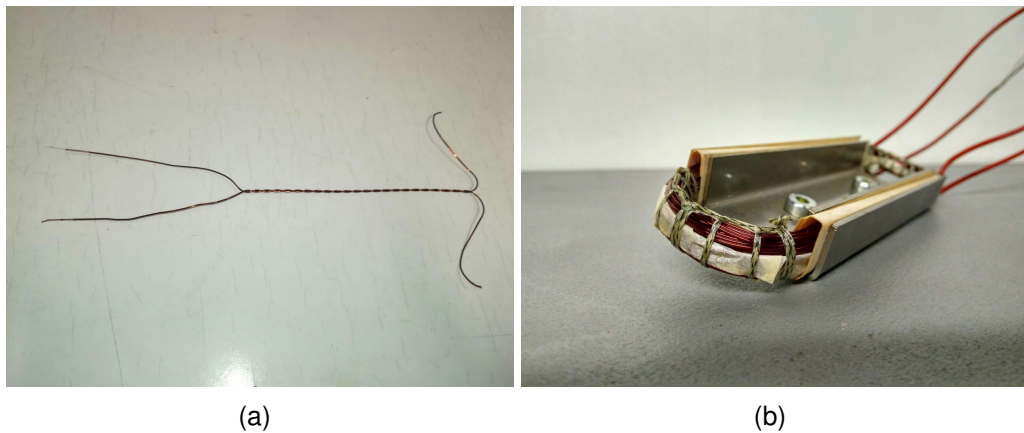
Figure 3.26: Example of (a) twisted pair and (b) motorette.

the corresponding enhancement factor ($TF = 1.1$), a value of $1885\,\mathrm{V_{pk}}$ is obtained, which is well below the maximum applicable voltage. This procedure means that, if no faults have been found so far on the other insulation systems, any detection of discharge activity will be attributable exclusively to a fault in the phase insulation of the W phase. Logically, also in this case, it is necessary, in rotation, to connect the other terminals to ground, repeating the same test procedure to verify the proper functioning of their phase insulation.

3.3 Qualification tests

The qualification consists in performing accelerated thermal ageing tests on at least five samples. The insulation system is suitable if it continues to be PD-free after a number of ageing cycles. This value is determined on the basis of a reference system with characteristics similar to the machine to be qualified.

The samples are simplified models representative of the insulating system investigated and can be of two types (see Fig. 3.26):

- twisted pairs, for testing the turn-to-turn insulation, are two enamelled wires twisted together according to IEC 60172 [21].

- Motorettes/formettes, for testing phase-to-phase and phase-to-ground insulation, are models that shall replicate the design features, including impregnation, creepage distances and clearances. They must be manufactured using the same materials and the same procedures as

Table 3.6: Recommended temperatures (in °C) and ageing sub-cycle exposure periods by standards [16, 17]. T_1 and T_2 are the extremes of the suggested thermal range associated with the given thermal class and referring to the indicated exposure period.

| Thermal class | | | | | | | | | | | | Days per ageing sub-cycle |
| 105 | | 120 | | 130 | | 155 | | 180 | | 200 | | |
T_1	T_2	T_1	T_2	T_1	T_2	T_1	T_2	T_1	T_2	T_1	T_2	
170	180	185	195	195	205	220	230	245	255	265	275	1-2
160	170	175	185	185	195	210	220	235	245	255	265	2-3
150	160	165	175	175	185	200	210	225	235	245	255	4-6
140	150	155	165	165	175	190	200	215	225	235	245	7-10
130	140	145	155	155	165	180	190	205	215	225	235	14-21
120	130	135	145	145	155	170	180	195	205	215	225	28-35
110	120	125	135	135	145	160	170	185	195	205	215	45-60

the original system and must comply with the instructions given in IEC 60034-18-21 [16] (for random-wound winding) or 60034-18-31 [17] (in case of form-wound winding).

The procedure prescribed by the standards begins with a pre-diagnostic test on the samples. A high-frequency voltage of the same intensity as the maximum applicable for PD and voltage tests is applied for 24 hours. This makes it possible to exclude from the outset flawed specimens that could breakdown due to poor manufacturing. In addition, it is useful to perform a preventive PD test, so as to verify that no test specimen is characterized by a $PDIV$ below the limit voltage at the start. This voltage, as seen in the previous section, is determined according to the following parameters: operating temperature, stress category (depending on the characteristics of the inverter and the connection) and type of insulation tested. In this case, since accelerated thermal ageing is carried out, it is not necessary to take into account the ageing factor.

Assuming to know the insulation thermal class (otherwise it is necessary to follow the procedure indicated on IEC 60034-18-21/31 for determining it), it is possible to identify the temperature at which the accelerated thermal ageing cycles are to be carried out, compatibly with the time that is to be allocated for the entire investigation. This is possible by consulting Table 3.6.

Once all the procedure parameters have been decided, it is possible to start the thermal sub-cycles. After each of these, mechanical conditioning will be performed (subjecting the samples to vibrations of a certain intensity, characterized by a frequency of 50 or $60\,\mathrm{Hz}$, for 1 hour) and humidity (48 hours in a climatic chamber). Finally, the voltage and PD diagnostic tests will be conducted, in go/no-go form, directly applying the limit voltage

previously determined.

For diagnostic tests, similarly to what happens in type tests, for the standard it is always possible to use sinusoidal generators, except in cases where the turn insulation is to be tested. In these cases, unless it is possible to intercept the terminals of a single loop, it is necessary to use an impulsive generator (square wave or surge), with rise-time comparable to the real ones in use.

The whole process is concluded when one of the diagnostic tests gives a "no-go" result. At that point, the number of thermal cycles is compared with those withstood by the reference insulation. If the number is equal or higher, the system is suitable for service. Otherwise, the operating temperature must be lowered or the design phase must be repeated. In any case, if the system is not suitable, it is necessary to repeat the qualification procedure with the new specifications.

However, as it is written, the standard does not take into account certain problems, which arise especially in the case of electric motors installed in vehicles (of any kind). Firstly, the characteristics of the pulse generator are important and the type of waveform fed to the test specimen terminals has a non-negligible influence on the outcome of the diagnostic test. Secondly, it should be noted that there is no reference to possible operation at a pressure other than sea-level atmospheric pressure. However, as already seen above, it has a strong impact on the discharge inception phenomenon and therefore it is necessary to take this into account for all those electric motors that must be used at high altitude.

In the following, these two issues will be addressed. The final objective is to provide an integration to the current rule, specific for the vehicle electrical insulation system qualification.

3.3.1 PD test of the turn insulation

Unlike what happens during testing of a real machine, the qualification process passes through a preliminary stage in which motorettes (or formettes, in the case of form-wound motors) are implemented. This means that it is possible to act on the specimen's geometry, instead of on the generator features, in order to verify the turn insulation.

In Chapter 2 it has been demonstrated that neither frequency nor slew rate have a direct influence on the phenomenon of discharge inception. They can only affect the maximum voltage level that can be reached inside the windings. This means that once this level has been determined - or rather estimated - for all three insulation systems, it would be sufficient to
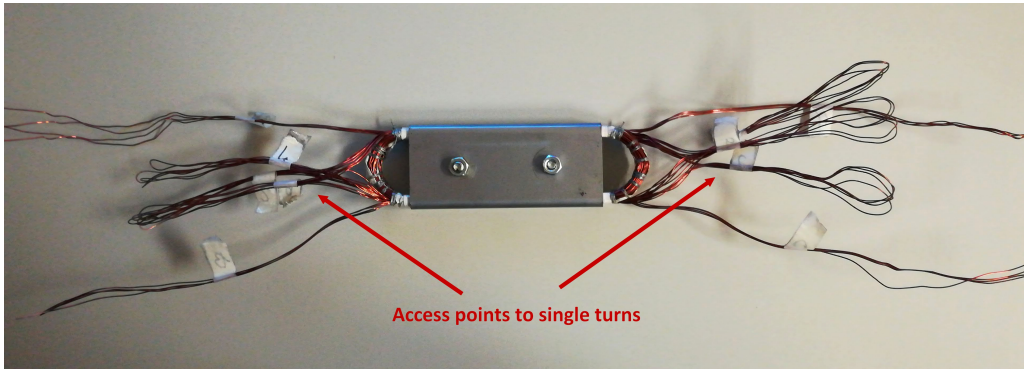
Figure 3.27: Photo of a motorette with the accesses to the single turns. In particular, it is possible to directly access the coils number 1, 2, 6, 9 and 15, in a winding formed by 20 turns of wire.

test them with a traditional $50\,\mathrm{Hz}$ AC transformer, if possible. This would save the various difficulties of performing accurate $PDIV$ tests by using an impulse generator with characteristics similar to those of the converter that is expected to match the machine. On the other hand, it has been demonstrated that it is not necessary to have to recreate the same type of waveform to which the insulation being tested is subjected. The only really important electrical parameter in this sense, in fact, seems to be the voltage polarity.

As a result, it is sufficient to modify the motorettes in such a way as to have access, at least, to the first turns, as shown in the photo in Fig. 3.27. In this way it is possible to connect to the single turns and test the insulation between consecutive turns in AC mode, connecting one to the high voltage and the other to the ground, as shown in the diagram in Fig. 3.28. The same thing, probably even more easily, can be achieved on a formettte.

3.3.2 Simulate high altitude conditions on the ground

As highlighted in the previous section, altitude plays a remarkable role in the partial discharge inception and, therefore, this factor should be taken into account in the qualification procedure.

It should be noted that a certain degree of vacuum could affect the degradation mechanisms of the insulating material, especially if combined with high temperature values and humidity concentrations. In addition, the presence of a negative pressure gradient allows any volatile substances to spread outward from the bulk region of the insulation systems. This combination of factors could lead to the partial discharge inception at
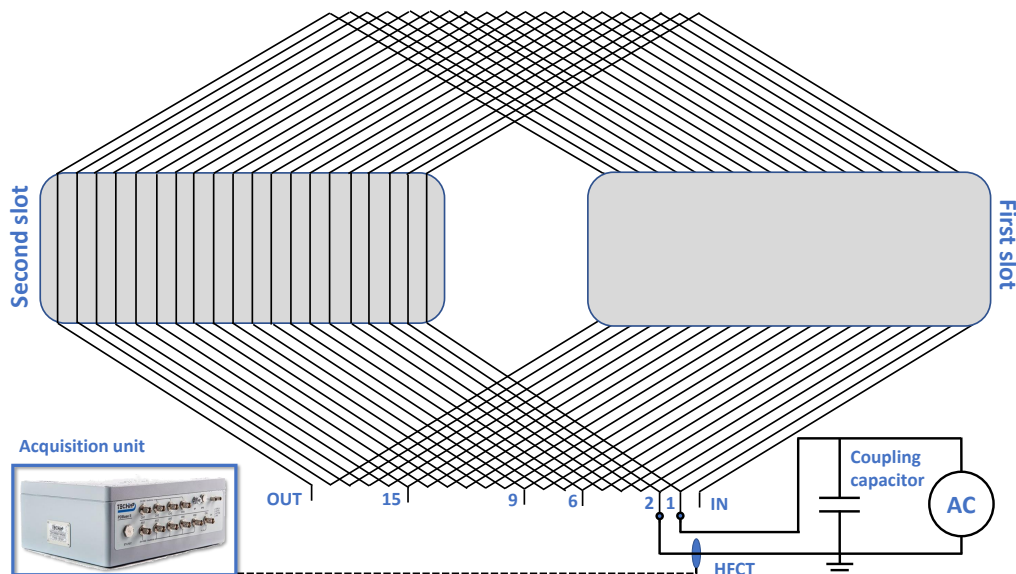
Figure 3.28: Example connection configuration to test in AC the turn insulation (coils 1-2) of a motorette.

high altitudes, and thus to a rapid failure of the machine, earlier than the expected time if it is not properly taken into account.

In the light of these observations, the qualification procedure should be improved to take into account the high quota effect on the system during its service life. Firstly, the ageing cycle should be modified in some way. In this respect, there are two possibilities:

- concurrent test, namely a low-pressure accelerated thermal ageing cycles could be performed; in other words, accelerated thermal ageing should be performed in a vacuum chamber to simulate high altitude conditions.

- sequential test, consisting of a further sub-cycle of a few days; in this case the system would be subjected to a certain temperature, below the class temperature (so as not to interfere with accelerated thermal ageing), and at the same time kept at low pressure. This sub-cycle should be placed before conditioning in the climatic chamber, so as to simulate the worst case (because in depression the insulating material tends to expel more easily the moisture absorbed).

The first approach has the advantage of not further lengthening the total time of the entire qualification process, since it simply acts on the

parameters of a sub-cycle. On the other hand, since thermal ageing sub-cycle can last several days, it may be expensive enough to set up a system to maintain an average vacuum for an extended period of time in a chamber containing air at a temperature above $150\,°C$. The second approach is less demanding for the vacuum system, but extends the ageing cycle time by a few days each.

The PD test should also be modified to take account of high altitude conditions. In this situation, too, there are two possibilities: either tests are carried out in a vacuum chamber to simulate high altitude pressure conditions, or the threshold voltage is increased using an enhancement factor that takes into account the level of depression (as suggested in the previous section). In one case the approach is more realistic, but also more expensive and time-consuming. In this respect, it should be remembered that low pressure makes it necessary to adopt longer waiting times between one voltage step and the next during PD tests (see Table 2.10). With the second approach, there is a simpler and faster technique to perform, but also less precise.

On the other hand, there is a spontaneous question about this issue, i.e. whether the behaviour of the $PDIV$ in relation to all the parameters taken into consideration, recorded and estimated for twisted pairs, is similar, if not equal, to that of windings in real electrical machines. This doubt is quite reasonable when one considers that the latter are equipped with additional insulation layers (phase separators and slot liners) and are impregnated. To ensure that the behaviour is similar, it is necessary to carry out tests on sample types other than twisted pairs, but made with the same enamelled wire.

In the laboratory, a comparison was made between the decrease in $PDIV$ in twisted pairs and that measured in motorettes made with the same wire, as a function of pressure. The tests were carried out with a sinusoidal voltage generator at $50\,Hz$ and a high-frequency current transformer connected to the TechImp acquisition system was used to detect the PDs. The circuit diagram is very similar to the one shown above in Fig. 2.25. Five samples were tested for each combination of conditions.

Fig. 3.29 shows the comparison of the data obtained (10th percentile) at 100 and $1013\,mbar$. The term 'P/P' indicates the PD tests performed on the phase insulation, connecting one of the two coils to high voltage and the other to ground. 'P/G' indicates the tests carried out on the mainwall insulation and the following number establishes which of the two coils has been connected to the high voltage. Finally, 'TP' indicates the measurements on the twisted pairs. It can be observed that for all four cases taken into consideration there is a substantially equal decrease in the value of the
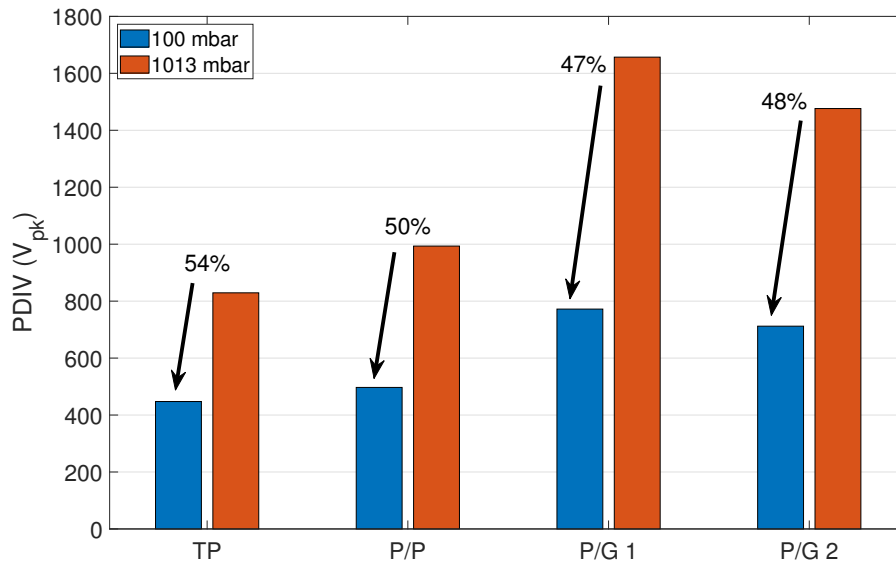
Figure 3.29: Effect of pressure on $PDIV$ values (each point represents the 10th percentile of the $PDIV$ distribution measured on 10 samples) for TPs and motorettes.

$PDIV$ as a function of pressure, demonstrating once again the validity of carrying out tests on simplified systems such as the twisted pairs.

3.4 Discharge: a tool for faster qualification

In light of recent innovations in power electronics and the increasing voltages and service temperatures of motors, the insulation of a motor or electric actuator must be designed with great care, taking into account the $PDIV$ of the system, rather than its dielectric strength. Unfortunately, this quantity depends not only on the material, but also on the geometry, and it is standard practice, when qualifying a new machine, to refer to an existing reference system for a first-attempt estimate. Then, through the qualification process and a trial-and-error repetition, a more precise value is attained.

To improve this approach and at least make it faster, it is possible to make use of the model already introduced in Chapter 2. Note that the insulation between the turns of the same phase is only stressed during voltage transients. This means that the voltage distribution along the
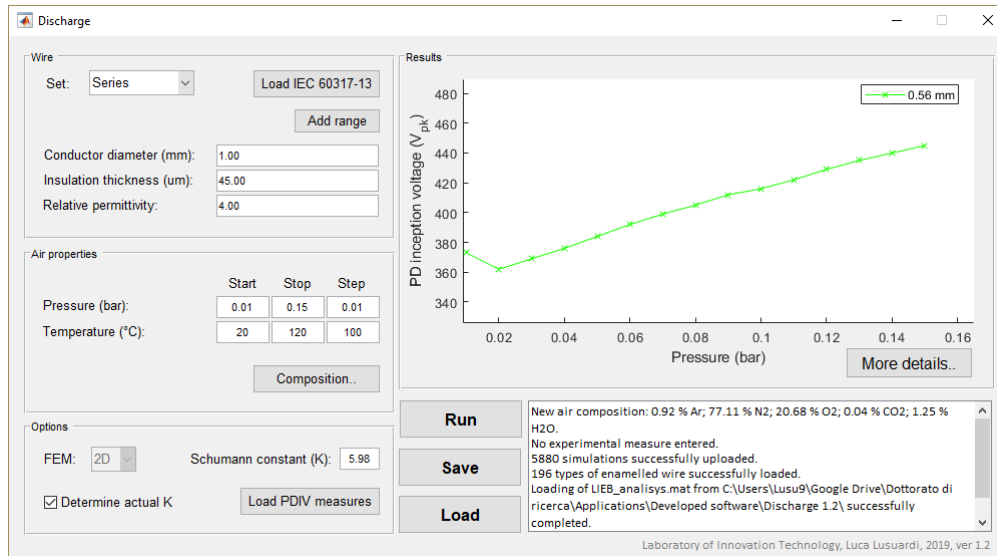
Figure 3.30: Main interface of Discharge.

windings must be evaluated separately to determine the maximum voltage drop between two consecutive turns. Furthermore, as far as the analysis of the spiral insulation is concerned, there is no need to worry about a possible polarity effect. With reference to 3.2, it can be noted that each voltage peak is always followed by a subsequent voltage peak of lower intensity and inverted polarity. This ensures that there is no effect on the $PDIV$ of space charge build-up.

If the initial insulation thickness is not sufficient to guarantee the absence of partial discharges, the degree of insulation chosen can be increased or the wire diameter enlarged. Clearly, in both cases the geometry inside the stator slot and the fill factor would be modified. Consequently, the machine should be redesigned, taking into account the new wire parameters, and the procedure repeated, until the solution that guarantees the absence of discharge activity is found.

In this regard, a complete software has been developed to facilitate the qualification process of the insulation of random-wound electric motors for the transport sector: it was called 'Discharge'. This software studies the worst case scenario where there is only air between two wires to which a potential difference is applied, simulating a *de facto* impregnation problem. It has been used within the European research project Horizon 2020 'RAISE' (Reliable Aircraft electrical Insulation System sElection) during the qualification process of an actuator for the aircraft field, proving its effectiveness. Fig. 3.30 shows the main interface of Discharge.
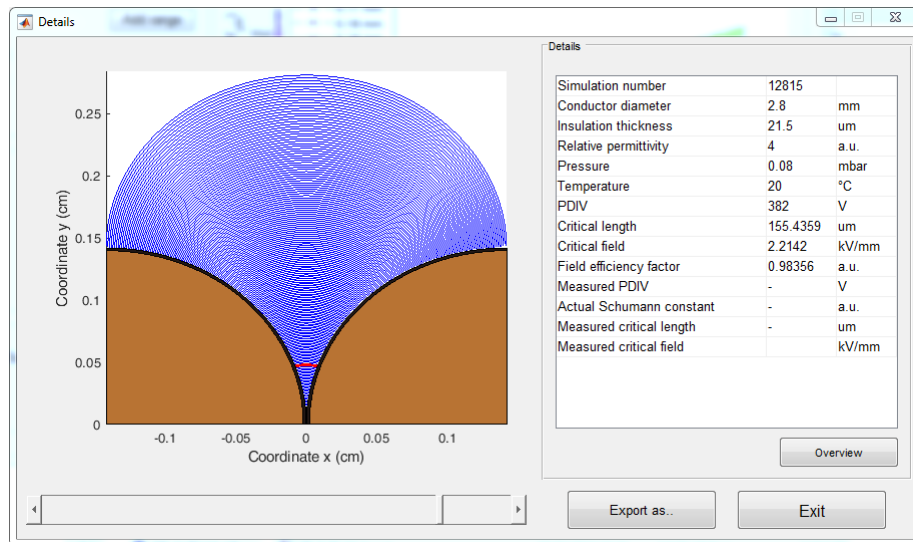
Figure 3.31: By clicking on *Simulations*, the distribution of the electric field in the air surrounding the two wires and the precise position of the discharge line can be displayed.

Discharge allows the calculation of the partial discharges inception voltage ($PDIV$) according to different parameters:

- conductor diameter;

- thickness and relative permittivity of insulation;

- ambient pressure and temperature;

- molecular composition of the surrounding air.

Within Discharge, it is possible to directly select the wires with the characteristics specified by the IEC 60317-13 standard, simply indicating the desired insulation grade. It should be noted that the insulation thickness considered in Discharge takes into account the worst case, that is the one in which its value is minimal according to the standard IEC 60317-13 (which establishes a tolerance range) [24]. The software in post-processing phase also allows to visualize a wide range of useful quantities for the sizing of the machine under examination, such as the critical average electric field, the minimum length of the discharge lines, etc..

Discharge was developed with MATLAB®2018a, according to the model depicted in Chapter 2, and makes use of two external applications, if necessary:
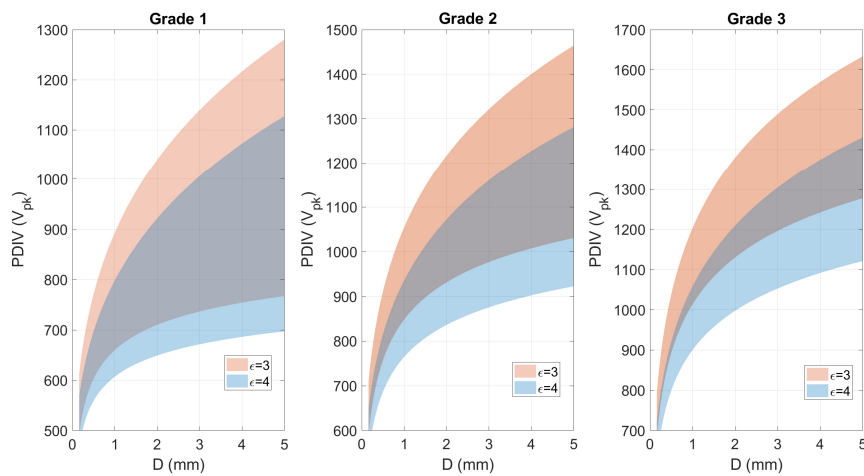
Figure 3.32: Peak-to-peak $PDIV$ ranges for the wires defined in the IEC 60317-0-1 in standard conditions ($20\,^{\circ}\mathrm{C}$ and $1\,\mathrm{bar}$).

- COMSOL Multiphysics®5.1, which is essential for determining the distribution of the electric field in the surrounding air, when selected wires are not already present in the database;

- BOLSIG-, which is essential to take into account the effect of the molecular composition of the air (when this is not dry) on the phenomena of partial discharges inception in the vicinity of the insulation.

It is also possible to directly display the discharge line at the inception voltage (see Fig. 3.31), which can be useful for assessing the importance of the role played by impregnation. Finally, it can be very useful to carry out a wide comparative analysis and to investigate more deeply the possible scenarios, thanks to the wide range of parameters that can be combined.

Using Discharge it was possible to draw the graphs shown in Fig. 3.32, which show the trend of the $PDIV$ as a function of the conductor diameter chosen for the wires, taking into account the desired degree of insulation, ambient conditions and air composition.

Therefore, having defined the characteristics of the chosen wire (diameter of the conductor and degree of insulation), from these graphs it is possible to determine the maximum permitted voltage drop between two consecutive turns. From this quantity, using the equation 3.4, the maximum line voltage of U_{max} can be determined. If it is not possible to estimate *a priori* the voltage waveform characteristics with which the machine is to be powered, the following estimates for jump factors can be used, based on
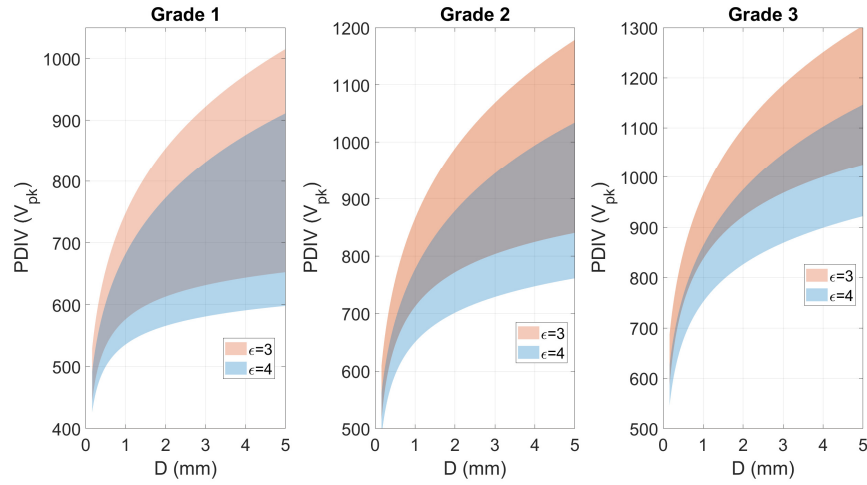
Figure 3.33: Peak-to-peak $PDIV$ ranges for the wires defined in the IEC 60317-0-1 at an altitude of $3\,\mathrm{km}$ ($20\,°\mathrm{C}$ and $0.65\,\mathrm{bar}$).

the inverter characteristics:

$$a = \begin{cases} [0.4, 0.7], & \text{IGBT-based} \\ ]0.7, 0.9], & \text{SiC/GaN-based} \end{cases} \qquad (3.28)$$

Note that U_{max} refers to the room temperature. To take into account the impact of the temperature on the discharge inception phenomena, this value must be multiplied by a reduction coefficient that depends on the service temperature for the windings (which, except in special cases, corresponds to the insulation thermal class):

$$U_{max}(T) = U_{max}(20\,°\mathrm{C}) \cdot \frac{293.15}{273.15 + T[°\mathrm{C}]} \qquad (3.29)$$

It should be noted that, if the insulation of the wires meets this criterion, it will be all the more so if it meets the constraint on dielectric strength. This is because the partial discharge inception critical electric field is always much lower than the insulation material breakdown field.

This approach remains valid even when a high altitude operation is anticipated. Fig. 3.33 shows the same graph as Fig. 3.32, but considering a different pressure value (equivalent to $3000\,\mathrm{m}$).

As an example, consider a machine with a nominal DC bus voltage of $500\,\mathrm{V}$ combined with a two-stage SiC-based inverter and assume to have an overshoot factor of 150 % in the worst case. Let's consider the possibility of implementing a grade 2 wire of $0.4\,\mathrm{mm}$ conductor diameter, thermal class

155 and relative enamel permittivity of 3. The graph in Fig. 3.32 shows a $PDIV$ of about $725\,\mathrm{V_{pk-pk}}$ in the worst case (i.e., minimum insulation thickness) in standard conditions. Assuming a jump factor of 0.8, this value therefore corresponds to a DC bus line voltage of approximately $855\,\mathrm{V}$, without considering either service temperature or ageing. Assuming the machine is operated at its class temperature (see Eq. 3.9), a maximum DC bus voltage of $488\,\mathrm{V}$ is obtained, which is lower than the proposed voltage.

At this point there are several possibilities to get around the problem: the most drastic is to choose the same wire but with a higher degree of insulation. Perhaps a more elegant solution is to adopt a wire with a lower relative enamel permittivity. Another option is to use a 3-level inverter, instead of a 2-level one, to halve the maximum voltage drop that can occur in two consecutive turns of the same phase. Again by acting on the motor-inverter system, the connection between the two can be improved to reduce the overshoot factor. Finally, a further possibility is to lower the operating temperature of the motor: note that a decrease of only $5\,^{\circ}\mathrm{C}$ is enough for the maximum admissible DC bus voltage to become $510\,\mathrm{V}$, higher than the desired one.

4

Evaluation of insulation ageing in vehicle and aircraft actuators

This chapter explores the the insulating system lifetime of low-voltage electrical motors and tries to understand how much one can stress the machine before it fails. Therefore, first of all, the reader becomes familiar with the main ageing factors affecting an inverter-fed low-voltage electric machine. On the basis of these notions, a study investigating the insulating system lifetime of an electric motor subject to the typical operating conditions of vehicles is first illustrated. Later on, the chapter presents the reader with an in-depth analysis of partial discharge impact on the insulating material ageing of low-voltage electrical machines, highlighting in particular the influence of the altitude and inverter's switching frequency, and trying to quantify the loss of life resulting from the phenomenon inception.

4.1   Introduction to the 'TEAM' stresses

There are many different stresses that can effect the deterioration rate in stator windings. In general, there are thermal, electrical, ambient and mechanical stresses, the so-called TEAM stresses [26].

They can be constant or variable over time. For example, the effect of the operating temperature, the operating voltage at 50 or $60\,\mathrm{Hz}$, or the mechanical vibrations caused by a rotor in stationary operation are constant. Transient stresses can be unpredictable in both duration and intensity. Consequently, in general terms, the time to failure in these cases is propor-

tional to the number of transients the machine suffers. However, in certain situations (such as lightning strikes), a single incident can be fatal.

The thermal stress is certainly the most popular, because it causes the gradual and irreversible deterioration of the insulation, until it leads to failure, at least in air-cooled machines. The Arrhenius model is a first-order approximation of the oxidative reactions that take place as a result of the high temperature:

$$L(T) = L_0 e^{-\frac{B}{T}} \tag{4.1}$$

with $B = \Delta W / k_B$, where L_0 is a constant, T is the absolute temperature, ΔW is the dominating reaction activation energy and k_B is the Boltzmann's constant.

Being a very simple and practical model, it has been rightly adopted in the standards as a tool for diagnostics and qualification of the insulations. However, it is not very precise, since very often the chemical reactions are multiple, and each characterized by a different activation temperature. Consequently, for more accurate estimates of the service life of a certain insulating system, an *ad hoc* study is always convenient.

Another type of stress often encountered is electrical stress. The latter is usually divided into two categories: intrinsic and extrinsic [94]. The first category indicates the ageing effect due to the pure application of an intense alternating electric field inside the insulation. Here, various causes contribute to the material deterioration, such as the heat production corresponding to dielectric losses or mechanical fatigue caused by the cyclical variation of electrostatic forces. Extrinsic electrical stress, on the other hand, means the inception of partial discharge activity that have the capacity to deteriorate the insulating material. Both in one case and in the other, there are two options for the life pattern:

- the inverse power model

$$L\left(\frac{E}{E_0}\right) = C\left(\frac{E}{E_0}\right)^{-n} \tag{4.2}$$

- the exponential model

$$L\left(\frac{E}{E_0}\right) = L_0 e^{-h\frac{E}{E_0}} \tag{4.3}$$

where L_0 is the lifetime for $E/E_0 = 0$ and C, h and n are empirical constants. It is common practice to express Eqs. 4.2 and 4.3 in logarithmic terms in order to facilitate the process of extrapolation after experiments. It should also be noted that the coefficient n (or h) clearly measures the system's resistance over time and can therefore be defined as the resistance coefficient.

Eq. 4.2 is usually used when PD is present (usually n has a value between 9 and 12 for medium and high voltage rotating machines), while Eq. 4.3 is used when n varies its value with the electric field strength or it is necessary to estimate the effect of intrinsic electric stress.

It should be remembered that the partial discharge initiation inside low-voltage machines is so damaging and rapidly deteriorates the insulating material that they are not considered a stress factor, but rather a type of failure. However, it also should be noted that the pulses generated by SiC-based or GaN-based converters are so short that partial discharge inception is not guaranteed within the machines (see Chapter 2), although the electrical field conditions can be met (due to the initial electron absence). This means that their effect could potentially be studied on the basis of one of the two life models mentioned above.

It is also worth mentioning that, even in the absence of PD, some have suggested the possibility of injecting the space charge into the insulation of low-voltage machines, always as a result of surges generated by converters. This phenomenon would consist in the emission, at each pulse, of electrons in correspondence of the surface imperfections of the insulating enamel towards the conductor. The repetitiveness of this process would cause, in the long run, the rupture of a sufficient number of chemical bonds between the polymer chains, finally leading to the perforation of the insulation and then the failure [9, 94, 101].

Turning to environmental factors, this term indicates a wide category of stress sources due to the external agents that surround any electrical machine. They include:

- the humidity of the air that condenses on the exposed surfaces and penetrates the first layers of insulating material;

- oil contamination from neighbouring bearings;

- aggressive chemicals, such as polluting or industrial emissions;

- abrasive particles, residual dust from machining, dirty depositions, etc..

Each of these may not pose a real threat to the electric machine if taken individually. However, a combination of these can be a real stress factor. Think, for example, of the effect that the deposition of a layer of oil mixed with moisture could have on an impregnated area in which there are traces of metal dust: in the hypothesis of a sufficiently intense electric field, the formation of such a conductive layer would be responsible for the generation of surface currents and, consequently, electrical tracking phenomena, which are decidedly dangerous for the proper motor functioning.

Mechanical vibrations are the last important type of stress source for the electric motor insulation. They are mostly produced by currents that oscillate at the main power frequency, which generate a magnetic force oscillating at twice that frequency. By indicating with f the radial force per unit length acting at the most peripheral part of the windings, it is possible to write [94]:

$$f = c\frac{I^2}{d} \tag{4.4}$$

where $I = n \cdot I_0$ is the rms current through a phase, being I_0 the rms coil current and n the number of turns in the coil; d is the width of the stator slot and c is a constant equal to $960\,\mathrm{N\,A^{-2}}$.

If the winding is not well tightened and in some points the wires are able to move, the force expressed by Eq. 4.4 makes these traits vibrate. As a result, the localized abrasion of the enamel will occur until it is completely removed.

Unlike thermal and electrical stresses, there are no universally accepted life models for the stress exerted by possible mechanical vibrations. Although there are attempts at formulation that relate the service life of an electric motor insulating system with the maximum amount of vibration exerted, they are not feasible from a practical point of view [4]. Nevertheless, the IEC 60505 standard indicates the inverse power model as the first empirical approach for estimating the service life of an insulation system as a function of the maximum mechanical stress M [26]:

$$L \propto M^{-m} \tag{4.5}$$

where m is the life line exponent.

At present, as already described in Chapter 3, the standard requires accelerated ageing tests to be carried out by subjecting the samples to mechanical vibrations of a pre-established intensity for one hour, on each cycle. The total life measured is then compared with that of a reference system. This circumvents the need to identify the precise life pattern for that particular insulation, being satisfied with the assurance that the machine will withstand for the desired service life.
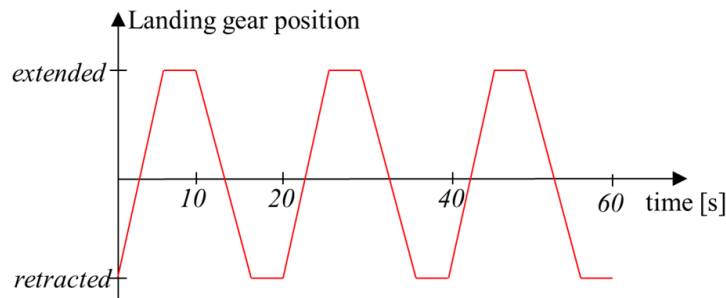
Figure 4.1: An example of electric motor actuator mission profile (source: [62]).

However, it should be noted that there have been attempts to model the effect of mechanical stresses, not specifically used for electric motors. These treatments typically make use of the exponential threshold model [72].

4.2 Thermal overload in short duty-cycle motors

As a rule, when assessing the service life that can be guaranteed for a certain insulation system, the Montsinger's rule is first used (which derives substantially from the application of the Arrhenius model, Eq. 4.1). Assuming that the only ageing mechanism of the insulation material is that due to oxidation reactions activated by high temperature, the Montsinger's rule estimates that the useful life of a material doubles each time the temperature decreases by $10\,°\mathrm{C}$ compared to the reference temperature [73, 68, 91].

This approach, however, has two limitations: first, it is not at all certain that the temperature jump, for life to double, is really equal to 10 (Montsinger at the time indicated this number more for convenience than for precise adherence to experimental data). In reality, the higher the temperature, the more the jump tends to narrow, and it is also for this reason that, very often, after a first rough estimate, accelerated thermal ageing tests are carried out, to verify the actual reliability of the system. Furthermore, it should be noted that the Montinsger's rule is valid as long as quasi-stationary situations are taken into consideration. In this regard, there are several examples in the literature where the Arrhenius law, in combination with the Miner's rule, is applied for the damage accumulation caused by regimes at different temperatures, but these are all cases where transitions from one
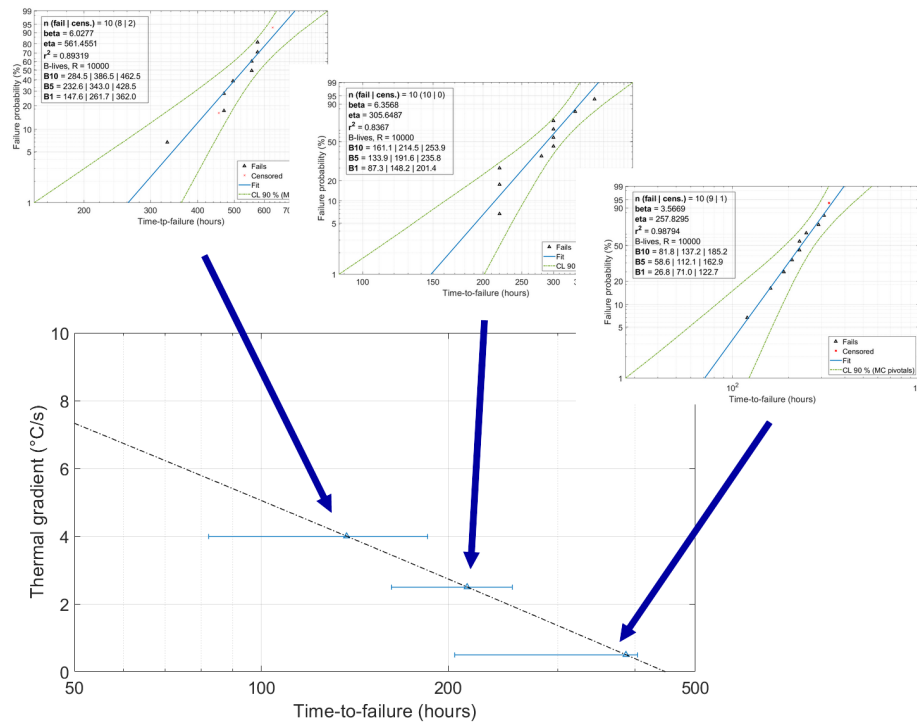
Figure 4.2: Weibull plots and life line derivation as a function of thermal gradient.

temperature to another take a considerable time (hours) to occur.

The electric motors that will be installed in the transport sector in the future will serve as actuators (for aircraft) or traction (for cars), which means that they will work often, dynamically and under often unfavourable environmental conditions. Fig. 4.1 shows, for example, the typical load curve of a motor that must operate the landing gear of a helicopter. In view of this, it is essential to understand whether the service life estimation of electric motors should take these new factors into account and whether insulation systems can continue to be qualified by subjecting specimens to accelerated thermal ageing at a constant temperature.

The life lines can be drawn generally by points, testing a certain number of samples, or rather a certain number of groups of samples, as each of them will behave differently and therefore there will be a certain statistical dispersion of the results. In this regard, experience and time have taught that the most functional statistical model for the evaluation of this type of test (i.e. life tests) is the Weibull distribution (see Appendix C) [91].

In any case, for the drawing of life lines, the necessary points must be no less than three, obtained by means of tests with higher stresses than those expected during operation and, therefore, with shorter failure times.

Table 4.1: Wire characteristics.

Parameter	Value
Copper core diameter	$0.4\,\mathrm{mm}$
Insulation grade	2
Minimum insulation thickness	$20\,\mathrm{\mu m}$
Insulation basecoat	Polyesterimide
Insulation overcoat	Polyamide-imide

Table 4.2: Coil specimen features.

Parameter	Value
Thermal class	200
Number of turns	20
Strand in parallel	2
Average turn length	$250\,\mathrm{mm}$

This is why they are called accelerated ageing tests. Once the results of these experiments have been attained, in order to get the behaviour at a longer time, it is necessary to extrapolate the line obtained, knowing the underlying life model that binds the stress S and the useful life L. An example is shown in Fig. 4.2.

Accelerated tests are widely adopted for estimating life of electric motors [94, 18]. However, for practical reasons, accelerated lifetime tests are generally performed on motorettes representative of the original electric motor stator insulation system. In laboratory, in a first preliminary study, it has been decided to adopt random wound coils specimens, more similar to the geometry configuration of the windings in the slots, but simpler and cheaper than motorettes.

On the other hand, it is necessary to get as close as possible to the theoretical case in which the temperature of the wires follows exactly a sawtooth load (therefore characterized by a single value of thermal gradient that is reversed at the middle of the cycle), in order to be able to better verify a possible numerical modelling and to better understand the phenomena involved. The presence of a metallic element would introduce a thermal inertia that would make it difficult to achieve this goal. The chosen specimens are coils made of a class 200 round magnet wire (see Table 4.1). The main features of the specimens are listed in Table 4.2. The coils were hung on a PTFE rod and inserted into a fume hood with variable air flow rate (see Fig. 4.3). The two strands were joined together with Kapton® adhesive tape
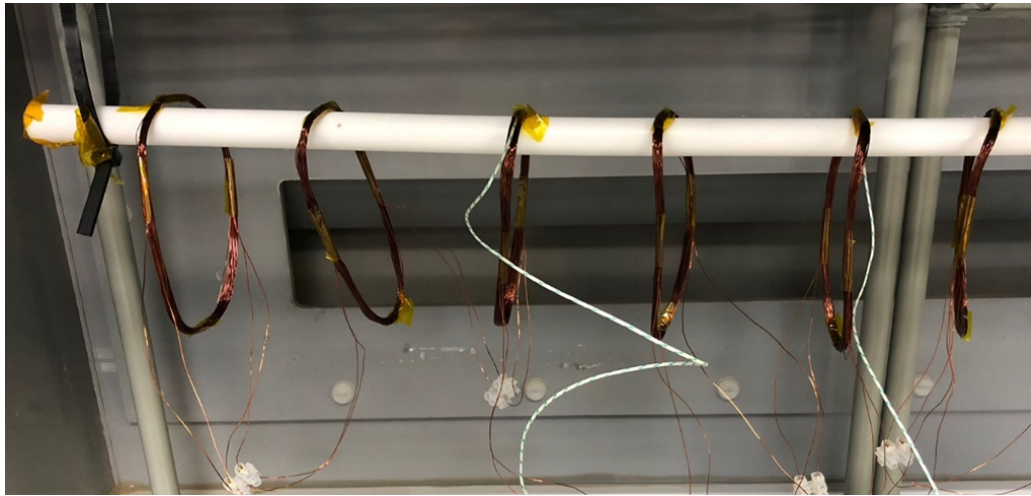
Figure 4.3: Coils hung to a PTFE rod inside the fume hood.

(thermal class 220) to ensure their contact during voltage testing.

Since the effect of the thermal slew rate (i.e. thermal gradient) is meant to be investigated, it was decided to carry out a matrix of tests in which the applied temperature profile ranged from $200\,°\mathrm{C}$ to a reference temperature, at three different thermal gradients each: $0.5\,°\mathrm{C/s}$, $2.5\,°\mathrm{C/s}$ and $4\,°\mathrm{C/s}$. Three reference temperatures were then chosen, so as to have nine accelerated thermal ageing tests in total to perform: $260\,°\mathrm{C}$, $275\,°\mathrm{C}$ and $290\,°\mathrm{C}$. Fig. 4.4 gives, as an example, the actual temperature trend for the cases at $260\,°\mathrm{C}$.

The insulation of the specimens has been assessed by monitoring the degradation rate of an electrical property via a non-destructive test, in accordance with IEC 60216-1 [22].

Therefore, every 20 hours, the samples were disconnected from the DC power supply, restored to room temperature by means of uncontrolled air cooling and the partial discharge inception voltage ($PDIV$) test is performed on each of them. Completed the $PDIV$ measurement, the samples are then reconnected to the ageing test bench and a new thermal cycle is run. The $PDIV$ was considered the most appropriate property to monitor, according to IEC 60034-18-41 [18]. The simplified scheme of the ageing test bench is depicted in Fig. 4.5. To heat the samples so as to ensure that they follow the desired temperature profile, the Joule loss resulting from the current flowing within the wire is exploited.

The current is controlled via a programmable DC power supply. Through four K-type thermocouples in intimate contact with the wires of four different samples, the temperature trend is monitored. The acquired temperatures
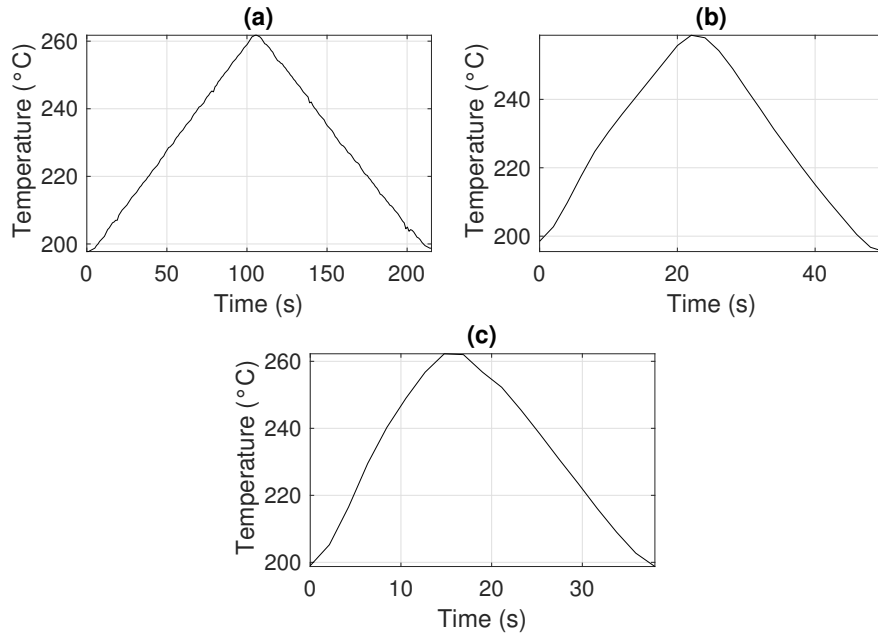
Figure 4.4: Temperature profiles (reference maximum temperature of $260\,°C$) for (a) $0.5\,°C/s$, (b) $2.5\,°C/s$ and (c) $4.0\,°C/s$.
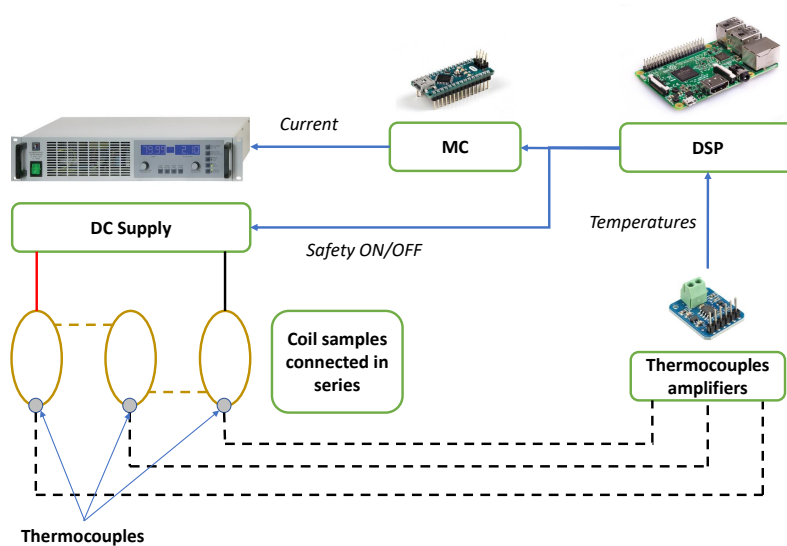
Figure 4.5: Circuit scheme for accelerated non-stationary thermal ageing of coils.
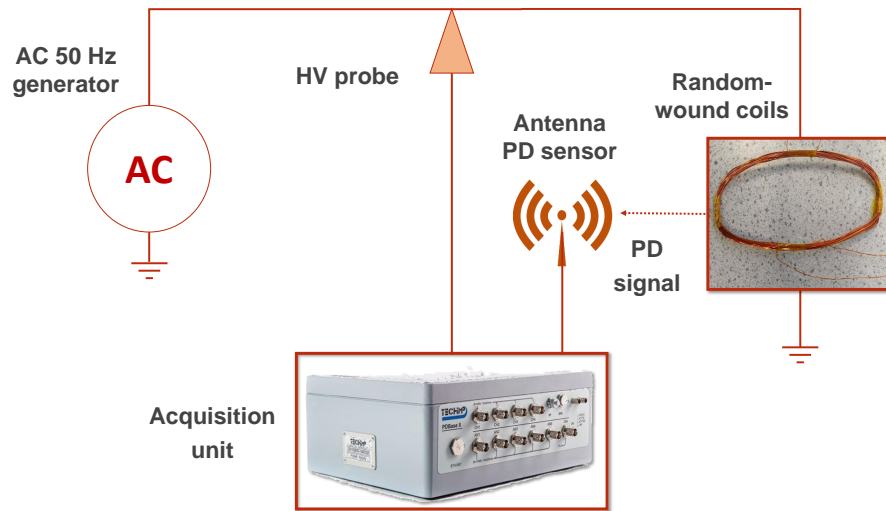
Figure 4.6: Diagram of $PDIV$ test to carry out during accelerated non-stationary thermal ageing tests.

Table 4.3: Working conditions assumed for the insulation system.

Parameter	Data
Maximum DC link voltage	$540\,\text{V}$
Insulation Thermal Class	$200\,\text{°C}$
Overvoltage Stress category	C
Average rise time	$200\,\text{ns}$

are elaborated by a digital signal processor (DSP). At the same time, the current is effectively modulated by a microcontroller (MC) connected to the DSP in order to keep the thermal slew rate ($d\theta/dt$) constant throughout the test campaign.

Fig. 4.6 shows the circuit used for the PD tests. These measures were carried out by applying an initial voltage of $25\,\text{V}$ and increasing by $25\,\text{V}$ every $10\,\text{s}$. As soon as the acquisition unit (TechImp PDbaseII®) detected the presence of PD via the antenna, the power was turned off and the detected $PDIV$ was recorded.

The end-of-life criterion was considered to be the time when a tested specimen is characterized by a $PDIV$ below a certain threshold. To determine the latter value, without losing any generality, some assumptions were made about the possible characteristics of the electric drive components (i.e. electric motor, power converter, connecting cables, etc..). They are summarized in Table 4.3.

Referring once again to IEC 60034-18-41, the limit voltage (i.e. $PDIV_{min}$)
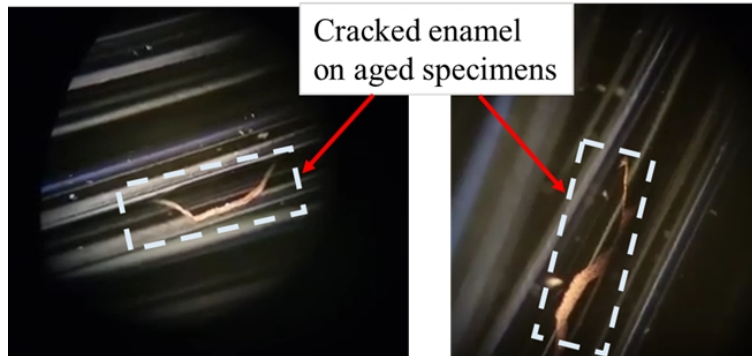
Figure 4.7: Optical microscope analysis of thermally aged specimen.

Table 4.4: Summary of the time-to-failure (TTF) and cycles-to-failure (CTF) values for the several accelerated non-stationary thermal ageing tests.

Thermal gradient $°C\,s^{-1}$	Maximum temperature $°C$	Cycles to failure (B10) a.u.	Time to failure (B10) h	Time to failure (average) h
0.5	260	6293	386.5	525.0
2.5	260	15813	214.5	300.0
4.0	260	13181	137.2	228.6
0.5	275	1701	122	318.5
2.5	275	6070	88.7	209.8
4.0	275	2087	26	40.4
0.5	290	301	29.5	50.0
2.5	290	1444	33.9	53.6
4.0	290	1344	18.6	28.3

was determined according to Eq. 3.5:

$$PDIV_{min} = WF \times OF \times EF \times V_{DC} = 436 \quad \text{V}_{\text{rms}} \tag{4.6}$$

where WF is the winding factor (equal to 0.7 for the turn-to-turn insulation), OF is the overshooting factor (corresponding to 2 for stress category C), EF is the enhancement factor depending on thermal class and grounding (equal to 1.63 following the data listed in Table 4.3) and V_{DC} the DC-bus voltage. However, in certain cases, cracks in the enamel coating were noted at the end of cycle, as proven by the enlargement in Fig. 4.7.

For each test cycle, as indicated by IEC 60216-1, the mean value of the $PDIV$ has been calculated. On the other hand, since in the automotive sector, and even more so in the aerospace one, the risk of failure is expected

to be very low (i.e. safety-critical applications requires modest probability of failure), it was also considered appropriate to extract the 10th percentile, i.e. the time to wait because statistically 10% of the test specimens compared to the initial population fails. The result of the tests is depict in detail in Table 4.4.

Looking at Fig. 4.8, it is possible to conclude that the service life of the test specimens is drastically reduced as the thermal slew rate increases. In particular, at best, the service life is reduced by more 50 %, when the results regarding the temperature profile featuring $4\,°\mathrm{C}\,\mathrm{s}^{-1}$ are compared to those related to $0.5\,°\mathrm{C}\,\mathrm{s}^{-1}$. Despite what has been typically done so far, for relatively short cycle times the outcome of the unconventional tests proved that considering the only average value of the temperature profile is not sufficient. Indeed, it is also necessary to take into account the effect of thermal transients (i.e., the temperature profile gradients).

Fig. 4.9 shows the development of the $PDIV$ over time for the three different thermal slew rates with the maximum temperature of $260\,°\mathrm{C}$. Looking at the plots, the trend of the two $PDIV$ curves (i.e., average and B10) is almost identical as expected. In any case, it should be noted that there is a difference of almost 50 % between the values, considering the same experimental point.

Until now, standards and literature have always considered cases of insulating systems ageing with very slow thermal transients (i.e., high voltage cables for electrical distribution or large rotating machines) [30, 68, 22]. In this cases, when the thermal ageing is analysed, only the temperature effect is considered, since other effects (e.g. thermal slew rate) are overlaid by the one of the operating temperature at steady-state. Further, in some circumstances, even an average temperature calculated over the entire service life is directly used.

Due to the inherent nature of the transportation applications, the employed low-voltage motors will be exposed to frequent thermal transients. Therefore, it is no longer sufficient to consider accelerated thermal ageing tests carried out at a constant temperature. In particular, the experimental data has been demonstrated the key role played by the speed of temperature variation (i.e. thermal gradient) on the service life of the motor insulation and how significant is its impact.

The drastic service life shortening might be explained by referring to the polyamide-imide (so-called PAI) fatigue and tensile curves as a function of the temperature, which are reported in Figs. 4.10 and 4.11 for sake of completeness. The PAI is often utilized for overcoating enamel wires that already feature a polyesterimide (PEI) basecoat. In fact, the PAI topcoat improves the magnet wire properties by ensuring a better abrasion
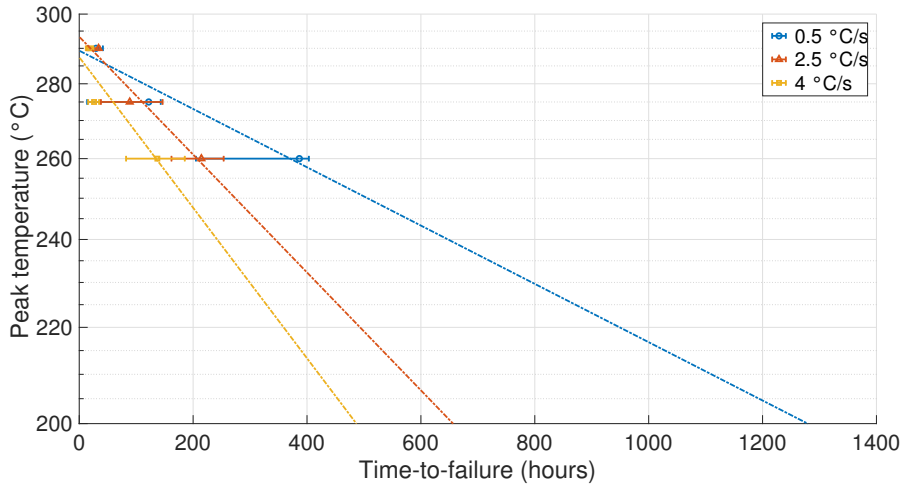
(a)
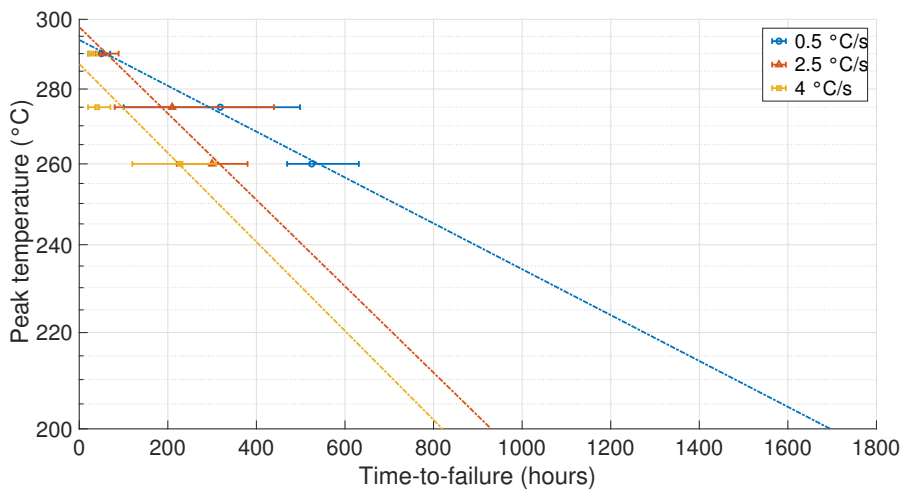
(b)

Figure 4.8: Thermal ageing curves for the three different thermal gradients. Each point represents (a) the 10th percentile and (b) the average value of the TTF distribution measured on 10 samples. End of life is set when $PDIV$ drops below $436\,\mathrm{V_{rms}}$.
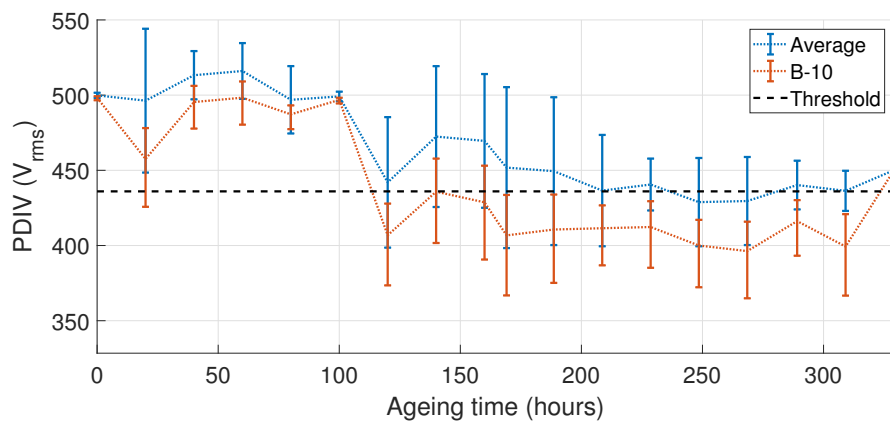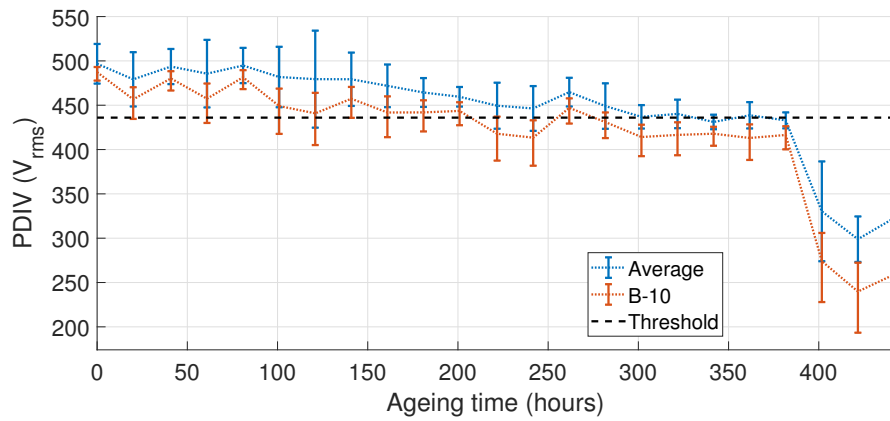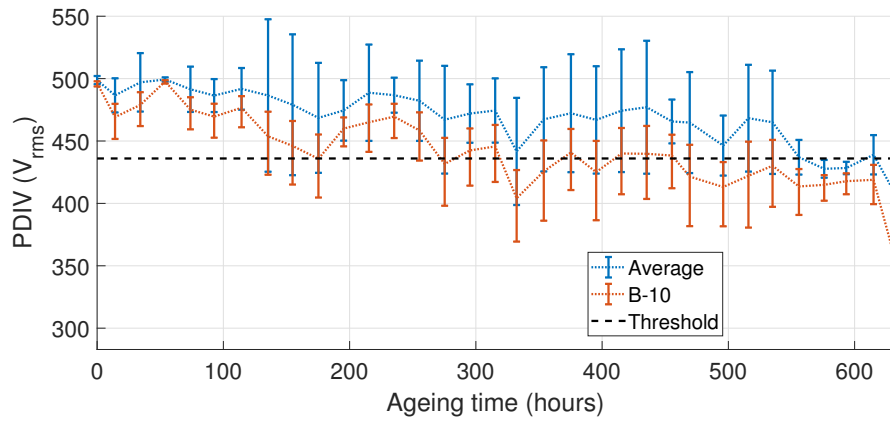
Figure 4.9: $PDIV$ monitoring during the accelerated thermal ageing with maximum temperature of $260\,°\mathrm{C}$ at (a) $0.5\,°\mathrm{C\,s^{-1}}$, (b) $2.5\,°\mathrm{C\,s^{-1}}$ and (c) $4\,°\mathrm{C\,s^{-1}}$.
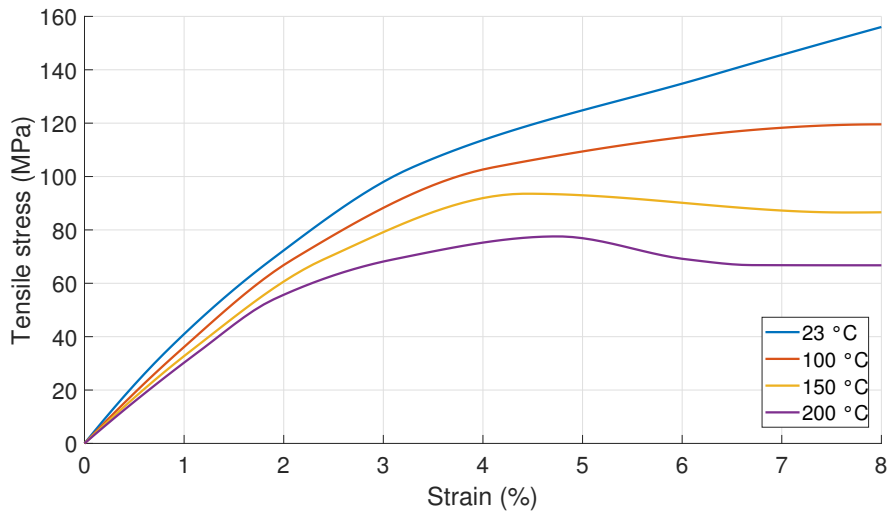
Figure 4.10: Stress-strain in tension for Torlon® PAI 4203LF over a broad temperature range. Adapted from [93].
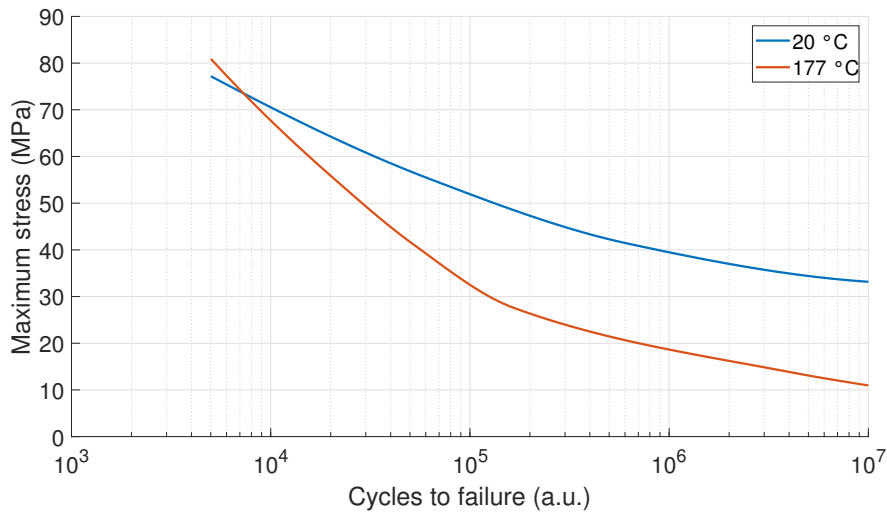
Figure 4.11: Flexural fatigue strength of Torlon® PAI 4203LF resins at $30\,\text{Hz}$ for two different temperature levels. Adapted from [93].

resistance along with an enhanced temperature resistance [13].

The tensile curve determines how much a material can stretch, under a certain pressure, up to the so-called ultimate tensile strength. In the case of PAI, it can be seen that at room temperature the polymer shows an almost completely elastic behaviour, while at higher temperatures the curve shows a much more plastic trend. This means that at high temperatures (in particular above $200\,°C$) the short-time thermal cycles are likely to give rise to strong stresses due to effects of insulation oxidation (which progressively makes the material more and more brittle) and mechanical hysteresis. This hypothesis is consistent with the fatigue curves, which establish the number of cycles that the PAI can withstand when subjected to a certain periodic stress: as the temperature rises, the number of cycles at break decreases with the same intensity of stress.

Another explanation could be the action of the electromechanical forces of attraction and repulsion between the wires due to the passage of the heating current. During the ageing cycles, a current of up to $15\,A$ was applied to the test specimens. Using the Ampere's law [91]

$$\frac{F}{l} = \frac{\mu_0}{2\pi}\frac{I^2}{r} \tag{4.7}$$

where r is the distance between the wires (equal to twice the enamel thickness, i.e., $80\,\mu m$), l is the wire length and I is the current, it can be estimated that the maximum force applied per unit length was $0.56\,\mathrm{N\,m^{-1}}$. The combination of this stress with that exerted by the high temperature can also in this case justify the trend of life curves found experimentally.

Based on such evidence, when the insulation is subject to sudden changes in temperature (i.e. temperature profile with remarkable thermal slew rate) due to electric losses, the enamel is not only stressed from a thermal point of view, but also on a mechanical one.

Therefore, in the future it is likely that in addition to the constant temperature ageing tests, further tests will have to be carried out in order to take into account the mechanical stresses due to the rapid expansion and thermal compression of the windings' insulating enamel. This could be done by providing temperature profiles characterized by thermal gradients similar to those expected in the specific application, or with mechanical fatigue tests at defined operating temperatures.

4.3 Partial discharge activity at high altitudes

One question that still needs to be answered is to actually quantify the potential damage that the possible partial discharge activity at high altitude on an insulating material could have. The point is that the propagation of high altitude discharges is longer (because the average free electronic path is greater) and, moreover, the maximum applicable electric field is lower (because the designer knows that the $PDIV$ decreases because of the pressure drop), but on the other hand the single discharge should be more energetic, since the electrons are accelerated longer.

This set of mechanisms interact with each other and it is not possible to know exactly if the discharge that occurs at sea level, at the same overvoltage with respect to the ignition point, is more or less dangerous than the one that occurs at high altitude. The answer to this question is quite important, especially if it turns out that they are less dangerous. Ideally, the insulation could be designed in such a way that the probability of triggering a PD is low, rather than completely non-existent. In this way, although the sporadic presence of partial discharge activities, the machine insulation system reliability remains guaranteed for the entire service life.

To unravel this doubt, two paths have been followed. On the one hand, the energy content of partial discharges at different pressure levels below $1\,\mathrm{bar}$ was analysed using optical emission spectroscopy. At the same time, extrinsic accelerated electrical ageing tests were carried out on twisted pairs at the same different pressure levels, using two different types of voltage generators and different frequency values. The objective is to compare the life times of the different sets of samples under different pressure conditions in order to highlight any possible trend.

In this section, reference will often be made to the kinetic theory of gases, which is described in detail in Appendix B. The reader is therefore invited to consult it if he is not familiar with the subject.

4.3.1 Optical emission spectroscopy of PDs

The term optical emission spectroscopy (sometimes referred to as OES) indicates those physical investigation techniques based on the emissions of electromagnetic radiation at specific wavelengths by the object (or compound) studied, such as to produce a characteristic spectrum, usually expressed in wavelengths and intensity of the emitted radiation [52].

In this specific case, the inception of partial discharges in a twisted pair enclosed inside a vacuum container was induced. The light emitted by

Table 4.5: Exposure times and number of acquisitions for each operating condition.

Frequency	Pressure	Exposure time	Number of acquisitions
kHz	mbar	ms	
	10	50	50
15	100	50	50
	500	1000	50
	1013	2000	50
25	500	1000	50
45	500	1000	50

the discharges was conveyed inside a monochromator that collimated it and separated some components of the emitted spectrum (those selected within a precise range of wavelengths) from the rest. Afterwards, only the selected waves were captured by a intensified CCD (Charge-Coupled Device) camera, which was able to associate to each pixel of the resulting image the number of photons that hit the optical sensor at that point. The photo is superimposed on a Cartesian diagram: the spatial unit of measurement and the reference are deduced knowing that the emission peaks are at certain wavelengths. Furthermore, the spectrum intensity has not been calibrated, so any measure that is performed will be a relative evaluation of intensity and not an absolute one.

The acquisition of the spectrum was performed with the software SpecE®. The process consisted, first, in the acquisition of the background radiation, after which a certain number of frames were acquired. The initial background scan allowed to reduce the thermal noise of the following photos. The set of frames associated with a single event, once obtained, was averaged so as to obtain a single image. Depending on the operating conditions, a certain combination of exposure time and number of acquisitions was chosen. Table 4.5 lists the values in detail.

In a plasma at thermodynamic equilibrium the velocity distribution is described by the Maxwell distribution, while the energy distribution is described by the Boltzmann one. Based on this premise, density relations between ionic states and electrons were predicted [15], while the behaviour of the photons is given by the Plank's law. In this experiment it is assumed that the radiation is decoupled from matter and ions and electrons have different Maxwellian distribution, leading to different characteristic temperatures (the so-called partial local thermodynamic equilibrium hypothesis, pLTE).

Under these assumptions, it is possible to evaluate how the energy is distributed between the degree of freedom of the molecules. Indeed, by means of the collisions, a molecule can start to rotate around a preferential axis or it can start to vibrate around equilibrium positions (see Appendix B). The excitation of these rotational and vibrational modes generates spectral emission when the molecules are de-excited.

The vibrational temperature is the one responsible of the intensity peaks in the spectrum and it can be estimated using the Boltzmann plot method. Consider two energy levels, E_i and E_j, such that $E_i < E_j$, of two different line intensities with respective atomic densities n_i and n_j. Under pLTE condition, the relation between these two quantities can be established using the Boltzmann distribution:

$$\frac{n_j}{n_i} = \frac{g_j}{g_i} \, e^{-\dfrac{\Delta E}{k_B T}} \tag{4.8}$$

where g_i and g_j are the statistical weights of the respective states, k_B is the Boltzmann constant, $\Delta E = E_j - E_i$ and T is the temperature of neutrals (in K). If the total population density in n_{tot}, the Boltzmann relation related to a single atomic state population distribution is given by

$$\frac{n_j}{n_{tot}} = \frac{g_j}{Z(T)} \, e^{-\dfrac{\Delta E}{k_B T}} \tag{4.9}$$

where $Z(T)$ is called partition function and is the sum of the weighted Boltzmann function of all the discrete energy levels:

$$Z(T) = \sum_m g_m \, e^{-\dfrac{E_m}{k_B T}} \tag{4.10}$$

When an atom is de-excited from the energy level E_j to the lower energy level E_i, the spectral line emission coefficient can be expressed as follows

$$\varepsilon_{ji} = \frac{hc_0}{4\pi \lambda_{ji} \, A_{ji} \, N_j} \tag{4.11}$$

where λ_{ji} is the wavelength of the emitted light, h is the Planck's constant ($6.626 \cdot 10^{-34}\ \mathrm{J\,s}$), c_0 is the light speed in vacuum ($\sim 3 \cdot 10^8\ \mathrm{m\,s^{-1}}$) and A_{ji} is the transition probability, defined as the probability per second that an atom in state j spontaneously emits a photon and is de-excited to state i.
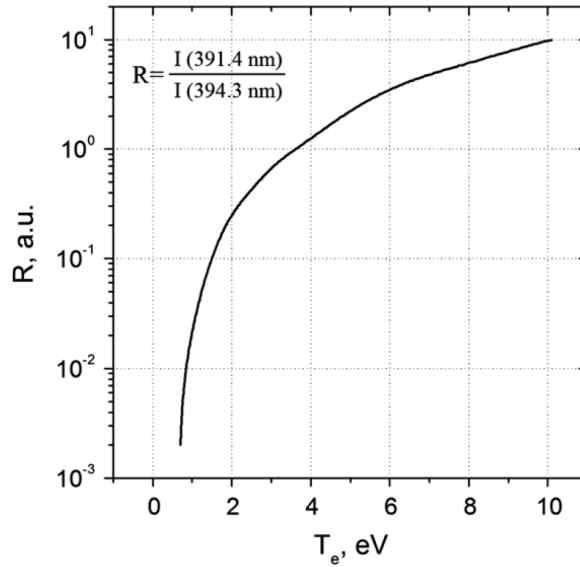
Figure 4.12: Variations of N_2^+ $391.4\,\text{nm}$ and N_2 $394.3\,\text{nm}$ band head intensities ratio as a function of electron temperature when a Maxwellian distribution is assumed (source: [15]).

Combining Eq. 4.11 with Eq. 4.9 and rearranging the terms, one gets

$$\frac{\varepsilon_{ji}\lambda_{ji}}{A_{ji}g_j} = \frac{hc_0 n}{4\pi Z(T)} e^{-\frac{E_j}{k_B T}} \tag{4.12}$$

Applying the logarithm to both sides of Eq. 4.12 results in

$$\log \frac{\varepsilon_{ji}\lambda_{ji}}{A_{ji}g_j} = -\frac{E_j}{k_B T} + C \tag{4.13}$$

where C is a constant.

Now, plotting Eq. 4.13, with $\log \dfrac{\varepsilon_{ji}\lambda_{ji}}{A_{ji}g_j}$ as a function of E_j, will result in a straight line, and the vibrational temperature can be determined from its slope.

The electronic temperature is responsible for the increase in intensity of the entire spectrum. For air, it has been shown that it is related to the ratio of the two first consecutive spectrum peaks R in the 385 - $410\,\text{nm}$ range (which are those at 390 and $393\,\text{nm}$). Therefore, it is possible to calculate it using an experimental curve (see Fig. 4.12) that shows its trend as a function of R.
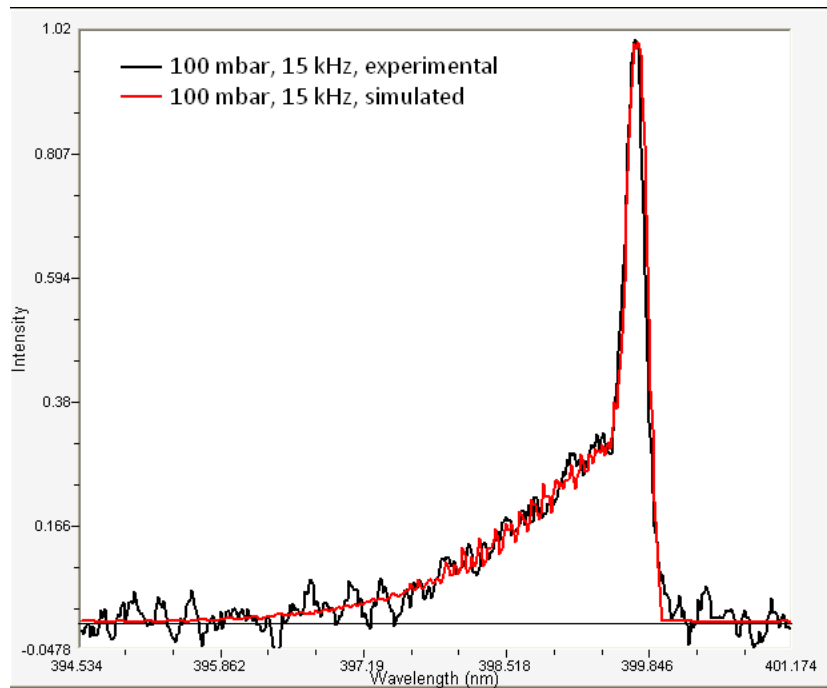
Figure 4.13: Fitting result of the normalised spectra from the rovibronic transition of the N_2 SPS at $10\,\text{mbar}$, using the resonant generator at $15\,\text{kHz}$.

Finally, the rotational temperature is calculated manipulating the acquired spectrum in the software SpecAir®. The latter is a spectrum simulation software, where different parameters can be modified (such as the composition, the pressure or the temperatures) to obtain a specific spectrum. Importing the acquired spectrum, it is possible to deduce, knowing the composition of the starting plasma, the parameters to obtain a similar spectrum, and in particular the rotational temperature. Fig 4.13 shows an example of the overlap procedure. The rotational temperature changes the shape of the spectrum, especially in the tail of the peaks. Different simulated spectra are generated by the software, inserting and adjusting the estimated electronic and vibrational temperatures (deducted using Eq. 4.13 and Fig. 4.12 as described above), together with the unknown rotational temperature, until the best fit is found.

In parallel to the spectroscopic measurements, in order to maximize the level of information obtainable, the absorbed power to sustain the PD activity on the twisted pairs was also monitored. To do this, the so-called Lissajous figure method was used. Downstream of the sample on which the OES was carried out, a $2.2\,\text{nF}$ capacitor C was connected in series and the voltage drop V_{cap} on it was monitored. In this way, it was possible to
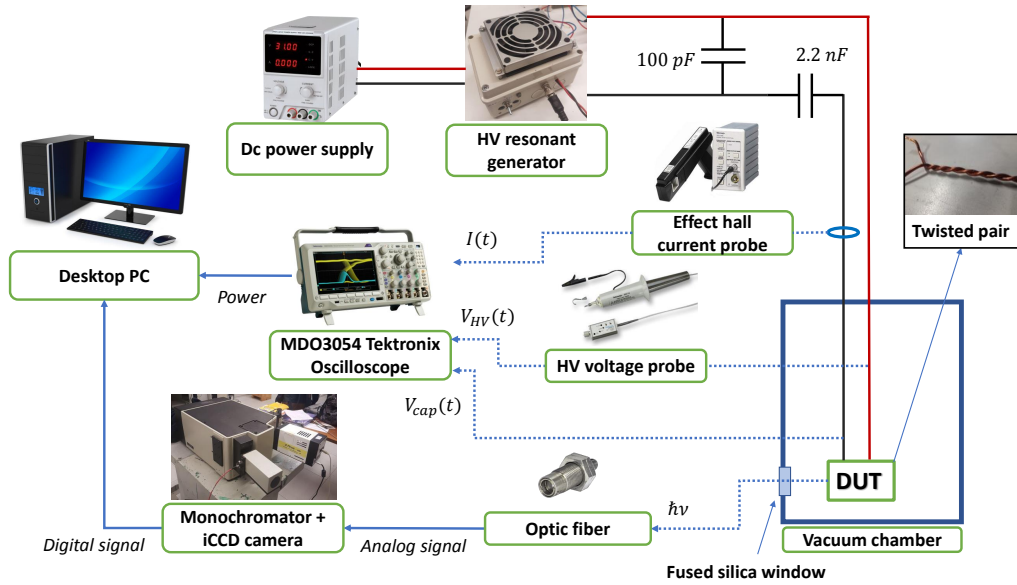
Figure 4.14: Circuit diagram for Optical Emission Spectroscopy using a resonant HV generator. The capacity upstream of the sample, connected in parallel, served exclusively to improve the resonant generator response.

build the curve of the stored charge from the capacity ($Q = C \cdot V_{cap}$) as a function of the voltage applied to the sample V_{HV}, which is a closed figure using periodic voltages (the so-called Lissajous figure). If there is discharge activity, the enclosed area, which represents the absorbed energy, is much greater than zero:

$$E_{abs} = \int Q(V)\, dV \gg 0 \qquad (4.14)$$

The average power absorbed in a single voltage cycle P_{cycle} is calculated by dividing the energy absorbed in a certain time interval, determined with the Lissajous figure, by the number of cycles N that have followed one another in the time considered, and multiplying by the frequency f

$$P_{cycle} = \frac{E_{abs}}{N}\, f \qquad (4.15)$$

Fig. 4.14 shows the complete circuit used to run the OES. With respect to what has been discussed, it is also necessary to add the periodic measurement of the current flowing through the sample, by means of a Hall effect probe. In this way, it was also possible to monitor the behaviour of the discharge current according to the different levels of pressure studied. Fig. 4.15 instead shows an example of what was captured by the optical fibre through the fused silica window, while inducing the PD activity on a
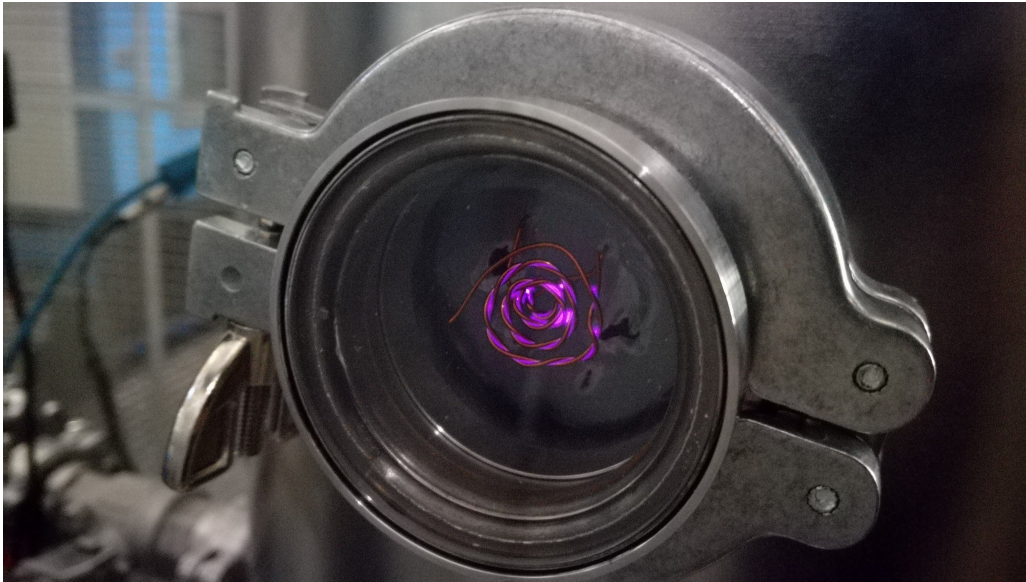
Figure 4.15: PD discharge optical emission, seen through the fused silica window, under $100\,\mathrm{mbar}$ and voltage 100% higher than the experimental $PDIV$.

(a)

(b)
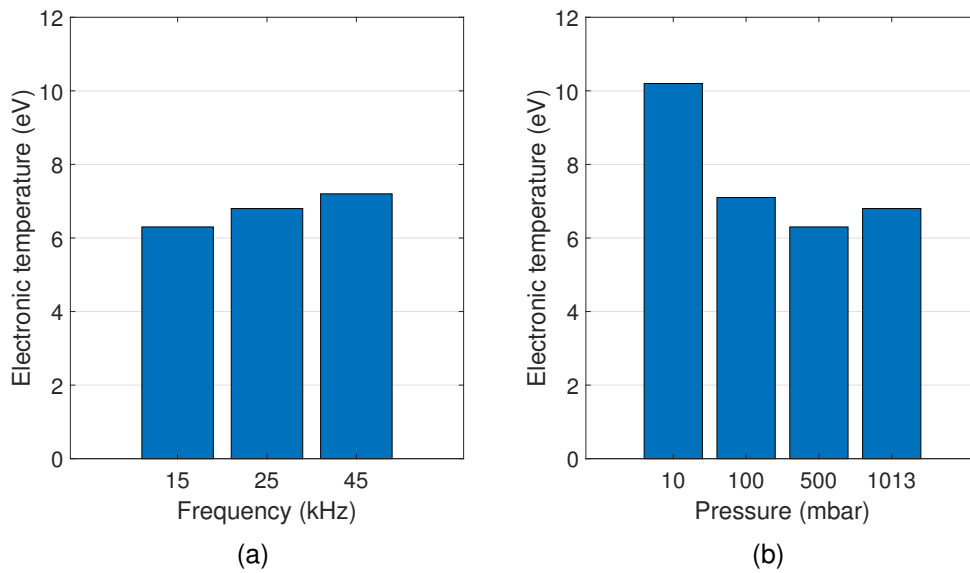
Figure 4.16: Measured electron temperature as a function of the frequency (a) and of the pressure (b).
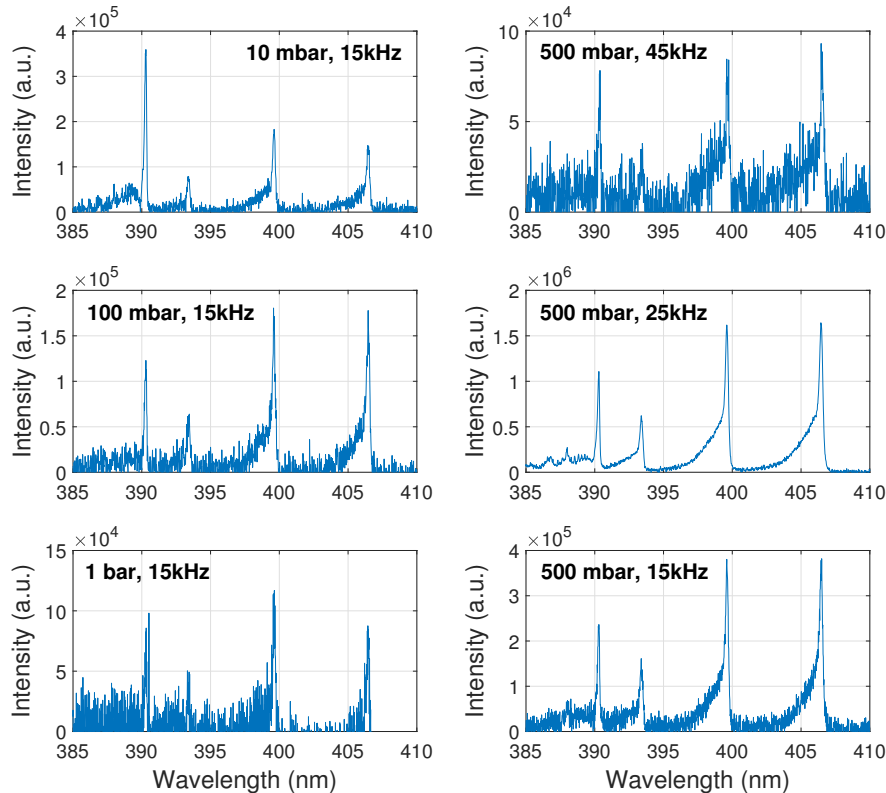
Figure 4.17: Optical emission spectra of the PD at different supply frequencies and pressures.

twisted pair in vacuum. Fig. 4.17 shows the PD spectra detected by the iCCD camera under the different conditions investigated.

In the first instance, a resonant high voltage sinusoidal generator with the possibility of varying its service frequency was used. Regardless of the frequency and pressure applied, $3\,kV$ peak-to-peak was always applied to the samples. Table 4.6 shows the results of the spectroscopic measurements. The values shown indicate that the discharges at the lowest pressure are the most energetic, with an electronic temperature of about $10.2\,eV$. However, the rotational temperature, which is correlated with the ion temperature, does not undergo major changes at the same time, indicating that the global temperature of the plasma is not dramatically affected by the energy increase of the electrons. It is also observed that, as the frequency increases, the electronic temperature tends to increase slightly: this means that not only do the discharges become more frequent, but also the energy

Table 4.6: Results of the optical emission spectroscopy using the resonant high voltage generator.

Pressure	Frequency	Peaks' wavelength				R	T_e	T_{rot}	T_{vib}
mbar	kHz			nm			eV	K	K
10	15	390.3	393.3	399.2	405.8	4.6	10.2	3241	400
100	15	390.3	393.4	399.2	405.8	1.9	7.1	2656	400
500	15	390.3	393.3	399.2	405.8	1.5	6.3	2912	450
500	25	390.3	393.3	399.2	405.8	1.8	6.8	2743	450
500	45	390.4	393.4	399.2	405.8	2.1	7.2	2884	450
1013	15	390.4	393.2	399.3	405.8	1.7	6.8	3332	450

Table 4.7: $PDIV$ values (10th percentile), PD amplitude and absorbed power under different pressures at $15\,\mathrm{kHz}$, using the resonant high voltage generator.

Pressure	Frequency	PDIV	Average power	Maximum PD amplitude	Total charge per cycle
mbar	kHz	V_{pk}	mW	mA	nC
10	15	511.7	1.25	46.4	690
100	15	448.5	0.90	61.4	390
500	15	641.5	0.43	428	371
1013	15	845.4	0.40	536	498

they release is higher. Fig. 4.16 shows the electronic temperature trend as a function of pressure and frequency. From the material point of view, therefore, it is expected that as the frequency increases and the pressure decreases, the ageing due to the partial discharge activity is more rapid, since electrons, having more energy, will more easily break the polymeric chains.

It is interesting to take a look at the measurement of the monitored electrical quantities. Tables 4.7 and 4.8 show the values that concern them. The total charge is calculated as the integral over time of the electrical current measured over a single period of the voltage wave. Fig. 4.18 shows the time pattern of the current, recorded in an entire cycle (when the frequency was set to $15\,\mathrm{kHz}$), at various pressure levels. It can be observed that, as the pressure decreases, current discharges tend to be less intense, but more prolonged over time, so much so that the amount of charge carried actually increases, rather than decrease. This may be due, given the so low value of the pressure and the $PDIV$ trend recognized, to a transition from a partial discharge mechanism to a pseudo-glow one [8].

In conclusion, these data would suggest that the most dangerous PD

Table 4.8: $PDIV$ values (10th percentile), PD amplitude and absorbed power under different frequencies at $500\,\mathrm{mbar}$, using the resonant high voltage generator.

Pressure	Frequency	PDIV	Average power	Maximum PD amplitude	Total charge per cycle
mbar	kHz	$\mathrm{V_{pk}}$	mW	mA	nC
500	15	641.5	0.43	428	371
500	25	655.8	1.51	457	280
500	45	648.3	2.21	328	135
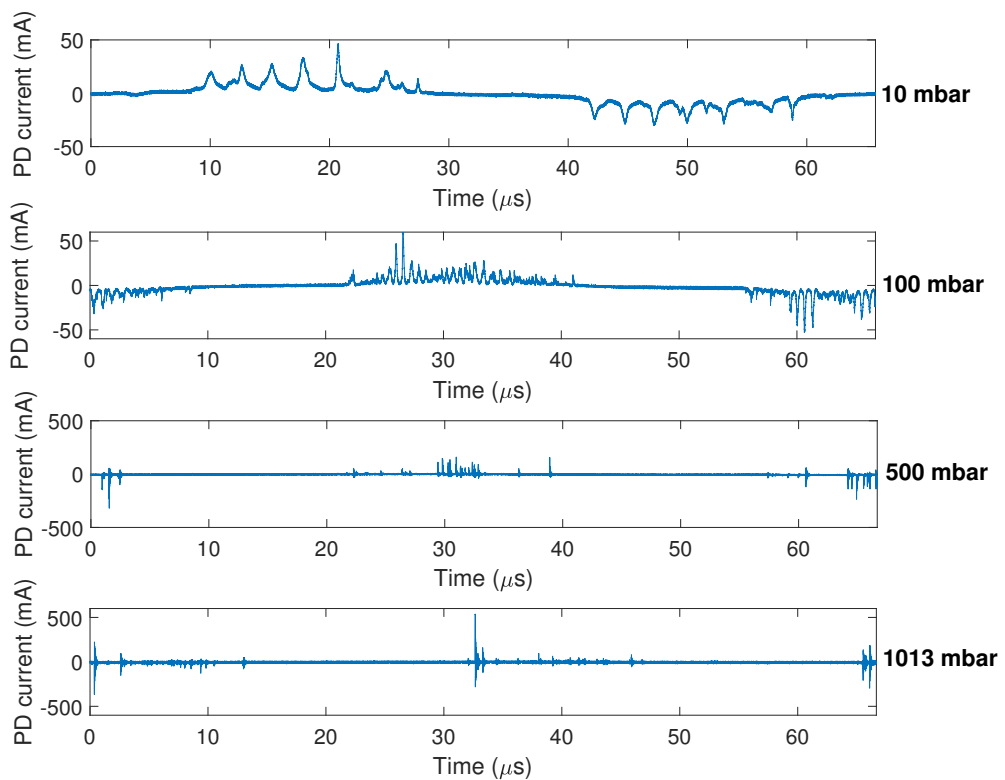
Figure 4.18: PD pulse waveforms in a single voltage cycle, under different pressures.

Table 4.9: Results of the optical emission spectroscopy using the square wave (SW) and resonant (R) generators at $100\,\mathrm{mbar}$ and applying $1\,\mathrm{kV_{pk-pk}}$ at $15\,\mathrm{kHz}$.

Generator	Peaks' wavelength				R	T_e	T_{rot}	T_{vib}
	nm					eV	K	K
SW	390.5	393.4	399.4	405.9	1.8	4.5	2846	400
R	390.4	393.4	399.3	405.9	1.1	3.8	2775	400

Table 4.10: Exposure times and number of acquisitions for the OES of square wave-induced PD activity at $100\,\mathrm{mbar}$, $1\,\mathrm{kV_{pk-pk}}$ and $15\,\mathrm{kHz}$.

Wave-shape	Exposure time	Number of acquisitions
	ms	
square	1000	25
sinusoidal	1000	25

conditions can be found at low pressures and high frequencies.

Subsequently, a similar analysis was carried out using a square wave generator, consisting of a bipolar converter, made with MOSFETs in SiC, powered by a high-voltage DC generator. Unfortunately it was not possible to reach the same voltage value, and it was limited to apply $1\,\mathrm{kV}$ peak-to-peak. In light of this limitation, only the case at $100\,\mathrm{mbar}$ pressure was studied, in order to guarantee sustained discharge activity. A power supply frequency of $15\,\mathrm{kHz}$ was selected. Clearly, in order to have a comparison, the spectroscopic measurements were repeated in addition under the above conditions using the high voltage resonant generator. In Table 4.10 are listed the operative conditions of the OES. The electrical power absorbed by the discharge activity could not be monitored with the same precision, due to the strong electromagnetic noise generated by the converter.

Table 4.9 shows the results of the OES and in Fig. 4.19 it is possible to observe the spectra recorded in the two cases studied. Comparing the data, the square wave results in discharges characterized by a higher electronic temperature. On the other hand, given the frequency-dependent behaviour previously observed, this result seems logical, since the square wave voltage has a very high harmonic content, with non-negligible components up to $30\,\mathrm{MHz}$. This means, therefore, that the partial discharge activity triggered when a converter is installed is more dangerous than that triggered by a sine wave, in energy terms. And the higher the frequency, the more repetitive the discharges will be and the easier it will be to break the
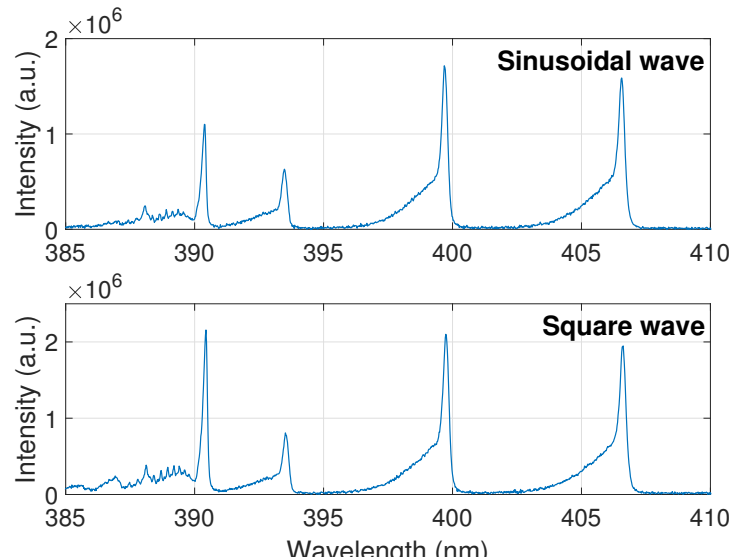
Figure 4.19: Optical emission spectra of the PD induced by different voltage wave-shapes.

polymeric chain bonds of the neighbouring insulating materials.

4.3.2 Time-to-breakdown at PD inception voltage levels

A more direct approach to quantify the real level of partial discharge harmfulness at low pressures is to carry out accelerated extrinsic electrical ageing tests, i.e. subjecting the twisted pair enamels to intense discharge activity until the breakdown is reached.

A delicate choice of these tests is whether to carry out them all applying the same voltage (i.e. constant electric field) or to select from time to time, depending on the conditions, a voltage that is higher than the $PDIV$ by a certain fixed percentage (i.e. variable electric field). This node is important because the $PDIV$ varies according to the vacuum level. Applying a constant electric field, regardless of this last parameter, would mean exerting different levels of stress. In particular, as discussed in Chapter 2, down to $50\,\mathrm{mbar}$ under pressure would also reduce $PDIV$ and, as a result, cause in more intense discharges with the same applied electric field.

Since the aim is to investigate whether, under the same conditions, low-pressure discharges (more energetic, but also less frequent) are more dangerous than atmospheric pressure discharges (less intense, but much more repeated), the reason indicates to carry out these electric field tests proportional to the $PDIV$. The latter was determined in the preliminary

Table 4.11: $PDIV$ detected for all the testing conditions and the applied voltages for the accelerated extrinsic electrical ageing tests.

Pressure	Frequency	PDIV	CL (95 %)	V_{app}
mbar	kHz	V_{pk}	V_{rms}	V_{pk}
10	15	511.7	[462.9; 543.1]	767.6
100	15	448.5	[437.4; 455.3]	672.8
500	15	641.5	[567.8; 689.3]	962.3
500	25	655.8	[626.9; 674.5]	983.7
500	45	648.3	[598.3; 681.2]	972.5
1013	15	845.4	[805.6; 870.4]	1268.1

phase on 10 fresh twisted pairs, for each combination of the conditions chosen. The test conditions that were investigated in the laboratory are the same as those shown in Table 4.6, because the purpose is to make a direct comparison between the data collected with spectroscopic measurements and the life-time values measured with these tests. Table 4.11 lists the results of the PD tests. The optical sensor approach, already discussed in detail in Chapter 2, was used for the detection. The voltage generator is the same as that used for OES measurements.

Accelerated electrical ageing tests were conducted, for each combination of conditions, on 10 fresh twisted pairs according to IEC 60216-1 [22]. The chosen overvoltage value was set arbitrarily (based on literature and operator experience [34, 90] to 1.5. The specimens were all connected together in parallel to the voltage generator and enclosed in a vacuum tank. Once this was done, the voltage chosen for the selected pressure level was applied (see Table 4.11). During the tests, the voltage applied to the ends of the samples was monitored by means of a differential probe, and the current supplied by the generator was monitored by means of a Hall-effect current probe. When the power delivered by the generator suddenly rose and remained at a high level, above 150 % of the power initially delivered, the breakdown of one of the samples was decreed. When this happened, the samples were temporarily removed from the test to examine them and identify the sample exhausted, so as to remove it, record its time-to-failure and resume the ageing process of the remaining ones. When all twisted pairs in a match have broken, the accelerated extrinsic electrical ageing test for that combination of conditions was completed. The time-to-failure values obtained were processed by determining the Weibull distribution that best approximated their behaviour. For each case considered, the 10th percentile (or B-10 life) was calculated.

Table 4.12: Measurements of twisted pair time-to-failure for different pressure and frequencies ($V = 1.5 \times PDIV$).

Pressure	Frequency	Time-to-failure (B10)	CL (95 %)
mbar	kHz	s	
10	15	8909	[8080; 9440]
100	15	7933	[6961; 8566]
500	15	3342	[2441; 4016]
1013	15	2177	[1634; 2571]
500	25	1819	[1057; 2533]
500	45	1259	[893; 1544]
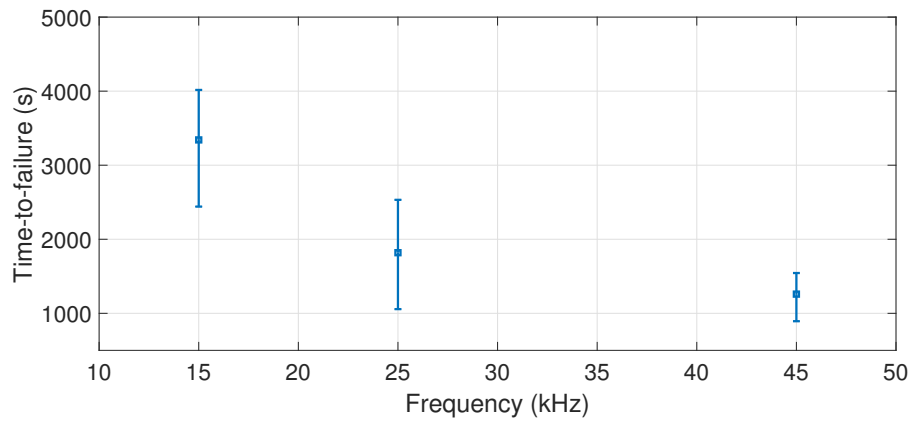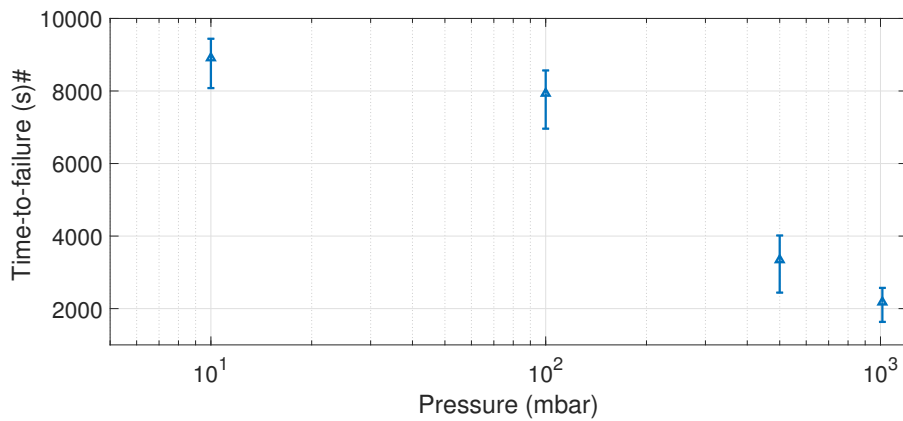
Figure 4.20: Variation of the twisted pair time-to-failure as a function of (a) the frequency ($p = 500\,\mathrm{mbar}$) and of (b) the pressure ($f = 15\,\mathrm{kHz}$).
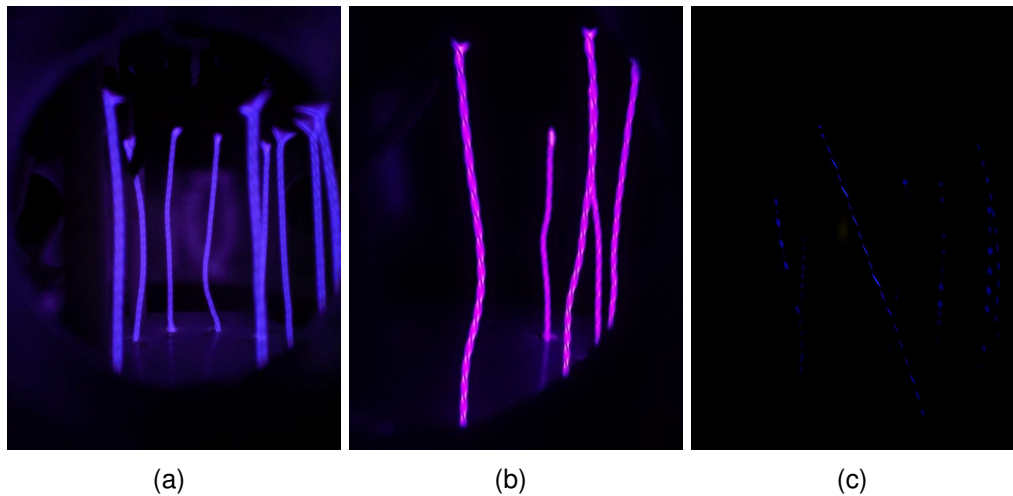
Figure 4.21: Images of partial discharge activity during accelerated electrical ageing tests at (a) $10\,\mathrm{mbar}$, (b) $100\,\mathrm{mbar}$ and (c) $500\,\mathrm{mbar}$.

Table 4.4 shows the results of the tests, while Fig. 4.20 shows the ageing curves as a function of pressure and frequency. As can be seen, there is a reduction in the lifetime of the insulation as the frequency increases, even at low pressure. This is not particularly surprising, since even at ambient pressure this behaviour occurs, as extensively documented in literature [34, 94, 55, 54, 71]. What is most surprising, however, is the pressure-dependent ageing curve. According to the data collected, it is evident that as the pressure increases, the useful life of twisted pairs subjected to partial discharges decreases.

Sili and colleagues found exactly the opposite behaviour [90]; however it should be noted that in their case flat specimens were aged through partial discharges induced in point-to-point configuration. This substantial difference could then explain why so many different results were obtained. In the case they examined, the discharge is confined to a very specific area of the ageing specimen. This means that all the energy emitted by the discharge is always dissipated in the same region of insulating material. This is true as much for the energy of the electrons that go to affect the surface, breaking the chemical bonds of the polymeric chains, as for the thermal energy transmitted to the surface, which increases the local temperature. In the situation investigated in laboratory, on the contrary, the discharge activity can trigger along the entire length of the twisted pair. From a visual investigation (see Fig. 4.21), it was seen in particular that at lower pressures the spread of discharges is much more pronounced, while
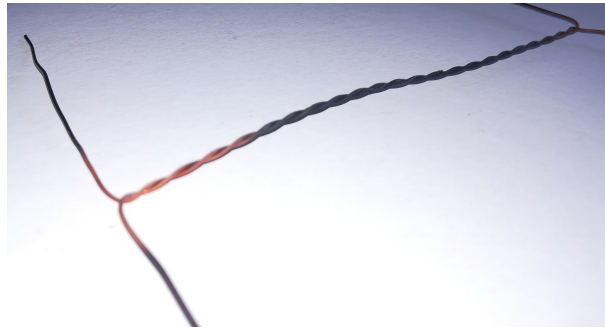
Figure 4.22: Image of an electrically aged specimen at $10\,\mathrm{mbar}$.

above $500\,\mathrm{mbar}$ the discharge activity tends to concentrate in the points of closest contact between the two wires that make up the samples.

In other words, although the decrease in pressure actually increases the energy associated with individual discharges (as evidenced both in the literature and by spectroscopic measurements), in the geometric configuration of twisted pairs, and by extension of stator windings, the specific energy deposited on the insulation tends to decrease, due to the greater diffusion of discharges. This means that, in reality, at high altitudes, the partial discharge inception is probably less dangerous than it could be under the same conditions at sea level pressure. This thesis is also supported by the fact that specimens with a pressure of more than $500\,\mathrm{mbar}$ have usually shown a rupture at a specific point, while those with a lower pressure are evenly blackened (see Fig. 4.22), and it is not possible, with just a visual inspection, to determine the actual breakdown point.

It should be pointed out, however, that if the failure occurs within a limited space (a micro-cavity for example), the low-pressure discharge is certainly the most dangerous, if able to trigger, as evidenced by the work of Sili and colleagues [90] and by spectroscopic measurements.

5

Conclusions

Today we are at a crucial moment, because the transport sector is at a turning point: born and developed thanks to fossil fuels, it must now accept the progressive and inevitable adoption of all-electric traction. In the not too distant future, most vehicles will no longer install endothermic engines, but electrical ones.

The speed of this transition depends on a number of factors, including the achievement of the levels indicated for the safety and reliability of the motors or actuators used. The main objective of this thesis was to discuss the challenges posed by this new frontier, especially with regard to the design, qualification and testing of electrical insulation systems.

The partial discharge inception is, in particular, the phenomenon that has proved to be of most concern. Traditionally, low-voltage motors have never shown any problems in this respect and their failures were mainly caused by thermal instability. However, the transport world demands exceptionally high performance from these motors, adopting DC bus rated voltages of up to $900\,\mathrm{V}$, incredibly small dimensions, extremely high service temperatures and great flexibility in terms of environmental and load conditions. All this has contributed decisively to the emergence of new problems, first of all the partial discharge ignition in engines that have never suffered historically.

There are many factors at stake, as discussed, and not all of them have a negative effect on the reliability of the insulation. As highlighted in Chapter 2, the interaction of environmental and electrical parameters can lead to highly non-linear behaviour, which is difficult to study in certain cases, and consequently difficult to assess in terms of its impact on the risk of insulation failure. As if that were not enough, the innovation in the field of power electronics, with the introduction on the market of new converters

based on broadband devices, although convenient for designers of electrical machines, who have thus been able to reach new levels of power density, has made the task of detecting the activity of partial discharges within an insulating system almost impossible.

However, this should not discourage us from studying, analysing and investigating the mechanisms that can lead to the partial discharge triggering inside (or near) the stator windings of an electric motor. The observations, models and solutions illustrated in Chapters 2 and 3, for example, are the result of intense experimental and theoretical work, committed to shed more light on the reasons that can lead the machine to fail as a result of the partial discharge inception in different working conditions. Not only: the same chapters have shown how it is possible to rely on a different approach for the online or offline partial discharge detection within a machine. PD tests based on optical sensors, although also affected by a number of problems, have nevertheless shown that they can be effectively implemented not only for measurements on simplified insulation systems, but also on machine stators. In the future, research should probably focus in this direction, improving the acquisition system and increasing the number of sensors, so as to maximize the detection probability of the photons released in discharge events.

This thesis has also shown that a part of the problems arises from the beginning, from an error in the insulation system design. Until now, the main stress factors for low-voltage machines were the thermo-mechanical stresses, and the enamel and the impregnation were subservient to the mechanical and thermal stability. The electric motors and actuators that will be used in the world of transport, instead, will have to undergo new logics, in which the electrical stress will play an important role as that of the other two. Chapter 3 therefore provides a new approach to the insulation design of a machine, based precisely on avoiding the partial discharge inception throughout the service period. It is clear that the method illustrated is not intended to be definitive: it must be subjected to extensive verification and, if necessary, refined to take account of the specific needs of designers. In any case, it is certainly an advancement in the design of a more reliable and secure insulation system.

Finally, in Chapter 4, two important aspects were highlighted, concerning the premature ageing of the insulating materials of an engine installed exclusively on board a vehicle. The first concerns the effect of frequent transients due to load variations (understood as changes in the mechanical torque delivered to the engine shaft). We have seen experimentally, on simplified systems, that the frequency with which these transients occur affects the ageing dynamics: the more sudden the variations, the greater

the stress exerted on the material, and consequently the shorter its useful life before the failure. This is clearly an important problem, since the engine (or actuator) will be subjected to a predominantly dynamic service regime on board vehicles, and research in the future will have to go into it in depth, so as to be able to provide guidelines to machine manufacturers.

A second interesting aspect that has emerged is that of having established that partial discharges can be less dangerous at high altitudes than at sea level pressure, at least when they do not occur in cavities. Thanks to the accelerated extrinsic electrical ageing tests on twisted pairs and to the optical emission spectroscopy measurements, it has been shown that, although the energy of the single discharge increases, the energy distribution is more uniform. This means that the insulating material ages more homogeneously at low pressure and, therefore, that the complete failure occurs in longer times than it does at standard pressure, under the same conditions. The fact remains, however, that the inception voltage is lower at high altitude. Moreover, it is not yet clear whether the low pressure discharge activity can deteriorate the mechanical properties of the enamel more rapidly, making the insulation more susceptible to breakdown due to mechanical, rather than electrical or thermal stresses.

Electric breakdown in gases

<div style="text-align: right;">*A*</div>

When designing an electrical insulation, it is essential to know the mechanisms by which a discharge can propagate in cavities and into the surrounding air. Today, an enormous amount of experimental data on gas breakdowns is available in literature. On the basis of these, several empirical formulas have been developed over time in parallel to the theoretical models, valid for a limited set of precise conditions. The electrical designer, therefore, has the possibility to use different alternatives and it is up to him (or her) to understand which is the most suitable and effective. In this appendix a complete description of the electric breakdown in gases is given, starting from the classic treatment given by John Sealy Townsend in 1897, up to the most recent theories proposed by Aage Pedersen in 1989.

A.1   Townsend mechanism and Paschen curves

Townsend's classical theory on the evolution of the electronic avalanche generated by ionization is the cornerstone from which one must start in any dissertation dealing with the subject. It was developed for short distances and uniform electric field between two bare electrodes with parallel flat faces. It is a simplified treatment of the phenomenon of ionization by impact. The latter occurs according to a certain probability, expressed by the first ionization coefficient of Townsend α, which indicates the number of ionizing impacts produced by an electron per unit length in the field direction and which depends on the value of the field itself and the density of the gas.

Assuming that the electric field does not change as a result of the electric charges generated by the ionization reactions, an electron moving

from the cathode to the anode will create in an infinitesimal tract dx, $\alpha \dot{d}x$ new electrons. By indicating with $n(x)$ the number of electrons at distance x, at distance $x + dx$ the number of electrons will increase by $dn = n\alpha dx$. Therefore, it results

$$\frac{dn}{n} = \alpha dx \tag{A.1}$$

The total number of electrons, crossed a distance s and starting with a known initial population of electrons n_0, will be given therefore by the integration of Eq. A.1 between 0 and s:

$$n(s) = n_0 e^{\alpha s} \tag{A.2}$$

In other words, the discharge starts when a free electron (generated by natural background decay, by the interaction of cosmic radiation with the atmosphere or simply by thermoelectric effect) acquires sufficient energy, thanks to the action of the electric field, to ionize the molecule against which it collides. This event generates a positive ion and an electron, which is added to the starting electron, now no longer energetic. These two electrons will then be accelerated again by the electric field and will collide with enough energy to cause two new ionization events, continuing the chain effect triggered by the first electron, called for this reason the initial electron.

The α coefficient, although it is a basic quantity that gives account of the ionization rate caused by electrons, is not easy to calculate. It is a function of the ionization cross-section σ_{ion}, which depends on the energy possessed by the electrons, so it is necessary to know the energy distribution of the latter in the gas. Assuming the swarm conditions were verified, Raether [85] derived an equation linking α to the function of the cross-section σ_{ion}:

$$\frac{\alpha}{N} = \frac{1}{u_e} \int_0^\infty v\sigma_{ion}(v)f(v)dv \tag{A.3}$$

where N is the particle concentration, $f(v)$ is the electronic velocity distribution function and u_e is the drift velocity of electrons in the field direction.

Swarm conditions usually indicate a group of electrons characterized by a reduced number density n in a gas with a much higher number density N [32]. Under these conditions, the energy distribution, as well as the average energy, of the electrons is uniquely determined by the E/N ratio and the swarm itself can be defined by the value of eight parameters: drift velocity u_e, diffusion coefficient D, mobility μ, excitation coefficient ε, electron attachment coefficient η, electron detachment coefficient ξ, ionization coefficient α and recombination coefficient r.

Table A.1: Ionization constants A and B (T=20 °C). Adapted from [59].

Gas	A	B	$\mathbf{E/p}$ **range**
	$\mathrm{mm^{-1}\,bar^{-1}}$	$\mathrm{kV\,mm^{-1}\,bar^{-1}}$	$\mathrm{kV\,mm^{-1}\,bar^{-1}}$
H2	375	9.75	11.25 - 45
N2	900	25.65	7.5 - 45
air	1125	27.38	7.5 - 60
CO2	1500	34.95	37.5 - 75
He	225	2.55	1.5 - 11.25
Hg	1500	27.75	15 - 45

From a more engineering point of view, it has been seen experimentally that α/p is a function of the E/p ratio, where p indicates the pressure, as well as of the gas considered. On the other hand, this is due to the fact that the distribution of energy depends exclusively on E/N, or E/p (assuming that the gas behaves in an ideal way). This allows the following relationship to be written:

$$\alpha = pf\left(\frac{E}{p}\right) \tag{A.4}$$

Assuming the Clausius distribution to express the energy of electrons as a function of position, it can be shown that Eq. A.4 can be rewritten as follows:

$$\frac{\alpha}{p} = A(T)\exp\left[\frac{B(T)}{E/p}\right] \tag{A.5}$$

where

$$A(T) = \frac{\sigma_{ion}}{k_B T} \qquad \text{and} \qquad B(T) = \frac{\lambda_i E \sigma_{ion}}{k_B T} \tag{A.6}$$

where k_B is the Boltzmann constant, T is the gas temperature and λ_i is the mean free path. The latter represents the average distance travelled by a particle between two successive ionizations. See Appendix B for a stricter definition.

It has been experimentally observed that, keeping the temperature fixed, the quantities A and B can be considered constant over a wide range, of practical interest, of the specific electric field E/p. Some of these experimental data, for the most common gases, are reported in Tab. A.1.

It should be noted that the value of α/p, for low values of the specific electric field, for many gases, is strongly influenced by attachment phenomena, so it is difficult to obtain true values of α and η (the electron attachment coefficient). Experimental measurements, in fact, report an

Table A.2: Experimental values for $\bar{\alpha}/p$ in oxygen [84], nitrogen [37], water vapour [48] and dry air [87].

E/p	Oxygen	Nitrogen	Water	Dry air
$\mathrm{kV\,mm^{-1}\,bar{-1}}$		$\mathrm{mm^{-1}\,bar{-1}}$		
1.5	0,25	-	-	-
3	5,1	-	-	-
4.5	17,6	7,0	24,8	9,8
6	44,4	22,4	54,1	25,2
7.5	71,2	40,1	81,4	49,4
9	99,1	64,8	112,8	73,6
15	-	174,6	235,2	174,9
20	-	264,6	315,8	274,4
25	-	347,8	370,2	363,1
30	-	418,4	443,7	445,1
35	-	474,2	491,9	497,5
40	-	529,9	521,0	599,3
45	-	571,0	553,5	643,8
50	-	603,8	583,8	671,3
55	-	636,5	583,8	685,0
60	-	658,0	614,6	742,5
65	-	677,5	649,9	795,8
70	-	696,1	667,7	-
75	-	701,4	-	-
80	-	706,7	-	-

effective ionization coefficient, defined as follows:

$$\bar{\alpha} = \alpha - \eta \tag{A.7}$$

In this case, it makes sense to calculate $\bar{\alpha}$ only for values higher than a certain specific electric field E/p, so that $\bar{\alpha}$ is positive (because a negative ionization coefficient makes no physical sense). As an example, Tab. A.2 shows the measurements made by different research groups for four recurrent gases.

Back to the discharge mechanism, since the value of the current is proportional to the number of electrons arriving at the anode in the unit of time, the current, from a certain value of the voltage on, should be represented by a relation analogous to Eq. A.2:

$$i(s) = i_0 e^{\alpha d} \tag{A.8}$$

where, in this case, d is the distance between the electrodes.

However, the trend of the discharge current detected experimentally had a steeper increase than that theorized by the equation just written. This is due, as Townsend himself discovered immediately afterwards, to an additional ionization phenomenon: the positive ions released by the electronic avalanche near the cathode generate an electric field that favours the extraction of new electrons from the cathodic material. These electrons are then immediately accelerated by the inter-electrode electric field and are added to the electronic avalanche being formed. By indicating with γ this probability of electronic extraction (which will depend on the applied electric field, the gas pressure and the material of the electrode in question), Eq. A.8 must be modified as follows:

$$i(d) = i_0 \frac{e^{\alpha d}}{1 - \gamma(e^{\alpha d} - 1)} \tag{A.9}$$

The discharge condition immediately descends from this; in fact, when the denominator tends to 0, the current tends to infinity, and therefore discharge occurs when

$$\gamma(e^{\alpha d} - 1) = 1 \tag{A.10}$$

which is in good agreement with the experimental evidence for relatively small distances, in the order of mm.

The equation just obtained allows to introduce a very popular and well-known instrument in the field of gas insulated systems (the so-called GIS): the Paschen curve. In fact, the latter directly relates the sparking voltage in the gas studied with the geometric and environmental parameters of the system being designed. From Eq. A.10 it can be deduced, assuming that the Townsend specific ionization coefficient $\overline{\alpha}/p$ can be expressed as a function of the specific electric field E/p, that:

$$e^{f(E/p)pd} = \frac{1}{\gamma} + 1 = e^K \tag{A.11}$$

Since γ depends to a large extent on the material and the surface roughness of the electrodes, it is possible to define a constant K so as to eliminate the exponential and obtain an equation easy to handle for practical use. Furthermore, remembering the hypothesis of uniform field, at this point it can be also defined the breakdown voltage V_b as the product between the electric field E to be applied necessary to satisfy the discharge criterion and the distance between the electrodes d:

$$V_b = Ed \tag{A.12}$$
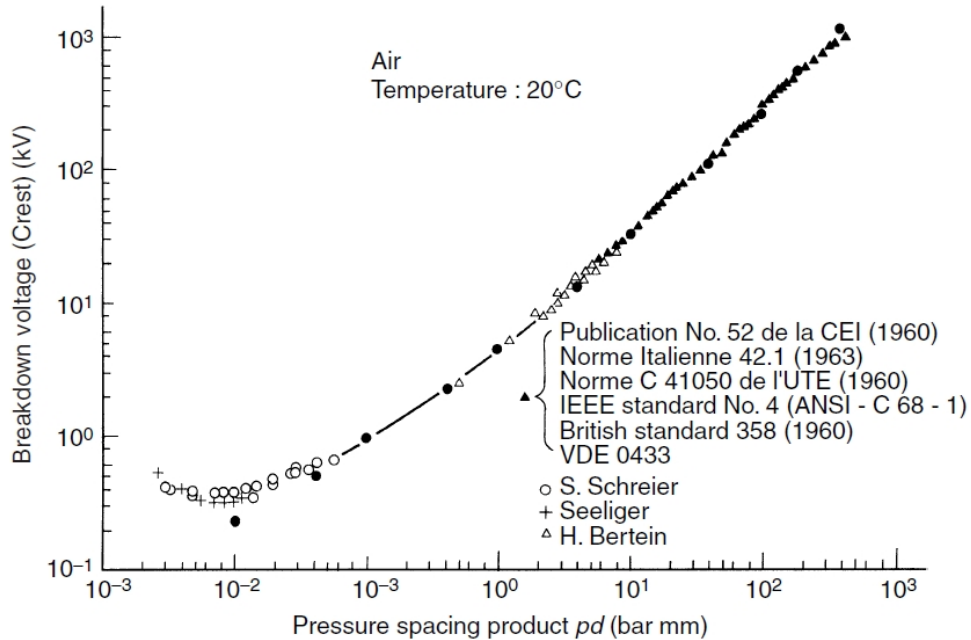
Figure A.1: Paschen curve for air (source: [59]).

Replacing this last definition in Eq. A.11 leads to:

$$V_b = F(pd) \qquad (A.13)$$

i.e. the breakdown voltage is a function of the product $p \cdot d$ and the material of which the electrodes are made.

The Eq. A.11 is known as Paschen's law, and was established experimentally in 1889. The $F(pd)$ function is usually experimentally determined and can be plotted for different combinations of gases and electrode materials. Fig. A.1 shows the trend of a typical Paschen curve. The breakdown voltage goes through a minimum value (V_b^{min}) at a particular value of the product $(pd)_{min}$. This behaviour is not surprising, as the cross section of the ionization events can be roughly expressed as follows:

$$\sigma \approx \frac{1}{N\overline{\lambda}} \qquad (A.14)$$

Hence, there are two reasons for the discharge voltage to rise again below the critical value $(pd)_{min}$:

- the pressure is so low, i.e. the gas is so rarefied, that the number of collisions occurring per unit length is not sufficient to generate the

Table A.3: Minimum breakdown voltage constants for various gases. Adapted from [59].

Gas	$(\mathbf{pd})_{\mathbf{min}}$ bar µm	$\mathbf{V_b^{min}}$ V
Air	7.33	352
Nitrogen	8.67	240
Oxygen	9.33	450
Carbon dioxide	7.60	420
Helium	53.3	155

electronic avalanche; consequently, it is necessary to increase the electric field in order for the electrons to be accelerated more quickly and to ensure ionization at each collision event.

- the distance between the two electrodes is so small that it is comparable to the average free path; this means that there is not enough space to actually generate the electronic avalanche within the gas gap.

It can be concluded that the $(pd)_{min}$ point is associated with the maximum ionization efficiency.

By replacing Eqs. A.5-A.12 in Eq. A.11 it is also possible to express Paschen's law in a more analytical form:

$$V_b = \frac{Bpd}{\ln \dfrac{Apd}{\ln(1 + 1/\gamma)}} \tag{A.15}$$

If the derivative of this last equation is set to zero with respect to pd, the minimum value of the breakdown voltage can theoretically be calculated:

$$V_b^{min} = 2.718 \frac{B}{A} \ln\left(\frac{1}{\gamma} + 1\right) \tag{A.16}$$

For example, for the air constants A, B and γ the values $A = 12$, $B = 365$ and $\gamma = 0.02$ are very often considered in literature, thus obtaining a minimum breakdown voltage equal to $325\,\text{V}$. More generally, in practice it is usual to experimentally measure the values V_b^{min} and $(pd)_{min}$: Tab. A.3 shows some of these for some gases of interest.

Given the typical shape of ionization curves, an approach quite used in practice is to approximate the trend of $\bar{\alpha}/p$ to that of a parabola:

$$\frac{\overline{\alpha}}{p} = C \left[\left(\frac{E}{p} \right) - \left(\frac{E}{p} \right)_c \right]^2 \tag{A.17}$$

where $(E/p)_c$ is the limiting value of the reduced field at which effective ionization starts and C is a constant. By replacing this formulation of $\overline{\alpha}/p$ in Eq. A.11 and rearranging the terms appropriately, one can write:

$$\frac{E}{p} = \left(\frac{E}{p} \right)_c + \sqrt{\frac{K/C}{pd}} \tag{A.18}$$

or, in terms of sparking voltage,

$$V_b = \left(\frac{E}{p} \right)_c pd + \sqrt{\frac{K}{C}} \sqrt{pd} \tag{A.19}$$

This relation has in general a good correspondence with the empirical data, except for very low values of the product pd, for which the quadratic relation is no longer valid. On the other hand, this region of the chart is of little interest to most applications. Empirical formulas are usually used for the design of vacuum insulated systems.

Finally, it should be noted that on some occasions it might be more useful to express Paschen's law in terms of gas density rather than pressure. In this way, the effect of temperature on the free average path of electrons is also taken into account.

Since air can be found in many different conditions, from a practical point of view it is convenient to consider only one reference breakdown voltage under established conditions ($1.013\,\mathrm{bar}$, $20\,°\mathrm{C}$); after that a conversion is made that takes into account the environmental working parameters defining a relative density,

$$\delta = \frac{293.15}{273.15 + T[°\mathrm{C}]} \frac{p[\mathrm{bar}]}{1.013} \tag{A.20}$$

and the real breakdown voltage is estimated:

$$V_b(\delta) = \delta V_b(\delta = 1) \tag{A.21}$$

Note that Paschen's law is valid for pd values up to $1\text{-}2\,\mathrm{bar\,cm}$. Above, the breakdown voltage (for non-attaching gases) tends to be higher [59].

This is probably due to the fact that the discharge no longer responds to the Townsend mechanism, but to the streamer mechanism (which will be discussed shortly), so it is no longer affected by cathodic emission.

Similarly, for too low a pressure, the discharge is no longer influenced by the presence of gas molecules and therefore depends exclusively on the electrodes (vacuum discharge).

A.2   Spark breakdown mechanism: the streamer

As anticipated, when the distance between the two electrodes begins to be greater than a few centimetres, the effect due to the presence of the two electrodes is diminishing. The only parameters that control the phenomenon become the space charge distribution and the interaction between ionization and electronic dissociation. It should be noted that this dynamic can also occur under the conditions indicated for the Townsend discharge, when one or both electrodes are covered with a layer of insulating material (the situation that occurs, for example, in stator windings or Dielectric Barrier Discharge/Resistive Barrier Discharge devices). In this case, the ionization and attachment coefficients of the dielectric gas are modified by the contribution due to the presence of the surface.

The discharge mechanism in the above conditions is based on the streamer concept. A streamer is a thin channel of ionized gas that propagates very rapidly between the electrodes, following the positive charges trail left by an intense primary electronic avalanche. This avalanche generates enough high energy photons to trigger new secondary avalanches in the immediate vicinity. The electrons of the latter are driven by the strong electric field and head towards the tail of positive charges, giving rise to the streamer between the two electrodes. Therefore, unlike the Townsend discharge, the breakdown depends, in theory, exclusively on the inception of a single avalanche, that is on the history of a single initial electron.

Since the whole mechanism is based on field distortion due to the localized accumulation of charged particles (the electronic avalanche) and the generation of new ions as a result of inter-molecular interactions (photo-ionization and attachment events), the concept of streamer has never been formalized in a complete and satisfactory physical theory. However, taking advantage of the exponential nature of the electronic population growth within the primary avalanche and assuming to know the distribution of the electric field, in the literature there are several quantitative criteria, validated experimentally for narrow intervals of operating parameters, for the estimation of the inception voltage of the discharges [69, 63, 77, 85].
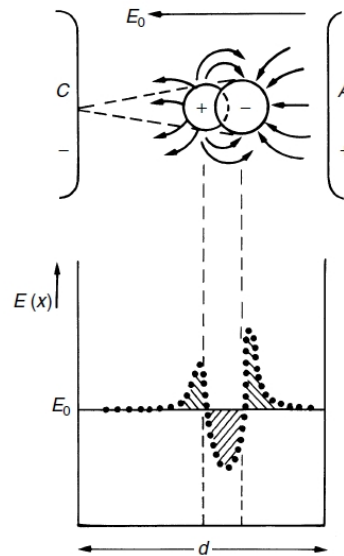
Figure A.2: Distortion of the electric field in an avalanche (Source: [59]).

All these criteria have one thing in common: they postulate that the electrical discharge occurs when the number of electrons inside the electronic avalanche reaches a critical value N_c. What distinguishes one criterion from another is precisely the definition of this parameter.

One of the pioneers of the streamer theory was J. M. Meek, who proposed, together with L. B. Loeb, an inception criterion based on the intensity of the electric field generated by the space charge induced by the electronic avalanche. Meek theorized that the space charge would produce an electric field distortion in the gap, as shown in Fig. A.2. In essence, he assumed that there is an increase in the electric field on the front and tail of the electronic avalanche, while in the remaining area the cloud is reduced. This means that in the 'depression' zone recombination events that generate photons are favoured. These, in turn, moving on the head, generate a multitude of secondary avalanches that further feed the electronic population, and by extension the space charge, until the actual streamer is generated. According to the Meek criterion, this happens when the electric field near the avalanche head equals the electric field applied externally E_0.

To calculate the electric field generated by the avalanche, one can imagine replacing all the electronic charges with a single charge Q enclosed within a sphere of radius r. The electric field at the spherical shell is then

determined after the avalanche has travelled a distance x, as:

$$E_r(x) = \frac{Q(x)}{4\pi r \varepsilon_0 [r(x)]^2} = \frac{4/3\pi [r(x)]^3 N(x) q_e}{4\pi \varepsilon_0 [r(x)]^2} = \frac{r(x) N(x) q_e}{3\varepsilon_0} \tag{A.22}$$

being $N(x)$ the electron density, $q_e = 1.602 \cdot 10^{-19}$ C the elementary charge and $\varepsilon_0 = 8.854 \cdot 10^{-12}$ Fm^{-1} the permittivity of free space.

Since electrons have a dramatically higher mobility than any type of ion, by virtue of the difference in mass, it can be assumed that the ions generated during the avalanche evolution remain stationary during the time period considered. Taking into account that the electronic population formed after a distance x, starting from a single initial electron, is equal to $e^{\overline{\alpha}x}$, the number of ions that will be generated in the infinitesimal path from x to $x + dx$ will be equal to $\overline{\alpha} e^{\overline{\alpha}x} \, dx$. Moreover, note that this will be enclosed within an infinitesimal cylinder of height dx and radius $r(x)$, i.e. equal to the size of the head of the avalanche at that time. In conclusion, this leads to:

$$N(x) = \frac{\overline{\alpha} e^{\overline{\alpha}x} \, dx}{\pi [r(x)]^2 \, dx} = \frac{\overline{\alpha} e^{\overline{\alpha}x}}{\pi [r(x)]^2} \tag{A.23}$$

Combining Eq. A.22 with Eq. A.23, one has

$$E_r(x) = \frac{q_e \overline{\alpha} e^{\overline{\alpha}x}}{3\varepsilon_0 \pi r(x)} \tag{A.24}$$

The avalanche radius, after a path of length x, can be determined on the basis of some observations on the diffusion of charge particles. In fact, it can be noticed that, with the passing of time, the electrons spread in all directions further and further away, following the subsequent law:

$$r(x) = \sqrt{2Dt(x)} \tag{A.25}$$

where D is the electronic diffusion constant and $t(x)$ is the time elapsed to travel the distance x.

Considering the previously encountered drift velocity u_e, which coincides also with the avalanche propagation speed, Eq. A.24 can be re-expressed as:

$$E_r(x) = \frac{q_e \overline{\alpha} e^{\overline{\alpha}x}}{3\varepsilon_0 \pi \sqrt{2xD/u_e}} \tag{A.26}$$

Eq. A.26 shows that E_r is a growing function of the path distance x, of the external applied field E_0 and of environmental conditions, through the ionization and diffusion coefficients (see Eq. A.4 in particular).
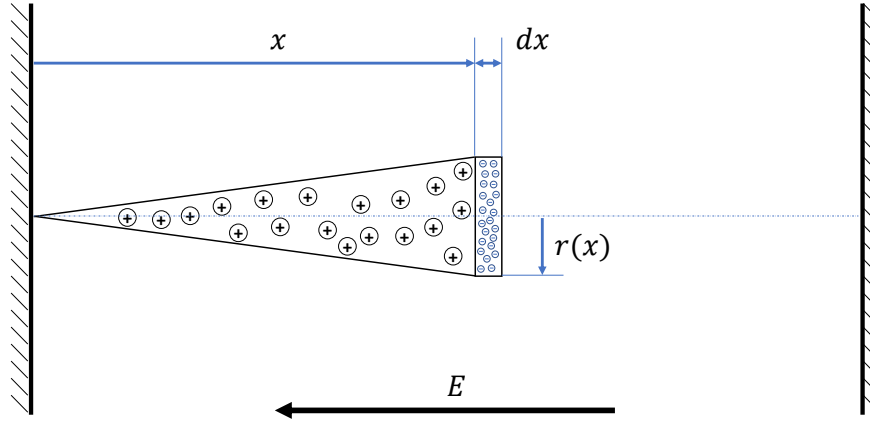
Figure A.3: Schematic representation of the electronic avalanche evolution along its linear path.

As an example, for air under standard conditions (pressure of $101\,325\,\mathrm{Pa}$ and temperature of $20\,°\mathrm{C}$), on the basis of fluid-dynamic considerations, Eq. A.26 can be re-written as follows:

$$E_r(x) = 6.09 \cdot 10^{-6} \frac{\overline{\alpha} e^{\overline{\alpha} x}}{\sqrt{x/p}} \qquad \text{(A.27)}$$

where the ionization coefficient $\overline{\alpha}$ is expressed in cm^{-1}, the pressure p in Pa and the electric field E_r in $\mathrm{V\,cm}^{-1}$.

Knowing the expression of the electric field generated by the electronic avalanche after it has travelled a distance of x, it is now possible to finally formalize the Meek criterion in mathematical terms:

$$E_r(x) = aE_0 \qquad \text{(A.28)}$$

where $a \approx 0.1$ is an empirical constant proposed by Meek [69], assuming that the applied electric field E_0 is uniform and constant (initially he proposed a unit value). It should be noted that in more recent times, literature has provided values of a different. Niemeyer has established that this parameter depends on the polarity of the streamer, the composition of the gas dielectric and any interfaces present. However, a is always a value between 0 and 1 [77].

In other words, indicated by d as the shortest path length to ground of a high voltage electrode, the maximum applicable voltage $V_{max} = E_0^{(max)} \cdot d$,

according to the Meek criterion, will be equal to:

$$V_{max} = \frac{q_e \overline{\alpha} e^{\overline{\alpha}}}{3 a \varepsilon_0 \pi \sqrt{2D/u_e}} \cdot \sqrt{d} \tag{A.29}$$

The main problem with the Meek criterion is the hypothesis of a uniform and constant field. When this hypothesis is not respected, the expression of $r(x)$ is no longer valid and Eq. A.28 strongly underestimates the electric field due to the space charge generated by secondary avalanches.

A.3   Schumann criterion of streamer formation

When the geometry of the system is rather complex, or the distances are less than one millimeter, and in any case in all cases in which the hypotheses of the Townsend or Meek criteria are not respected, the only simplified approach consists in supposing the existence of a critical electronic population beyond which there is the trigger of the discharge (or breakdown). This is commonly called Schumann's criterion and can be written in the following form:

$$n_c = n(x_c)_{max} \tag{A.30}$$

with

$$n(x_c) = n(x_0) \exp\left[\int_{x_0}^{x_c} \overline{\alpha}(x)\, dx \right] \tag{A.31}$$

where $n(x_0)$ is the initial population at the curvilinear coordinate x_0, while $n(x_c)$ is the population that occurs after having travelled a length $(x_c - x_0)$ following the corresponding electric field line. In other words, a discharge occurs when Eq. A.30 is verified in correspondence of, at least, one field line.

Note that Eq. A.31 can be rewritten, rearranging the terms, as follows:

$$n(x_c) = \frac{n(x_0) \exp\left[\int_0^{x_c} \overline{\alpha}(x)\, dx \right]}{\exp\left[\int_0^{x_0} \overline{\alpha}(x)\, dx \right]} \tag{A.32}$$

From Eq. A.32 it is evident that, in correspondence of the inception, one has

$$n_c \neq \exp\left[\int_0^{x_c} \overline{\alpha}(x)\, dx \right] \tag{A.33}$$
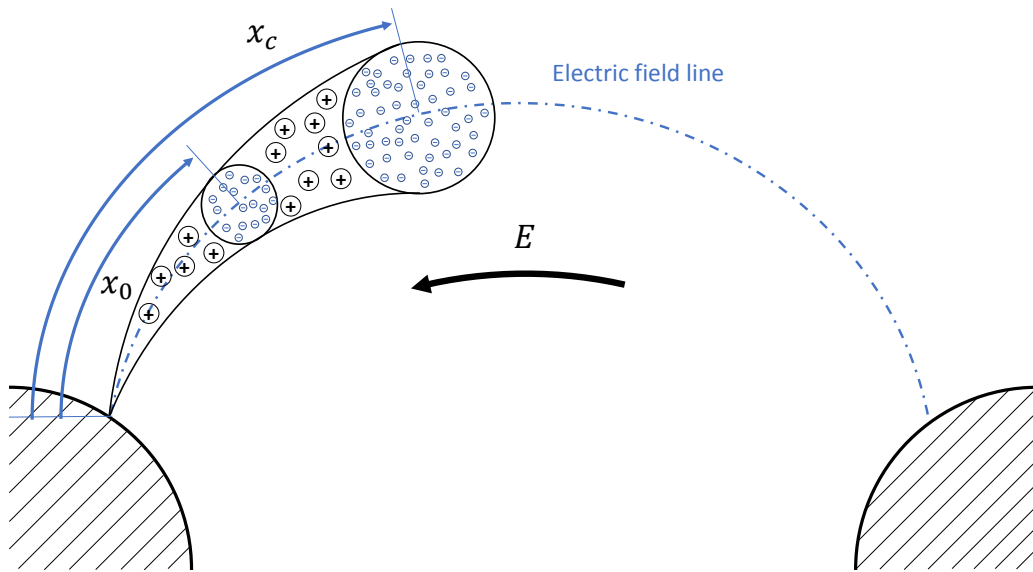
Figure A.4: Schematic representation of the electronic avalanche evolution along a non-linear path.

This contradicts what is often reported in the literature [80, 66, 77], namely that the right member in Eq.A.33 is actually equal to the true size of the electronic avalanche. However, due to the exponential nature of the variations of the effective ionization coefficient $\overline{\alpha}$ as a function of the electric field E, it very often happens that the integral to the numerator of Eq. A.32 is dominant with respect to the other terms, to the point of controlling in practice the conditions for the discharge inception.

In conclusion, the most famous form of Schumann's criterion is that without the presence of the exponential, resulting from a manipulation of Eq. A.33:

$$\int_0^{x_c} \overline{\alpha} \, dx = K \tag{A.34}$$

where K is an empirical constant, called Schumann's constant, which in literature is typically assumed to be equal to 18 (because a critical population of $10^8 \approx e^{18}$ electrons was deduced for the streamer ignition in air). However, there is no reason, except by custom, to consider K equal to this value.

In this regard, Malik in 1981 observed that when the product $p \cdot x_c$ is less than $1 \, \mathrm{bar} \, \mathrm{cm}$, the breakdown voltage values estimated using a $K = \log(10^8)$ were more than 50% higher than those measured. From the experimental

results he was then led to provide the following formula [66]:

$$K = 17.55 + 3.51 \log(px_c), \qquad \text{with} \quad 0.01 \leq px_c < 1 \, \text{bar cm} \qquad \text{(A.35)}$$

Replacing, one can see that K ranges from 1.39 for $px_c = 0.01 \, \text{bar cm}$ to 17.5 for $px_c = 1 \, \text{bar cm}$.

A.4 A more accurate approach: electro-hydrodynamics and transport of charged species

The criteria and mathematical models seen so far are applicable only up to the first moments of life of the discharge. If one is interested in understanding or predicting the entire evolution of the phenomenon, a much more complex theoretical description must be used.

A partial discharge can be considered a cold plasma, as it consists of four species of particles in such quantities as to make it globally neutral: positive ions, negative ions, electrons and neutral molecules. To predict their behaviour it is necessary to combine the Maxwell electromagnetic equations with those of diffusion. In this way it is possible to follow the course in time of the charge transport, allowing the prediction of the effects due to the alteration of the charge distribution [40].

This approach can be applied at the earliest stages of the phenomenon, when the electronic avalanche has yet to form. Therefore, theoretically, it could also be applied to predict the conditions for partial discharge inception for a given geometrical conformation. However, the solution of the equations involved is very demanding and a large number of simplifications are often required. Therefore, it is not the most correct way if there is no need to have more information about the current or the species generated.

In any case, for the sake of completeness, the following are the so-called electro-hydrodynamic equations, capable of giving the most complete description of the discharge phenomenon in a gas:

$$-\nabla^2 V = \frac{q_e}{\epsilon_0}(n_p - n_e - n_n) \qquad \text{(A.36)}$$

$$\frac{\partial n_e}{\partial t} - (\mu_e \vec{E})\nabla n_e - D_e \nabla^2 n_e = \alpha|\Gamma_e| - \eta|\Gamma_e| - \beta_{pe} n_p n_e + \beta_{ne} n_n n_e \qquad \text{(A.37)}$$

$$\frac{\partial n_p}{\partial t} - (\mu_p \vec{E})\nabla n_p - D_p \nabla^2 n_p = \alpha|\Gamma_e| - \beta_{pe} n_p n_e \qquad \text{(A.38)}$$

$$\frac{\partial n_p}{\partial t} - (\mu_p \vec{E})\nabla n_p - D_p \nabla^2 n_p = \eta|\Gamma_e| - \beta_{ne} n_n n_e \qquad \text{(A.39)}$$

where the subscripts e, p and n indicate the quantities associated with electrons, positive ions and negative ions, respectively, while α and η are respectively the Townsend coefficients of ionization and attachment, Γ_e is the electronic flux, β_{ij} is the recombination coefficient between the species i and j, V is the voltage applied between the two electrodes, n_i is the number of i-th species particles per volume unit, μ is the mobility, D is the diffusion coefficient, q is the quantity of charge and finally ϵ_0 is the dielectric constant in vacuum.

These equations contain typical diffusion quantities, which are the diffusion coefficient and molecular mobility.

When a swarm of electrons travels with speed u_e under the action of an electric field E, at the same time it diffuses, by virtue of the thermal agitation, following the following law:

$$j = -D\nabla n \tag{A.40}$$

where j is the number of electrons flowing normally across unit area per second. For sufficiently low electric field strengths, D is a direction-independent constant. As the field intensifies, logically the diffusion will be favoured in the direction towards which the field lines are oriented and D takes the form of a tensor, characterised in particular by a transverse component D_T and a longitudinal component D_L to the field.

A very often measured and reported quantity is the u_e/D_T ratio [32], because:

- it is directly related to the mean energy of the electrons;

- it is related to the collision cross sections;

- D_T is a difficult quantity to measure singularly.

On the other hand, the u_e/D_T ratio is a function of the specific electric field E/N, i.e. the ratio between the applied electric field and the studied particle density. Therefore, very often the result of the measurements is expressed in terms of the parameter

$$D_T \frac{E}{u_e} = \frac{D_T}{\mu} \tag{A.41}$$

where $\mu = u_e/E$ is the electron mobility.

$\mathcal{B}$ Ionization and deionization processes

To better understand the nature and the techniques for partial discharge detection, it is necessary to provide some notion of elementary atomic processes in a gas subject to a strong electric field. Therefore, this analysis aims to briefly analyse, from a gas kinetic point of view, the causes that lead to the ionization of this and, consequently, to the partial discharge inception. It is on the basis of these observations that the measurement methods' functioning and the validity of the physical-mathematical models adopted for the insulation system $PDIV$ prediction are justified.

B.1 Elementary charged particles

In a weakly ionized gas, just before an actual electrical discharge inception, many types of atomic processes involving ions and atoms can occur, and some of these processes also include interaction with photons. When the discharge is triggered, for a fraction of a second, a so-called plasma is obtained, that is a gas consisting of a prevalence of charged particles, which allows it to be traversed by an electric current, behaving like a liquid with ions in solution. The most natural way to obtain a plasma, however, is to heat a gas to temperatures such that the average energy of the particles is comparable to or higher than the ionization energy of the atoms. In this way, a so-called thermal (or equilibrium) plasma is obtained; in the previous case, the plasma generated by an electric discharge is difficult to remain stable, because the ions produced tend to recombine: consequently, it is

often called cold (or non-equilibrium) plasma.

Usually, in quasi-neutral plasmas the density of positive ions and electrons are equal. However, in the case of so-called electronegative gases, which have a high electronic affinity, there is also an important presence of negative ions. Since ionization is the process directly responsible for the plasma formation and sustenance, it is first necessary to briefly describe the main characteristics of charged elementary particles and the elastic and inelastic collisions that may occur between them.

Electrons are the first to acquire energy from the electric field, because of their reduced mass. As a result, they are also the main protagonists of the collisions that occur inside a gas, allowing the energy transfer from the electric field to the other constituents of the gas. This can happen through different mechanisms: ionization, excitation and dissociation. The frequency of these processes therefore depends on how many electrons have enough energy to activate them. This last quantity is described by the so-called electronic energy distribution function (EEDF) $f(\epsilon)$, which indicates the probability density for an electron to possess an energy ϵ. The expression of this function strongly depends on the distribution of the electric field and on the composition of the gas. Very often, even when unbalanced, it is assumed that the EEDF is largely dependent on the electronic temperature T_e and, therefore, can be described by the quasi-equilibrium Maxwell-Boltzmann distribution function:

$$f(\epsilon) = 2 \sqrt{\frac{\epsilon}{\pi (k_B T_e)^3}} \cdot \exp\left(-\frac{\epsilon}{k_B T_e} \right) \tag{B.1}$$

where k_B is the Boltzmann constant. Thus, as can be seen from Eq. B.1, the average electronic energy, which is defined as the first moment of the EEDF, is proportional only to T_e:

$$\langle \epsilon \rangle = \int_0^{\inf} \epsilon \cdot f(\epsilon) d\epsilon = \frac{3}{2} T_e \tag{B.2}$$

Atoms and molecules lose some of their electrons during the ionization processes, becoming positive ions. In cold plasmas (i.e. those of interest in this context) their charge is usually equal to the elementary electronic charge q_e. Since ions are heavy particles, the electric field usually fails to impress high energy on them before they collide again. Consequently, their energy distribution function is very often similar (if not coincident) to the Maxwellian one, with the ionic temperature T_i close to that of the neutrals T_0.
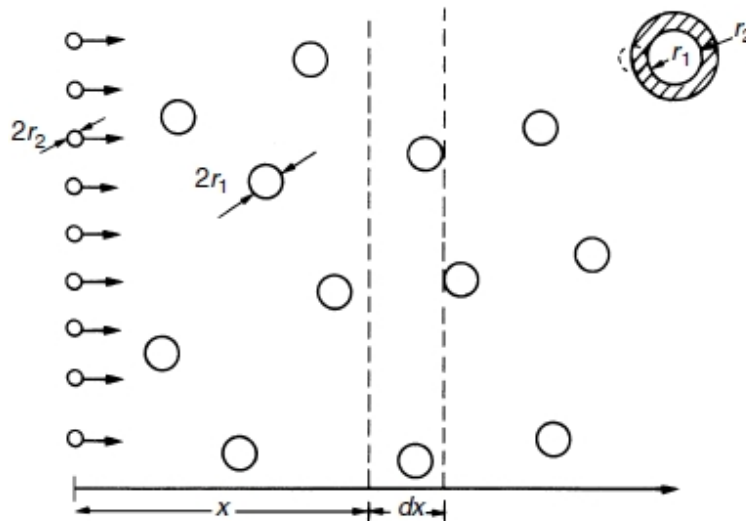
Figure B.1: Classical model for determining collisional cross sections (source: [59]).

Electron attachment leads to the formation of negative ions with elementary charge. The production of multi-charge negative ions is in fact impossible due to electrical repulsion. As with positive ions, they also have an energy distribution function very close to that of Maxwell.

The elementary collision processes can be of two types:

- elastic, purely mechanical collisions in which both kinetic energy and momentum are preserved;

- inelastic, collisions in which part of the kinetic energy is converted into potential energy, which can be spent in other processes.

In some cases, it is possible that part of the internal energy possessed by atoms or molecules is returned, in the form of kinetic energy, to the electrons during a collision: this process is called superelastic collision.

The most important characteristic quantity of all these processes is the so-called cross section, which can be imagined, in the first instance, as the circular area σ measured around a target particle, within which the presence of a second particle generates interaction phenomena between the two bodies. In other words, the cross section can be interpreted as the effective area of a given collision process.

The inverse of the product between the concentration of a certain species of particles N and the cross section associated with a certain

Table B.1: Mean free paths measured at $15\,°\text{C}$ and $101\,325\,\text{Pa}$. Adapted from [59].

Type of gas	H_2	O_2	N_2	CO_2	H_2O
λ (10^{-8} m)	11.77	6.79	6.28	4.19	4.18
Molecular weight	2.016	32.00	28.02	44.00	18

collisional event σ determines the so-called mean free path λ:

$$\lambda = \frac{1}{N\sigma} \tag{B.3}$$

It is defined more appropriately as the average distance travelled by an incident particle, within the gas, before it is involved in a collision event. In particular, returning to the study of electric discharges in gases, knowing the dependence of the mean free path on the energy of electrons, it clarifies the origin of the relationship between the ionization coefficient α and the specific electric field E/N (see Eq. A.3, even assuming a simple ballistic model.

If two particles that collide can be considered perfectly rigid spheres of radius r_1 and $_r2$, then their cross section will be equal to $\pi(r_1+r_2)^2$, because there will be a collision every time the two centres come into contact (see Fig. B.1). Actually, the range of action may exceed this geometric measure, since the forces acting on the particles are long distance actions. In addition, it has been assumed that the affected particles are stationary at the moment of impact, while instead they are characterized by a velocity, given by the thermal gas agitation. Table B.1 lists some values of the electronic free mean path for some types of interesting gas.

Finally, it should be noted that, from the perfect gas law $N = p/k_B T$, assuming that it is valid for the cases taken into consideration here, it follows that the mean free path is directly proportional to the gas temperature and inversely proportional to its pressure:

$$\lambda(p, T) = \lambda_0 \frac{p_0}{p} \frac{T}{T_0} \tag{B.4}$$

where λ_0 is the mean free path measured at pressure p_0 and temperature T_0.

B.2   Excitation events

The elementary processes that govern the exchange of energy between all species within a weakly ionized gas are typically the events of excitation

(or transition). They are divided into three types:

- vibrational;

- rotational;

- electronic.

The first is the most important in non-equilibrium molecular plasmas and consists of a sudden change in the vibrational energy of the atom (or molecule) under consideration. It is known that, as for all the other properties of a quantum particle, the vibrational energy is quantized, meaning that it can only assume certain discrete values that correspond to different energy states. When a particle loses a vibrational energy unit, known as a phonon, it is said to have passed to a lower state of vibrational energy. Similarly, when a particle gains vibrational energy, it is said that a positive vibrational transition has occurred.

Rotational transition, on the other hand, is a sudden change in the angular momentum, which is also quantized.

Finally, electronic excitation is that physical phenomenon, on an atomic scale, that involves the transition of an electron from one stationary state to another. The passage between two states involves radiation phenomena in which the nature of electromagnetic radiation is linked to the difference in energy level between the two states.

The energy transferred to the electrons through the application of an electric field, in the end, is divided between the energy losses due to elastic collisions and the different modes of excitation and ionization that can occur.

Fig. B.2 shows the energy distribution of electrons in air as a function of the specific electric field E/n_0. It can be observed that the contributions of rotational excitation and elastic energy losses are important only at reduced values of the specific electric field. This is not surprising, as these phenomena are not resonant and only occur when the electronic energy is low ($<< 1\,\mathrm{eV}$). At electronic temperatures of about $1\,\mathrm{eV}$ (typical of non-equilibrium discharges), on the other hand, most of the energy is involved in the vibrational excitation of the molecules. This makes this process very important, especially when treating the non-equilibrium chemistry of partial discharges. In reality, to this phenomenon must be added also those of electronic attachment, which, however, can seriously compete, at the temperatures considered, only in the case of strongly electronegative gases. In fact, the exact composition of the gas has a not negligible impact on the electron energy distribution.
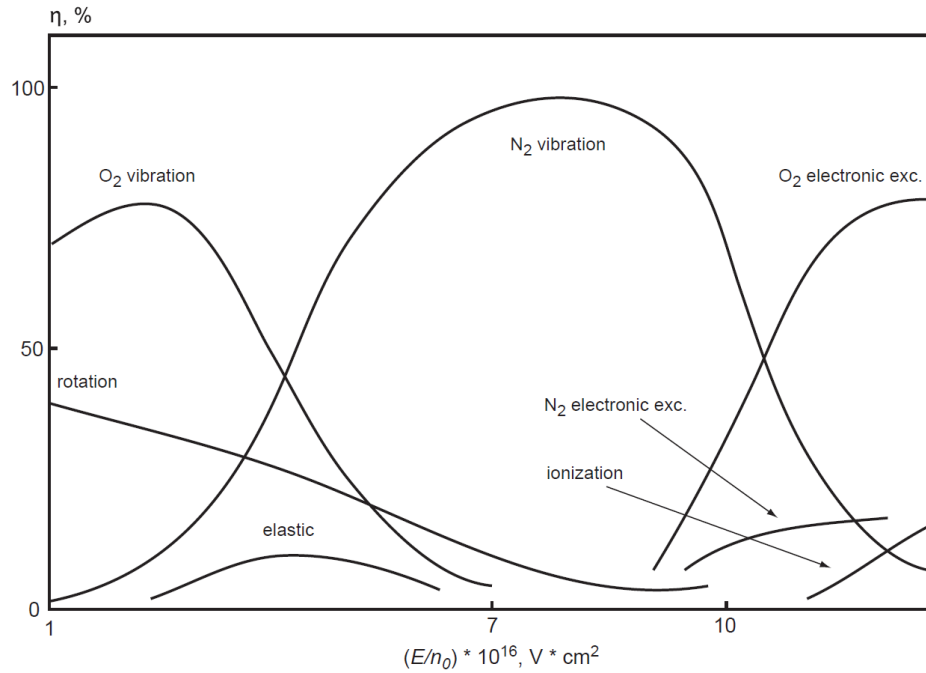
Figure B.2: Electron energy distribution between different excitation and ionization channels in air (source: [38]).

B.2.1 Vibrational excitation

As already mentioned in the introduction of this section, vibrational excitation is probably the most important elementary process to consider in the study of non-thermal plasmas. This is due to the fact that the energy exchange in elastic collisions is inefficient, due to the strong disparity between the mass of electrons and that of a generic molecule. It is possible to demonstrate that the energy transferred ΔE to a molecule of mass M by a free electron that has an energy ϵ is equal to

$$\Delta E = \epsilon \frac{m_e}{M} \tag{B.5}$$

The vibrational excitation process of a molecule AB from the vibrational level ν_1 to ν_2 can usually be schematized as follows:

$$\mathrm{AB}(\nu_1) + \mathrm{e}^- \longleftrightarrow \mathrm{AB}^-(\nu_1) \longrightarrow \mathrm{AB}(\nu_2) + \mathrm{e}^- \tag{B.6}$$
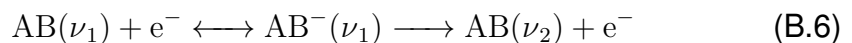
It can be immediately noticed that this is not a direct elastic process, but a resonant phenomenon with the intermediate formation of a metastable negative ion. Moreover, observing Fig. B.3, it can be noticed that the cross
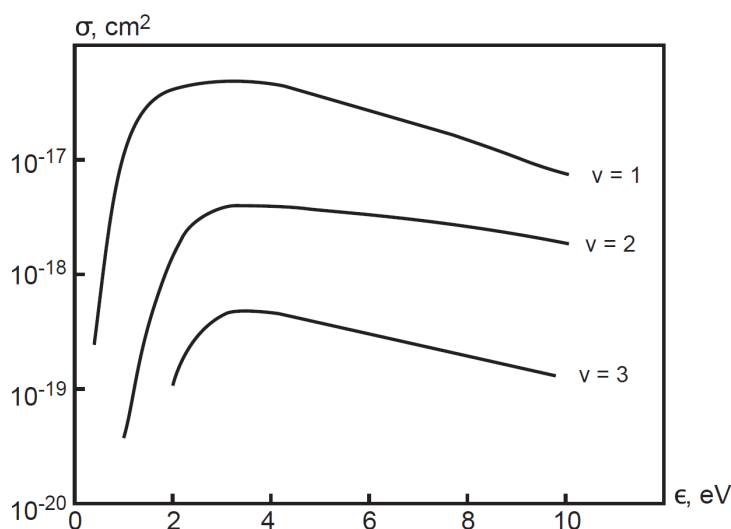
Figure B.3: Cross sections of some vibrational excitation modes (short-lifetime resonances) as a function of electron energy for bi-atomic hydrogen (source: [38]).

section is not a monotonous function of the electronic energy, as it would be supposed, from a classical treatment, using Eq. B.5.

Finally, there is also to consider the meta-stable state lifetime in relation to the period of molecular oscillation (which is approximately equal to 10^{-14} s). When the life of the self-ionized state AB^- is much lower than this quantity, then there are so-called short-lifetime resonances, which give rise to curves such as those shown in Fig. B.3. Mixtures of H_2, N_2O or H_2O are typical examples of gases characterized by cross sections of this type.

When the metastable state lifetime is approximately equal to the molecular oscillation period, then there are the so-called boomerang resonances, corresponding for example to those at low energy for N_2, CO and CO_2. As can be seen in Fig. B.4, they are characterized by trains of gradually decreasing peaks, usually separated in succession from each other by $0.3\,eV$. These peaks are the consequence of the phase interference between the molecular oscillatory movement and the periodic formation/decay of the metastable state. This results, for the cross section, in the typical behaviour of the interference spectra. Furthermore, boomerang resonances require a higher electronic energy to excite the higher levels: for example, the excitation threshold of $N_2(\nu=1)$ is $1.9\,eV$, while that of $N_2(\nu=10)$ is about $3\,eV$.

Finally, long-lifetime resonances correspond to those states of self-ionization with a life longer than 10^{-14} s. Examples include low-energy resonances of O_2, NO, C_6H_6, etc. The resulting cross section curves
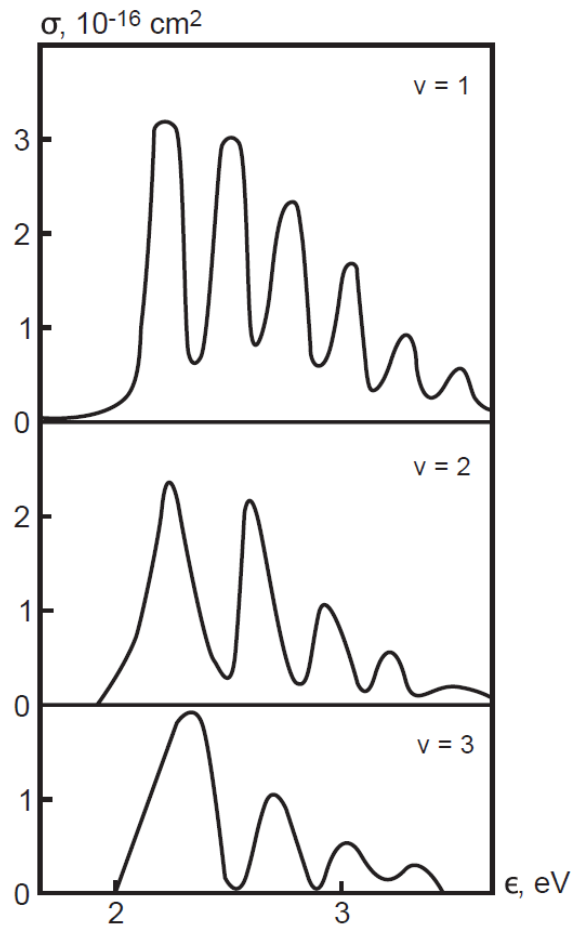
Figure B.4: Cross sections of some vibrational excitation modes (boomerang resonances) as a function of electron energy for bi-atomic nitrogen (source: [38]).

Table B.2: Cross section of vibrational excitation of molecules by electron impact. Adapted from [38].

Molecule	Most effective electron energy eV	Maximum cross section 10^{-16} cm^2
N_2	1.7 - 3.5	3
CO	1.2 - 3.0	3.5
CO_2	3 - 5	2
H_2	3	0.4
H_2O	2 - 3	0.1
O_2	0.1 - 1.5	0.1
NO	0 - 1	0.1
NO_2	0 - 1	-

are characterized by rather narrow isolated peaks (about $0.1\,\text{eV}$). Unlike boomerang resonances, in this case the maximum value of the cross section remains constant as the quantum number changes.

Electron energies that provide the most effective vibrational excitation, as well as corresponding maximum cross sections, are presented in Table B.2.

B.2.2 Rotational excitation

If the electronic energy exceeds $1\,\text{eV}$, the rotational excitation takes place in a resonant manner, similar to the vibrational excitation. However, as shown in Fig. B.2, the rotational contribution is much less than the vibrational contribution.

Non-resonant rotational excitation due to electron impact can be illustrated using the classical approach. Remember that Eq. B.5 establishes the energy transferred during a collision between an electron with energy ϵ and a molecule of mass M. The difference between one rotational energy level and the next is typically $I\dfrac{m}{M}$, where I is the ionization potential. Consequently, the non-resonant cross-section of the rotational excitation can be correlated to the gas-kinetic collisional cross-section $\sigma_0 \approx 10^{-16}$, obtaining:

$$\sigma_{rotational}^{elastic} \approx \sigma_0 \frac{\epsilon}{I} \tag{B.7}$$

As a matter of fact, its maximum value can exceed this reference by about

100 times. On the other hand, quantum considerations lead to very similar conclusions.

An electron collision with a dipole molecule induces rotational transitions with a change of rotational quantum number $\Delta J = 1$. Homonuclear molecules, like N_2 or H_2, have no dipole moment, and rotational excitation is due to electron interaction with their quadruple moment. In this case the rotational transition takes place with a change of rotational quantum number, $\Delta J = 2$. In other words, it is more difficult for these molecules to make a rotational transition, as the energy threshold is higher.

B.2.3   Electronic excitation

Electronic excitation is the most energy-intensive elementary process. The electron, in fact, must have an initial energy higher than $10\,\text{eV}$ to make the affected molecule make a transition of this type.

To determine the cross section it is possible to use the Born approximation. In general, the maximum value that one has for the excitation obtained in an optical way is about equal to the collisional cross section. However, to reach this cross section, the electron energy should be two to three times greater than the transition energy (which means at least $30\,\text{eV}$).

Note, however, that it is still possible to have electronic excitation where optically stimulated transitions are not allowed. In these cases, the maximum cross section (which is always about $10^{-16}\,\text{cm}^2$) can be reached at much lower energy values, such that the ratio between the electronic energy and the transition energy is about 1.5. This makes it possible to witness a predominant excitation of metastable and optically forbidden states in non-thermal discharges, where the electronic temperature T_e is usually much lower than the transition energy. This justifies the significant contribution of electronic excitation from $10\,\text{eV}$ onwards, which can be observed in Fig. B.2.

B.3   Ionization events

In a weakly ionized gas, typically several ionization mechanisms can occur, which in literature are classified into five classes [59, 38]:

- direct ionization by electron impact;

- stepwise ionization by electron impact;

- ionization by collision of heavy particles;

- photo-ionization;

- surface ionization (electron emission).

The first consists in the ionization of neutrals (atoms, molecules or unexcited radicals) by an electron whose kinetic energy is sufficient for creating the process. This is the most important mechanism for non-equilibrium plasmas, where the electric fields are relatively high, but the level of neutral excitation is rather low (since the gas temperature is typically equal to the ambient one).

However, te second is the main ionization mechanism in the case of thermal plasmas, when the gas temperature is very high and therefore the excitation level of the neutrals is already high.

The third mechanism consists of collisions between molecules and ions (or between atoms and ions), including electronically or vibrationally excited species. a possible chemical reaction between the collision partners (called the associative ionizing process) may also contribute to the final energy balance that causes ionization.

Photo-ionization is the phenomenon in which a photon collides with a neutral, producing an ion-electron pair. This mechanism is mostly important in thermal plasmas, but it can also be fundamental in the propagation of certain types of non-thermal discharges (such as partial discharges or coronas).

Finally, surface ionization identifies all those mechanisms that involve the collision of ions, electrons and/or photons with a solid surface facing a gas, or the generation of ionized or excited species by heating a surface.

To these mechanisms must then be added those that tend to reduce the number of excited or ionized species, which are divided into two types:

- recombination;

- attachment.

The first consists of reactions that lead to the removal of charged species, which tend to acquire electrons, or to release them, with or without the presence of intermediate catalysts. The first effect is to change the chemical gas composition and, consequently, to activate (or deactivate) certain reactions in favour of others (or against, respectively).

The attachment phenomenon, instead, consists mainly in the capture of a free electron by an atom, or a molecule, with particularly strong electronegative affinity. This makes it difficult to incept the initial ionization reactions necessary to create the electronic avalanche inside the gas. Mixtures

with molecules of this type can only become plasmas if incredibly intense electric fields are applied or by raising the temperature, which makes them perfect candidates as gaseous dielectric insulators (an example is SF_6).

B.3.1 Direct ionization

The direct ionization of an atom (or molecule) is a collision event with an electron equipped with a high kinetic energy ϵ, which produces a positive ion and another electron, coming from the outermost orbits of the affected particle. By indicating with A, the target atom or molecule, the reaction is written as follows:

$$A + e^- \longrightarrow A^+ + 2\,e^- \tag{B.8}$$

This process occurs only if the energy transferred $\Delta\epsilon$ to the valence electron, following the impact, is higher than the ionization potential I.

To estimate the cross section associated with reaction (B.8), it is possible to use the classic Thomson model [96]. It is assumed that the valence electron at the beginning is at rest and the energetic contribution of the rest of the atom is neglected. The differential cross section of the incident electron can be expressed as a function of the energy yielded by $\Delta\epsilon$ using the Rutherford formula [41]:

$$d\,\sigma_i = \frac{1}{(4\pi\varepsilon_0)^2}\frac{\pi q_e^4}{\epsilon(d\epsilon)^2}d\,(\Delta\epsilon) \tag{B.9}$$

where ε_0 is dielectric constant in vacuum and q_e is the elementary electronic charge. Therefore, by integrating Eq. B.9 on $\Delta\epsilon$, from I to infinity, it is possible to obtain the macroscopic cross-section of the ionization by direct electronic impact, known as Thomson's formula:

$$\sigma_i = \frac{1}{(4\pi\varepsilon_0)^2}\frac{\pi q_e^4}{\epsilon}\left(\frac{1}{I} - \frac{1}{\epsilon}\right) \tag{B.10}$$

In general, the equation just obtained must then be multiplied by the number of electrons of valence possessed by A, Z. At high energies, much higher than I, the Thomson cross section tends to asymptotic value $1/\epsilon$. A more rigorous quantum treatment allows to establish that the asymptotic value is actually equal to $\log(\epsilon)/\epsilon$. In any case, it is worth observing that the Thomson cross section has its maximum value when the energy possessed by the incident electron is equal to twice the ionization energy.

It should also be noted that any interaction between molecules and electrons is really very fast (it takes a time of about 10^{-15} - 10^{-16} s), even
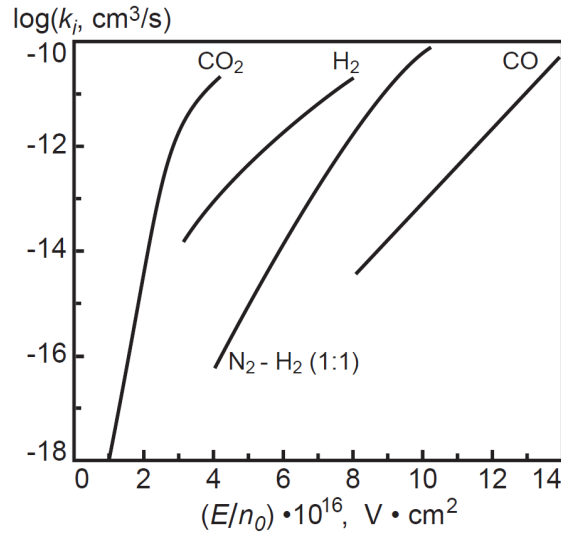
Figure B.5: Reaction rates of ionization by direct electron impact as a function of the specific electric field for some molecular gases. Adapted from [38].

faster than the vibrational movement of the atoms within the molecules (which is about 10^{-13} - 10^{-14} s). This means that all atoms within a molecule can be considered motionless during the electronic transition process caused by the impact with an external electron. This mechanism is known as the Frank-Condon principle.

The ionization reaction rate $k_i(T_e)$ can be calculated by integration of the cross section $sigma_i(\epsilon)$ over the electron energy distribution function. Assuming the Maxwellian one, it can be presented as

$$k_i(T_e) = \sqrt{\frac{8T_e}{\pi m_e}} \sigma_0 e^{-I/T_e} \tag{B.11}$$

where the cross section $\sigma_0 = Z_v \pi (4\pi\varepsilon_0)^2 e^4/I^2$ is about the geometric cross section (for example, for molecular nitrogen is equal to 10^{-16} cm^{-2}).

Data on the ionization by electron impact for different gases are presented in Fig. B.5 as a function of the specific electric field E/n_0, i.e. the ratio of the electric field over the neutrals concentration.

B.3.2 Photo-ionization

It is a process in which an ion is generated due to the absorption of a photon; the latter, in most cases, as will be seen in more detail below, derives from the energy emission of an excited atom when it returns to its

Table B.3: Photo-ionization cross sections for some gas molecules and atoms. Adapted from [38].

Type of gas	Wavelength nm	Cross sections cm^2
Ar	78.7	$3.5 \cdot 10^{-17}$
N_2	79.8	$2.6 \cdot 10^{-17}$
N	48.2	$0.9 \cdot 10^{-17}$
H_2	80.5	$0.7 \cdot 10^{-17}$
H	91.2	$0.6 \cdot 10^{-17}$
O	91.0	$0.3 \cdot 10^{-17}$
O_2	102.0	$0.1 \cdot 10^{-17}$

fundamental state. The constraint that must be satisfied can be expressed as $h\nu > I$, where h is the Planck constant and ν is wave frequency associated with the photon. To trigger ionization, the photon's wavelength must be below $400\,\mathrm{nm}$, i.e. it must be ultraviolet radiation.

Photo-ionization typically begins with a collision in which the energy involved is not sufficient to ionise by direct impact. Nevertheless, it can still lead to an excited state of the affected atom (or molecule). Since the excitement state is unstable, the atom (or molecule) returns to its fundamental state after a few fractions of a second, releasing a photon of energy $h\nu$. The energy emitted is then absorbed by another neutral atom (or molecule), perhaps of a different species. If this time the energy is sufficient to ionise the particle involved, an ion-electron pair is produced. This is the so-called Penning effect. The chain of reactions can be summarized as follows:

$$A + e^- \longrightarrow A^* + e^- \tag{B.12a}$$

$$A^* \longrightarrow A + (h\nu) \tag{B.12b}$$

$$B + (h\nu) \longrightarrow B^+ + e^- \tag{B.12c}$$

On the other hand, the reaction (B.12c) can also be triggered independently by a photon coming from outside the physical system under consideration. Think of the lighting bolt triggering, initiated by the photo-ionization of the surrounding air by the solar wind.

Note that the cross section of the photo-ionization increases very steeply in the area of the spectrum from zero to threshold energy, reaching the geometric cross section in correspondence of the latter. Table B.3 shows the values of the cross sections for some technological gases. They are

quite high. The contribution of the photo-ionization mechanism is usually not significant due to the low number of ultraviolet photons in most practical situations. However, it plays a key role in triggering discharges, as it is the most efficient and rapid way to generate the very first free electrons capable of activating other types of ionization.

B.3.3   Surface ionization

Surface ionization processes are important for sustaining currents near the cathode and supporting the positive balance of charged particles in non-equilibrium discharges.

The most important mechanism in thermal plasma, in this sense, is certainly the thermionic emission. It consists of the continuous expulsion of electrons from a metal surface that is at high temperature. The thermal energy produced helps to drastically reduce the extraction work necessary to tear the valence electrons from the metal surface, which therefore find themselves free in the gas and equipped with a certain kinetic energy. The emitted electrons can remain near the electrode, forming a layer of charged particles that locally neutralizes the electric field and prevents the further emission of electrons. When the latter condition is met, a saturation value is reached for the current density, which is a characteristic parameter of the ionization mechanism. It can be quantified using the so-called Sommerfeld formula:

$$j = \frac{4\pi m_e q_e}{(2\pi\hbar)^3} \, T^2 \, (1 - R) \, e^{-W/T} \tag{B.13}$$

where W is the work function (i.e. the minimum energy necessary to extract an electron form a metal surface), $R = -0.8$ is a quantum-mechanical coefficient describing the reflection of electrons form a potential barrier at the metal surface, T is the surface temperature and $\hbar$ is the reduced Planck's constant.

It should be noted that by varying the electric field, the amount of space charge formed near the cathode, and consequently the saturation current, changes at the same time. To take account of this phenomenon, called the Schottky effect, the work function must be expressed in relation to the local electric field E:

$$W = W_0 - 3.8 \cdot 10^{-4} \cdot \sqrt{E} \tag{B.14}$$

where W is expressed in eV and E in $\mathrm{V\,cm^{-1}}$.

When the field is particularly intense (greater than about $1\,\mathrm{MV\,cm^{-1}}$), it may be able to extract electrons directly from a cold metal surface, without the contribution of temperature. This is possible thanks to the tunnel effect,
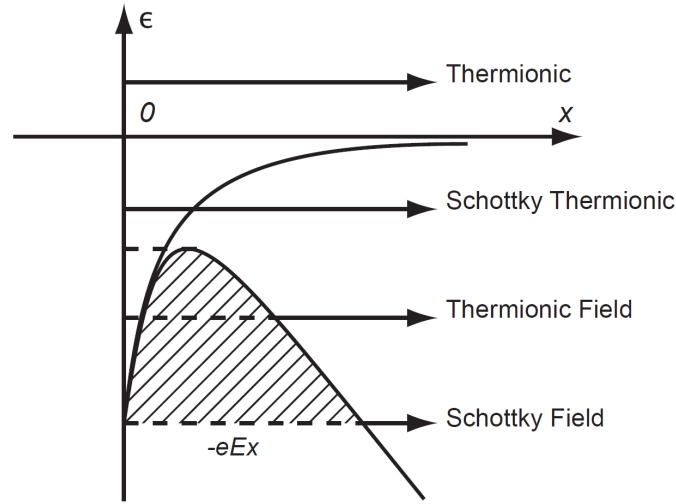
Figure B.6: Schottky effect in thermionic and field emission (source: [38]).

which allows electrons to emerge from their potholes without having the full energy required. This type of mechanism is called field emission effect and is described by the Fowler-Nordheim formula:

$$j = \frac{q_e}{4\pi^2\hbar} \frac{1}{W_0 + \epsilon_F} \sqrt{\frac{\epsilon_F}{W_0}} \exp\left(-\frac{4\sqrt{2m_e}W_0^{3/2}}{3q_e\hbar E}\right) \tag{B.15}$$

where ϵ_F is the Fermi energy of the metal and W_0 its work function not perturbed by an external electric field. Electron tunnelling across the potential barrier influenced by the Schottky effect and corresponding field emission are depicted in Fig. B.6.

When there is the emission of electrons from a solid surface as a result of a heavy particle bombardment, then the phenomenon falls into the category of so-called secondary electronic emission. Of this group, the most important mechanism is the secondary ion-electron emission. It consists in the electronic emission due to the collision between the ions present inside a gas and the atoms (or molecules) that make up the solid surface.

Fig. B.7 shows the trend of the secondary electronic emission coefficient γ_i (electrons produced per ion). As can be seen, the values become important only for very high ionic energies, proving that the energy transfer between electrons and heavy particles is very inefficient. On the other hand, although it is rather low at more modest ionic energies, this phenomenon remains not negligible and the quantity of electrons produced remains about constant below a certain threshold. This can be explained in a similar way
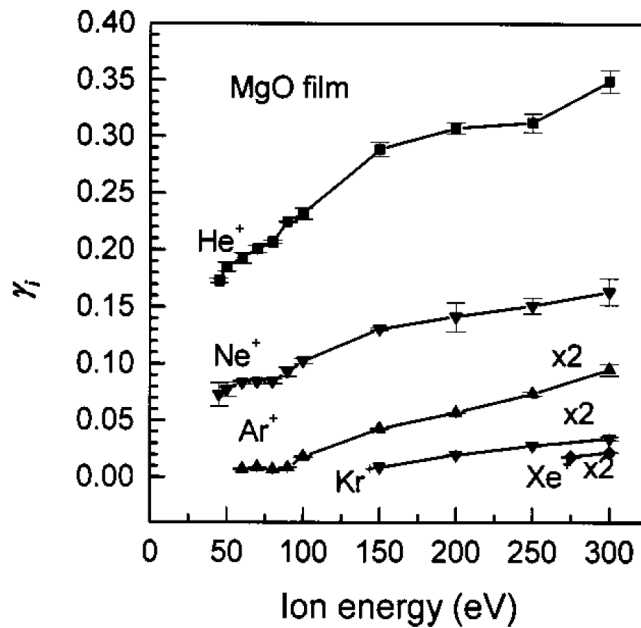
Figure B.7: Secondary electron emission from a polycrystalline MgO thin film for various noble gas as a function of ion energy (source: [74]).

to what happens with the Penning effect: for secondary emission, the so-called potential mechanism is introduced. An ion colliding with the surface extracts an electron from it due to the fact that the ionization potential I exceeds the work function W. The energy difference is usually high enough to allow more than one electron to escape from the surface. This process is not adiabatic and its occurrence probability is not negligible. Consequently, the secondary electronic emission coefficient can be estimated using the following empirical formula:

$$\gamma_i \approx 0.016 \cdot (I - 2W) \qquad \text{(B.16)}$$

where I and W are expressed in eV.

A secondary emission mechanism analogous to the one just described is that of potential electron emission induced by metastable atoms. This is due to the collision between the solid surface and the excited metastable atoms whose energy exceeds that of the work function. In Table B.4 are listed some values for example. It can be noted that in some cases there are quite high electronic emissions.

Another mechanism is that due to the exposure of the surface to high-energy radiation. Photo-electron emission is usually characterized by the quantum yield $\gamma_{h\nu}$, which is defined as the ratio between the number of

Table B.4: Secondary emission coefficient γ for the potential emission induced by collisions with metastable atoms (source: [38]).

Metastable atom	Surface material	γ_m
He($2\,^3$S)	Pt	0.24 electrons/atom
He($2\,^1$S)	Pt	0.4 electrons/atom
Ar*	Cs	0.4 electrons/atom
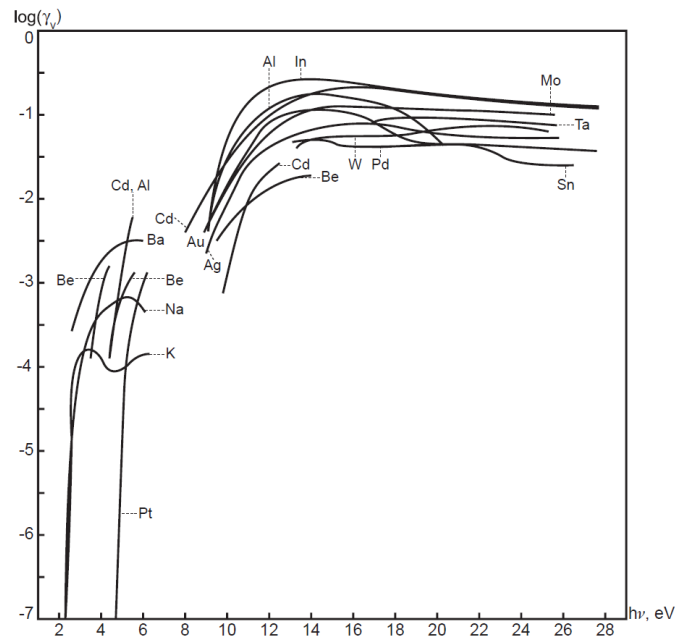
Figure B.8: Secondary photo-electron emission from different metal surfaces as a function of photon energy (source: [38]).

electrons produced and the amount of radiation energy absorbed. Fig. B.8 shows the trend of this parameter as a function of the photon energy $h\nu$ for different types of metal surfaces. It can be seen that, in the case of visible light or low-energy UV radiation, the secondary emission is highly dependent on the material.

Finally, it may be interesting to mention the possibility of having the so-called secondary electron-electron emission, which consists in the extraction of electrons from a solid surface induced by the impact of other electrons. This mechanism can be not negligible in the case of high frequency breakdown of gaps at very low pressures, or even in heterogeneous discharges. In this situation, the so-called multiplication coefficient γ_{e-e},

which is defined as the ratio between the number of emitted electrons and the number of incident electrons, is used.

B.4   Attachment and detachment events

Some chemical reactions may release or remove an electron inside the gas. This does not mean that a consequent ionizing phenomenon occurs automatically. However, it helps to increase or decrease the average rate of ionizing events, since these are mostly due by electrons, the main intermediary between the applied electric field and the other components of the gaseous mixture.

These reactions can be divided into three groups:

- ion-electron recombination;

- negative ion formation;

- negative ion destruction.

B.4.1   Ion-electron recombination

Recombining an ion with an electron is a chemical reaction that releases an abundant amount of energy. The peculiarity of this mechanism provides a method for classifying the different reaction types:

- dissociative electron-ion recombination;

- three-body electron-ion recombination;

- radiative electron-ion recombination;

The first is definitely the fastest mechanism for the removal of a free electron within a gaseous mixture. Its reaction can be written as follows:

$$e^- + AB^+ \longrightarrow (AB)^* \longrightarrow A + B^* \tag{B.17}$$
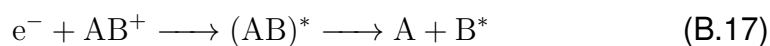
The energy produced in this situation is partly used to break the bond between A and B and partly accumulated by the reaction products in the form of excitation energy. This mechanism is entirely common in molecular gases and can also be important in atomic gases, since it can carry out the so-called ion conversion:

$$A^+ + A + A \longrightarrow A_2{}^+ + A \tag{B.18}$$

The reaction rate for most diatomic and triatomic ions is of the order of 10^{-7} $\mathrm{cm}^3 \, \mathrm{s}^{-1}$. The latter decreases as the temperature increases. However, since this process does not have an activation energy, its dependence on neutrals and electronic temperature is not strong.

The ion conversion reaction rate is also quite high. When the pressure is above $15 \, \mathrm{mbar}$ $(1500 \, \mathrm{Pa})$, the latter type of reaction is usually faster than subsequent dissociative recombinations. The effect of ion conversion is not only a preliminary recombinational stage for single atom ions, but also for molecular ions. Some polyatomic ions have very high recombination rates, often above 10^{-6} $\mathrm{cm}^3 \, \mathrm{s}^{-1}$ at room temperature. This phenomenon means, for example, that molecular air ions, such as N_2^+ and O_2^+, can recombine at ambient pressure to form dimers such as N_4^+ and O_4^+ [38].

If there are no molecular ions, the three-body recombination is mainly responsible for neutralising the ion-electron pairs. A typical reaction of this type can be written as follows:

$$\mathrm{e}^- + \mathrm{e}^- + \mathrm{A}^+ \longrightarrow \mathrm{A}^* + \mathrm{e}^- \tag{B.19}$$
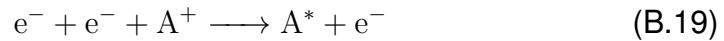
The excess energy is released in the form of kinetic energy acquired by the remaining free electron, which is precisely the third body that activates the reaction. This kind of reaction could not happen if instead of the electron there was a heavier particle, because it would not be able to absorb as quickly the energy generated by the recombination. However, three-body recombination is the most important mechanism in high-density quasi-equilibrium plasmas. Consequently, in this context it is of little interest to further investigate its specific properties.

The last remaining mechanism, the radiative recombination, as the word suggests, releases the energy produced in the form of radiation, expelling a photon:

$$\mathrm{e}^- + \mathrm{A}^+ \longrightarrow \mathrm{A}^* \longrightarrow \mathrm{A} + (\mathrm{h}\nu) \tag{B.20}$$
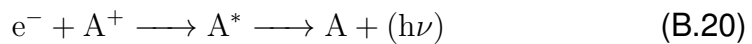
The reaction rate of this process is rather low, as is its cross section, since it requires the emission of a photon in the narrow time window left by the ion-electron recombination. In a similar way to three-body recombination, it is favoured when there are no molecular ions, but it can only compete with the latter if the plasma density is rather low. The cross section of the radiative recombination is of the order of 10^{-21} cm^2 and its reaction rate is inversely proportional to the electronic temperature.
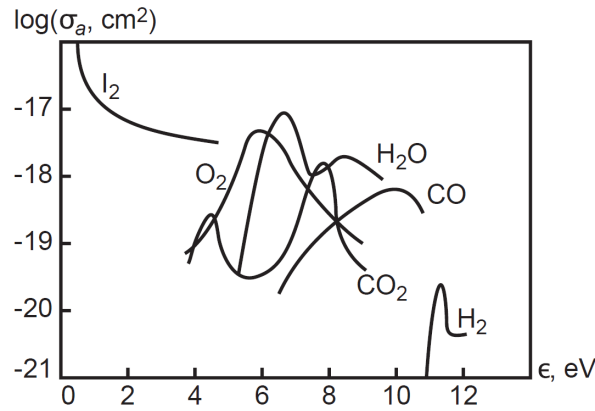
Figure B.9: Cross sections of electron dissociative attachment to different molecules as a function of electron energy. Adapted from [38].

B.4.2 Negative ion formation

The collision of electrons with atoms or molecules does not in all cases lead to ionization or excitation of the latter. For example, when the products of potential reactions are characterized by an electropositive affinity, the so-called dissociative attachment is likely to occur:

$$e^- + AB \longrightarrow (AB^-)^* \longrightarrow A + B^- \tag{B.21}$$
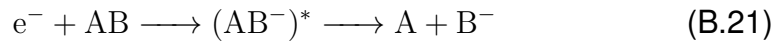
This process is similar to dissociative recombination and proceeds through the formation of an intermediate self-ionizing state. By its very nature, the latter is a highly unstable condition and consequently decays in a very short time, generating dissociation ($A + B^-$) or going back to the initial stage (AB + e^-). Note that, for the reaction to take place, the electron energy must be close enough to a well-defined value: a value too low or too high would lead to the return to the reagents after the intermediate stage, because in the first case it would not have enough energy, while in the second it would not be able to release the excess energy.

The maximum cross-section of this process can be estimated as follows:

$$\sigma_{d.a.}^{(max)} \approx \sigma_0 \sqrt{\frac{m_e(M_A + M_B)}{M_A M_B}} \tag{B.22}$$

where σ_0 is the gas-kinetic cross section, m_e is the electronic mass and M_i is the i-th atom molar mass. Typically there are two orders of magnitude less than σ_0, about 10^{-18} cm^2.

Thanks to its resonant nature, the curve of the cross section as a function of the electronic energy $\sigma_{d.a.}(\epsilon)$ (see Fig. B.9) allows to estimate the reaction

Table B.5: Resonance parameters for dissociative attachment of electrons. Adapted from [38].

Dissociative attachment	$\epsilon_{\mathbf{max}}$ eV	$\sigma_{\mathbf{d.a.}}^{\mathbf{(max)}}$ cm^2	$\Delta\epsilon$ eV
$e^- + O_2 \longrightarrow O^- + O$	6.7	10^{-18}	1
$e^- + H_2 \longrightarrow H^- + H$	3.8	10^{-21}	3.6
$e^- + CO \longrightarrow O^- + C$	10.3	$2 \cdot 10^{-19}$	1.4
$e^- + H_2O \longrightarrow H^- + OH$	6.5	$7 \cdot 10^{-18}$	1
$e^- + H_2O \longrightarrow O^- + H_2$	8.6	10^{-18}	2.1
$e^- + H_2O \longrightarrow H + OH^-$	5	10^{-19}	2
$e^- + CO_2 \longrightarrow O^- + CO$	4.35	$2 \cdot 10^{-19}$	0.8

speed $k_{d.a.}$ as a function of the electronic temperature. Integrating this curve over the Maxwellian distribution, one obtains:

$$k_{d.a.}(T_e) \approx \sigma_{d.a.}^{(max)}(\epsilon_{max})\sqrt{\frac{2\epsilon_{max}}{m_e}}\frac{\Delta\epsilon}{T_e}e^{-\epsilon_{max}/T_e} \tag{B.23}$$

where ϵ_{max} and $\sigma_{d.a.}(\epsilon_{max})$ are the electron energy and the maximum cross section, corresponding to the resonance, and $\Delta\epsilon$ is its energy width. Table B.5 lists the values of these parameters for some reactions of particular technological interest.

Another process that leads to the negative ions formation, with the consequent removal of an electron, is the three-body attachment:

$$e^- + A + B \longrightarrow A^- + B \tag{B.24}$$

This mechanism is the main responsible for the loss of free electrons when the energies involved are not sufficient for the dissociative attachment, or when the pressure is sufficiently high (typically, greater than $100\,\mathrm{mbar}$) to promote three-body kinetics. Unlike the other type of attachment, this reaction is exothermic and its speed does not depend strictly on the electronic temperature.

Atmospheric-pressure air discharges are probably the most important systems, among those in which the three-body attachment plays a fundamental role in the balance of charged particles. The reaction of particular interest is as follows:

$$e^- + O_2 + M \longrightarrow O_2^- + M \tag{B.25}$$

This reaction is the consequence of the so-called Bloch-Bradbury mechanism, which takes place in two successive stages. Initially there is the

Table B.6: Electron three-body attachment reaction rate for Oxygen molecules at room temperature and different third-body partners. Adapted from [38].

Three-body attachment	Reaction rate $\mathrm{cm^6\,s^{-1}}$
$e^- + O_2 + Ar \longrightarrow O_2^- + Ar$	$3 \cdot 10^{-32}$
$e^- + + O_2 + N_2 \longrightarrow O_2^- + N_2$	$1.6 \cdot 10^{-31}$
$e^- + O_2 + O_2 \longrightarrow O_2^- + O_2$	$2.5 \cdot 10^{-30}$
$e^- + O_2 + H_2O \longrightarrow O_2^- + H_2O$	$1.4 \cdot 10^{-129}$
$e^- + O_2 + H_2 \longrightarrow O_2^- + H_2$	$\cdot 10^{-31}$
$e^- + O_2 + CO_2 \longrightarrow O_2^- + CO_2$	$3 \cdot 10^{-30}$

formation of a negative ion excited as a result of a free electron attachment:

$$e^- + O_2 \xleftrightarrow{\mathrm{k_{att}, \tau}} (O_2^-)^* \tag{B.26}$$

where k_{att} is the attachment rate and τ is the average meta-stable lifetime.

The second stage consists in the collision with another particle M (characterized by a density n_M) that leads to the relaxation, and therefore to the stabilization, of the ion O_2^-, or to the return to the initial state of the reaction (B.24). Assuming a stationary condition for the $(O_2^-)^*$ density, the reaction rate of the three-body attachment k_{3M} can be expressed as follows:

$$k_{3M} = \frac{k_{att}}{k_{st}} \frac{1}{\tau} + (k_{st} + k_{dec} n_M) \tag{B.27}$$

where k_{st} is the reaction rate for the relaxation of O_2^- and k_{dec} is the reaction rate for the collisional decay of the unstable ion. If the pressure is not too high, and therefore $(k_{st} + k_{dec})n_0 \ll 1/\tau$, Eq. B.27 is simplified in

$$k_{3M} \approx k_{att} k_{st} \tau \tag{B.28}$$

In other words, the speed of this reaction depends on both the formation and the stabilisation rates of the negative ions. The latter in particular is strongly influenced by the third particle nature: the more complicated the molecule M, the easier it will be to stabilize the meta-stable ion $(O_2^-)^*$ and therefore the greater k_{3M}. Table B.6 shows some reaction speeds as a function of the incident molecule.

A negative ion may be formed through three additional mechanisms, but these are usually less significant. The first is called polar dissociation, and occurs by involving both an ionization and dissociation reaction:

$$e^- + AB \longrightarrow A^+ + B^- + e^- \tag{B.29}$$
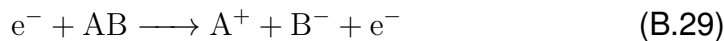
Due to its nature, the threshold energy is quite high. On the other hand, one can notice that there is no capture of an electron, therefore, the process is non-resonant and can take place over a broad energy spectrum.

Although unlikely, due to the short time window available during electronic attachment, excess energy can be released in the form of a photon:

$$e^- + M \longrightarrow (M^-)^* \longrightarrow M^- + (h\nu) \tag{B.30}$$
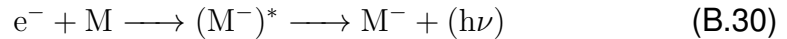
In this case the term is radiative attachment. The cross section for this type of reaction is in the order of 10^{-21} - 10^{-23} cm^2, but it has a rather low threshold energy.

Finally, there are some polyatomic molecules, such as SF$_6$, characterized by a negative ion state very close to the ground one (the energy difference is only $0.1\,\mathrm{eV}$ in the case of SF$_6$). This means that the average life of meta-stable negative ions is really very long, so much so that they can be considered stable in some situations. This type of single-stage attachment is a resonant process and, for really low-energy electrons, its maximum cross-section can reach about 10^{-15} cm^2.

B.4.3 Negative ion destruction

There are several mechanisms that can lead to the removal of a negative ion and the release of a free electron. The most important for non-equilibrium discharges is the so-called associative attachment:

$$A^- + B \longrightarrow (AB^-)^* \longrightarrow AB + e \tag{B.31}$$

This process is evidently the reverse reaction of the dissociative attachment. Reaction speeds typically range between 10^{-10} and 10^{-9} cm^3 s^{-1}.

Another quite important mechanism, especially when there is a high degree of ionization, is that of the electronic impact detachment:

$$e^- + A^- \longrightarrow A + e^- + e^- \tag{B.32}$$

For electrons with energies of about $10\,\mathrm{eV}$, the cross-section for this process can be quite high, about 10^{-14} cm^2.

Finally, a last mechanism worthy of note is the detachment during the collision between excited particles:

$$A^- + B^* \longrightarrow A + B + e^- \tag{B.33}$$

If the excitation energy of particle B exceeds the electronic affinity of particle A, the process results in an electronically non-adiabatic reaction, i.e. there

will be essentially no exchange of kinetic energy between the heavy particles. The exothermic detachment of an electron due to the collision of an oxygen ion with an oxygen molecule in an electronically excited metastable state (excitation energy of $0.98\,\mathrm{eV}$) is an example of such processes:

$$\mathrm{O_2}^- + \mathrm{O_2}(^1\Delta_g) \longrightarrow \mathrm{O_2} + \mathrm{O_2} + \mathrm{e}^-, \quad \Delta H = -0.6\,\mathrm{eV} \tag{B.34}$$
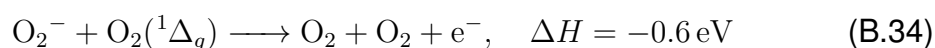
The rate of this reaction is really very high: $2 \cdot 10^{-10}\,\mathrm{cm^3\,s^{-1}}$ at room temperature.

Electronic detachment can also be significant in collisions with vibrationally excited molecules, for example:

$$\mathrm{O_2}^- + \mathrm{O_2}^*(\nu > 3) \longrightarrow \mathrm{O_2} + \mathrm{O_2} + \mathrm{e}^- \tag{B.35}$$
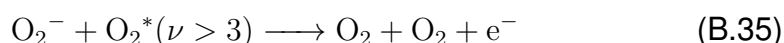
B.5 Some important plasma-chemical reactions

To underline once again the complexity of the discharge phenomenon, the following analyses some types of elementary reactions in which the electrons are not involved, but which nevertheless indirectly influence the evolution of the discharge. In fact, although they are not directly responsible for the generation or capture of an electron, they influence the chemical gas composition, producing or subtracting the ions involved in the events with the electrons.

The first mechanisms of this type to be treated in order of importance are ionic-molecular reactions. These have already been encountered in the form of an intermediate stage, for example, in the dissociative ion-electron recombination. Another example is the chain of ionic-molecular reactions that lead to the oxidation of SO_2 in air, and thus to its subsequent removal, during the cleaning of exhaust combustion gases.

The ionic-molecular reactions start when there is dispersion in a polarization potential, which leads to the so-called Langevin capture of a charged particle and the formation of an intermediate ion-molecule complex. If a neutral particle has no dipole moment, the interaction occurs because of the dipole moment impressed on the neutral particle by the effect of the electric field E generated by the ion. An overview of the polarization scattering process is shown in Fig. B.10. Overall, the phenomenon can be reformulated into the following chemical reaction:

$$\mathrm{A}^+ + \mathrm{B} + \mathrm{M} \longrightarrow \mathrm{AB}^+ + \mathrm{M} \tag{B.36}$$

Another interesting phenomenon that occurs within ionized gases is the ion-atomic charge transfer, which corresponds to the exchange of an
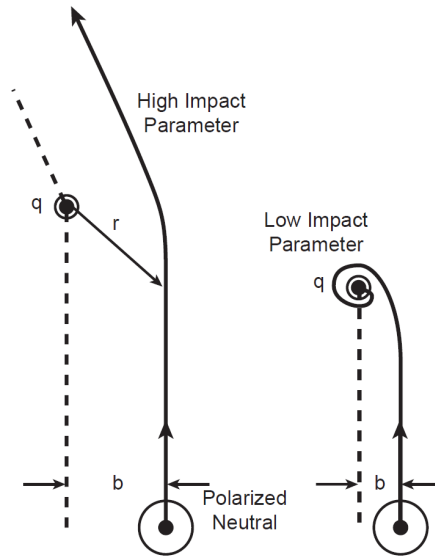
Figure B.10: Langevin scattering or capture in polarization potential in two different cases. Adapted from [38].

electron from a neutral particle to a positive ion, or from a negative ion to a neutral particle. If the reaction occurs without energy release or absorption, i.e. $\Delta E = 0$, then it is called resonant charge transfer; otherwise, it is named non-resonant. The first typology is characterized by a very wide cross section and it is a non-adiabatic phenomenon.

Consider the reaction between a neutral particle B, initially assumed at rest, and a positive ion A$^+$:

$$A^+ + B-> A + B^+ \tag{B.37}$$

The system potential energy is given by the Coulomb formula, referred to an electron that is in the field of A$^+$ and B$^+$:

$$U(z) = -\frac{q_e^2}{4\pi\varepsilon_0 z} - \frac{q_e^2}{4\pi\varepsilon_0 |r_{AB} - z|} \tag{B.38}$$

where r_{AB} is the distance between the centres of A and B. The maximum potential energy is reached at $z = r_{AB}/2$. As a result, charge exchange is possible, in the classic scenario, if the maximum potential energy U_{max} is lower than the initial electronic energy E_B:

$$E_B = -\frac{I_B}{n^2} - \frac{q_e^2}{4\pi\varepsilon_0 r_{AB}} \geq U_{max} \tag{B.39}$$

where I_B is the ionization potential of B and n is its state number. This means that the maximum distance permitted between the interacting heavy particles is

$$r_{AB}^{(max)} = \frac{3q_e^2 n^2}{4\pi\varepsilon_0 I_B} \tag{B.40}$$

In the hypothesis that the process is resonant and not energetically limited, its classical cross section is expressed as follows:

$$\sigma_{chtr}^{(class)} = \pi r_{AB}^2 = \frac{9q_e^4 n^4}{16\pi\varepsilon_0^2 I_B^2} \tag{B.41}$$

This does not depend on the kinetic energy of the interacting species and its value is about equal to the kinetic cross section for neutral collisions when considering the resting state ($n = 1$). Note that, in reality, the cross section of the resonant charge transfer can be much higher if quantum effects are considered and it is expected that the electron can overcome the potential barrier for tunnel effect. In this case, the dependence on the speed of the species in play is had and, in numerical terms, values can be reached up to $10^{-14}\,\mathrm{cm^2}$, for speed around $10^5\,\mathrm{cm\,s^{-1}}$.

Electronic transfer from Oxygen to Nitrogen is a typical example of non-resonant charge transfer with an energy defect of $1\,\mathrm{eV}$:

$$\mathrm{N^+ + O \longrightarrow N + O^+}, \quad \Delta E = -0.9\,\mathrm{eV} \tag{B.42}$$
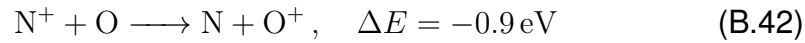
The ionization energy of oxygen ($13.6\,\mathrm{eV}$ eV) is lower than that of nitrogen (which is $14.5\,\mathrm{eV}$). This means that the transfer of charge from the first to the second is an exothermic process.

This reaction is important to consider during the air ionization because it manifests to the latter an acidic behaviour. Ionization mainly generates a large amount of $\mathrm{N_2^+}$ ions, due to the strong presence of nitrogen in the mixture composition, while the low ionization potential and the high dipole moment of water molecules activate the following charge exchange:

$$\mathrm{N_2^+ + H_2O \longrightarrow N_2 + H_2O^+}, \quad k(300\mathrm{K}) = 2.2 \cdot 10^{-9}\,\mathrm{cm^3, s^{-1}} \tag{B.43}$$

The whole mechanism can therefore catalyse the formation of water ions $\mathrm{H_2O^+}$ even when the molar fraction of water is low. Thus, the generated ions can then react, in turn, with the water molecules that have remained neutral by means of the following ion-molecular reaction:

$$\mathrm{H_2O^+ + H_2O \longrightarrow H_3O^+ + OH}, \quad \Delta E = -0.52\,\mathrm{eV} \tag{B.44}$$
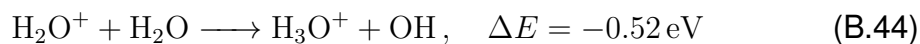
This reaction is characterized by a fairly high speed ($k\,(350\,\mathrm{K}) = 0.5 \cdot 10^{-3}$ $\mathrm{cm^3\,s^{-1}}$) and the generation of $\mathrm{H_3O^+}$ ions and OH-radicals causes the air plasma to show acidic behaviour.

A further type of reaction to consider is the recombination of negative and positive ions to reform a neutral molecule. The loss of charged particles in electronegative gases is mainly due to this class of reactions or to three-body collisions. The recombination of ion-ion, however, can occur through different mechanisms, depending on the level of pressure at which the gas is. A common feature of all these modes is a high reaction rate.

In particular, above $40\,\mathrm{mbar}$ ($4\,\mathrm{kPa}$) ion-ion recombination is dominated by three-body reactions. In this situation, the maximum attainable speed is $3 \cdot 10^{-6}\,\mathrm{cm^3\,s^{-1}}$, at a pressure slightly lower than atmospheric pressure and at room temperature. At lower pressures, three-body reactions are slowed down and, therefore, binary collisions with energy release, in the form of electronic excitation, take over.

In the first case, the reaction takes place by means of a triple collision, involving a heavy neutral:

$$\mathrm{A^- + B^+ + M \longrightarrow A + B + M} \tag{B.45}$$
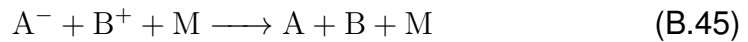
At pressures above $30\,\mathrm{mbar}$, according to Thomson's theory, recombination occurs when the ions involved approach a shorter distance than the critical one,

$$b \approx \frac{q_e^2}{4\pi\varepsilon_0 T_0} \tag{B.46}$$

and at the same time the reaction can reach the thermal energy (T_0), so that it can be absorbed effectively by the third body. It can be shown that the reaction speed can be written as follows:

$$w_{ii} =\approx (\sigma v_t)\frac{q_e^6}{(4\pi\varepsilon_0)^3 T_0^3}n_0 n_- n_+ \tag{B.47}$$

where σ is the cross section of ion-neutral elastic scattering, v_t is the average velocity of heavy particles, n_0 is the neutral particle density, n_- and n_+ are the negative and positive ion densities. The third and second ($k_{r2}^{ii} = k_{r3}^{ii} n_0$) kinetic order rate coefficients are presented in Table B.7 for some specific processes. Binary and triple collisions contribute equally to the ion-ion recombination at pressures between 15 and $40\,\mathrm{mbar}$. Growth is limited to moderate pressures due to the fact that the critical distance b must be less than the average free ion path, which is equal to $1/n_0\sigma$. For the same reason, at pressures equal to or greater than atmospheric pressure, the number of recombinations is reduced, since the ions undergo

Table B.7: Reaction rates of three-body ion-ion recombination at room temperature and moderate pressures. The second kinetic order reaction rates are recalculated assuming a pressure of $1\,\mathrm{bar}$ and a concentration of neutrals of $2.7 \cdot 10^{19}\ \mathrm{cm}^{-3}$. Adapted from [38].

Ion-ion recombination reaction	Rate coefficient	
	third order	second order
$O_2{}^- + O_4{}^+ + O_2 \longrightarrow O_2 + O_2 + O_2 + O_2$	$1.55 \cdot 10^{-25}\ \mathrm{cm}^6\,\mathrm{s}^{-1}$	$4.2 \cdot 10^{-6}\ \mathrm{cm}^3\,\mathrm{s}^{-1}$
$O^- + O_2{}^+ + O_2 \longrightarrow O_3 + O_2$	$3.7 \cdot 10^{-25}\ \mathrm{cm}^6\,\mathrm{s}^{-1}$	$10^{-5}\ \mathrm{cm}^3\,\mathrm{s}^{-1}$
$NO_2{}^- + NO^+ + O_2 \longrightarrow NO_2 + NO + O_2$	$3.4 \cdot 10^{-26}\ \mathrm{cm}^6\,\mathrm{s}^{-1}$	$0.9 \cdot 10^{-6}\ \mathrm{cm}^3\,\mathrm{s}^{-1}$
$NO_2{}^- + NO^+ + N_2 \longrightarrow NO_2 + NO + N_2$	$10^{-25}\ \mathrm{cm}^6\,\mathrm{s}^{-1}$	$2.7 \cdot 10^{-6}\ \mathrm{cm}^3\,\mathrm{s}^{-1}$

Table B.8: Reaction rates and released energies of ion-ion recombination in binary collisions at room temperature ($300\,\mathrm{K}$). Adapted from [38].

Recombination reaction	Energy eV	Rate coefficient $\mathrm{cm}^3\,\mathrm{s}^{-1}$
$H^- + H^+ \longrightarrow H + H$	12.8	$3.9 \cdot 10^{-7}$
$O^- + O^+ \longrightarrow O + O$	12.1	$2.7 \cdot 10^{-7}$
$O^- + N^+ \longrightarrow O + N$	13.1	$2.6 \cdot 10^{-7}$
$O^- + O_2{}^+ \longrightarrow O + O_2$	11.6	10^{-7}
$O^- + NO^+ \longrightarrow O + NO$	7.8	$4.9 \cdot 10^{-7}$
$NO_2{}^- + NO^+ \longrightarrow NO_2 + NO$	5.7	$4 \cdot 10^{-8}$
$O_2{}^- + O^+ \longrightarrow O_2 + O$	13.2	$3 \cdot 10^{-7}$
$O_2{}^- + O_2{}^+ \longrightarrow O_2 + O_2$	11.6	$4.2 \cdot 10^{-7}$
$O_2{}^- + N_2{}^+ \longrightarrow O_2 + N_2$	15.1	$1.6 \cdot 10^{-7}$

a multitude of collisions, but without having enough energy to actuate the reaction. The highest recombination rate coefficient is achieved at neutral density equal to

$$n_0 \approx \frac{4\pi\varepsilon_0 T_0}{\sigma q_e^2} \tag{B.48}$$

corresponding more or less to atmospheric pressure.

The ion-ion recombination in the form of a binary collision can be written as follows:

$$A^- + B^+ \longrightarrow A + B^* \tag{B.49}$$

Below $15\,\mathrm{mbar}$, the reaction speed typically assumes a value in the order of $10^{-17}\ \mathrm{cm}^3\,\mathrm{s}^{-1}$. Some of the exact values, together with the energies released, are listed in Table B.8.

Finally, it should be mentioned that the impact between an electron
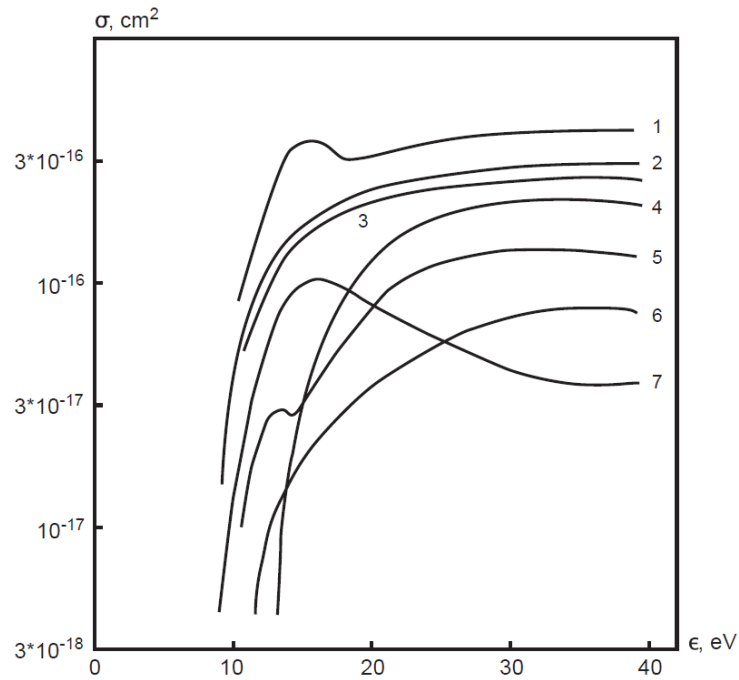
Figure B.11: Cross sections of dissociation of molecules through electronic excitation as a function of electron energy. 1: CH_4; 2: O_2; 3: NO; 4: N_2; 5: CO_2; 6: CO; 7: H_2. Adapted from [38].

and a molecule can sometimes stimulate the dissociation of the latter. The dissociation due to a vibrational excitation occurs through an indirect process of multiple stages. This type of mechanism is only effective for a limited set of gases, such as N_2, CO_2, H_2 and CO, which are nevertheless of great interest from a practical point of view. On the contrary, the dissociation due to an electronic excitation can occur in a single collision: this makes it possible to describe it as a direct electronic impact. Cross sections of the dissociation by direct electron impact are presented as a function of electron energy in Fig. B.11.

C

The Weibull distribution

In many cases, a statistical analysis of the data has been used, making use of the Weibull distribution. In this appendix the aim is to give some historical notes on the above mentioned mathematical instrument and on the theoretical and experimental reasons that lead to its widespread use for the analysis of partial discharges and accelerated ageing tests. Furthermore, some additional information from the literature is provided, explaining how to evaluate the quality of the collected data and how to pay attention to possible laboratory errors during post-processing.

C.1   Introduction

The intrinsic characteristic of the partial discharge inception voltage, the service life and the breakdown voltage (i.e. the dielectric strength) of a real insulator is that they are a random variable.

For instance, it has been seen that in a gas there is a voltage range in which the discharge may or may not occur, depending on the presence or not, in the inter-electrode space, of initial electrons capable of being accelerated to initialize the electronic avalanche. In this range, each voltage value corresponds to a discharge probability that can be estimated from the frequency with which the discharge occurs during the tests, a frequency defined by the ratio n/N between the number of discharges and the total number of tests with that voltage value.

Below a certain value V_{min} the discharge never occurs (zero probability), while above a value V_{max} it always occurs (unit probability). The interval between V_{min} and V_{Vmax} varies depending on the system geometry, the nature of the materials present and the environmental conditions: in this

specific case, it is the smaller the more the test conditions are defined, in particular irradiation and humidity.

Since the dispersion of the values is evidently greater the less homogeneous the material and the geometry are, it is understood that only by examining the results from a statistical point of view is it possible to face and solve the problem of extrapolating the results of the tests on samples to the much larger complete insulations.

This is one of the problems that arise in practice, but alongside it other equally important problems, such as the knowledge of the confidence level of a certain result or the risk that one runs by adopting certain constructive solutions or test voltages. Indeed, the tendency is to face the problem of insulation from a statistical point of view, accepting a certain probability of failure in the search for the best technical-economic compromise. The probability function normally used in such cases is the Weibull distribution [91].

Wallodi Weibull invented the distribution that now bears his name in 1937 and officially published his comments on it in 1951. He stated at the time that his function could be applied in a large number of cases, ranging from estimating the useful life of bearings to establishing the average height of adult males in Britain. In his article he wrote *«[..] may sometimes render good service»* [99].

The first to recognize the potential of this instrument were the researchers of the U.S. Air Force, who financed the experimentation of Weibull until 1975. Dorian Shainin, meanwhile, introduced Weibull to the Hartford Graduate Center in the mid-1950s and encouraged Pratt & Whitney Aircraft to use his analysis.

Later, E. J. Gumbel demonstrated that if a part has several possible failure mechanisms, the Weibull distribution is the best model for estimating its useful life. This is the so-called *weakest-link-in-the-chain* concept. The same author also discovered that the Weibull method can give some information even in cases where the sample is extremely small, even two or three failures for engineering analysis [44].

The greatest merit of Weibull's technique, and what has decreed its undoubted success, is precisely the possibility of giving some indication of a practical-engineering nature, even when the number of tests is very small. This is particularly appreciated in those cases where the objects to be tested are expensive to make or when the nature of certain failures must be understood in order to avoid new ones in the near future.

A further advantage is that it provides information even in the event of inconsistencies in the data. A bad Weibull graph usually presents data that can be used by the experienced engineer to read them.

The origin of this robustness is due to the fact that several distributions
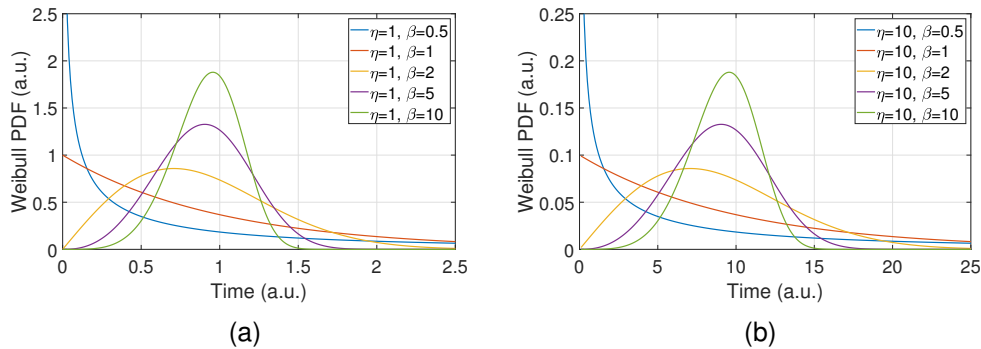
Figure C.1: The shapes of the 2-parameter Weibull family. Weibull PDF for (a) $\eta = 1$ and (b) $\eta = 10$.

are included, some in an exact way, others in an approximate way, in the family of functions defined by Weibull distribution, including the Gaussian, the exponential, the binomial, the Rayleigh and the Poisson.

The Log Normal is not a member of the Weibull family and it is a better choice for some material characteristics, for crack growth rate and for non-linear accelerating system ageing [2]. However, usually a consistent sample (at least twenty failures) is required for another distribution to be preferred in place of Weibull's. With less than 20 failures, the Weibull is the best choice and, therefore, best practice.

C.2 Theoretical background

The Weibull distribution can be of two types: with two or three parameters. The first is by far the most widely used for life data analysis. Weibull's two-parameter cumulative distribution function (CDF) provides the probability of failure $F(t)$ to arrive at a life t and is expressed as follows:

$$F(t) = 1 - e^{-(t/\eta)^{\beta}} \tag{C.1}$$

where $F(t)$ is the fraction up-to-time t, t is the failure time, η is the so-called scale parameter, while β is the shape parameter.

The function of probability density from which it derives is as follows:

$$f(t) = \frac{\beta}{\eta} \left(\frac{t}{\eta} \right)^{\beta-1} e^{-(t/\eta)^{\beta}} \tag{C.2}$$
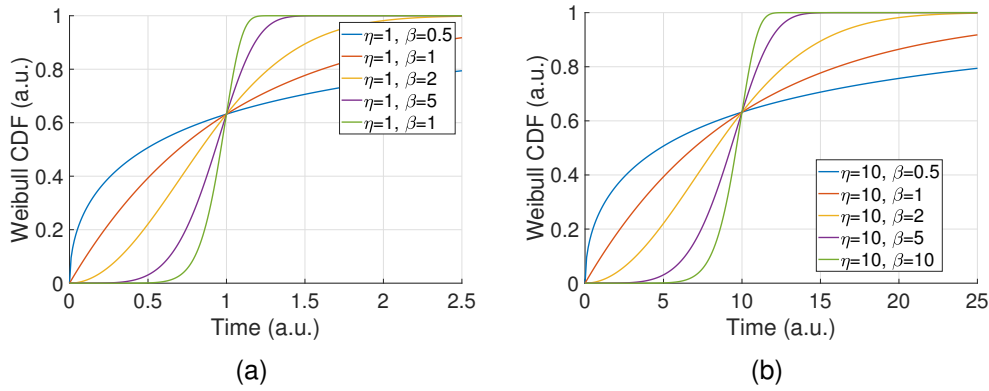
Figure C.2: The shapes of the 2-parameter Weibull family. Weibull CDF for (a) $\eta = 1$ and (b) $\eta = 10$.

The values of the two parameters characterize the distribution. Figs. C.1 and C.2 show the reason why these two quantities were defined in this way. As can be seen, when β varies, the curve assumes very different trends (shapes), while η enlarges or reduces the curve (i.e. it acts on the scale factor).

Sometimes it may be useful to express instead the complementary function, the so called reliability $R(t)$: it is defined as the probability that there is no failure until time t. It is written as:

$$R(t) = 1 - F(t) = e^{-(t/\eta)^{\beta}} \tag{C.3}$$

Finally, for the sake of completeness, the hazard function $h(t)$ is also shown, which corresponds to the instantaneous fault rate:

$$h(t) = \frac{\beta}{\eta} \left(\frac{t}{\eta} \right)^{\beta - 1} \tag{C.4}$$

It can be noted that the distribution of parameters $(\eta, 1)$ corresponds to the exponential distribution $E(\eta)$, which describes the life span of a phenomenon without memory. Similarly, the distribution of parameters $(\eta, 2)$ corresponds instead to Rayleigh distribution, which is essentially a two-degree freedom chi distribution.

It is possible to demonstrate that the two parameters are linked by the so-called mean-time-to-failure, indicated by the acronym $MTTF$, and the relationship is expressed by:

$$MTTF = \eta \Gamma (1 + 1/\beta) \tag{C.5}$$
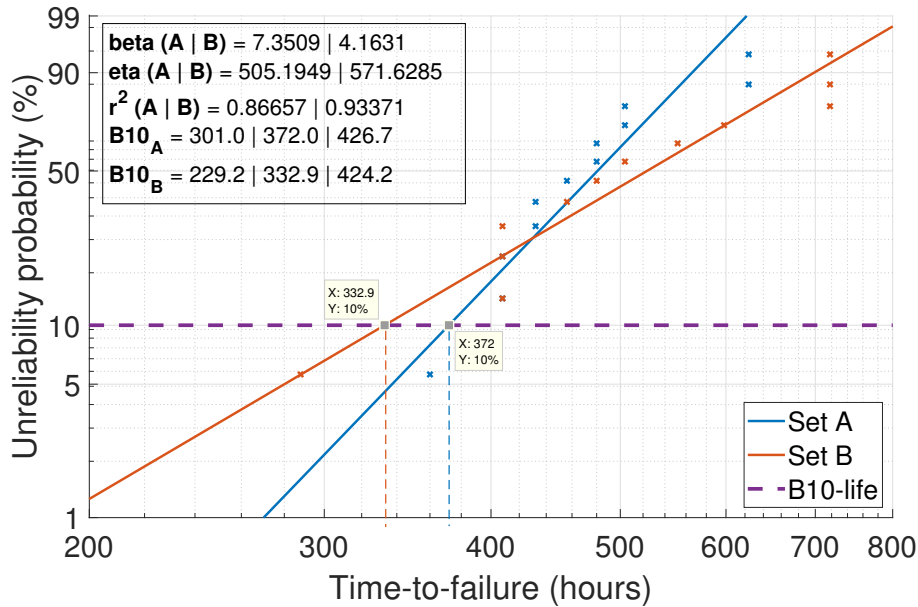
Figure C.3: A typical Weibull plot for the statistical analysis of the failure data.

where $\Gamma(x)$ is the Gamma function. It should also be noted that η represents the service life of 63.2% of the units studied.

Weibull coined a definition to quickly indicate the useful lives corresponding to a certain percentage of failures. He called them *B-lives*. In Fig. C.3, the B10-life for the second set of samples is about $333\,\text{h}$. This means that 1% of a hypothetical population of those pieces will fail in about $333\,\text{h}$. It also means that one can be confident that at least 99% of the parts will reach $333\,\text{h}$ of service (i.e. the reliability of the component is expressed). Note that the scale is defined in such a way that, if the data follow the Weibull distribution, they will be placed close to a straight line. In addition, the graph shows the confidence intervals for B10-life (5% and 95%) and the value of r^2, which establishes the goodness of the interpolation.

Graphs like the one shown in Fig. C.3 are called Weibull plots. From these one can get all the information of interest. However, as one can see immediately, these graphs do not depict the Weibull distribution normally, but make sure that its trend is linear with the time-to-failure.

To draw a Weibull plot, one must first sort the data from the smallest to the largest and estimate the corresponding value of $F(t)$ related to the corresponding rank. Note that the true percentage is unknown. The most appropriate technique to do this is that of the *median rank*. In practice, the value of $F(t)$ is calculated using the incomplete Beta distribution, setting

the probability value at 50%:

$$F(t_i) = \frac{1}{\beta(i, N - i + 1)} \int_0^{0.5} x^{i-1}(1 - x)^{N-i+1} dx \qquad \text{(C.6)}$$

where i is the sequence number assigned to the time-to-failure t_i after sorting, N is the size of the data set and $\beta(x, y)$ is the Beta function:

$$\beta(x, y) = \int_0^1 \tau^{x-1}(1 - \tau)^{y-1} d\tau \qquad \text{(C.7)}$$

At this point, one is able to estimate the pair of parameters to choose because the Weibull curve better approximates the behaviour of the data collected. Rearranging (C.1), applying for two consecutive times the logarithmic function to both members, it is possible to obtain a linear trend:

$$\log\left\{\log\left[\frac{1}{1 - F(t)}\right]\right\} = \beta \log(t) - \beta \log(\eta) \qquad \text{(C.8)}$$

By making a change of variable, one obtains the equation of the straight line and the relationships between its coefficients and the parameters β and η:

$$Y = p_1 X + p_2, \qquad \text{with } \beta = p_1 \text{ and } \eta = e^{-p_2/\beta} \qquad \text{(C.9)}$$

Therefore, the data is interpolated, fixing as variables $X = \log(t)$ and $Y = \log\log[1/(1 - F(t)]$, and the value of the parameters of the desired Weibull distribution is estimated through (C.9).

A variant of this procedure can be used to censor data collected that have not failed or that have undergone a failure mechanism unlike any other. These data cannot be ignored altogether, although they are not entirely relevant to the analysis.

The so-called suspended points are therefore not shown in the graph, but the sorting and the median ranks must be adjusted to their presence. The procedure involves ordering the data first, taking into account the suspensions, after which the so-called Auth formula is used to determine the adjusted ranks:

$$n_j = \frac{(N - i + 1)n_{j-1} + (N + 1)}{(N - i + 1) + 1} \qquad \text{(C.10)}$$

where n_j is the j-th adjusted rank of a non-suspended point, i is the non-suspended point original sequence number and N is the total number of points (sum of failures and suspensions). The major effect of the suspensions is to increase η. β generally is minimally affected (earlier failure times

Table C.1: Example of calculation of adjusted ranks and median ranks with censored or suspended data.

Rank	Hours to failure	Reverse rank	Adjusted rank	Median rank
1	288	12	suspended	-
2	408	11	1.0833	6.27%
3	408	10	2.1667	14.94%
4	408	9	3.2500	23.69%
5	456	8	4.3333	32.46%
6	480	7	suspended	-
7	504	6	5.5714	42.48%
8	552	5	6.8095	52.51%
9	598	4	8.0476	62.53%
10	718	3	9.2857	72.55%
11	718	2	suspended	-
12	718	1	suspended	-

have no adjusted rank numbers, so they haven't an impact on parameters' variations). Table C.1 shows an example of a complete calculation that takes into account the presence of suspended and censored data.

For the calculation of the median ranks, which can be a bit laborious, it is possible to use the so-called Benard's approximation, which gives a sufficiently accurate estimate (accuracy of 1% for $N = 5$ and 0.1% for $N = 50$):

$$F(t_i) = \frac{i - 0.3}{N + 0.4}$$

(C.11)

This formula can also be used in the case of suspensions, replacing i with the adjusted rank n_j.

C.3 Confidence intervals for B-lives and reliability

The strength, but at the same time the weakness, of Weibull's analysis lies in the robustness of the results even in situations where the number of samples is really small. One way to improve the quality of information obtained with this approach is to visualize the confidence intervals associated with the estimated B-lives.

Generally, confidence levels of 90% are used and silently implied. In applications where safety and reliability are essential, such as in the medical or aerospace industries, it is not uncommon to see wider confidence intervals of up to 99%.

To calculate the 90% confidence levels, for example, for the B-lives one must find the 5th and 95th percentiles of the distribution of the latter at the desired uncertainty. This distribution, however, is not at all easy to determine and it is practically impossible to give an analytical definition. However, there are several methods to estimate it, or approximating it to a known distribution or applying transformations to the B-lives.

The most popular techniques are as follows:

- beta-binomial bounds;

- Fisher's matrix bounds;

- likelihood ratio bounds;

- Monte Carlo pivotal bounds.

In practice, especially at the software level, it is common to use the last of the methods listed. In literature [2, 95], moreover, it is argued that the technique with Monte Carlo pivotals is the best practice when using the median rank regression. If the sample size was large enough (> 400), then the likelihood ratio bounds would be faster to calculate. The following is a description of the approach used to analyse the data obtained from the experiments described in this thesis.

To depend as little as possible on the data set one is processing, as very often done in statistics to perform a bootstrap, a pivotal quantity is defined. In this case, the pivot for determining the distribution of B-lives is written as follows:

$$Z_p = \frac{u - y_p}{b} \tag{C.12}$$

with

$$u = \log(\eta) \tag{C.13}$$
$$y_p = \log(t_p) \tag{C.14}$$
$$b = 1/\beta \tag{C.15}$$

where t_p is the B[$100 \cdot p$]-life. Practically, t_p is the B[$100 \cdot p$]-life where the confidence bound is to be calculated.

At this point, a Monte Carlo method is implemented in which R sets of data of the same size as that obtained from real measurements are generated.

For the sake of clarity, the following will indicate the set of data actually collected, characterized by an estimated Weibull of parameters $(\hat{\beta}, \hat{\eta})$, such as:

$$T = \{t_1, t_2, .., t_N\} \tag{C.16}$$

where N is the sample size (sum of failures and suspensions), while a synthetic sample shall be identified with the following wording:

$$T*_i = \{t_1^i, t_2^i, .., t_N^i\}, \qquad \text{with } i = 1, .., R \tag{C.17}$$

The R synthetic samples, since by definition the pivot is independent of the parameters, are randomly generated by sampling a standard Weibull distribution ($\beta = \eta = 1$). On the other hand, the synthetic sample will be characterized by slightly different actual parameters, which will be indicated as (β_i, η_i). Their estimation can be obtained by always applying the (C.9).

Once the R synthetic samples have been generated, it is possible to calculate the pivot for each one and thus build a distribution. Once this is done, to determine the confidence interval it is sufficient to identify the 5th and 95th percentile of Z_p and calculate the corresponding B[$100 \cdot p$]-life through the (C.12):

$$y_{(p,q)} = \log(\hat{\eta}) - Z_{(p,q)}/\hat{\beta} \tag{C.18}$$
$$t_{(p,q)} = e^{y_{(p,q)}} \tag{C.19}$$

where q is the desired percentile.

C.4   Interpreting the Weibull plot

The analysis of fault data using Weibull distribution must always be carried out bearing in mind that this is a compromise between theory and practice. The point is that this function, after having been extensively tested in the engineering field, has given excellent results for the estimation of failure times, even with a very small number of samples.

In view of this, the role of the shape parameter, β, needs to be further investigated as it is linked to the mechanisms that cause the failure. In particular, four main zones can be identified:

- $\beta < 1$, which implies so-called infant mortality;

- $\beta = 1$, which implies random failures, independent from ageing;

- $1 < \beta < 4$, which implies early wear out;

- $\beta > 4$, which implies old age wear out.

When $\beta < 1$, i.e. when a considerable percentage of the part population suffers a failure in a short time, one of the following situations may arise:

- inadequate or too much severe test conditions;

- production problems;

- solid state electronic failures.

In the case of test measures, of course it must be ensured that no failed lot has been tested, that there are no failures in the test system and, finally, that there are no errors in the statistical analysis of the data collected.

When $\beta = 1$ means that the faults are time independent. Evidently, somehow a mistake is being made:

- incorrect maintenance may be carried out;

- external events, independent of the monitored equipment, could cause the failure (think of the possibility of a lightning strike falling near a power line);

- competition from different failure mechanisms, each characterised by different β;

- sampling times too long, which do not allow to appreciate the interval between one fault and the next.

If faults occur within the expected service life, they are an unpleasant surprise. There are several fault mechanisms that are characterized by a β between 1 and 4:

- low cycle fatigue, with β which varies from 2.5 to 4;

- corrosion (erosion), with $\beta = 2 - 3.5$;

- ball bearing failures, with β equal to 2;

- V-belts, with $\beta = 2.5$.

If the failure generates a safety hazard, the recommended service life should be vary low, so one has to consider B.1/B.01-life. If the failure mode is benign, the recommended age for overhaul or part replacement may be much higher, for instance B1/B10-life.

Finally, there are those components that are characterized by fault mechanisms with high β. In other words, referring to Fig. C.1, they show a rather low variance, indicating an almost deterministic phenomenon, for which you can have some confidence over their actual service life. They fall into this category:

- parts subjected to corrosion;

- brittle materials, such as ceramics;

- parts stressed by some forms of erosion.

However, it should be noted that β cannot assume indiscriminately high values. In fact, Weibull distributions with too large β are degenerated, because they no longer have information on the shape: any Weibull distribution with steep β can fit well data obtained from random sampling of another Weibull distribution featured by a different, but always elevated, β [29].

In addition, there is also the fact that, as the value of β increases, the phenomenon studied tends to be more and more deterministic. When β is exaggerated, this may be due to an error in the measurement system. In particular, the following cases may occur

- low sensitivity of measuring instruments;

- too high stress;

- too low sampling frequency.

In general, the steep plot often hides bad Weibull data. All the messages from them, as curves, outliers, doglegs, etc., tend to disappear. One expert suggests a distribution analysis is needed for all Weibulls with $\beta > 6$.

Note that the value of β is not the only index to be evaluated, to understand whether the statistical analysis is reliable or not. The other parameter to take into account is the coefficient of determination r^2. Obviously, it is not enough to have a β comparable to that expected to be sure that one has not made mistakes. The coefficients that indicate the goodness of the fitting are able to provide information about the test modes and, in some cases, can identify the overlap of two or more failure mechanisms.

A low value of the coefficient of determination always deserves further investigation. This can typically be caused for two reasons: the presence of outliers or the concomitance of different failure mechanisms. In both cases, the problem must be reflected in the plot.

The presence of outliers is always a difficult problem to approach. If one stays within the purely mathematical sphere, it is impossible to settle

the matter. On the other hand, a physical investigation that discovers the potential reasons that generated that point in the graph usually makes it possible to clarify whether it was an accident, or is actually part of the Weibull data set.

A different matter is the coexistence of different failure mechanisms. This phenomenon is usually easy to spot on the Weibull plot, since one should be able to distinguish two groups of points, within the same data set, characterized by a different linear pattern. Usually, this behaviour is commonly called 'dog-leg' bending and is, indeed, generated by the competition of different failure mechanisms, characterized by different values of β (hence the difference in the angular coefficient of the two subgroups of points). In this situation, beyond a thorough investigation of the parts tested to determine the actual nature of the failure of each, it is possible to estimate the data of interest considering the two data subgroups as separate sets for the Weibull analysis. It should be noted, however, that some points in the first set are very likely to be part of the second set and vice versa. This technique is only useful to obtain approximate estimates, or if it is no longer possible to carry out a physical investigation of the faulty components.

Acknowledgements

This work marks the end of an important chapter in my life. It crowns the success of a journey that began four years ago. However, I did not undertake this journey alone and I want to make it clear that, although there is only my name written on the cover, as they say where I come from, all this flour does not just come from my sack.

First of all I want to thank my supervisor, Prof. Andrea Cavallini. It is thanks to him that the trip was possible and it is thanks to him that I had the chance to collect so many beautiful experiences. His practical approach, without ever neglecting the importance of the theoretical aspects, was an inspiration and an example. Moreover, his total openness to dialogue and comparison make him not only an excellent researcher, but also an incredible mentor.

My heartfelt thanks go to my parents, who can stand my pedantry day after day. A lot has changed in these four years, but I want to put on paper that I will always be grateful to them for the guidance and support they have given me and are still giving me. Wherever my choices take me, it is reassuring to know that I will always find the support I need in them.

Speaking of changes, during this journey, started alone, on the road I met a special person, someone able to give serenity and balance to my daily life. Thank goodness she decided to share the road with me and now we are keeping each other company. Thank you Elisa, for your love and support.

To undertake a PhD and, above all, to complete it successfully, satisfied with experience and pregnant with new knowledge, I found it to be damn difficult. This is true both in Italy and abroad, and it surprised me. The

love for research and scientific divulgation, in some cases, can be a heavy burden. This first reflection led me to (re)found the ADI headquarters in Bologna in 2017, together with Niccolò, Luisa, Elisabetta, Sara and Giovanni. I learned a lot from this experience, both about people and the hidden motivations that pushed me to do what I did every day. But I hope it wasn't a one-sided exchange: I hope I gave some of that passion that animates me to the people I met, so that the researchers of tomorrow can do even better than those of today. Thanks again!

Finally, it is clear that I want to thank all the people with whom I have formed a bond and with whom I usually share my joys and sorrows. The discussions, as well as the activities outside the laboratory or office, are sometimes more important than those with colleagues. What I have understood in these four years is that research has no rules, because we are constantly exploring unknown territories. One can start from a well known atoll, but in order to innovate, sooner or later he will have to navigate on sight, without knowing where he is going. One should never underestimate the importance of talking to others, of listening to their stories and their ideas, of trying to adopt their way of thinking. Sharing has been recognized as an indispensable tool for research, precisely because it stimulates new ways of thinking, of seeing things, of finding solutions to problems that could torment one for years. So, thanks to all of you, whether willingly or not, you have contributed to the crowning achievement of this work!

Ringraziamenti

Questo lavoro sancisce la fine di un importante capitolo della mia vita. Corona il successo di un viaggio iniziato ormai quattro anni fa. Questo viaggio, però, non l'ho intrapreso da solo e voglio chiarire che, sebbene ci sia solo il mio nome scritto sulla copertina, come si suol dire dalle mie parti, tutta questa farina non proviene soltanto dal mio sacco.

Innanzitutto voglio ringraziare il mio supervisore, il Prof. Andrea Cavallini. È per merito suo che il viaggio è stato possibile ed è grazie a lui che ho avuto la possibilità di collezionare così tante belle esperienze. Il suo approccio pratico, senza mai tralasciare l'importanza degli aspetti teorici, è stato di ispirazione e di esempio. Inoltre, la sua totale apertura al dialogo e al confronto fanno di lui non solo un ottimo ricercatore, ma anche un incredibile mentore.

Un sentito ringraziamento va ai miei genitori, che riescono a sopportare la mia pedanteria giorno dopo giorno. In questi quattro anni sono cambiate tante cose, ma voglio mettere nero su bianco che sarò loro sempre riconoscente per la guida ed il supporto che mi hanno dato e che, tutt'ora, mi stanno dando. Dovunque mi porteranno le mie scelte, è rassicurante sapere che in loro troverò sempre il sostegno di cui ho bisogno.

A proposito di cambiamenti, durante questo viaggio, iniziato in solitaria, sulla strada ho incontrato una persona speciale, qualcuno in grado di donare serenità ed equilibrio alla mia quotidianità. Grazie al cielo ha deciso di condividere assieme a me la via e adesso ci facciamo compagnia a vicenda. Grazie Elisa, per il tuo amore e per il tuo sostegno.

Intraprendere un dottorato di ricerca e, soprattutto, portarlo a termine con successo, appagati dall'esperienza e gravidi di nuove conoscenze, ho

scoperto essere dannatamente difficile. Questo vale tanto in Italia, quanto all'Estero, e la cosa mi ha sorpreso. L'amore per la ricerca e per la divulgazione scentifica, in alcuni casi, può essere un pesante fardello. Questa prima riflessione mi ha spinto a (ri)fondare la sede di ADI a Bologna nel 2017, insieme a Niccolò, Luisa, Elisabetta, Sara e Giovanni. Ho imparato molto da questa esperienza, sia sulle persone che sulle motivazioni recondite che mi spingevano a fare quello che facevo tutti i giorni. Ma spero non sia stato uno scambio unilaterale: spero di aver dato un po' di quella passione che mi anima alle persone che ho incontrato, affinché i ricercatori di domani possano fare ancora meglio di quelli di oggi. Ancora grazie!

Infine, é chiaro che voglia ringraziare tutte le persone col quale ho stretto un legame e col quale sono solito condividere gioie e dolori. Le discussioni, nonché le attività che si fanno al di fuori del laboratorio o dell'ufficio, sono a volte più importanti di quelle coi colleghi. Quello che ho capito in questi quattro anni è che la ricerca non ha regole, perché si esplorano continuamente territori inesplorati. Uno può partire da un atollo ben conosciuto, ma, per innovare, prima o poi dovrà navigare a vista, senza sapere dove va. Non si deve mai sottovalutare l'importanza di parlare con gli altri, di ascoltare le loro storie e i loro ragionamenti, di cercare di adottare il loro modo di pensare. La condivisione è stata riconosciuta essere uno strumento indispensabile per fare ricerca, proprio perché stimola nuovi modi di pensare, di vedere le cose, di trovare le soluzioni a problemi che potrebbero tormentarti per anni. Quindi, un grazie a tutti voi, che volenti o nolenti, avete contribuito al coronamento di questo lavoro!

Bibliography

[1] Cédric Abadie, Thibaut Billard, and Thierry Lebey. "Partial discharges in motor fed by inverter: From detection to winding configuration". In: *IEEE Transactions on Industry Applications* 55.2 (2018), pp. 1332–1341.

[2] Robert B. Abernethy et al. *The new Weibull handbook*. North Palm Beach, Florida, 1996.

[3] European Environment Agency. "Towards clean and Smart mobility". In: *EEA Signals* (2016).

[4] G. Anders et al. *Motor and generator insulation life estimation*. Tech. rep. Electric Power Research Inst. (Palo Alto); Ontario Hydro (Toronto), 1992.

[5] International Air Transport Association et al. "IATA Technology Roadmap". In: *IATA Technology Roadmap 2013* (2013).

[6] Edward Balaban et al. "A diagnostic approach for electro-mechanical actuators in aerospace systems". In: *2009 IEEE Aerospace conference*. IEEE. 2009, pp. 1–13.

[7] Constantine A. Balanis. *Advanced engineering electromagnetics*. John Wiley & Sons, 1999.

[8] R. Bartnikas and J. P. Novak. "On the character of different forms of partial discharge and their related terminologies". In: *IEEE transactions on electrical insulation* 28.6 (1993), pp. 956–968.

[9]   J. P. Bellomo et al. "Influence of rise time on the dielectric behavior of stator insulation materials". In: *Proceedings of Conference on Electrical Insulation and Dielectric Phenomena-CEIDP'96*. Vol. 2. IEEE. 1996, pp. 842–845.

[10]   Nicola Bianchi and Grazia Berardi. "Analytical Approach to Design Hairpin Windings in High Performance Electric Vehicle Motors". In: *2018 IEEE Energy Conversion Congress and Exposition (ECCE)*. IEEE. 2018, pp. 4398–4405.

[11]   Berker Bilgin et al. "Making the case for electrified transportation". In: *IEEE Transactions on Transportation Electrification* 1.1 (2015), pp. 4–17.

[12]   T. Billard, T. Lebey, and F. Fresnet. "Partial discharge in electric motor fed by a PWM inverter: off-line and on-line detection". In: *IEEE Transactions on Dielectrics and Electrical Insulation* 21.3 (2014), pp. 1235–1242.

[13]   Giovanna Biondi. "Polyesterimide wire enamels: coatings with the right combination of thermal and mechanical properties for many applications". In: *Macromolecular Materials and Engineering* 293.5 (2008), pp. 361–372.

[14]   I. Boldea et al. "Automotive Electric Propulsion Systems With Reduced or No Permanent Magnets: An Overview". In: *IEEE Transactions on Industrial Electronics* 61.10 (2014), pp. 5696–5711.

[15]   N. Britun et al. "Determination of the vibrational, rotational and electron temperatures in N2and Ar–N2rf discharge". In: *Journal of Physics D: Applied Physics* 40.4 (2007), pp. 1022–1029.

[16]   IEC International Electrotechnical Commission. "IEC 60034-18-21: Rotating electrical machines. Part 18-21: Functional evaluation of insulation systems — Test procedures for wire-wound windings — Thermal evaluation and classification". In: (2013).

[17]   IEC International Electrotechnical Commission. "IEC 60034-18-31: Rotating electrical machines. Part 18-31: Functional evaluation of insulation systems — Test procedures for form-wound windings — Thermal evaluation and classification of insulation systems used in rotating machines". In: (2013).

[18] IEC International Electrotechnical Commission. "IEC 60034-18-41: Rotating electrical machines. Part 18-41: Partial discharge free electrical insulation systems (Type I) used in rotating electrical machines fed from voltage converters - Qualification and quality control tests". In: (2014).

[19] IEC International Electrotechnical Commission. "IEC 60034-18-42: Rotating electrical machines. Part 18-42: Partial discharge resistant electrical insulation systems (Type II) used in rotating electrical machines fed from voltage converters - Qualification tests". In: (2017).

[20] IEC International Electrotechnical Commission. "IEC 60034-27-5 CD: Off-line measurement of partial discharge inception voltage on winding insulation under repetitive impulse voltage". In: (2018).

[21] IEC International Electrotechnical Commission. "IEC 60172: Test procedure for the determination of the temperature index of enamelled and tape wrapped winding wires". In: (2015).

[22] IEC International Electrotechnical Commission. "IEC 60216-1: Electrical insulating materials — Thermal endurance properties. Part 1: Ageing procedures and evaluation of test results". In: (2013).

[23] IEC International Electrotechnical Commission. "IEC 60270:2000 High-voltage test techniques - Partial discharge measurements". In: (2000).

[24] IEC International Electrotechnical Commission. "IEC 60317-0-1: Specifications for particular types of winding wires. Part 0-1: General requirements - Enamelled round copper wire". In: (2013).

[25] IEC International Electrotechnical Commission. "IEC 60317-0-2: Specifications for particular types of winding wires. Part 0-2: General requirements - Enamelled rectangular copper wire". In: (2013).

[26] IEC International Electrotechnical Commission. "IEC 60505: Evaluation and qualification of electrical insulation systems". In: (2011).

[27] IEC International Electrotechnical Commission. "TS 61934: Electrical insulating materials and systems. Electrical measurement of partial discharges (PD) under short rise time and repetitive voltage impulses". In: (2011).

[28] Ian Cotton et al. "Design considerations for higher electrical power system voltages in aerospace vehicles". In: *2016 IEEE International Power Modulator and High Voltage Conference (IPMHVC)*. IEEE. 2016, pp. 57–61.

[29] Denis Cousineau. "The fallacy of large shape parameters when using the two-parameter Weibull distribution". In: *IEEE Transactions on Dielectrics and Electrical Insulation* 18.6 (2011), pp. 2095–2102.

[30] Thomas W. Dakin. "Electrical insulation deterioration treated as a chemical rate phenomenon". In: *Transactions of the American Institute of Electrical Engineers* 67.1 (1948), pp. 113–122.

[31] SK Dhali and PF Williams. "Two-dimensional studies of streamers in gases". In: *Journal of applied physics* 62.12 (1987), pp. 4696–4707.

[32] J. Dutton. "A survey of electron swarm data". In: *Journal of Physical and Chemical Reference Data* 4.3 (1975), pp. 577–856.

[33] A. M. El-Refaie. "Motors/Generators for traction/propulsion applications: a review". In: *IEEE Transactions in Vehicle Applications* 5.1 (2013), pp. 90–99.

[34] Davide Fabiani. *Accelerated Degradation of AC Motor Insulation due to Voltage Waveforms Generated by Adjustable Speed Drives*. 2003.

[35] Davide Fabiani et al. "Relation between space charge accumulation and partial discharge activity in enameled wires under PWM-like voltage waveforms". In: *IEEE Transactions on Dielectrics and Electrical Insulation* 11.3 (2004), pp. 393–405.

[36] M. Fenger and Greg C. Stone. "Investigations into the effect of humidity on stator winding partial discharges". In: *IEEE transactions on dielectrics and electrical insulation* 12.2 (2005), pp. 341–346.

[37] M. A. Folkard and S. C. Haydon. "Experimental investigations of ionization growth in nitrogen. I". In: *Journal of Physics B: Atomic and Molecular Physics* 6.1 (1973), p. 214.

[38] Alexander Fridman. *Plasma chemistry*. Cambridge university press, 2008.

[39] S. Fuss et al. "Negative emissions—Part 2: Costs, potentials and side effects". In: *Environmental Research Letters* 13.6 (2018), p. 063002.

[40] I Gallimberti. "The mechanism of the long spark formation". In: *Le Journal de Physique Colloques* 40.C7 (1979), pp. 193–250.

[41] Hans Geiger and Ernest Rutherford. "LVII. Photographic registration of α particles". In: *The London, Edinburgh, and Dublin Philosophical Magazine and Journal of Science* 24.142 (1912), pp. 618–623.

[42] Richard M Goody and Yuk Ling Yung. *Atmospheric radiation: theoretical basis*. Oxford university press, 1995.

[43] U.S. Government. *United States Environmental Protection Agency (EPA)*. 1970. URL: http://www.epa.gov/climate-indicators (visited on 08/01/2016).

[44] Emil Julius Gumbel. *Statistics of extremes*. Courier Corporation, 2012.

[45] Jürgen Hagedorn, Florian Sell-Le Blanc, and Jürgen Fleischer. *Handbook of Coil Winding*. Springer, 2018.

[46] G. J. M. Hagelaar and L. C. Pitchford. "Solving the Boltzmann equation to obtain electron transport coefficients and rate coefficients for fluid models". In: *Plasma Sources Science and Technology* 14.4 (2005), p. 722.

[47] Gerjan Hagelaar. *BOLSIG+ - Electron Boltzmann equation solver*. 2013. URL: https://www.bolsig.laplace.univ-tlse.fr/ (visited on 08/05/2019).

[48] H. Hasegawa, H. Date, and M. Shimozuma. "Electron swarm parameters in water vapour". In: *Journal of Physics D: Applied Physics* 40.8 (2007), p. 2495.

[49] Naoki Hayakawa and Hitoshi Okubo. "Lifetime characteristics of nanocomposite enameled wire under surge voltage application". In: *IEEE Electrical insulation magazine* 24.2 (2008), pp. 22–27.

[50] Naoki Hayakawa, Fuminobu Shimizu, and Hitoshi Okubo. "Estimation of partial discharge inception voltage of magnet wires under inverter surge voltage by volume-time theory". In: *IEEE Transactions on Dielectrics and Electrical Insulation* 19.2 (2012), pp. 550–557.

[51] Naoki Hayakawa et al. "Time variation of partial discharge activity leading to breakdown of magnet wire under repetitive surge voltage application". In: *IEEE Transactions on Dielectrics and Electrical Insulation* 15.6 (2008), pp. 1701–1706.

[52] Jane Hodgkinson and Ralph P Tatam. "Optical gas sensing: a review". In: *Measurement Science and Technology* 24.1 (2012), pp. 1–59.

[53] Yannis L. Karnavas, Ioannis D. Chasiotis, and Emmanouil L. Peponakis. "Cooling system design and thermal analysis of an electric vehicle's in-wheel PMSM". In: *2016 XXII International Conference on Electrical Machines (ICEM)*. IEEE. 2016, pp. 1439–1445.

[54]   Martin Kaufhold et al. "Electrical stress and failure mechanism of the winding insulation in PWM-inverter-fed low-voltage induction motors". In: *IEEE Transactions on industrial electronics* 47.2 (2000), pp. 396–402.

[55]   Martin Kaufhold et al. "Failure mechanism of the interturn insulation of low voltage electric machines fed by pulse-controlled inverters". In: *IEEE Electrical insulation magazine* 12.5 (1996), pp. 9–16.

[56]   L. J. Kieffer. "JILA Information Center Report 13". In: 1 (1973), p. 973.

[57]   Yusuke Kikuchi et al. "Effects of ambient humidity and temperature on partial discharge characteristics of conventional and nanocomposite enameled magnet wires". In: *IEEE Transactions on Dielectrics and Electrical Insulation* 15.6 (2008), pp. 1617–1625.

[58]   Ken Kimura et al. "$PDIV$ characteristics of twisted-pair of magnet wires with repetitive impulse voltage". In: *IEEE Transactions on Dielectrics and Electrical Insulation* 14.3 (2007), pp. 744–750.

[59]   E. Kuffel, W. S. Zaengl, and J. Kuffel. *High voltage engineering - Fundamentals*. Elsevier, 2000.

[60]   Laboratoire des Plasmas et Conversion d'Energie LAPLACE. *LXCat*. 2009. URL: https://fr.lxcat.net/home/ (visited on 08/05/2019).

[61]   S. A. Lawton and A. V. Phelps. "Excitation of the $b^1\Sigma_g^+$ state of O2 by low energy electrons". In: *The Journal of Chemical Physics* 69.3 (1978), pp. 1055–1068.

[62]   Wei Li and J. P. Fielding. "Preliminary study of EMA landing gear actuation". In: *Proc. 28th Int. Congress of the Aeronautical Sciences, Brisbane, Australia*. 2012, pp. 23–28.

[63]   Leonard Benedict Loeb. *Basic processes of gaseous electronics*. University of California Press, 1960.

[64]   Vincenzo Madonna, Paolo Giangrande, and Michael Galea. "Electrical Power Generation in Aircraft: Review, Challenges, and Opportunities". In: *IEEE transactions on transportation electrification* 4.3 (2018), pp. 646–659.

[65]   Kenta Maeda et al. "Partial Discharge Inception Voltage of Enameled Cellular Wire under Impulse Voltage". In: *2018 IEEE 2nd International Conference on Dielectrics (ICD)*. IEEE. 2018, pp. 1–6.

[66]   N. H. Malik. "Streamer breakdown criterion for compressed gases". In: *IEEE Transactions on Electrical Insulation* 5 (1981), pp. 463–467.

[67] Satoshi Matsumoto et al. "Partial discharge characteristics of twisted magnet wire under high frequency AC voltage". In: *Proceedings of 2014 International Symposium on Electrical Insulating Materials*. IEEE. 2014, pp. 57–60.

[68] Giovanni Mazzanti. "The combination of electro-thermal stress, load cycling and thermal transients and its effects on the life of high voltage ac cables". In: *IEEE Transactions on Dielectrics and Electrical Insulation* 16.4 (2009), pp. 1168–1179.

[69] J. M. Meek and Craggs J. D. *Electrical breakdown of gases*. Oxford University Press, 1953.

[70] Doris Ragna Meyer et al. "Influence of impulse voltage repetition frequency on $RPDIV$ in partial vacuum". In: *IEEE Transactions on Dielectrics and Electrical Insulation* 25.3 (2018), pp. 873–882.

[71] Davoud Esmaeil Moghadam et al. "Parameters affecting the turn insulation lifetime and durability". In: *IEEE Transactions on Dielectrics and Electrical Insulation* 25.2 (2018), pp. 516–523.

[72] Gian Carlo Montanari and Luciano Simoni. "Aging phenomenology and modeling". In: *IEEE Transactions on Electrical Insulation* 28.5 (1993), pp. 755–776.

[73] V. M. Montsinger. "Loading transformers by temperature". In: *Transactions of the American Institute of Electrical Engineers* 49.2 (1930), pp. 776–790.

[74] Kyoung Sup Moon, Jihwa Lee, and Ki-Woong Whang. "Electron ejection from MgO thin films by low energy noble gas ions: Energy dependence and initial instability of the secondary electron emission coefficient". In: *Journal of applied physics* 86.7 (1999), pp. 4049–4051.

[75] R Morrow and JJ Lowke. "Streamer propagation in air". In: *Journal of Physics D: Applied Physics* 30.4 (1997), pp. 614–627.

[76] Daisuke Muto et al. "A study on partial discharge phenomena of winding wires". In: *Furukawa Review* 45 (2014), pp. 13–21.

[77] L. Niemeyer. "A generalized approach to partial discharge modeling". In: *IEEE transactions on Dielectrics and Electrical insulation* 2.4 (1995), pp. 510–528.

[78] J. P. Novak and R. Bartnikas. "Theoretical and experimental investigations on the process of high-pressure discharge development". In: *IEEE Transactions on Plasma Science* 19.2 (1991), pp. 95–101.

[79] U.S. Committee on Extension to the Standard Atmosphere. *US Standard Atmosphere*. National Oceanic and Atmospheric Administration, 1976.

[80] A. Pedersen. "On the electrical breakdown of gaseous dielectrics-an engineering approach". In: *IEEE transactions on electrical insulation* 24.5 (1989), pp. 721–739.

[81] W Pfeiffer and M Paede. "About the influence of the frequency on the partial discharge characteristics of enamelled wires". In: *Proceedings: Electrical Insulation Conference and Electrical Manufacturing and Coil Winding Conference (Cat. No. 99CH37035)*. IEEE. 1999, pp. 485–488.

[82] L. C. Pitchford and V. Phelps. "Comparative calculations of electron-swarm properties in N2 at moderate E/N values". In: *Physical Review A* vol. 5 (1982), pp. 540–554.

[83] Eraldo Preci et al. "Hairpin and Random Windings: Advantages and Disadvantages for Automotive Applications". In: *IECON 2019 - 45th Annual Conference of the IEEE Industrial Electronics Society*. IEEE. 2019.

[84] D. A. Price, J Lucas, and J. L. Moruzzi. "Ionization in oxygen-hydrogen mixtures". In: *Journal of Physics D: Applied Physics* 5.7 (1972), p. 1249.

[85] Heinz Raether. "Über den Aufbau von Gasentladungen. II". In: *Zeitschrift für Physik* 117.7 (1941), pp. 524–542.

[86] K. Rajashekara. "Parallel between More Electric Aircraft and ElectricHybrid Vehicle Power Conversion Technologies". In: *IEEE Electrification Magazine* 2.2 (2014), pp. 50–60.

[87] C. R. Rao and G. R. G. Raju. "Growth of ionization currents in dry air at high values of E/N". In: *Journal of Physics D: Applied Physics* 4.4 (1971), p. 494.

[88] J. Richnow et al. "Influence of different impregnation methods and resins on thermal behavior and lifetime of electrical stators". In: *2014 4th International Electric Drives Production Conference (EDPC)*. IEEE. 2014, pp. 1–7.

[89] Pallavi Saxena and Vaishali Naik. *Air Pollution: Sources, Impacts and Controls*. CABI, 2018.

[90] E. Sili et al. "Polyimide lifetime under partial discharge aging: effects of temperature, pressure and humidity". In: *IEEE Transactions on Dielectrics and Electrical Insulation* 20.2 (2013), pp. 435–442.

[91] Luciano Simoni. *Dielettrici: proprietà e comportamento nel tempo*. Cooperativa Libraria Universitaria Editrice Bologna, 1974.

[92] Ray Simpkin. "Derivation of Lichtenecker's logarithmic mixture formula from Maxwell's equations". In: *IEEE Transactions on Microwave Theory and Techniques* 58.3 (2010), pp. 545–550.

[93] Solvay. *Torlon® PAI - Design guide*. 2015.

[94] Greg C. Stone et al. *Electrical insulation for rotating machines: design, evaluation, aging, testing, and repair*. Vol. 21. John Wiley & Sons, 2004.

[95] Jurgen Symynck and Filip De Bal. "Monte Carlo pivotal confidence bounds for Weibull analysis, with implementations in R". In: *New Technologies and Products in Machine Manufacturing Technologies* 18.1 (2011), pp. 43–50.

[96] Joseph John Thomson. "On the structure of atom: an investigation of the stability and periods of oscillation of a number of corpuscles arranged at equal intervals around the circumference of a circle; with applications of the results to the theory of atomic structure". In: *Phil. Mag., ser. 6* 7 (1904), pp. 237–265.

[97] Peng Wang et al. "Effect of repetitive impulsive voltage duty cycle on partial discharge features and insulation endurance of enameled wires for inverter-fed low voltage machines". In: *IEEE Transactions on Dielectrics and Electrical Insulation* 24.4 (2017), pp. 2123–2131.

[98] Peng Wang et al. "The influence of repetitive square wave voltage rise time on partial discharge inception voltage". In: *2016 IEEE Conference on Electrical Insulation and Dielectric Phenomena (CEIDP)*. IEEE. 2016, pp. 759–762.

[99] Waloddi Weibull. "A statistical distribution function of wide applicability". In: *Journal of applied mechanics* 18.3 (1951), pp. 293–297.

[100] C. Yamabe, S. J. Buckman, and A. V. Phelps. "Measurement of free-free emission from low-energy-electron collisions with Ar". In: *Physical Review A* 27.3 (1983), p. 1345.

[101] Weijun Yin. "Failure mechanism of winding insulations in inverter-fed motors". In: *IEEE Electrical Insulation Magazine* 13.6 (1997), pp. 18–23.

[102] M. Yousfi et al. "Electron-molecule collision cross sections and electron swarm parameters in some atmospheric gases (N2, O2, CO2 and H2O)". In: *Data base collection* 1 (1987).

[103] Markus Zahn et al. "Dielectric properties of water and water/ethylene glycol mixtures for use in pulsed power system design". In: *Proceedings of the IEEE* 74.9 (1986), pp. 1182–1221.